

OPEN HEAVY FLAVOR AND OTHER HARD PROBES IN ULTRA-RELATIVISTIC HEAVY-ION COLLISIONS

Dissertation

zur Erlangung des Doktorgrades
der Naturwissenschaften

vorgelegt beim Fachbereich Physik
der Johann Wolfgang Goethe-Universität
in Frankfurt am Main

von

Jan Uphoff

aus Essen

Frankfurt am Main 2013
(D 30)

Vom Fachbereich Physik (13) der Johann Wolfgang Goethe-Universität
als Dissertation angenommen.

Dekan: Prof. Dr. Joachim Stroth

Gutachter: Prof. Dr. Carsten Greiner, Prof. Dr. Marcus Bleicher

Datum der Disputation:

Contents

Deutsche Zusammenfassung	xi
1. Introduction	1
2. QCD and heavy-ion collisions	5
2.1. The standard model and QCD	5
2.1.1. Running coupling and asymptotic freedom	7
2.1.2. Confinement	8
2.1.3. The phase diagram of QCD	8
2.2. Ultra-relativistic heavy-ion collisions	9
2.2.1. Overview of results from RHIC and LHC	11
2.2.2. Collective flow	12
2.2.3. Hard probes	14
3. Partonic cross sections	25
3.1. Elastic heavy quark scattering	26
3.1.1. Elastic heavy quark scattering with a gluon in vacuum	27
3.1.2. DEBYE screening in a medium	29
3.1.3. Running coupling	30
3.1.4. Elastic heavy quark scattering with a gluon in medium	32
3.1.5. Elastic heavy quark scattering with a light quark in medium	32
3.1.6. Average value of the running coupling in a thermal medium	34
3.2. Inelastic heavy quark scattering	36
3.2.1. GUNION-BERTSCH calculation for heavy quark scattering with a light quark	37
3.2.2. GUNION-BERTSCH calculation for heavy quark scattering with a gluon	46
3.2.3. Radiative heavy quark processes in FEYNMAN gauge	50
3.2.4. Dead cone effect	51
3.2.5. Total cross section	57
3.2.6. Formation time of a gluon emitted off a heavy quark	59
3.2.7. LANDAU-POMERANCHUK-MIGDAL effect	60
3.2.8. Phase space constraints due to kinematics and the LANDAU-POMERANCHUK-MIGDAL effect	62
3.2.9. Comparison of GUNION-BERTSCH and exact cross sections	65
3.3. J/ψ dissociation and regeneration	74
4. Parton cascade BAMPS	77
4.1. The framework	77
4.2. Details of the numerical implementation of the cross sections	83

4.3. Initial heavy quark distribution—MC@NLO	84
4.4. Initial J/ψ production	87
4.5. Initial light parton distribution—PYTHIA and minijet model	91
4.6. Non-heavy-flavor BAMPS studies	92
5. Energy loss of heavy quarks	95
5.1. Elastic energy loss in a static medium	95
5.1.1. s , t , and u channel—hard part	97
5.1.2. t channel—soft part	98
5.1.3. Total energy loss	100
5.1.4. From quantum statistics to the classical BOLTZMANN limit	100
5.1.5. Comparison to BORN cross section	101
5.1.6. Running coupling	103
5.2. Elastic energy loss in a flowing medium	104
5.3. Elastic vs. radiative energy loss in a static medium	107
6. Open heavy flavor in heavy-ion collisions	121
6.1. Elliptic flow and nuclear modification factor from elastic collisions	121
6.1.1. RHIC	121
6.1.2. LHC	128
6.2. Elliptic flow and nuclear modification factor from elastic and radiative processes	137
6.2.1. Comparison between heavy and light flavor	138
6.2.2. Open heavy flavor at RHIC and LHC with improved screening	143
7. J/ψ in heavy-ion collisions	151
7.1. J/ψ suppression	152
7.2. Elliptic flow of J/ψ	154
8. Conclusions	159
8.1. Summary	159
8.2. Outlook	163
A. Appendices	167
A.1. Natural units	167
A.2. MANDELSTAM variables	167
A.3. Binary light parton cross sections	168
A.3.1. Matrix elements	168
A.3.2. Overview of the processes	172
A.4. Detailed balance	174
A.5. GLAUBER model	174
A.6. Sampling with the rejection method and the METROPOLIS algorithm	175
Bibliography	179
Index	205
Acknowledgements	207

List of Figures

2.1. Running coupling with measurements	7
2.2. QCD phase diagram	9
2.3. Anisotropic flow coefficients at LHC	13
2.4. R_{AA} of light hadrons at SPS, RHIC, and LHC	16
2.5. R_{AA} of D mesons and v_2 of heavy flavor electrons at LHC	18
2.6. J/ψ R_{AA} at LHC	22
3.1. FEYNMAN diagrams for $gQ \rightarrow gQ$	26
3.2. FEYNMAN diagram for $qQ \rightarrow qQ$	26
3.3. Schematic illustration of a $2 \rightarrow 2$ process	27
3.4. Parameterization of the running coupling	31
3.5. Total cross section of $gc \rightarrow gc$	33
3.6. Differential cross section of $gc \rightarrow gc$	34
3.7. Average value of running coupling in thermal medium	35
3.8. FEYNMAN diagrams for $qQ \rightarrow qQg$	38
3.9. FEYNMAN diagram for $qQ \rightarrow qQg$ with notation for momenta	38
3.10. FEYNMAN diagrams for the t channel of the process $gQ \rightarrow gQg$	48
3.11. Angle dependence of dead cone factor of DOKSHITZER and KHARZEEV	53
3.12. Angle dependence of dead cone factor for $M/\sqrt{s} = 0.1$	54
3.13. Angle dependence of dead cone factor for $M/\sqrt{s} = 0.8$	55
3.14. Angle and mass dependence of dead cone factor	55
3.15. Comparison of dead cone factor to DOKSHITZER and KHARZEEV result	56
3.16. Kinematics of gluon radiation off a heavy quark jet	59
3.17. Illustration of medium-induced gluon radiation	61
3.18. Illustration of reference frames for the LPM cut-off	62
3.19. Phase space sampling of emitted gluon off heavy quark with $E = 3$ GeV.	64
3.20. Phase space sampling of emitted gluon off heavy quark with $E = 2, 10, 50$ GeV.	65
3.21. Differential cross section in y for $qq' \rightarrow qq'g$	68
3.22. Differential cross section in k_{\perp} and q_{\perp} for $qq' \rightarrow qq'g$	69
3.23. Differential cross section in y for $gg \rightarrow ggg$	70
3.24. Center-of-mass energy dependence of total cross section ratio of improved GUNION-BERTSCH and exact matrix elements for different processes	71
3.25. Screening cut-off dependence of total cross section ratio of improved GUNION-BERTSCH and exact matrix elements for different processes	72
3.26. Differential cross section in y for $qq' \rightarrow qq'g$ with standard DEBYE screening and cut-off procedure	73
3.27. As Figure 3.25 with the exact $2 \rightarrow 2$ gluon propagator	73
3.28. Differential cross section in y for $qQ \rightarrow qQg$	75

3.29. As Figure 3.27 for different heavy quark masses	75
4.1. Evolution of heavy-ion collision in BAMPS simulation	80
4.2. Sketch of heavy flavor in BAMPS	81
4.3. PETERSON fragmentation function	82
4.4. Decay distribution of heavy flavor electrons	83
4.5. Heavy flavor electron spectrum in p+p collisions at $\sqrt{s} = 200$ GeV	85
4.6. Heavy flavor particle spectra in p+p collisions at $\sqrt{s} = 7$ TeV	86
4.7. Differential J/ψ production cross section in p+p collisions at RHIC	89
4.8. As Figure 4.7 for LHC	89
4.9. Differential J/ψ production cross section in Au+Au collisions at RHIC with only cold nuclear matter effects	91
5.1. Elastic energy loss of charm quark in static medium I	101
5.2. Elastic energy loss of charm quark in flowing medium	106
5.3. Elastic energy loss of charm quark in static medium II	107
5.4. Rate and energy loss per collision of charm quark in static medium	109
5.5. Elastic and radiative energy loss of light and heavy quarks with constant coupling and $\kappa_t = 1$	110
5.6. Angle distribution of emitted gluon for light, charm, and bottom jets	111
5.7. As Figure 5.5 for running coupling	112
5.8. As Figure 5.5 for running coupling and $\kappa_t = 0.2$	112
5.9. Elastic and radiative energy loss of charm quark for constant or running coupling and different κ_t	113
5.10. Energy loss per collision of charm quark for elastic and radiative processes	114
5.11. Collision rate of charm quark for elastic and radiative processes	114
5.12. Radiative collision rate of gluon and light quark with a fixed mean free path	115
5.13. Radiative collision rate of gluon and light quark with iterative mean free path	116
5.14. Influence of LPM effect on radiative energy loss of charm quark	117
5.15. Influence of LPM effect on radiative energy loss of light and heavy quarks	117
5.16. Influence of mean free path choice on radiative energy loss of gluon, light quark, and charm quark	118
6.1. Heavy flavor electron v_2 and R_{AA} at RHIC for $n_f = 0 + 2$	123
6.2. Heavy flavor electron v_2 and R_{AA} at RHIC for $n_f = 3 + 2$	125
6.3. Heavy flavor electron R_{AA} in central events at RHIC	126
6.4. Heavy flavor electron v_2 and R_{AA} at RHIC for different heavy quark formation times	127
6.5. D meson R_{AA} at RHIC	128
6.6. Heavy flavor electron v_2 in minimum bias events at RHIC	129
6.7. Heavy flavor electron R_{AA} at LHC	130
6.8. Heavy flavor muon R_{AA} at LHC	131
6.9. D meson R_{AA} at LHC	132
6.10. Non-prompt J/ψ R_{AA} at LHC	133
6.11. N_{part} dependence of D meson and non-prompt J/ψ R_{AA} at LHC	133
6.12. Muon, electron, non-prompt J/ψ , and D meson v_2 at LHC	134

6.13. D meson v_2 at LHC	135
6.14. Heavy flavor electron v_2 at LHC	135
6.15. Mean transport cross section and transport rate at LHC	137
6.16. R_{AA} of gluons, light and charm quarks at LHC	140
6.17. Charged hadron R_{AA} at LHC	141
6.18. Charged hadron and D meson R_{AA} at LHC	141
6.19. Charged hadron, D meson, and non-prompt J/ψ R_{AA} at LHC	142
6.20. Heavy flavor electron v_2 and R_{AA} at RHIC	144
6.21. Energy loss and transport cross section of charm quarks in static medium . . .	145
6.22. D meson R_{AA} at LHC	146
6.23. Non-prompt J/ψ R_{AA} at LHC	146
6.24. Heavy flavor electron R_{AA} at LHC	147
6.25. Heavy flavor electron v_2 at LHC	147
6.26. D meson v_2 at LHC	148
7.1. Time dependence of J/ψ R_{AA} at RHIC	152
7.2. As Figure 7.1 with cold nuclear matter effects and J/ψ formation time	153
7.3. As Figure 7.2 compared to Tsinghua model	154
7.4. N_{part} dependence of J/ψ R_{AA} at RHIC	155
7.5. Elliptic flow of J/ψ at RHIC	156
7.6. Elliptic flow of secondary J/ψ at RHIC	157
8.1. Word cloud with most frequent words	163
A.1. Total cross sections of various processes with a constant coupling	173
A.2. As Figure A.1 with a running coupling	173

List of Tables

2.1. Overview of open heavy flavor models	19
5.1. Useful integrals of equilibrium particle distribution functions	98

Deutsche Zusammenfassung

In ultrarelativistischen Schwerionenkollisionen werden Schwerionen auf nahezu Lichtgeschwindigkeit beschleunigt und anschließend in Detektoren zur Kollision gebracht. Bei diesem Vorgang wird sehr viel Energie in einen winzigen Raumbereich deponiert, so dass bei einer Temperatur von mehr als einer Billion Grad Celsius eine besondere Form von Materie entsteht – das Quark-Gluon-Plasma (QGP). Aufgrund der hohen Energiedichte können einige der elementarsten Bausteine der Materie, die Quarks und Gluonen, frei miteinander wechselwirken und sind daher nicht mehr in Protonen und Neutronen eingeschlossen. Ihre Wechselwirkungen untereinander werden durch die starke Kraft beschrieben, welche – neben der schwachen, elektromagnetischen und Gravitationskraft – eine der vier Kräfte des Standardmodells der Teilchenphysik darstellt. Durch die Untersuchung von Schwerionenkollisionen lassen sich somit Rückschlüsse auf die Quantenchromodynamik (QCD) ziehen, welche die zugrundeliegende Theorie der starken Kraft ist.

Zahlreiche experimentelle Messungen, z.B. an dem Relativistic Heavy-Ion Collider (RHIC) am Brookhaven National Laboratory, USA, oder dem Large Hadron Collider (LHC) am CERN bei Genf, Schweiz, weisen darauf hin, dass das QGP interessante Eigenschaften besitzt. Beispielsweise verhält es sich wie eine nahezu ideale Flüssigkeit mit einem kleinen Verhältnis von Scherviskosität zu Entropiedichte, wie der Vergleich des gemessenen kollektiven Flusses mit hydrodynamischen Modellen zeigt. Hierbei ist vor allem der elliptische Fluss v_2 zu erwähnen, welcher durch den zweiten FOURIER-Koeffizienten der azimuthalen Winkelverteilung der gemessenen Teilchen gegeben ist. Ein anderer bemerkenswerter Fund ist das sogenannte *jet quenching*. Demnach deponieren hochenergetische Teilchen (Jets) einen großen Teil ihrer Energie im entstehenden Medium. Eine experimentelle Observable hierfür ist der nukleare Modifikationsfaktor R_{AA} , der das Verhältnis der Anzahl von Jets in Schwerionenkollisionen und in skalierten Proton-Proton-Kollisionen angibt. Aus der Untersuchung von Schwerionenkollisionen kann man zudem Rückschlüsse auf die ersten Mikrosekunden nach dem Urknall ziehen, da hier die Materie so heiß und verdichtet war, dass das gesamte Universum aus einem einzigen großen Quark-Gluon-Plasma bestand.

Sogenannte harte Sonden (*hard probes*) sind besonders geeignet, um das QGP zu untersuchen. Ihr Name weist bereits darauf hin, dass diese Teilchen in harten Prozessen mit einem großen Impulstransfer erzeugt werden. Beispiele für harte Sonden sind die bereits genannten Jets, aber auch schwere Quarks (relevant sind vor allem Charm- und Bottom-Quarks) aufgrund ihrer großen Massen. Da für die Produktion dieser harten Teilchen viel Energie aufgebracht werden muss, können sie nur in anfänglichen harten Parton-Parton-Stößen der kollidierenden Kerne oder in einer sehr frühen Phase des QGP erzeugt werden und geben dadurch Einblicke in das Verhalten des Plasmas kurz nach seiner Entstehung. Weil die harten Teilchen so früh produziert werden, propagieren sie zudem lange Zeit durch das QGP, wobei sie wechselwirken, Energie verlieren sowie am kollektiven Fluss teilnehmen und daher wertvolle Informationen über das entstandene Medium tragen.

Eine bedeutende Komplikation bei der Erforschung des QGP ist die Tatsache, dass es

nur indirekt untersucht werden kann. Nach der Kollision der Schwerionen expandiert das produzierte QGP, wodurch seine Temperatur fällt und die Quarks und Gluonen hadronisieren. Die entstandenen Hadronen oder ihre Zerfallsprodukte werden dann in Detektoren gemessen, die den Kollisionspunkt umschließen. Da der Quarkflavor – im Fall schwerer Quarks Charm bzw. Bottom – in der QCD eine Erhaltungsgröße ist, kann aber aus den gemessenen D - bzw. B -Mesonen (sie bestehen aus einem schweren und einem leichten Quark) – oder genauer gesagt aus ihren Zerfallsprodukten – auf das Charm- bzw. Bottom-Quark-Spektrum geschlossen werden. Schwere Quarks sind somit eine eindeutige Sonde für die Untersuchung des QGP.

Von besonderer Bedeutung sind auch Mesonen, die sich aus schweren Quarks und Antiquarks zusammensetzen, wie zum Beispiel das J/ψ -Meson bestehend aus Charm- und Anticharm-Quark. Rechnungen der Gittertheorie weisen darauf hin, dass die schweren J/ψ -Mesonen zu einem gewissen Grad im Medium überleben können. Nur wenn die Temperatur über die Dissoziationstemperatur steigt, schmelzen sie im QGP. Bei niedrigerer Temperatur ist es sogar möglich, ein neues J/ψ -Meson durch ein Charm- und Anticharm-Quark zu erzeugen. Aus diesem Wechselspiel zwischen Dissoziation und Regeneration können interessante Rückschlüsse auf die Eigenschaften des produzierten Mediums gezogen werden, wie zum Beispiel dessen Temperaturevolution.

Das verwendete Modell

Aufgrund der enormen Anzahl an erzeugten Quarks und Gluonen im QGP und der großen Komplexität ihrer Wechselwirkungen untereinander sind numerische Simulationen ein vielversprechendes Mittel, um diesen Materiezustand von der theoretischen Seite näher zu untersuchen. In dieser Arbeit wird hierfür das 3+1-dimensionale Transportmodell *Boltzmann Approach to Multi-Parton Scatterings* (BAMPS) angewendet, das numerisch die Boltzmann-Transportgleichung löst. Dabei werden alle während der Schwerionenkollision entstehenden Quarks und Gluonen durch Raum und Zeit propagiert und können in $2 \rightarrow 2$ und $2 \leftrightarrow 3$ Kollisionen miteinander wechselwirken. Die Wirkungsquerschnitte für diese zahlreichen Kollisionen werden im Rahmen der perturbativen Quantenchromodynamik (pQCD) ausgerechnet. Mit Hilfe von BAMPS wird versucht, die Realität mit dem theoretischen, uns zur Verfügung stehenden Wissen möglichst genau in ein Modell abzubilden und damit Vorhersagen für verschiedene Observablen zu machen, die experimentell überprüft werden können.

Als Teil dieser Arbeit sind alle relevanten elastischen und radiativen Wechselwirkungen schwerer Quarks mit anderen Teilchen in BAMPS implementiert worden. Der Wirkungsquerschnitt für diese Interaktionen ist mit pQCD in führender Ordnung errechnet. Da dieser für lange Reichweiten divergiert, die Interaktionen aber in einem Plasma stattfinden, kann er mit einer Abschirmmasse regularisiert werden, welche von der Größenordnung der (QCD-)DEBYE-Masse ist. Der Vergleich mit Rechnungen höherer Ordnung, die resummierte harte thermische Schleifenkorrekturen (*hard thermal loops*, HTL) enthalten, zeigt, dass der genaue Wert der Abschirmmasse μ kleiner als die DEBYE-Masse m_D ist, genaugenommen $\mu^2 = \kappa_t m_D^2$ mit $\kappa_t = 1/(2e) \approx 0.2$. Zudem ist in BAMPS im Zuge dieser Arbeit für alle Prozesse – sowohl für leichte als auch schwere Teilchen – die laufende Kopplung der QCD implementiert worden, welche in vielen anderen Modellen als konstant angenommen wird.

Für radiative $2 \rightarrow 3$ Bremsstrahlungsprozesse wird in der vorliegenden Dissertation die pQCD-Rechnung in der sogenannten GUNION-BERTSCH-Näherung (GB-Näherung) für weiche

Impulsüberträge auf endliche Massen schwerer Quarks erweitert. In dieser Näherung faktoriisiert das Matrixelement in einen elastischen Anteil und einen Faktor, der die Emission des abgestrahlten Gluons beschreibt. Im Zuge dieser Rechnung fiel jedoch auf, dass das in der Literatur weit verbreitete, originale GB-Matrixelement für masselose Teilchen in Vorwärts- und Rückwärtsrapidität des abgestrahlten Gluons vom exakten Ergebnis des Matrixelements deutlich abweicht. Basierend auf einer detaillierten analytischen Rechnung führen wir eine verbesserte Version des GB-Matrixelements ein, das in allen relevanten Phasenraumbereichen sehr gut mit dem exakten Resultat übereinstimmt, wie unsere umfangreichen numerischen Vergleiche des totalen Wirkungsquerschnitts und differentieller Größen zeigen. Diese Ergebnisse verbessern nicht nur den radiativen Wirkungsquerschnitt schwerer Quarks in der GB-Approximation, sondern auch das in der Literatur weit verbreitete GB-Matrixelement für leichte Partonen. Weiterhin berechnen wir das Matrixelement für schwere Quarks in FEYNMAN-Eichung (im Gegensatz zur Lichtkegeleichung im GB-Fall) sowie leicht unterschiedlichen Approximationen und zeigen, dass dieses Ergebnis konsistent mit unserer GB-Rechnung ist. Analog zu elastischen Streuungen wurde auch für radiative Prozesse die laufende Kopplung in BAMPS eingebaut.

Weiterhin wird explizit gezeigt, dass der sogenannte *dead-cone*-Effekt in unserem Ergebnis der verbesserten GB-Rechnung für schwere Quarks enthalten ist. Dieser von DOKSHITZER und KHARZEEV eingeführte Effekt besagt, dass die Gluonabstrahlung von einem schweren Quark bei kleinen Abstrahlwinkeln unterdrückt ist. Unser Ausdruck für den Unterdrückungsfaktor ist für alle Winkel und alle Werte der Masse von schweren Quarks gültig und verallgemeinert somit den Ausdruck von DOKSHITZER und KHARZEEV, der nur für kleine Winkel und kleine Massen gilt. Wichtig für radiative Prozesse ist der sogenannte LANDAU-POMERANCHUK-MIGDAL-Effekt (LPM-Effekt), der die Unterdrückung mehrfacher Gluonbremsstrahlung in einem Medium durch Interferenzeffekte beschreibt. Der LPM-Effekt ist phänomenologisch über das Abschneiden großer Formationszeiten des abgestrahlten Gluons in BAMPS implementiert, wobei ebenfalls die endliche Masse schwerer Quarks berücksichtigt ist.

Energieverlust schwerer Quarks im statischen Medium

Als analytische Referenz wird die HTL-Rechnung von PESHIER und PEIGNE für den elastischen Energieverlust von energetischen schweren Quarks in einem statischen thermischen Medium mit Quantenstatistik dargelegt und auf Boltzmann-Statistik erweitert, um sie mit numerischen BAMPS-Simulationen, in denen alle Teilchen als Boltzmann-Teilchen behandelt werden, vergleichen zu können. Mit der HTL-inspirierten DEBYE-Abschirmung ($\kappa_t = 0.2$) wird eine sehr gute Übereinstimmung zwischen BAMPS und dem analytischen Resultat gefunden. Weiterhin berechnen wir eine analytische Formel für den Energieverlust schwerer Quarks in einem fließenden Medium, die ebenfalls eine hervorragende Übereinstimmung mit den numerischen BAMPS-Resultaten zeigt.

In einer umfangreichen numerischen Studie wird der elastische und radiative Energieverlust von Charm- und Bottom-Quarks in einem statischen Medium für Standard- ($\kappa_t = 1$) und HTL-inspirierter ($\kappa_t = 0.2$) DEBYE-Abschirmung sowie laufender und konstanter Kopplung gegenübergestellt und diskutiert. Obwohl die HTL-DEBYE-Abschirmung den totalen Energieverlust pro Einheitslänge aus der HTL-Rechnung korrekt reproduziert, kann aus diesem Vergleich keine Aussage getroffen werden, ob auch differentielle Größen wie der Energieverlust pro

Kollision oder die mittlere freie Weglänge richtig beschrieben werden. Die bei der Abschirmung mit $\kappa_t = 0.2$ auftretende sehr kleine mittlere freie Weglänge für elastische Kollisionen führt aufgrund der effektiven LPM-Implementierung zu einem sehr kleinen radiativen Energieverlust schwerer Quarks. Wenn man jedoch nicht diese effektive Beschreibung der Abschirmmasse, sondern den Standardwert der DEBYE-Masse nutzt, ist der Energieverlust aufgrund radiativer Prozesse etwa doppelt so groß wie der elastische Energieverlust. Obwohl die Raten von elastischen und radiativen Interaktionen vergleichbar sind, ist der Energieverlust pro Kollision von radiativen Prozessen größer, was durch den modifizierten Phasenraum aufgrund der drei auslaufenden Teilchen erklärt werden kann.

Vergleicht man den radiativen Energieverlust von leichten Quarks und Charm-Quarks für die Standard-DEBYE-Abschirmung, so sind beide gleich groß, obwohl man aufgrund des *dead-cone*-Effekts einen kleineren Energieverlust von Charm-Quarks erwarten würde. Der Grund hierfür liegt darin, dass der *dead-cone* aufgrund der endlichen Charm-Masse (*dead-cone*-Effekt) von einem zweiten *dead-cone* entstehend durch den LPM-Effekt überlagert wird. Da der LPM-Effekt sowohl für schwere als auch leichte Quarks wirkt, ist der *dead-cone* aufgrund der Charm-Masse nicht mehr sichtbar und beide Teilchen haben den gleichen Energieverlust. Die Masse von Bottom-Quarks hingegen ist wesentlich größer und der *dead-cone* aufgrund der Masse wird nicht mehr komplett durch die LPM-Implementierung überdeckt, was in einen kleineren radiativen Energieverlust resultiert. Zusätzlich untersuchen wir im Detail die Sensitivität der Ergebnisse bezüglich des LPM-Effekts, indem wir die Phasenraummodifikation der LPM-Implementierung variieren und entweder die freie Weglänge des Jets oder des abgestrahlten Gluons mit der Gluonformationszeit vergleichen.

Schwere (und leichte) Quarks in Schwerionenkollisionen

Um mit experimentellen Daten von D - und B -Mesonen oder ihrer Zerfallsprodukte am RHIC und LHC zu vergleichen, werden schwere Quarks in 3+1-dimensionalen BAMPS-Simulationen von ultrarelativistischen Schwerionenkollisionen untersucht. Die Anfangsverteilung schwerer Quarks wird mit dem Monte-Carlo-Event-Generator MC@NLO erzeugt, welcher gute Übereinstimmung mit der experimentell gemessenen Produktion schwerer Mesonen in Proton-Proton-Kollisionen am RHIC und LHC liefert. Die Untersuchungen zeigen, dass elastische Kollisionen schwerer Quarks mit pQCD-Wirkungsquerschnitten unter expliziter Berücksichtigung der laufenden Kopplung und mit DEBYE-Abschirmung, die aus resummierten HTL-Rechnungen entnommen ist, eine große Rolle spielen. Dennoch reichen sie allein nicht aus, um die experimentellen Daten zu beschreiben.

Bevor wir auch radiative Prozesse in BAMPS eingebaut haben, schätzten wir ihren Anteil an den Interaktionen ab, indem der elastische Wirkungsquerschnitt effektiv mit einem Faktor $K = 3.5$ multipliziert wurde. Der genaue Wert ist so angepasst, dass eine gute Übereinstimmung mit dem elliptischen Fluss der Elektronen von schweren Quarks am RHIC erhalten wird. Gleichzeitig stimmt auch der mit dem gleichen Faktor berechnete nukleare Modifikationsfaktor der Elektronen am RHIC gut mit den Daten überein. Nachdem der Wert für K durch die RHIC-Daten bestimmt wurde, erhält man für den gleichen Wert ebenfalls eine gute Übereinstimmung mit dem experimentell am LHC mit einer Schwerpunktsenergie von $\sqrt{s} = 2.76$ TeV gemessenen nuklearen Modifikationsfaktor von D -Mesonen, nicht-direkten J/ψ (aus B -Mesonen-Zerfällen) und Myonen, die von schweren Quarks stammen. Weiterhin machten wir Vorhersagen für den

nuklearen Modifikationsfaktor von Elektronen von schweren Quarks sowie für den elliptischen Fluss von D -Mesonen, nicht-direkten J/ψ , Elektronen und Myonen von schweren Quarks am LHC. Mittlerweile veröffentlichte Daten für D -Mesonen und Elektronen zeigen eine exzellente Übereinstimmung mit unseren Vorhersagen.

Es ist äußerst interessant, dass die mit schweren Quarks assoziierten experimentellen Daten für den nuklearen Modifikationsfaktor und den elliptischen Fluss bei RHIC und LHC simultan sehr gut nur durch elastische Kollisionen beschrieben werden, falls deren Wirkungsquerschnitt durch den Faktor $K = 3.5$ vergrößert wird. Während die Übereinstimmung bei beiden Beschleunigern für die korrekte Extrapolation von RHIC- zu LHC-Energien in unserem Modell spricht, ist die phänomenologische Vergrößerung des elastischen Wirkungsquerschnitts von einem theoretischen Standpunkt nicht zufriedenstellend. Daher drängt sich die Frage auf, ob radiative Prozesse die restliche Diskrepanz zwischen den Ergebnissen mit nur elastischen Kollisionen und den Daten erklären können.

Der oben bereits dargelegte Einbau radiativer Prozesse in BAMPS erlaubt die Simulation von Schwerionenkollisionen mit sowohl elastischen als auch radiativen Prozessen für schwere und leichte Partonen in einem gemeinsamen Modell. Da die Abschirmprozedur mit $\kappa_t = 0.2$ aus HTL-Rechnungen nur für schwere Quarks hergeleitet ist, setzen wir zunächst die Abschirmmasse auf den Standardwert der DEBYE-Masse ($\kappa_t = 1$), damit leichte und schwere Quarks gleich behandelt werden und wir den Einfluss der endlichen Quarkmasse im Detail untersuchen können. Wie schon im statischen Medium beobachtet, ist der Energieverlust von leichten Quarks und Charm-Quarks in Schwerionenkollisionen sowohl für konstante als auch laufende Kopplung sehr ähnlich, was sich in einem vergleichbaren nuklearen Modifikationsfaktor manifestiert. Wieder ist hierfür ein zweiter *dead-cone* durch die LPM-Implementierung verantwortlich, der den *dead-cone* aufgrund der Charm-Masse überdeckt. Gluonen hingegen sind angesichts eines größeren Farbfaktors stärker unterdrückt. Jedoch verursachen Masseneffekte in der Fragmentation von Gluonen und leichten Quarks zu (leichten) geladenen Hadronen und Charm-Quarks zu D -Mesonen einen vergleichbaren nuklearen Modifikationsfaktor auf hadronischer Ebene. Dies ist eine bemerkenswerte Erklärung für die überraschende experimentelle Entdeckung am RHIC und LHC, dass geladene Hadronen und Teilchen, die von Charm-Quarks stammen, gleich stark unterdrückt sind.

Obwohl der Verlauf des nuklearen Modifikationsfaktors als Funktion des transversalen Impulses sehr gut mit den Daten übereinstimmt, ist die absolute Unterdrückung verglichen mit den Daten unterschätzt. Der Grund für diese Diskrepanz ist vermutlich die effektive Implementierung des LPM-Effekts in BAMPS, bei der alle Gluonemissionen verworfen werden, die zu Interferenzen führen könnten. Dadurch werden nur Prozesse erlaubt, die vollkommen unabhängig voneinander sind. Eine weniger phänomenologische Implementierung des LPM-Effekts würde jedoch einen Teil der Interferenzprozesse erlauben, was zu einem höheren Energieverlust führen würde. Wenn wir nun einen Faktor $X < 1$ in der LPM-Implementierung einführen, der effektiv einen Teil der Interferenzprozesse zulässt, finden wir die beste Übereinstimmung für den nuklearen Modifikationsfaktor geladener Hadronen für $X = 0.3$. Für den gleichen Wert wird ebenso der nukleare Modifikationsfaktor von D -Mesonen sehr gut beschrieben. Obwohl der genaue Wert von X ein freier Parameter ist, erwarten wir, dass eine verbesserte Implementierung des LPM-Effekts effektiv äquivalent zu $X < 1$ wäre. An dieser Stelle sei noch einmal angemerkt, dass für diese Rechnung leichte und schwere Quarks komplett konsistent inklusive laufender Kopplung in BAMPS behandelt werden und dass wir somit eine mikroskopische Beschreibung für die gleiche Unterdrückung von geladenen Hadronen und D -Mesonen gefunden

haben. Für Bottom-Quarks hingegen ist der *dead-cone*-Effekt stärker ausgeprägt. Dadurch liegt der nukleare Modifikationsfaktor von B -Mesonen für $X = 0.3$ höher als der von D -Mesonen, aber auch leicht höher als die Daten.

Wenn wir für schwere Quarks die DEBYE-Abschirmung aus HTL-Rechnungen verwenden, so sind radiative Prozesse aufgrund der großen Rate elastischer Kollisionen in Verbindung mit der LPM-Implementierung stark unterdrückt. Demzufolge ist der nukleare Modifikationsfaktor aller mit schweren Quarks assoziierten Teilchen größer als die Daten. Allerdings kann man auch hier wieder phänomenologisch Interferenzprozesse zulassen, indem man ein $X < 1$ wählt. Für $X = 0.2$ finden wir eine sehr gute Übereinstimmung mit dem experimentell gemessenen nuklearen Modifikationsfaktor von D -Mesonen, nicht-direkten J/ψ und Elektronen von schweren Mesonen am LHC. Es sei anzumerken, dass der Wert für X in der gleichen Größenordnung wie für die Standard-DEBYE-Abschirmung liegt.

Obwohl der nukleare Modifikationsfaktor der mit schweren Quarks assoziierten Teilchen gut mit $X = 0.2$ beschrieben werden kann, ist der elliptischer Fluss dieser Teilchen für den gleichen Parameter deutlich kleiner als die experimentellen Daten. Verglichen mit dem oben betrachteten Szenario, in dem elastische Kollisionen mit $K = 3.5$ skaliert wurden und eine gute Übereinstimmung mit dem nuklearen Modifikationsfaktor und dem elliptischen Fluss gefunden wurde, ist der Energieverlust im Szenario mit sowohl elastischen als auch radiativen Kollisionen sehr ähnlich, aber der Transportwirkungsquerschnitt deutlich kleiner. Da letzterer für die Isotropisierung und den Aufbau des elliptischen Flusses eine wichtige Rolle einnimmt, ist das v_2 kleiner als das mit elastischen Kollisionen sowie $K = 3.5$ berechnete und daher auch kleiner als die Daten. Eine Erklärung für den fehlenden Anteil im elliptischen Fluss könnten zum Beispiel *event-by-event*-Fluktuationen, Koaleszenzeffekte oder Beiträge aus der hadronischen Phase sein, die in der Studie nicht berücksichtigt werden.

Unsere Resultate stimmen mit den meisten Ergebnissen in der Literatur überein. Alle Modelle, die sowohl elastische als auch radiative Prozesse betrachten (mit Ausnahme des Modells der Nantes-Gruppe), können den nuklearen Modifikationsfaktor und den elliptischen Fluss nicht gleichzeitig beschreiben. Mit nur elastischen Kollisionen (entweder mit Wirkungsquerschnitten aus der pQCD wie in dieser Arbeit oder aus dem Resonanzstreuungsmodell) sind beide Observablen in einigen Modellen simultan erklärbar. Wie wir allerdings in der vorliegenden Studie sehen, beeinflusst die Hinzunahme von radiativen Prozessen den nuklearen Modifikationsfaktor und den elliptischen Fluss in sehr unterschiedlicher Weise. Demnach ist es nicht klar, ob diese Modelle weiterhin beide Observablen beschreiben können, wenn auch radiative Interaktionen betrachtet werden.

J/ψ -Mesonen in Schwerionenkollisionen

Ein weiteres Thema dieser Dissertation ist das Verhalten von J/ψ -Mesonen im Quark-Gluon-Plasma. J/ψ -Mesonen bestehen aus einem Charm- und einem Anticharm-Quark und sind wegen möglicher Rekombinationsprozesse sehr eng mit den Eigenschaften freier Charm-Quarks verknüpft. Daher haben wir in Ergänzung zu Gluonen, leichten und schweren Quarks auch J/ψ -Mesonen in BAMPS eingebaut, welche dynamisch in ihre Bestandteile dissoziieren können, falls sie mit Gluonen aus dem Medium interagieren oder falls die Umgebungstemperatur über die Dissoziationstemperatur steigt. Auf der anderen Seite können unabhängige Charm- und Anticharm-Quarks während der QGP-Evolution zu einem J/ψ -Meson rekombinieren. Ein

wichtiger Punkt ist auch der Einfluss von sogenannten Effekten der kalten Kernmaterie (*cold nuclear matter effects*). Das sind Modifikationen der J/ψ -Anzahl, die von anderen Effekten (wie *Shadowing* in der Partonverteilungsfunktion, CRONIN-Effekt, nukleare Absorption) herrühren und nicht auf den Einfluss des QGP zurückzuführen sind. Sie spielen eine wichtige Rolle für die anfängliche J/ψ -Verteilung und sind ebenfalls in BAMPS implementiert worden.

In 3+1-dimensionalen BAMPS-Simulationen von Schwerionenkollisionen am RHIC wird die Zeitentwicklung der J/ψ -Dissoziation und -Regeneration betrachtet. Unter Beachtung der Effekte in kalter Kernmaterie und mit einer J/ψ -Formationszeit von $\tau_0 = 0.6$ fm, um das Schmelzen von J/ψ in der anfänglichen, nicht-thermischen Phase zu verhindern, in der die Temperatur noch nicht korrekt definiert werden kann, finden wir eine gute Übereinstimmung mit dem experimentell gemessenen nuklearen Modifikationsfaktor von J/ψ -Mesonen bei zentraler Rapidität für verschiedene Kollisionszentralitäten. Im Gegensatz zu den experimentellen Daten ist die J/ψ -Unterdrückung bei Vorwärtsrapidität in zentralen und semi-zentralen Kollisionen jedoch kleiner als bei zentraler Rapidität. Der Grund hierfür liegt in der kleineren Temperatur in BAMPS bei Vorwärtsrapidität verglichen zur zentralen Rapidität.

Experimentelle Messungen am RHIC zeigen, dass der elliptische Fluss von J/ψ -Mesonen sehr klein ist. Dies ist im Widerspruch zum Regenerationsbild, in dem der elliptische Fluss von Charm-Quarks auf J/ψ übertragen werden sollte. BAMPS ist bestens geeignet, um das im Detail zu untersuchen, da es den elliptischen Fluss von D -Mesonen reproduzieren kann und auch die dynamische Rekombination von Charm-Quarks zu J/ψ beinhaltet. Da die meisten J/ψ -Mesonen bereits am Anfang erzeugt werden und dadurch keinen elliptischen Fluss besitzen, sehen wir auch in BAMPS einen sehr kleinen elliptischen Fluss von J/ψ , der konsistent mit den experimentellen Daten ist. In einer weiteren Studie untersuchen wir die Abhängigkeit des elliptischen Flusses der sekundär produzierten J/ψ -Mesonen von der J/ψ -Dissoziationstemperatur. Dabei finden wir, dass J/ψ -Mesonen, die spät in der QGP-Evolution erzeugt werden, einen elliptischen Fluss annehmen, der nicht mit den experimentellen Daten verträglich ist. Demnach müssen die meisten der experimentell gemessenen J/ψ -Mesonen früh in der zeitlichen Entwicklung des QGP erzeugt worden sein.

Abschließende Worte

Am Ende der Arbeit werden nach einer kurzen Zusammenfassung mögliche Erweiterungen und Verbesserungen für das Modell BAMPS vorgeschlagen. Die wahrscheinlich interessanteste Erweiterung ist hierbei die mikroskopische Implementierung des LPM-Effekts basierend auf einer Summation des transversalen Impulses des abgestrahlten Gluons während seiner Formationszeit, was die kohärente Natur des Effekts besser wiedergibt als die momentan implementierte Modifikation des Phasenraums. Aufgrund der Komplexität des Problems handelt es sich hierbei eher um ein längerfristiges Projekt, was den oben besprochenen phänomenologischen X -Faktor in der jetzigen Implementierung erklären könnte.

Wie in dieser Arbeit gezeigt wird, ist das partonische Transportmodell BAMPS ideal dafür geeignet nicht nur Charm- und Bottom-Quarks, sondern auch leichte Quarks, Gluonen und J/ψ -Mesonen in relativistischen Schwerionenkollisionen zu untersuchen. Durch den Vergleich der mit BAMPS simulierten Ergebnisse (und zum Teil auch Vorhersagen) mit den experimentellen Daten lassen sich eine Vielzahl von Rückschlüsse auf die Interaktion von schweren Quarks mit dem Medium und auf die Eigenschaften des QGP ziehen. Die dabei wohl interessanteste

Beobachtung ist die Überlagerung des *dead-cone*-Effekts aufgrund der endlichen Charm-Quark-Masse durch den LPM-Effekt, was zu einem gleichen nuklearen Modifikationsfaktor von geladenen Hadronen und *D*-Mesonen führt, wie es experimentell ebenfalls gemessen wurde.

1. Introduction

Dass ich erkenne, was die Welt
Im Innersten zusammenhält.
(So that I may perceive whatever holds
The world together in its inmost folds.)

Faust: The First Part of the Tragedy
JOHANN WOLFGANG VON GOETHE

Ultra-relativistic heavy-ion collisions are an ideal tool to study the properties of quantum chromodynamics (QCD), which is the underlying theory of the strong force. The latter is one of the four known forces in nature—strong, weak, gravitation, and electromagnetic force—that form together with the known elementary particles the standard model of particle physics. The standard model contains all our knowledge of the fundamental properties and interactions of particles and has been very successful in explaining nature.

QCD is a remarkably complex theory with many interesting—and not yet completely understood—phenomena such as confinement or asymptotic freedom and describes the dominant interactions on subatomic scales. Collisions of protons or heavy-ions, which are accelerated to nearly the speed of light, are an excellent system to study these interactions in more detail. In contrast to proton-proton collisions, where only a small number of particles is created, the particle production in heavy-ion collisions is so enormous that a medium with collective behavior and unique properties is produced. It consists of quarks and gluons and is, therefore, called quark gluon plasma (QGP). Quarks are the elementary building blocks of protons and neutrons and gluons the exchange particles of the strong force, which renders the QGP a unique opportunity to study QCD.

Ultra-relativistic heavy-ion collisions are carried out, for instance, at the Large Hadron Collider (LHC) at CERN¹ and the Relativistic Heavy-Ion Collider (RHIC) at BNL², where several experimental hints have been found that in those collision indeed a new state of matter, i.e., the QGP, is produced. For instance, the created medium acts like a nearly perfect fluid with a very small shear viscosity to entropy density ratio, as is indicated by comparing the experimentally measured elliptic flow v_2 and other collective flow observables to hydrodynamic models. Another finding is the quenching of jets, i.e., highly energetic particles, which deposit lots of their energy in the medium. An experimentally accessible observable for this jet suppression is the nuclear modification factor R_{AA} .

Hard probes are a particular interesting type of particles created in heavy-ion collisions. As the name suggests they are produced in hard processes with a large momentum transfer, typically at an early stage of the collision, and then traverse the medium, revealing information about its properties. An example for hard probes are the aforementioned jets with a large transverse momentum, which can only be generated in hard collisions. Most relevant for this

¹*European Organization for Nuclear Research*

²*Brookhaven National Laboratory*

thesis, heavy quarks, i.e., charm and bottom quarks, are also produced in hard processes due to their large mass, which qualifies them as hard probes as well. After their early production, they traverse the medium, lose energy, and participate in the collective flow. Because of flavor conservation in QCD, heavy quarks are tagged particles, transferring their flavor during hadronization to D and B mesons, which allows the identification of heavy flavor particles in measurements.

In contrast to open heavy flavor particles, that are hadrons consisting of only one heavy quark, hidden heavy flavor denotes particles with a heavy quark and anti-quark of the same flavor. Prominent examples are J/ψ mesons, which can survive in the medium to some extent. Since their dissociation depends on the temperature of the medium, J/ψ suppression in heavy-ion collisions can act as a thermometer for the QGP. However, at the LHC, due to the abundance of charm quarks, secondary J/ψ can be formed from two independent charm and anti-charm quarks, leading to the counteractive effect of J/ψ enhancement, which complicates the picture considerably.

In this work hard probes are studied in the partonic transport model BAMPS. Employing Monte Carlo techniques, this model describes the 3+1 dimensional evolution of the QGP phase by propagating all particles in space and time and carrying out their collisions according to the BOLTZMANN equation. Since hard probes are produced in hard processes with a large momentum transfer, the value of the running coupling is small and their interactions should be describable within perturbative QCD (pQCD). This work focuses on open heavy flavor, but also addresses the suppression of light parton jets, in particular to highlight differences due to the mass. For light partons, radiative processes are the dominant contribution to their energy loss. For heavy quarks, we show that also binary interactions with a running coupling and an improved DEBYE screening matched to hard-thermal-loop calculations play an important role. Furthermore, the impact of the mass in radiative interactions, prominently named the dead cone effect, and the interplay with the LANDAU-POMERANCHUK-MIGDAL (LPM) effect are studied in great detail. Since the transport model BAMPS has access to all medium properties and the space time information of heavy quarks, it is the ideal tool to study the dissociation and regeneration of J/ψ , which has also been started during the course of this work.

It is an exciting time for the field of ultra-relativistic heavy-ion collisions. More than a decade of collisions at RHIC has produced a wealth of data, which has been used to constrain theoretical models and learn a lot about the properties of the QGP. This knowledge allowed to make predictions for the LHC at even higher energies. During the last two years, many new measurements have been performed at the LHC, which can be compared to those predictions. Having made several predictions for open heavy flavor ourselves, we compare them in this work to now available data.

The thesis is organized as follows. After a brief introduction to the standard model and QCD we address the phenomenology of ultra-relativistic heavy-ion collisions in Chapter 2 and put the topic of this work into context. In Chapter 3 partonic cross sections of heavy quarks with light quarks and gluons are calculated. We discuss the explicit consideration of the running coupling as well as an improved DEBYE screening to regularize the gluon propagator in presence of a medium for both binary and radiative processes. The focus is put on the cross section of the latter, which is calculated within the GUNION and BERTSCH approximation. Due to comparisons with the exact cross sections, it is found that the standard GUNION-BERTSCH matrix element exhibits problems at forward and backward rapidity of the emitted gluon. Consequently, we propose an improved version of the matrix element, which also modifies the

cross sections of light partons. In addition, we discuss the presence of the dead cone effect in our results and outline the implementation of the LPM effect.

In Chapter 4 the partonic transport model BAMPS is introduced in detail with a focus on the heavy flavor implementation. Furthermore, we address the initial conditions of the different particle types in BAMPS. The energy loss of a heavy quark in a thermal quark gluon plasma is calculated in Chapter 5. After the elastic energy loss in a static and flowing medium is analytically derived from hard-thermal loop calculations, it is compared to simulations with BAMPS. In addition, we examine elastic and radiative contributions to the total energy loss and discuss the influence of the running coupling, improved DEBYE screening, and LPM effect. Furthermore, the heavy flavor energy loss is compared to the energy loss of light partons and differences due to the mass are pointed out.

The BAMPS results on open heavy flavor observables are compared to experimental data from heavy-ion collisions at RHIC and LHC in Chapter 6. In particular, the difference of binary and radiative heavy quark processes with the improved GUNION-BERTSCH cross sections are highlighted. Simultaneously, we study the effects of the improved GUNION-BERTSCH cross sections on high-energy light partons and compare to heavy flavor observables.

Chapter 7 addresses J/ψ melting and regeneration in ultra-relativistic heavy-ion collisions as well as the elliptic flow of J/ψ . Finally, we conclude this thesis with a short summary and outlook in Chapter 8.

The present thesis is based on results that have been published (or submitted for publication) in Refs. [UFXG10a, UFXG10b, UFXG10c, UFXG11a, UFXG11b, UZF⁺11, FUXG11, AGM⁺12, UFXG12a, UFXG12b, UFXG13a, UFXG13b, MPUG13, FUXG13].

2. QCD and heavy-ion collisions

Nature has always looked like a horrible mess, but as we go along we see patterns and put theories together; a certain clarity comes and things get simpler.

QED: The Strange Theory of Light and Matter
RICHARD P. FEYNMAN

While the standard model of particle physics describes all known elementary particles and their interactions, the most important interaction for this work—the strong force—is governed by quantum chromodynamics (QCD). In the next section the standard model is briefly outlined with a focus on QCD. Moreover, we address important QCD phenomena such as confinement (Section 2.1.2) and asymptotic freedom (Section 2.1.1) as well as discuss the QCD phase diagram in Section 2.1.3.

In Section 2.2 an overview of ultra-relativistic heavy-ion collisions is given and the prominent observables elliptic flow (Section 2.2.2) and nuclear modification factor (Section 2.2.3) are introduced. In particular, we highlight the importance of hard probes in heavy-ion collisions (Section 2.2.3).

2.1. The standard model and QCD

All known elementary particles and all interactions are included in the standard model. Matter is build of spin-1/2 fermions, i.e., quarks and leptons, each type consisting of six particles and the respective anti-particles. Quarks are distinguished by their flavor, namely, up, down, strange, charm, bottom, and top—often abbreviated with their first letter. The lepton sector consists of electrons, muons, and taus as well as the respective neutrinos.

The four interactions—strong, weak, electromagnetic, and gravitation—are governed by their respective exchange particles—gluon, photon, W as well as Z bosons, and graviton. The graviton is the only exchange particle that has not been discovered yet. The first three interactions are described by quantum field theories. For gravitation, which is related to EINSTEIN’s general relativity, this has not been possible yet, which leads to tension with the quantum descriptions of the other interactions at the PLANCK scale. However, on the scales of heavy-ion collisions, gravitation can be completely neglected.

In 1967 GLASHOW, SALAM, and WEINBERG managed to unify quantum electrodynamics (QED), which describes electromagnetic processes, and the weak interaction to the electro-weak theory. Within this framework, the large masses of the W and Z bosons can be explained due to spontaneous symmetry breaking. Three of the four components of the HIGGS field are absorbed by the mass creation (GOLDSTONE bosons are “eaten” by the gauge bosons), but the remaining degree of freedom should be detectable as the HIGGS boson in high-energy

proton-proton collisions. And indeed, recently, a promising candidate for the HIGGS boson has been discovered at the LHC [ATLAS12b, CMS12c].

So far, it has not been possible to also incorporate quantum chromodynamics (QCD) in the electro-weak theory to form a *grand unified theory*, despite some efforts, for instance, *supersymmetry* [Ait05, Mar97]. Besides the tension of the quantum field theories with gravitation, there are some other problems with the standard model (matter-anti-matter asymmetry, hierarchy problem, massive neutrinos, too many free parameters), which lead to the investigation of physics beyond the standard model, most prominently, *string theory* [Zwi04, Kir97]. More details concerning the standard model can be found, for instance, in Refs. [Nov99, Ros01].

Electromagnetic and weak interactions have only minor relevance for heavy-ion collisions (for instance, for photon production or decay of hadrons). The most important theory for this work, however, is QCD, which describes the interactions of quarks through gluon exchange. The Lagrangian of QCD is given by

$$\mathcal{L}_{\text{QCD}} = \sum_k \bar{\psi}_k (i\gamma^\mu D_\mu - m_k) \psi_k - \frac{1}{4} F_{\mu\nu}^a F_a^{\mu\nu} \quad (2.1)$$

with the covariant derivative $D^\mu = \partial^\mu - igT_a A_a^\mu$ and gluon field strength tensor $F_{\mu\nu}^a = \partial_\mu A_\nu^a - \partial_\nu A_\mu^a + gf_{abc}A_\mu^b A_\nu^c$, where T_a denote the eight generators of the gauge group $SU(3)$ with the structure constants f_{abc} . The generators fulfill the LIE algebra of the group, $[T_a, T_b] = if_{abc}T_c$. A_μ^a are the eight gluon fields, γ the DIRAC matrices, ψ_k ($\bar{\psi}_k = \psi_k^\dagger \gamma^0$) the DIRAC four-spinor of the (anti-)quark field with flavor k and $g = \sqrt{4\pi\alpha_s}$ the coupling. The Lagrangian obeys a local $SU(3)$ gauge symmetry¹, where quarks are in the fundamental and gluons in the adjoint representation of the group. This leads to quarks and gluons carrying *color*, which is the charge of QCD.

The first term of Equation (2.1) describes the propagation of quarks and their interactions with gluons, whereas the second term characterizes the dynamics of the gluons. Unique in QCD is that gluons carry color charge and, therefore, couple to themselves, which can be seen if the last term is multiplied out and terms proportional to A^3 and A^4 occur. This non-Abelian feature of QCD renders it to be considerably more complex than QED, which is an Abelian quantum field theory. In principle, every QCD phenomenon is described by the Lagrangian above. However, in practice, only the perturbative regime with a small coupling is theoretically accessible. Non-perturbative effects like confinement (see Section 2.1.2) are hardly understood and can only be studied by discretizing the phase space on a lattice and extrapolating to the continuum limit.

The Lagrangian is nearly symmetric under transformations of right and left handed components of the quark spinor. Only the mass term m_k breaks this *chiral symmetry*² [DGH94, Koc97] explicitly. Furthermore, the spontaneous breaking of the chiral symmetry leads to a rather complex vacuum state, which is filled with chiral condensates of quark and gluon fields. Due to these QCD vacuum effects, quarks acquire larger masses within hadrons than their bare

¹ $SU(3)$ symmetry: Equation (2.1) is symmetric under the local transformation $\psi_k \rightarrow U\psi_k$ and $F^{\mu\nu} \rightarrow UF^{\mu\nu}U^+$, where $U(x) = e^{i\alpha_a(x)T_a}$. The arbitrary real field $\alpha_a(x)$ depends on the position x .

²Chiral symmetry: In the case of only two massless flavors, Equation (2.1) is globally symmetric under the vector transformation $\psi \rightarrow e^{i\tau\cdot\alpha}\psi$ and the axial-vector transformation $\psi \rightarrow e^{i\gamma^5\tau\cdot\alpha}\psi$ with τ being a vector of the PAULI matrices and $\psi = (\psi_u, \psi_d)$ a vector of the spinors of the two flavors. $\gamma^5 = i\gamma^0\gamma^1\gamma^2\gamma^3$ is a combination of the DIRAC matrices and α an arbitrary real vector (not depending on position). Thus, for two flavors it is a $SU(2)_V \times SU(2)_A$ symmetry [Koc97].

masses. This effect is responsible for about 95 % of the total visible mass in the universe and only the remaining 5 % are due to the coupling to the HIGGS boson [DFF⁺08].

2.1.1. Running coupling and asymptotic freedom

The coupling $g = \sqrt{4\pi\alpha_s}$ from Equation (2.1) is actually not constant, but depends on the momentum transfer Q of the considered process. In leading order pQCD it is given by

$$\alpha_s(Q) = \frac{12\pi}{(11N_c - 2n_f) \ln(Q^2/\Lambda_{\text{QCD}}^2)}. \quad (2.2)$$

$N_c = 3$ is the number of colors and n_f the number of active quark flavors. The scale of QCD Λ_{QCD} has to be measured experimentally and is of the order of 200 MeV—the exact value [Bet07] depends on the number of active flavors. Figure 2.1 depicts the running coupling as a function of the momentum scale together with measurements.

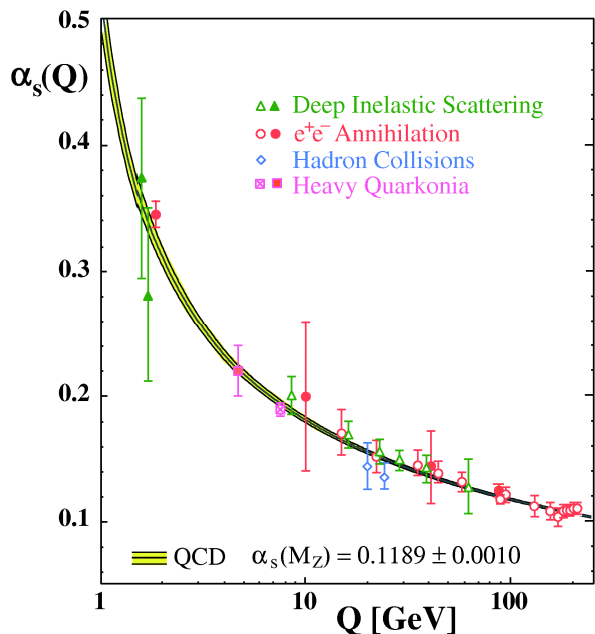


Figure 2.1.: Overview of measurements of the coupling α_s as a function of the energy scale Q . Open (closed) symbols mark measurements, whose analysis was done with QCD calculations in next-to-leading order (next-to-next-to-leading order). The curves are QCD predictions for α_s within the four-loop approximation for a world average of $\alpha_s(M_{Z^0})$. The plot is taken from Ref. [Bet07], where also more details can be found.

In contrast to QED, the running coupling in QCD gets smaller with increasing energy scale or—according to the Heisenberg uncertainty principle—decreasing distance. GROSS, POLITZER, and WILCZEK denoted this feature as asymptotic freedom [GW73, Pol73], which is a consequence of QCD being a non-Abelian gauge theory. Nevertheless, asymptotic freedom only exists if $n_f \leq 16$ as seems to be the case in nature with $n_f = 6$.³ If n_f were larger than 16, the β function of QCD would be positive and the coupling would increase with Q , as it is the case in QED.

At large energy scales, the agreement of theory and data is best since the coupling is small and pQCD applicable. At small energies, however, the coupling rises and non-perturbative effects take over. The most prominent effect in this regard is *confinement*.

³Actually, the number of active flavors depends on the the considered energy scale. For most applications, the masses of the heavy quarks charm, bottom, and top are too large to be produced and, thus, n_f is only 3.

2.1.2. Confinement

At large distances, which correspond—according to the uncertainty principle—to small energies, the coupling is large. As a consequence, two quarks cannot be separated, which explains why free quarks have never been observed. Instead they are *confined* in hadrons. Because quarks carry color, this is equivalent to postulating that only colorless objects can be observed in nature. Examples for colorless objects are mesons with a quark and an anti-quark or baryons with three quarks.⁴ Prominent examples for mesons are pions, D mesons, or J/ψ mesons and for baryons protons or neutrons. Due to the strong coupling at large distances, non-perturbative effects are at play that have prevented a clear understanding of the details of confinement.

Phenomenologically, however, the potential between two quarks, separated by distance r , can be expressed by

$$V(r) = -\frac{4}{3} \frac{\alpha_s(r)}{r} + \kappa r . \quad (2.3)$$

The first term describes the binding of two quarks at small distances and is analogous to the COULOMB potential in QED. The second term, however, is unique to QCD and prevents that two quarks can be separated since the needed energy rises with r . Lattice results confirm that the potential of two charm quarks in a J/ψ can indeed be described by Equation (2.3) to a good approximation [B⁺04].

2.1.3. The phase diagram of QCD

Under ordinary conditions, quarks and gluons are confined in protons and neutrons, which make up nuclei in atoms. Let us consider the following *Gedankenexperiment*: If one compresses such nuclear matter, protons and neutrons start to overlap and it is intuitively clear that at some point one cannot distinguish to which nucleon each parton belongs. The matter is such dense that individual nucleons cannot be identified anymore. Instead, their constituents—quarks and gluons—compose the matter. Since the relevant degrees of freedom changed, a phase transition from ordinary nuclear matter to a plasma of quarks and gluons occurred.

The same effect takes place if one heats nuclear matter instead of compressing it. Increasing temperature is equivalent to increasing kinetic energy, not only of the nucleons, but also of their constituents. Due to asymptotic freedom, quarks and gluons are less and less bound in the nucleons. Again, at some point a phase transition to the quark gluon plasma occurs.

These simple considerations lead to the phase diagram of QCD, which is sketched in Figure 2.2. Increasing temperature or baryochemical potential, which is a measure for the density, implies a phase transition from nuclear matter to the QGP. More precisely, for a small baryochemical potential, lattice QCD calculations show not a rapid phase transition but a smooth crossover at a temperature of around $T_c = 150 - 170$ MeV [AEF⁺06, B⁺10, HotQCD10]. At larger baryochemical potentials lattice QCD has difficulties due to the sign problem [Phi10] and one has to rely on more phenomenological models [BR99, HJS⁺98, SMMR01, HI03, Bub05]. It is thought that at small temperatures and large baryochemical potentials a first order phase transition occurs to a color superconducting plasma [RW00, Ris04, Ste06], where two quarks

⁴Mesons as well as baryons are also called hadrons.

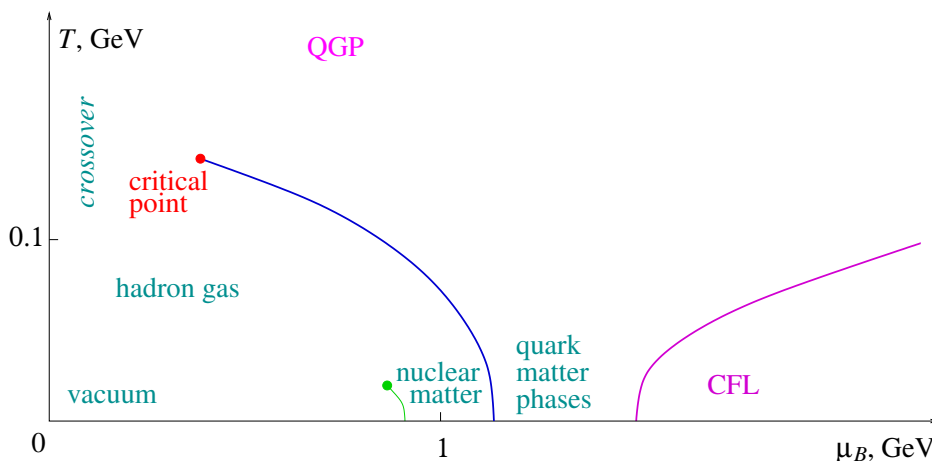


Figure 2.2.: Semi-quantitative sketch of the QCD phase diagram in the plane of temperature T and baryochemical potential μ_B . Taken from Ref. [Ste06].

are correlated in COOPER pairs analogously to the BCS⁵ theory. Nevertheless, this region is difficult to access experimentally, but might exist in the core of compact neutron stars. More details on the QCD phase diagram can be found, for instance, in Refs. [Ste06, BMW09].

A cross over at small baryochemical potential and large temperature and a first order phase transition at large baryochemical potential and small temperature imply that there is somewhere in between a critical point [Ste06].⁶ In a laboratory on earth, the only possible measurements to find the critical point or study the production and properties of the QGP are heavy-ion collisions. In particular, in ultra-relativistic heavy-ion collisions, which are most relevant for hard probes and will be discussed in more detail in the next section, nuclei are collided at a very large energy. Therefore, the baryochemical potential of the produced medium is small, but the temperature large. Thus, they explore mostly the upper left part of the QCD phase diagram in Figure 2.2. Also the universe was located in this region of the phase diagram shortly after the big bang since the matter was so hot that a QGP existed. During its expansion, the universe cooled off and went down along the temperature axis to its current state. Since the trajectory of the matter created in heavy-ion collisions is very similar, they are often referred to as little big bangs and might be able to explore the properties of the early state of the universe.

2.2. Ultra-relativistic heavy-ion collisions

At ultra-relativistic heavy-ion colliders atomic nuclei are accelerated to nearly the speed of light and then brought to collision within huge detectors, which measure the produced particles. The energy deposition within the created medium as well as its compression are thought to be so large that a QGP is formed. Subsequently, it expands, cools down, and hadronizes to a hadron gas. These hadrons or their decay products are then measured in the detector.

⁵after BARDEEN, COOPER, and SCHRIEFFER

⁶On the other hand, however, some recent lattice results [dFP07, dFP08] indicate that there might be no critical point for physical quark masses.

It is important to note that the QGP itself cannot be detected since quarks and gluons are not color-neutral objects. Even if this were possible, the lifetime of the QGP (approximately $3 \cdot 10^{-38}$ seconds) would be much too small to study its properties. Therefore, one has to rely on the indirect measurements of the several thousand particles that are produced during or after the phase transition. At this point, theoretical models come into play, which try to explain what happens in the QGP phase. From comparisons between experimental data and model predictions for experimental observables, one can learn about the properties of the QGP. In this work, we employ this idea as well by comparing hard probes observables, which literally probe the medium properties, to experimental data (see Section 2.2.3).

The heavy-ion collider facilities with the largest center-of-mass energies per nucleon are RHIC and LHC with $\sqrt{s_{NN}} = 200$ GeV and 2.76 TeV, respectively. The latter has been running for two beam times and will increase its energy after a shut-down to 5.5 TeV next year. RHIC measurements have been performed for more than a decade. Recently, a beam energy scan was done to study heavy-ion collisions at smaller center-of-mass energies. Several other heavy-ion accelerator facilities such as LBNL⁷ Bevalac, BNL AGS⁸, CERN SPS⁹, and GSI¹⁰ SIS18¹¹ studied heavy-ion collision at smaller energies—the latter planning a huge upgrade named FAIR¹².

In the following we present the generally acknowledged picture of the evolution of an ultra-relativistic heavy-ion collision as well as highlight possible models for different stages. The initial partons are produced in initial hard and soft processes. According to the GLAUBER model (see Appendix A.5), a heavy-ion collision consists of a superposition of several binary nucleon-nucleon collisions. The hard parton scatterings can be described by pQCD, for instance, within the *mini-jet model* (cf. Section 4.5), but the soft part depends on non-perturbative effects and is, thus, difficult to model. One option is the use of event generators like PYTHIA (see Section 4.5), which are fitted to experimental proton-proton (p+p) collision data and try to incorporate—at least phenomenologically—both soft and hard components. Another option for the initial conditions is derived from the *color glass condensate* (CGC) description of highly energetic nuclei [IV03, McL03, Ven05, McL08]. The particle production in the collision of two nuclei consisting in this framework of coherent and dense gluon matter lead to the creation of a non-thermal plasma with highly occupied gauge field modes (*glasma*) [LM06].

After its creation, the QGP thermalizes on a short time scale. This stage of the collision is least understood. The best tool to study it in detail are non-equilibrium partonic transport models [GM92, Zha98, MG00, BMS03, XG05, LKL⁺05], such as BAMPS, which is used in this work (cf. in particular Chapter 4). After thermalization either transport models or relativistic hydrodynamic models [HKH⁺01, HT02, RR07, LR08, GJS⁺13b] can be employed to describe the expansion and collective motion of the QGP. In particular, the success of ideal hydrodynamics in comparing to elliptic flow data lead to the characterization of the QGP as a nearly perfect liquid with a small shear viscosity to entropy density ratio. When the temperature of the medium drops below the critical temperature, hadronization sets in. Since the phenomenon of confinement is not well understood, no reliable microscopic model exists

⁷Lawrence Berkley National Laboratory

⁸Alternating Gradient Synchrotron

⁹Super Proton Synchrotron

¹⁰Helmholtzzentrum für Schwerionenforschung (former *Gesellschaft für Schwerionenforschung*)

¹¹Schwerionensynchrotron 18 (the number results from the magnetic rigidity of the synchrotron of 18 Tm)

¹²Facility for Antiproton and Ion Research

that describes the phase transition in heavy-ion collisions. The best approach to model this stage is probably hydrodynamics with an equation of state that incorporates both QGP and hadron gas and is matched to lattice QCD results [HP10]. To obtain the final hadrons from the macroscopic hydrodynamic variables the COOPER-FRYE prescription [CF74] is usually applied.

In the remaining hadron gas further scatterings and particle decays take place, which can be simulated with hadronic cascades such as UrQMD [B⁺98, BZS⁺99, PSB⁺08] or HSD [EC96, CB99]. After further expansion, the hadron gas decouples, the yields stay fixed (chemical freeze-out), and the momenta remain unchanged (kinetic freeze-out). These final particles after freeze-out or their decay products are actually the particles measured in the detector, from which one tries to draw conclusions about the properties of the QGP. It is noteworthy that the final identified particle yields are well described by the Statistical Hadronization Model [BMRS03, Bec09, ABMRS11], which assumes that all hadrons are statistically produced at the phase transition and that their numbers are given only by the thermodynamic properties (temperature, baryochemical potential, etc.) of the thermalized medium obtained from a global fit to the yields.

In general, the properties of the bulk medium can be studied, for instance, with particle yields, momentum spectra, or collective flow of soft particles with a transverse momentum of $p_T < 2 - 3$ GeV. It is best described by thermal models and hydrodynamics. In contrast, hard probes physics can be best investigated at large $p_T > 6 - 10$ GeV or for heavy particles via, for instance, momentum spectra or reconstructed jets. While the most prominently applied theory for this kinematic range is pQCD, hard probes can be studied, for instance, with a transport model as is done in this work, with a LANGEVIN evolution on a hydrodynamic background, which is often used for heavy quarks, or the statistical model, that is prominently employed for studying J/ψ suppression.

Being at the intersection of soft and hard physics, the intermediate p_T region is theoretically least understood. Within our transport model BAMPS we employ pQCD not only for hard probes, but for all particles, and, hence, provide a tool to study all momentum regions within a single framework. Details concerning BAMPS are given in Chapter 4.

2.2.1. Overview of results from RHIC and LHC

A comprehensive overview of the first experimental results at RHIC is given in the white papers of the collaborations [STAR05, PHENIX05a, PHOBOS05, BRAHMS05], which are named STAR¹³, PHENIX¹⁴, PHOBOS¹⁵, and BRAHMS¹⁶. Only the first two still exist and are actively taking as well as analyzing data. An excellent review of more recent RHIC findings is given in Ref. [JM12].

At the LHC, the ALICE¹⁷ experiment is dedicated to measure heavy-ion collisions due to its specialization in handling large particle multiplicities and both soft and hard momenta. In contrast, CMS¹⁸ and ATLAS¹⁹ are designed for p+p collisions, although they also take

¹³*Solenoidal Tracker At RHIC*

¹⁴*Pioneering High Energy Nuclear Interactions eXperiment*

¹⁵Not an acronym.

¹⁶*The Broad RAnge Hadron Magnetic Spectrometer*

¹⁷*A Large Ion Collider Experiment*

¹⁸*Compact Muon Solenoid*

¹⁹*A Toroidal LHC ApparatuS*

heavy-ion data. Their main advantage lies in the hard probes sector since this is the relevant scale for p+p events. The newest experimental results from LHC can be found, for instance, in the overview article [MSW12].

The most compelling evidence for the creation of the QGP is the collective behavior of the medium and the jet quenching, which will be discussed in more detail in Sections 2.2.2 and 2.2.3, respectively. Most relevant for this work are the suppression and elliptic flow of open heavy flavor and J/ψ . Experimental results in this regard are also shown in Section 2.2.3.

Another intriguing phenomenon that has been measured in heavy-ion collisions [STAR09, CMS11b], but also—less pronounced—in proton-lead (p+Pb) [CMS13b], and even in high multiplicities p+p events [CMS10], is the so called *ridge* of two-particle correlations. A theoretical explanation for these long-range correlations in the beam direction could be initial color flux tubes and subsequent hydrodynamic expansion [WKP11]. However, the origin of the ridge has not been fully understood yet and is actively debated—see Ref. [Li12] for a recent review.

Several other interesting results such as large baryon to meson ratios [PHENIX03, STAR06], strangeness enhancement [BM11], indication of chiral restoration from di-lepton measurements [RWvH09], QGP “temperature” from thermal photons [PHENIX10], system sizes from HBT [LPSW05], particle chemistry from identified hadron yields [BMRS03], and many more have been found at RHIC and LHC. For the details we refer to the above mentioned reviews.

Recent p+Pb measurements at LHC are crucial to constrain cold nuclear matter effects [SAMA⁺12], which are important for the initial particle distribution in heavy-ion collisions. The analysis of the data is currently under way and will, for instance, reveal how well the color glass condensate or other models serve as initial conditions.

2.2.2. Collective flow

The medium produced in heavy-ion collisions exhibits a collective behavior. To study this quantitatively, the invariant particle yield is decomposed in a FOURIER series [PV98],

$$\begin{aligned} E \frac{d^3N}{d^3p} &= \frac{d^3N}{p_T dp_T dy d\phi}(p_T, y, \phi) = \frac{1}{2\pi} \frac{d^2N}{p_T dp_T dy} \left[1 + \sum_{n=1}^{\infty} 2v_n(p_T, y) \cos[n(\phi - \Psi_n)] \right] \\ &= \frac{1}{2\pi} \frac{d^2N}{p_T dp_T dy} [1 + 2v_1(p_T, y) \cos(\phi - \Psi_1) + 2v_2(p_T, y) \cos[2(\phi - \Psi_2)] + \dots] . \end{aligned} \quad (2.4)$$

The v_n are called FOURIER coefficients or harmonics. The first three are named directed (v_1), elliptic (v_2), and triangular (v_3) flow according to their geometrical origin. The factor 2 in front of each coefficient is just due to normalization and ensures the descriptive relation $v_n = \langle \cos[n(\phi - \Psi_n)] \rangle$ [VZ96]. Ψ_n is the angle of the spatial plane of symmetry of harmonic n , which maximizes v_n . Neglecting event-by-event fluctuations, it coincides with the reaction plane for directed and elliptic flow. Hence, expressed by the momenta of the particles with respect to the reaction plane, the directed flow is $v_1 = \langle p_x/p_T \rangle$ and the elliptic flow

$$v_2 = \left\langle \frac{p_x^2 - p_y^2}{p_T^2} \right\rangle , \quad (2.5)$$

where the average over all particles is taken. Experimentally, these quantities are more difficult to define since the reaction plane is not known. Consequently, other approaches are applied such as the event plane method [PV98] or two- or four-particle cumulant methods [BDO01].

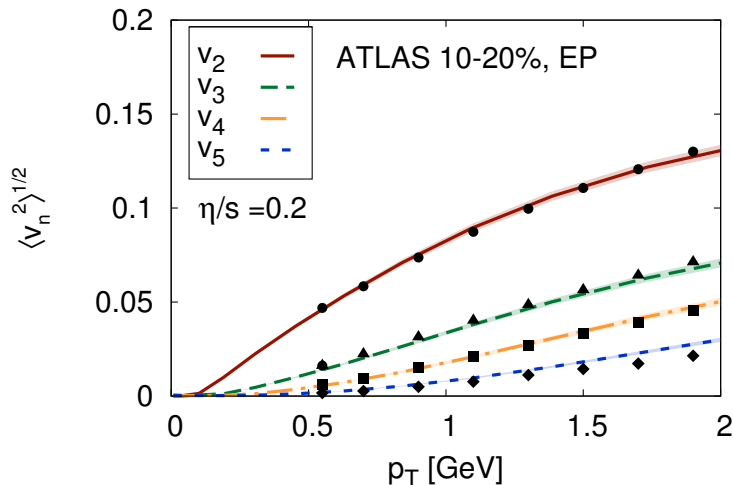


Figure 2.3.: Root-mean-square of anisotropic flow coefficients $\langle v_n^2 \rangle^{1/2}$ from the hydrodynamic model MUSIC [GJS⁺13b] with data [ATLAS12a] as a function of transverse momentum p_T . The experimental errors are smaller than the points. Figure taken from [GJS⁺13b].

Whereas the directed flow is caused by the sideward motion of the particles within the reaction plane, the elliptic and triangular flow are due to the spatial geometry of the collision zone. If the nuclei do not collide head-on but peripherally, the collision region looks like a cigar. Because of different pressure gradients in x and y direction, this spatial deformation is translated to a momentum anisotropy and, hence, a non-zero v_2 . In other words, the medium minimizes— analogously to a liquid—its surface, which is a first hint on the hydrodynamic behavior of the QGP. The time scale of the conversion from pressure to momentum anisotropy is a measure of the interaction strength in the medium. A finite v_3 is caused by a triangular initial shape, which is due to fluctuations. In contrast to the elliptic flow, v_3 only depends weakly on centrality since fluctuations are present regardless of the impact parameter.

Figure 2.3 depicts the ATLAS measurements of the first five FOURIER coefficients v_n at LHC. The agreement with the curves of the relativistic viscous hydrodynamic model MUSIC [GJS⁺13b] is remarkably good. The employed ratio of shear viscosity to entropy density of $\eta/s = 0.2$ is quite small and close to the conjectured lower bound of $\eta/s = 1/4\pi \simeq 0.08$, obtained from AdS/CFT²⁰ correspondence [KSS05, PSS01]. That hydrodynamics with a small shear viscosity to entropy density ratio works so well implies a) that a rapid thermalization in the early phase of the QGP evolution occurs since hydrodynamics as a local equilibrium theory is applicable, and b) that the medium behaves like a nearly perfect liquid. Other relativistic hydrodynamic models [HKH⁺01, HT02, RR07, LR08] also find a good agreement with data, although in order to describe all five harmonics at RHIC and LHC a 3+1 dimensional viscous hydrodynamic model with event-by-event fluctuations [GJS⁺13b] seems to be needed. A recent overview of hydrodynamics in heavy-ion collisions can be found in Ref. [GJS13a].

As a note, being a macroscopic model, hydrodynamics cannot make any statements about the microscopic processes within the medium or explain the large interaction strength. For those microscopic details, transport models like BAMPS (see Chapter 4) are better suited. That the plasma seems to have a small viscosity was also shown recently within BAMPS [XGS08, EMXG09, WER⁺11, RBE⁺12] (cf., however, Section 4.6 for some remarks on this study concerning the GUNION-BERTSCH cross section).

²⁰anti de Sitter/conformal field theory

At RHIC a scaling of elliptic flow of identified particles with their quark number n_q is observed [PHENIX07d]. If v_2/n_q is plotted as a function of $(m_T - m)/n_q$, where m (m_T) is the (transverse) mass, all curves for different particle species lie on top of each other, which can be readily understood in the coalescence picture. However, such a quark number scaling is not observed at LHC [ALICE11d], which suggests that the scaling at RHIC is just coincidence.

2.2.3. Hard probes

Hard probes, which are particles with either a large momentum or a large mass, are exclusively produced in hard processes. Since the scales of such a hard production process and the subsequent fragmentation to hadrons are very different, these contributions factorize. Consequently, the invariant production cross section of two hard hadrons H_1 and H_2 —for instance, two jets or a heavy meson and heavy anti-meson—in a collision of two heavy ions $A + B$ can be written in leading order pQCD as [G⁺95, MVL11]

$$E_{H_1} E_{H_2} \frac{d\sigma_{H_1 H_2}^{AB}}{d^3p_{H_1} d^3p_{H_2}} = \sum_{i,j,k,l=g,q,Q} \int dx_i dx_j dz_k dz_l f_i^A(x_i) f_j^B(x_j) \frac{d\hat{\sigma}_{ij \rightarrow kl}}{d\hat{t}} \frac{x_i x_j s}{2\pi} \frac{E_{H_1} E_{H_2}}{E_k E_l} \times \frac{\bar{D}_{H_1/k}(p_k, z_k)}{z_k^3} \frac{\bar{D}_{H_2/l}(p_l, z_l)}{z_l^3} \delta^4(p_i + p_j - p_k - p_l), \quad (2.6)$$

where $p_n = (E_n, \mathbf{p}_n)$ denotes the four momentum of particle n , s the squared center-of-mass energy per nucleon of the process $A + B$, and $d\hat{\sigma}/d\hat{t}$ the partonic cross section, which is discussed in more detail in Chapter 3 for heavy quarks and Appendix A.3 for light partons. The parton distribution function of a parton i in a nucleus A , $f_i^A(x_i)$, can be factorized in the proton parton distribution function, $f_i^p(x_i)$, and a parameterization of cold nuclear matter effects, $R_i^A(x_i)$, i.e., $f_i^A(x_i) = R_i^A(x_i) f_i^p(x_i)$. An up-to-date parameterization of the latter is EPS09 [EPS09], which includes, for instance, shadowing [Arn94, Arm06] and the CRONIN effect [Acc02]. As a note, Equation (2.6) also depends on the factorization and renormalization scale μ_F and μ_R , respectively, which have been suppressed above. The sum runs over all gluon and quark initial and final states and the δ function ensures energy and momentum conservation.

The medium modified fragmentation function $\bar{D}_{H/k}(p_k, z_k)$ of a parton k to a hadron H with a momentum ratio $z_k = |\mathbf{p}_H|/|\mathbf{p}_k|$ includes the medium influence on the parton and its fragmentation to a hadron. Recent experimental data of jet shower shapes [CMS12b] comparing the fragmentation patterns of jets in heavy-ion and p+p collisions suggests that the medium modified fragmentation function can be separated in a part describing the in-medium energy loss and a subsequent vacuum fragmentation similar to p+p events. Thus, the medium modified fragmentation function can be schematically written as a convolution of these two,

$$\bar{D}_{H/k}(p_k, z_k) = P(p_k|\text{medium}) \otimes D_{H/k}(z_k). \quad (2.7)$$

$D_{H/k}(z_k)$ is the vacuum fragmentation function, which is experimentally measured. For heavy quarks we use in this work the PETERSON parameterization [PSSZ83] (see Section 4.1) and for light partons the AKK fragmentation functions [AKK08] (see Section 6.2.1). The energy loss in the QGP is described by $P(p_k|\text{medium})$, which depends on the geometry and the properties of the medium. Although it looks rather simple in this form, it is probably the most complex

and least understood contribution of the hard probes sector. In this work we use the transport model BAMPS to study the medium effects on hard probes in detail.

To get a more intuitive idea of the meaning of Equation (2.6), we write it in a more schematic form,

$$E_{H_1} E_{H_2} \frac{d\sigma_{H_1 H_2}^{AB}}{d^3 p_{H_1} d^3 p_{H_2}} \sim \sum_{i,j,k,l=g,q,Q} f_i^A(x_i) f_j^B(x_j) \otimes \frac{d\hat{\sigma}_{ij \rightarrow kl}}{d\hat{t}} \otimes P(p_k|\text{medium}) P(p_l|\text{medium}) \otimes D_{H_1/k}(z_k) D_{H_2/l}(z_l) . \quad (2.8)$$

It can then be read as the following. Two partons, i and j , which stem from the nuclei A and B , produce—after colliding in a hard process—two hard partons, k and l , which traverse the medium, lose energy, and subsequently fragment to the hadrons H_1 and H_2 .

The production of hard probes in p+p collisions can also be described by Equation (2.8) if the parton distribution function in a proton is taken instead of that in a nucleus and the medium influence $P(p_k|\text{medium})P(p_l|\text{medium})$ is omitted. Since cold nuclear matter effects in the high transverse momentum region are considered to be small, the only differences between the hard probes production cross sections in p+p and A+B collisions are the in-medium energy loss effects. Therefore, studying the ratio of these two can reveal valuable information about the properties of the QGP. This ratio is commonly named the *nuclear modification factor* and is addressed in more detail in the following section.

Jet quenching and nuclear modification factor of light particles

In leading order pQCD high transverse momentum particles are always produced in pairs back-to-back in the transverse plane. Proton-proton measurements of two particle angular correlations of high-energy particles show indeed a peak at the near side and the away side shifted by 180° [STAR05]. In contrast to p+p events, the away side is strongly suppressed in heavy-ion collisions [STAR05], which was one of the most striking early RHIC results.

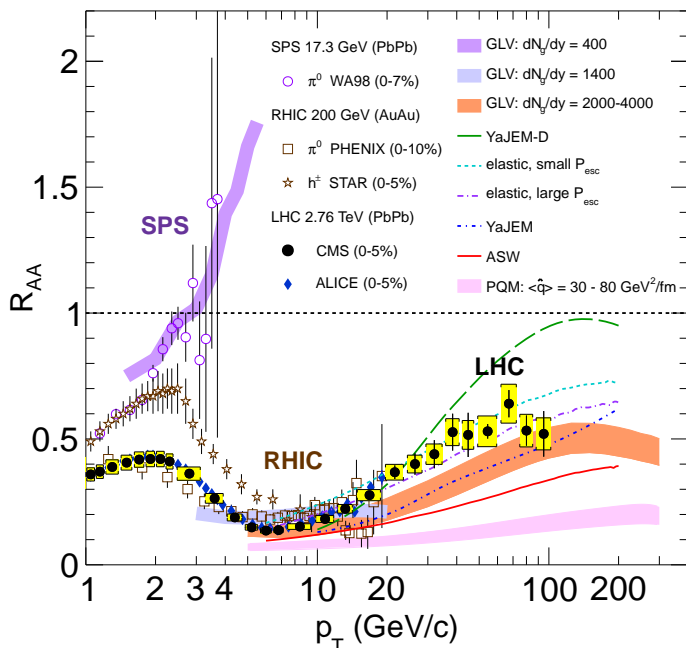
The suppression can be explained by different path lengths of the two produced high-energy particles. Considering a pair production near the edge of the medium, one particle flies out without many interactions, whereas the second particle traverses the whole medium and deposits a large fraction of its energy, failing to pass the momentum threshold for the measurement. This picture is also confirmed at the LHC by measuring the momentum imbalance A_J of fully reconstructed jets in heavy-ion collisions and finding a significant deviation compared to p+p collisions [ATLAS10, CMS11c].

The effect of this suppression can also be seen for single particles without studying correlations or fully reconstructed jets. A suitable quantity is the *nuclear modification factor*, which is defined as the particle yield in heavy-ion collisions divided by the scaled p+p yield,

$$R_{AA} = \frac{d^2 N_{AA}/dp_T dy}{N_{\text{bin}} d^2 N_{pp}/dp_T dy} . \quad (2.9)$$

The appropriate scaling factor is the number of binary collisions N_{bin} , defined in Equation (A.21) and calculated within the GLAUBER model (see Appendix A.5). If no medium effects occurred, the R_{AA} would be one for highly energetic particles, which is indeed the case for gauge bosons

Figure 2.4.: Compilation of measured R_{AA} of neutral pions π^0 , charged hadrons h^\pm , and charged particles at SPS [WA9802, d'E04], RHIC [PHENIX08b, STAR03], and LHC [ALICE11b, CMS12e] as a function of transverse momentum p_T together with several theoretical models [DLP05, VG02, Vit04, SW03, ADSW05, RHPE11]. Figure taken from [CMS12e].



such as photons, W and Z bosons [PHENIX05b, CMS12j] that do not interact strongly with the medium.²¹

Figure 2.4 depicts the R_{AA} of light particles for SPS, RHIC, and LHC. It is clearly visible that high-momentum particles are strongly suppressed at RHIC and LHC. The rising R_{AA} at LHC suggests that the coupling of the jets to the medium decreases with their energy, as one would expect from asymptotic freedom (cf. Section 2.1.1). Several theoretical models for the energy loss of light partons in the QGP are on the market [Zak96, BDM⁺97a, GLV01, AMY02, VG02, Vit04, SW03, DLP05, ADSW05, WHDG07, FXG09, SGJ09, RHPE11], some of which are also depicted in Figure 2.4. For some excellent overviews and comparisons see Refs. [MVL11, BGM⁺09, ACG⁺12]. In Section 6.2.1 we also present results for the light parton R_{AA} within BAMPS.

Open heavy flavor

Open heavy flavor particles such as D and B mesons are ideal probes to study the QGP. Their heavy constituents, namely, charm and bottom quarks, are well calibrated in a sense that they are entirely produced in the early stage of the heavy-ion collision due to their large mass [UFXG10a] and are also tagged during hadronization because of flavor conservation in QCD. After their early production they traverse the QGP for a rather long time, collide with other medium particles, lose energy, and participate in the collective behavior. Due to these processes their distributions are modified and can reveal—via experimentally accessible observables like the elliptic flow and nuclear modification factor—information about the properties of the medium.

Both the elliptic flow and nuclear modification factor are suitable observables to study the

²¹Soft processes do not scale with N_{bin} and, thus, the R_{AA} is below one for small transverse momenta even without suppression.

energy loss of heavy quarks and their coupling to the medium. The larger the v_2 , the stronger heavy quarks interact with the medium and adopt its momentum anisotropy. A small value of R_{AA} indicates a strong suppression and, therefore, large energy loss of heavy quarks in the QGP.

Of course, heavy quarks themselves cannot be measured in the detector directly due to confinement. Instead, charm and bottom quarks hadronize at the phase transition to D and B mesons, respectively, which contain one heavy and one light quark. For charm quarks in particular the following D mesons exist: D^+ ($c\bar{d}$), D^- ($\bar{c}d$), D_s^+ ($c\bar{s}$), D_s^- ($\bar{c}s$), D^0 ($c\bar{u}$), and \bar{D}^0 ($\bar{c}u$). Nevertheless, the mesons themselves can also not be detected since their life time is too small ($\tau = (1040 \pm 7) \cdot 10^{-15}$ s for D^\pm mesons [PDG12]). However, D mesons can be reconstructed by measuring their decay products, which has been done—for the first time in ultra-relativistic heavy-ion physics—by the ALICE collaboration [ALICE12f]. The golden channels are the decays to pions and kaons, $D^0 \rightarrow K^- \pi^+$ (branching ratio (BR) of 3.88 ± 0.05 % [PDG12]), $D^+ \rightarrow K^- \pi^+ \pi^+$ (BR of 9.13 ± 0.19 % [PDG12]), and $D^{*+} \rightarrow D^0 \pi^+ \rightarrow K^- \pi^+ \pi^+$ (BR of the first (strong) decay: 67.7 ± 0.5 % [PDG12]). After searching for decay topologies with a secondary vertex that is displaced in respect to the primary vertex (the heavy-ion collision), D meson candidates are extracted by cutting on the invariant mass of the decay products. A recent upgrade enables also STAR to reconstruct D mesons at RHIC [STAR13b]. As a complimentary measurement to D mesons, CMS reconstructs non-prompt J/ψ via the di-muon channel (BR of 5.93 ± 0.06 % [PDG12]) [CMS12f]. Non-prompt J/ψ are produced in the decay of B mesons (combined BR of about 0.5 % [PDG12]), for instance, in $B \rightarrow J/\psi K$, and, thus, probe the bottom sector. In contrast, prompt J/ψ are created initially or in the fireball evolution, which is discussed in the next section. Experimentally, non-prompt J/ψ can be separated from prompt J/ψ via the displaced secondary vertex of the B meson decay due to its comparably long life time ($\tau = (1641 \pm 8) \cdot 10^{-15}$ s for B^\pm mesons in comparison to the J/ψ life time of $(71 \pm 16) \cdot 10^{-22}$ s [PDG12])

Another possibility, which has been extensively used at RHIC [STAR07, PHENIX07a, PHENIX11b, STAR13a], is the measurement of heavy flavor electrons. These are electrons produced in the decay of heavy flavor mesons. Prominent channels for D mesons are, for instance, the decay to an electron, kaon, and electron neutrino, $D^+ \rightarrow e^+ \bar{K}^0 \nu_e$ and $D^- \rightarrow e^- K^0 \bar{\nu}_e$ (BR of 8.83 ± 0.22 % [PDG12]). The heavy flavor electron signal suffers from a huge contamination due to different electron sources, mainly decay photon conversions (~ 85 %) and DALITZ decays (~ 15 %) [STAR07]. Those contributions are usually subtracted either via a cocktail of various measured and simulated non-heavy-flavor electron sources [PHENIX07a, ALICE13e], cuts on the invariant mass of di-electrons [STAR07], or via the converter method [PHENIX07a], where additional radiation material is added to the beam pipe for part of the run, which allows an estimation of the electrons from photon conversions. Quite analogous is the measurement of heavy flavor muons, which is performed by ALICE at forward rapidities behind several thick absorbers with the muon arm of the detector [ALICE12e] in addition to the electron measurement at mid-rapidity [ALICE13e]. However, a disadvantage of the heavy flavor lepton measurements is that the contribution from charm and bottom quarks cannot be separated. Details concerning the decay channels or branching ratios can be found in the *Particle Data Book* [PDG12].

The heavy flavor electron data from RHIC [STAR07, PHENIX07a, PHENIX11b] and the heavy flavor electron [ALICE13e], muon [ALICE12e], D meson [ALICE12f, ALICE13f], non-prompt J/ψ [CMS12f], and bottom tagged jets [CMS13c, CMS12g] data from LHC show that

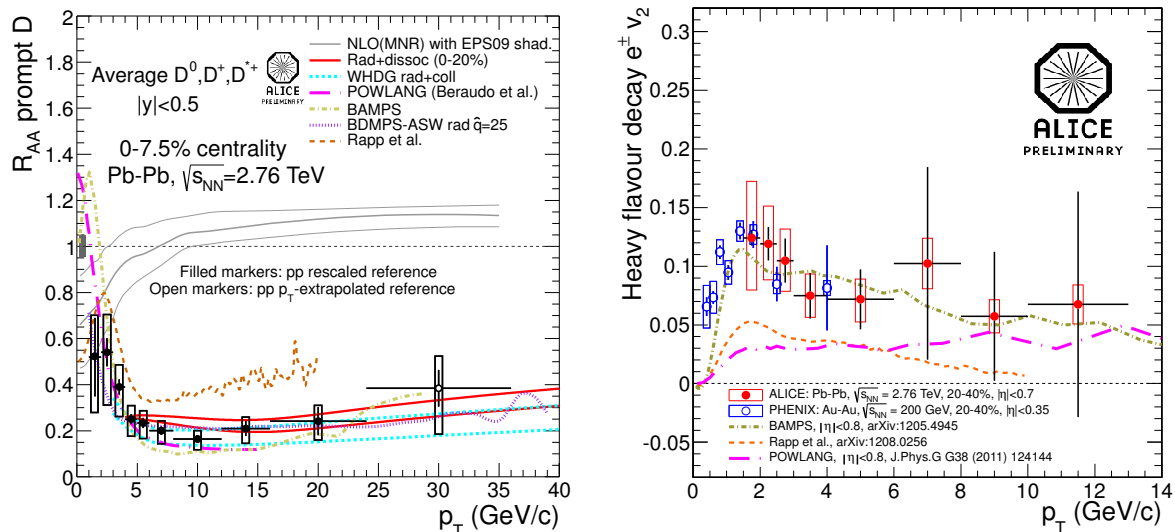


Figure 2.5.: R_{AA} of D mesons (left) and v_2 of heavy flavor electrons (right) at $\sqrt{s} = 2.76$ TeV measured with the ALICE detector. Model predictions from BAMPS [UFXXG11a, UFXXG12b], BDMPS-ASW [ADSW05], POWLANG [ABDP⁺11, MAB⁺11], “Rad+disso” [SVZ09, HVZ12], Rapp et al. [vHGR06, HFR12b], and WHDG [HG11] are also shown. For comparison, NLO MNR calculations [MNR92] with EPS09 shadowing parameterizations [EPS09] are depicted for the R_{AA} . The R_{AA} and v_2 plots are taken from Refs. [ALICE13e] and [ALICE12h], respectively.

the suppression of heavy flavor is comparable to that of light particles. From the theory perspective it was thought that radiative processes involving heavy quarks are reduced due to the *dead cone effect* (see Section 3.2.4), which would imply a smaller suppression for massive particles. Whether this is indeed the case or what is the exact mechanism of the intense interaction with the medium is actively debated and also subject of this work. Elliptic flow v_2 measurements of heavy flavor electrons at RHIC [PHENIX11b] as well as of D mesons [ALICE12i] and heavy flavor electrons [ALICE13g] at LHC also show that heavy quarks interact strongly with the other particles of the medium.

Figure 2.5 depicts the R_{AA} of D mesons in central events and the v_2 of heavy flavor electrons in non-central collisions at the LHC. Several model calculations are also shown. Although the D meson R_{AA} is in agreement with most of the models, the v_2 data seems to be more difficult to describe. A very good agreement is found with BAMPS, which are our predictions with a scaled binary cross section. We will discuss the details of this calculation in Section 6.1.

Table 2.1 gives an overview of various open heavy flavor models on the market. Most models employ pQCD cross sections, where the complete picture should include both elastic and radiative processes. The resonance scattering models assume that D - and B -meson-like resonances can form and decay in the QGP, which contribute quite effectively to the energy loss of heavy quarks through the isotropic outgoing momentum distribution of these s channel processes. Within the AdS/CFT framework the heavy quark energy loss is calculated from a string in five dimensional AdS space, which is attached to the horizon of a black hole, and subsequently matched to a four dimensional supersymmetric YANG-MILLS theory, which

Table 2.1.: Overview of open heavy flavor models.

Theory	Authors	References
pQCD elastic only	Alberico, Beraudo, De Pace, Molinari, Monteno, Nardi, Prino	[ABDP ⁺ 11, ABDP ⁺ 13]
	Gossiaux, Aichelin	[GA08, GBA09]
	Molnar	[Mol07]
	Meistrenko, Uphoff, Greiner, Peshier	[MPUG13]
	Moore, Teaney	[MT05]
	Uphoff, Fochler, Xu, Greiner	this work ^a & [UFXG11a, UFXG12b]
	Young, Schenke, Jeon, Gale	[YSJG12]
	Zhang, Chen, Ko	[ZCK05]
	...	
	radiative only	Abir, Jamil, Mustafa, Srivastava
...		
elastic+radiative	Armesto, Cacciari, Dainese, Salgado, Wiedemann	[ACD ⁺ 06]
	Buzatti, Gyulassy	[BG12b, BG12a]
	Cao, Bass	[CB11, CQBM13]
	Wicks, Horowitz, Djordjevic, Gyulassy	[DGVW06, WHDG07]
	Nahrgang, Gossiaux, Aichelin	[GNB ⁺ 13, NAGW13]
	Mazumder, Bhattacharyya, Alam, Das	[MBAD11, MBA13]
	Mustafa	[Mus05]
	Sharma, Vitev, Zhang	[SVZ09]
	Uphoff, Fochler, Xu, Greiner	this work ^b
	...	
Resonance scatterings	Adil, Vitev	[AV07]
	He, Fries, Rapp	[HFR12a, HFR13]
	v. Hees, Greco, Rapp	[vHGR06, vHMGR08]
	Lang, v. Hees, Bleicher	[LvHSB12a, LvHSB12b]
	...	
AdS/CFT	Chesler, Lekaveckas, Rajagopal	[CLR13a, CLR13b]
	Horowitz, Gyulassy	[HG08, Hor13]
	...	

^a The results with only elastic interactions are summarized in Section 6.1.

^b The results with elastic and radiative interactions are presented in Section 6.2.

can be interpreted as an estimate of the energy loss in the strong coupling regime of QCD. AdS/CFT models predict a very strong suppression at the LHC, which is not compatible with the data [Hor13]. A comprehensive overview of heavy flavor in heavy-ion collisions is given in Ref. [RvH10], and more recently in Ref. [GAG12]. In the following, we highlight five models and discuss a few details.

- **Wicks, Horowitz, Djordjevic, Gyulassy: WHDG**

WHDG [DGVW06, WHDG07, Hor13] calculate radiative processes within the DGLV opacity expansion from pQCD matrix elements. The result includes all orders in opacity, the QCD analog of the TER-MIKAELIAN effect by considering finite gluon masses, and the LANDAU-POMERANCHUK-MIGDAL (LPM) effect through the coherent resummation of multiple gluon emission. Elastic scatterings are implemented incoherently. The medium is parameterized within a basic geometric picture and its initial density is constrained such that the pion R_{AA} at RHIC is well described. With the same parameters, the heavy flavor electron data at RHIC can also be explained if path length fluctuations are considered. Predictions for the LHC show a slight underestimation of the charged hadron R_{AA} , although the D meson R_{AA} is reasonably well described. However, the elliptic flow of heavy flavor particles at small and intermediate p_T in the WHDG model is much smaller than the data both at RHIC and LHC.

- **Gossiaux, Aichelin: MC@_sHQ**

The model MC@_sHQ [GA08, GBA09, GNB⁺13, NAGW13] studies elastic and radiative heavy quark interactions with pQCD matrix elements. The initial heavy quark distribution is obtained from fixed-order-next-to-leading-log (FONLL) calculations [CFH⁺12] (cf. Section 4.3). The interactions of heavy quarks with medium particles, which are sampled from a hydrodynamic model [KSH00], are determined from transition probabilities. Elastic interactions are calculated with a running coupling parameterization as well as a DEBYE screening matched to the transition between hard-thermal-loop calculations and semi-hard processes. Radiative interactions are employed in the GUNION-BERTSCH approximation with the inclusion of the LPM effect and gluon damping [BGGA12]. With only binary collisions the RHIC heavy flavor electron v_2 and R_{AA} data can be described if the binary cross section is scaled by $K = 2$. Including also radiative processes, the heavy quark energy loss is overestimated since a rather small factor $K = 0.7$ is needed to fit the data, which could be caused by theoretical uncertainties within the calculation. With these parameters the R_{AA} agreement at LHC is rather good, whereas the v_2 data is slightly underpredicted. Furthermore, the suppression of heavy quarks in p+p collisions at LHC was studied with MC@_sHQ [VGWA11].

- **Uphoff, Fochler, Xu, Greiner: BAMPS**

Heavy flavor transport within BAMPS [UFXG11a, UFXG12b] is the main topic of this work and is described in detail in the following chapters. The initial heavy quark distribution is obtained from MC@NLO (see Section 4.3) and the medium interactions are carried out by solving the BOLTZMANN equation with pQCD cross sections (see Chapters 3 and 4), not only for heavy quarks but for all other medium particles as well. Elastic processes employ a running coupling and an improved DEBYE screening matched to hard-thermal-loop calculations, quite analogous to MC@_sHQ. Details are given in Sections 3.1 and 5.1.5. As is shown in Section 6.1, RHIC heavy flavor electron data can

be reproduced with only binary interactions if the cross section is scaled with $K = 3.5$.²² With this parameter fixed, our predictions for v_2 at LHC are in very good agreement with the data, but the R_{AA} is slightly underestimated. Also as part of this work, we have included radiative processes for heavy quarks in BAMPS. Many details concerning the radiative processes are given in Section 3.2 and the results are shown in Section 6.2. In contrast to most other heavy flavor models, BAMPS also treats all light partons on the same footing, allowing enlightening comparisons between light and heavy particles within the same framework.

- **He, Fries, v. Hees, Greco, Rapp**

The model [vHGR06, vHMGR08, HFR12a, HFR13] investigates heavy quarks within LANGEVIN simulations with transport coefficients from the T matrix approach for heavy quark interactions with medium particles. For the input heavy quark potential, the internal energy is taken, which is extracted from lattice QCD calculations. The idea behind this approach is that D - and B -meson-like resonances can form and decay again in the medium close to the critical temperature. While in early versions a fireball parameterization has been used [vHGR06, vHMGR08], recent results [HFR12a, HFR13] are obtained with an ideal hydrodynamic model as a background. Furthermore, interactions in the hadronic phase are taken into account via effective hadronic theory. The R_{AA} of D mesons and electrons at RHIC can be rather well described. At LHC the R_{AA} of D mesons is a bit larger than the data, whereas the predicted v_2 is too small, as can be seen in Figure 2.5.

- **Lang, v. Hees, Bleicher: UrQMD**

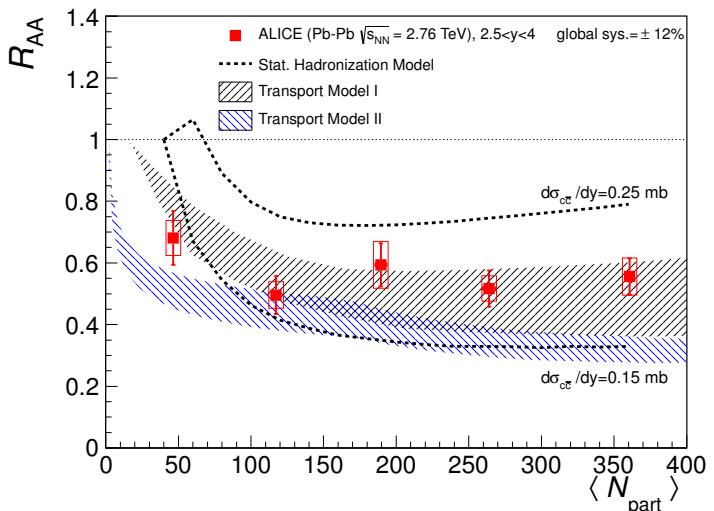
Recently, resonance scattering has been implemented in a LANGEVIN approach in the UrQMD hybrid model [LvHSB12a, LvHSB12b, LvHSB13]. The UrQMD hybrid model [PSB⁺08] combines the traditional UrQMD model with a hydrodynamical evolution for the hot and dense phase. To this end, initial nucleon-nucleon interactions in the heavy-ion collision are simulated with UrQMD. Then the particle distributions are mapped to a hydrodynamical model where the QGP evolution and phase transition are carried out. Finally, through a COOPER-FRYE freeze-out hadrons are obtained, which are evolved further within the UrQMD hadronic cascade. Heavy quarks interact only in the hydrodynamical phase with drag coefficients taken from Refs. [vHGR06, vHMGR08]. Including event-by-event fluctuations and coalescence for heavy quarks, both v_2 and R_{AA} at RHIC and LHC can be described. Furthermore, predictions are made for Pb+Pb collisions with $\sqrt{s} = 25$ GeV at FAIR [LvHSB13].

J/ψ suppression

A J/ψ meson is a bound state of a charm and anti-charm quark, whose potential can be described by Equation (2.3). For a J/ψ in the QGP, however, the confining term vanishes ($\kappa = 0$). Furthermore, the COULOMB term must be modified to take color screening effects

²²The discrepancy to MC@_sHQ, which needs only $K = 2$, can be easily explained. In MC@_sHQ the scale of the running coupling within the definition of the DEBYE mass (see Equation (3.18)) is taken as the DEBYE mass itself, whereas in BAMPS the momentum transfer of the considered process is used. Taking the constant DEBYE mass instead of the momentum transfer as the scale makes the DEBYE mass smaller and, thus, the cross section larger, which in turn results in a smaller K factor.

Figure 2.6.: R_{AA} of inclusive J/ψ measured at forward rapidity in Pb-Pb collisions at $\sqrt{s_{NN}} = 2.76$ TeV compared to the predictions by the Statistical Hadronization Model [ABMRS11], Transport Model I [ZR11] and II [LQXZ09]. Figure taken from [ALICE12d].



into account, [Won94]

$$V(r) = -\frac{4}{3} \frac{\alpha_s(r)}{r} e^{-r/\lambda_D}, \quad (2.10)$$

where λ_D is the DEBYE length, which is related to the DEBYE mass $m_D = 1/\lambda_D$, defined in Equation (3.18). This DEBYE screening is analogous to electromagnetic plasmas, but is due to color charge instead of regular charge. Around the heavy quark bound state, a cloud of other partons is formed that weakens the binding and can lead to a dissociation of the J/ψ meson in the medium.

The suppression of J/ψ in heavy-ion collisions was first proposed by MATSUI and SATZ [MS86] to be a signature of QGP formation. Since lattice calculations [AH04, MP07] indicate that the probability of the J/ψ melting depends on the medium temperature, J/ψ suppression could be used as a thermometer for the QGP. However, the interpretation of the data is significantly complicated because of J/ψ regeneration in the medium (cf. Section 3.3) as well as J/ψ suppression due to cold nuclear matter effects (see Section 4.4). Regeneration denotes the in-medium formation of J/ψ from independent charm and anti-charm pairs and is expected to be important at LHC and maybe also RHIC energies [GR02, vHR05, TM06, ABMRS07, YS10, LQXZ09, ZXZ10]. Cold nuclear matter effects, on the other hand, are all phenomena contributing to J/ψ suppression that would also be present if no QGP were formed. The best systems to study these effects are nucleon-nucleus or deuteron-nucleus collisions since one can measure directly the impact of nuclear effects on J/ψ production in the absence of a QGP. A detailed overview of J/ψ in heavy-ion collisions can be found in Ref. [B⁺11].

Experimental data show indeed a strong suppression of J/ψ at RHIC [PHENIX07c]. Nevertheless, in central collisions at LHC this effect is not as pronounced [ALICE12d], which could be a hint that the abundance of charm quarks at LHC allows for regeneration of J/ψ . Figure 2.6 shows recent ALICE data of the J/ψ R_{AA} for different collision centralities. The Statistical Hadronization Model [BMS00, BMS01, ABMRS07, ABMRS11], which assumes that all initial J/ψ melt and all final J/ψ statistically form at the phase boundary, is in good agreement with the data. Also the two transport models [ZR08, ZR11, LQXZ09, ZXZ10] with a hydrodynamic background are compatible with the data.

Recent measurements show that the elliptic flow of J/ψ is consistent with zero at RHIC [PHENIX08c, STAR12] and quite small at LHC [ALICE13a]. This challenges the picture of the Statistical Hadronization Model, in which the J/ψ would acquire a large v_2 from the flowing charm quarks. Nevertheless, the two previously mentioned transport models (also depicted in Figure 2.6 for the R_{AA}) are in good agreement with the v_2 data [ZER13, LXZ10].

Since in BAMPS we have access to all space-time properties of charm quarks and light medium particles, it is very promising to study J/ψ suppression and flow as well. First calculations are shown in Chapter 7.

At the LHC a wealth of new data on quarkonia states besides J/ψ suggests that the suppression depends on the binding energy of the states [CMS12k] and, hence, fits well in the MATSUI and SATZ picture. Especially clean probes are the Υ states [CMS11a, CMS12d, LCXZ11, SB12, EZR12], consisting of two bottom quarks, since the regeneration can be neglected in view of the small in-medium bottom production at LHC [UFXG10a].

3. Partonic cross sections

We do not know a truth without knowing its cause.

Nicomachean Ethics, I.1
ARISTOTLE

In this chapter we outline the partonic cross sections of heavy flavor processes. The binary cross sections of heavy quarks with light quarks and gluons are calculated within pQCD with a running coupling and an improved DEBYE screening matched to hard-thermal-loop calculations in Section 3.1. Radiative contributions are presented in great detail in Section 3.2, which includes the derivation of the GUNION-BERTSCH cross section, the explanation of the dead cone effect, as well as the introduction of the LANDAU-POMERANCHUK-MIGDAL effect. All these calculations are done for massive quarks. However, they also apply to light quarks if the mass is set to zero. As a reference, we summarize all binary light parton cross sections with a running coupling in Appendix A.3. The dissociation and regeneration cross sections of J/ψ mesons in the QGP are addressed in Section 3.3.

The cross section of two particles in the initial state and n particles in the final state ($2 \rightarrow n$ process) is given by [PS95]

$$\sigma = \frac{1}{2E_1 2E_2 v_{\text{rel}}} \frac{1}{\nu} \left(\prod_{i=3}^{n+2} \int \frac{d^3 p_i}{(2\pi)^3 2E_i} \right) (2\pi)^4 \delta^{(4)}(p_1 + p_2 - \sum_{i=3}^{n+2} p_i) |\overline{\mathcal{M}}_{12 \rightarrow 34 \dots n+2}|^2, \quad (3.1)$$

where we labeled the momenta of the particles according to the notation $p_1 p_2 \rightarrow p_3 p_4 \dots p_{n+2}$. The relative velocity of the two incoming particles is given by [CGR93]

$$v_{\text{rel}} = \frac{\sqrt{(p_1^\mu p_{2\mu})^2 - m_1^2 m_2^2}}{E_1 E_2}, \quad (3.2)$$

which simplifies for massless particles to $v_{\text{rel}} = s/2E_1 E_2$, where s is the squared center-of-mass energy (cf. also Appendix A.2). As a note, this relative velocity can be larger than the velocity of light $c = 1$ (using natural units, see Appendix A.1) and, therefore, is not the actual relativistic invariant relative velocity but proportional to it. A detailed discussion can be found in Ref. [Sch08]. $|\overline{\mathcal{M}}_{12 \rightarrow 34 \dots n+2}|^2$ denotes the mean squared matrix element that is averaged over all initial and summed over all final color and spin states. The delta function ensures energy and momentum conservation and the symmetry factor $\nu = m!$ differs only from unity if $m > 1$ identical particles are in the final state.

The kinematic prefactor simplifies in the center-of-mass frame for the three most interesting cases of the scattering of two light partons, one light and one heavy parton, and two heavy partons to

$$2E_1 2E_2 v_{\text{rel}} = 2\sqrt{(s - m_1^2 - m_2^2)^2 - 4m_1^2 m_2^2} = \begin{cases} 2s & m_1 = m_2 = 0 \\ 2(s - M^2) & m_1 = M, m_2 = 0 \\ 2s\sqrt{1 - 4M^2/s} & m_1 = m_2 = M \end{cases} \quad (3.3)$$

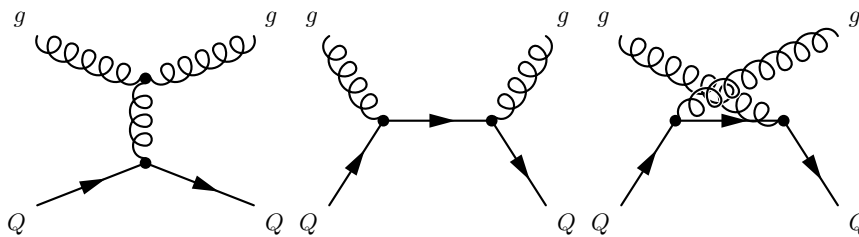


Figure 3.1.: FEYNMAN diagrams in leading order pQCD for elastic heavy quark scattering off a gluon, $g + Q \rightarrow g + Q$. Time goes from left to right.

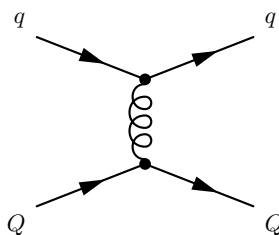


Figure 3.2.: FEYNMAN diagram for elastic heavy quark scattering with a light quark, $q + Q \rightarrow q + Q$.

As a note, differential cross sections (e.g. $d\sigma/dy$) can be obtained from Equation (3.1) by projecting out variables with delta functions (e.g., writing $\delta(y - y')$ in the integrand, where y' is one of the integration variables hidden in d^3p in Equation (3.1)).

3.1. Elastic heavy quark scattering

In the pQCD expansion of the cross section in orders of the coupling α_s elastic scatterings are the lowest order contribution. Although radiative processes lead to a larger energy loss due to the three particles in the final state (see Section 5.3), elastic collisions also play an important role in the evolution of heavy quarks.

Heavy quarks interact in the QGP via the following elastic collisions with light partons:

$$\begin{aligned} Q + g &\rightarrow Q + g \\ Q + q &\rightarrow Q + q . \end{aligned} \tag{3.4}$$

The FEYNMAN diagrams for these processes are shown in Figures 3.1 and 3.2, respectively. The cross sections for both processes can be calculated in leading-order pQCD. To treat this accurately, we explicitly take the running of the coupling into account. Furthermore, we employ an improved DEBYE screening that is more precise than the standard procedure in the literature. This is done by comparing the energy loss per unit length dE/dx of the BORN cross section¹ to the energy loss within the hard-thermal-loop approach (see Section 5.1.5).

¹The BORN cross section denotes the cross section calculated in lowest order perturbation theory.

3.1.1. Elastic heavy quark scattering with a gluon in vacuum

Especially interactions with gluons play an important role since gluons dominate the dynamics of the QGP [MSW12] and the cross section is enhanced compared to interactions with light quarks. Therefore, we outline in the following the calculation of the cross section for $g + Q \rightarrow g + Q$ in detail. Gluon scattering with a heavy anti-quark, $g + \bar{Q} \rightarrow g + \bar{Q}$, has the same cross section due to time reversal invariance (see Appendix A.4) [ORG78].

For general $2 \rightarrow 2$ processes in the center-of-mass frame, a simple expression for the differential cross section can be derived from Equation (3.1),

$$\frac{d\sigma}{dt} = \frac{1}{16\pi\sqrt{s}|\mathbf{p}_1|} \frac{1}{2E_1 2E_2 v_{\text{rel}}} |\overline{\mathcal{M}}_{2 \rightarrow 2}|^2, \quad (3.5)$$

where we introduced the MANDELSTAM variable $t = (p_1 - p_3)^2$ (cf. Appendix A.2) and used the notation of Figure 3.3.

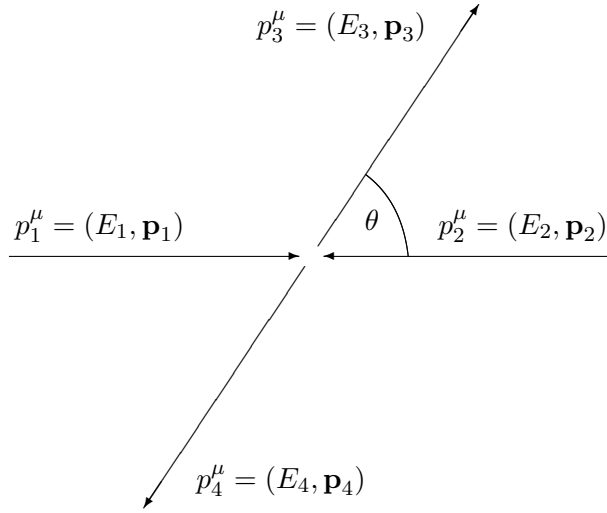


Figure 3.3.: Schematic illustration and notation of a $2 \rightarrow 2$ process.

Employing the relevant kinematic relations, for instance, Equation (3.3), the differential cross section for the process $g + Q \rightarrow g + Q$ is explicitly given by

$$\frac{d\sigma}{dt} = \frac{|\overline{\mathcal{M}}_{gQ \rightarrow gQ}|^2}{16\pi(s - M^2)^2}. \quad (3.6)$$

The most important contribution to the cross section comes from the t channel, which is the left diagram in Figure 3.1. Therefore, we outline in the following how the matrix element can be derived for this channel. Employing the FEYNMAN rules (see for instance Ref. [PS95]), the matrix element of the t channel is given by (spin indices are suppressed)

$$\begin{aligned} \mathcal{M}_{gQ \rightarrow gQ}^t \text{ channel} &= \bar{u}(p_3) i g \gamma^\mu \lambda_{ki}^b u(p_1) \frac{-i g_{\mu\nu} \delta^{bc}}{q^2} \epsilon_\delta^*(p_4) \epsilon_\sigma(p_2) \\ &\quad \times g f^{cmn} \left[g^{\nu\sigma} (-q - p_2)^\delta + g^{\sigma\delta} (p_2 + p_4)^\nu + g^{\delta\nu} (-p_4 + q)^\sigma \right], \end{aligned} \quad (3.7)$$

where u denotes the DIRAC quark spinor and ϵ the gluon polarization vector. While g , γ^μ , and f have been introduced in Section 2.1, λ are the color matrices and q represents the momentum of the internal gluon line. After squaring the matrix element, it can be considerably simplified by using the relations [PS95]

$$\sum_s u^s(p)\bar{u}^s(p) = \not{p} + m \quad \text{and} \quad \sum_{\text{polarizations}} \epsilon_\mu^*(p)\epsilon_\nu(p) = -g_{\mu\nu} + \text{vanishing terms} , \quad (3.8)$$

where we used the FEYNMAN slash notation, $\not{p} = \gamma^\mu p_\mu$. In principle, one also has to take into account the interactions with the ghost field since the gluon is a non-Abelian gauge boson. However, one can circumvent this extra task by considering only the physical polarization states of the gluon [PS95], which are transverse to the gluon momentum, $p \cdot \epsilon(p) = 0$. After collecting all the terms, the averaged squared matrix element, which is summed over final and averaged over initial color, spin, and polarization states, is given by

$$\begin{aligned} |\overline{\mathcal{M}}_{gQ \rightarrow gQ}^t \text{ channel}|^2 &= \frac{1}{d_Q} \frac{1}{d_g} \sum_{\text{color}} \sum_{\text{spin}} \sum_{\text{polarizations}} |\mathcal{M}_{gQ \rightarrow gQ}^t \text{ channel}|^2 \\ &= \frac{1}{6} \frac{1}{16} 32g^4 \sum_{\text{color}} \lambda_{ki}^b \lambda_{ik}^c f^{bmn} f^{cmn} \frac{1}{q^4} \\ &\quad \times [(p_1 \cdot p_2)(p_3 \cdot p_4) + (p_1 \cdot p_3)(p_2 \cdot p_4) + (p_1 \cdot p_4)(p_2 \cdot p_3) + (p_2 \cdot p_4)M^2] , \end{aligned} \quad (3.9)$$

where $d_Q = 2 \cdot 3$ and $d_g = 2 \cdot 8$ are the degeneracy factors of heavy quarks and gluons, respectively. The color factor evaluates to

$$\sum_{\text{color}} \lambda_{ki}^b \lambda_{ik}^c f^{bmn} f^{cmn} = C(N)\delta^{bc}C_2(G)\delta^{bc} = 12 , \quad (3.10)$$

where $C(N) = 1/2$ and $C_2(G) = N$ are constants of the fundamental and adjoint representation of $SU(N)$, respectively. Since QCD has a $SU(3)$ gauge symmetry, it is $N = 3$.

Inserting the color factor in Equation (3.9) and expressing the latter in terms of MANDELSTAM variables yields the final result for the squared matrix element of the t channel of the process $gQ \rightarrow gQ$,

$$|\overline{\mathcal{M}}_{gQ \rightarrow gQ}^t \text{ channel}|^2 = 2g^4 \frac{(s - M^2)(M^2 - u)}{t^2} = 32\pi^2 \alpha_s^2 \frac{(s - M^2)(M^2 - u)}{t^2} , \quad (3.11)$$

where $g^2 = 4\pi\alpha_s$ has been used.

By generalizing the argumentation also to the s and u channel, the averaged squared matrix element $|\overline{\mathcal{M}}_{gQ \rightarrow gQ}|^2$ for all three channels and their interference terms reads [Com79]

$$\begin{aligned} |\overline{\mathcal{M}}_{gQ \rightarrow gQ}|^2 &= \pi^2 \alpha_s^2 \left[\frac{32(s - M^2)(M^2 - u)}{t^2} + \frac{64}{9} \frac{(s - M^2)(M^2 - u) + 2M^2(s + M^2)}{(s - M^2)^2} \right. \\ &\quad + \frac{64}{9} \frac{(s - M^2)(M^2 - u) + 2M^2(u + M^2)}{(M^2 - u)^2} + \frac{16}{9} \frac{M^2(4M^2 - t)}{(s - M^2)(M^2 - u)} \\ &\quad + 16 \frac{(s - M^2)(M^2 - u) + M^2(s - u)}{t(s - M^2)} \\ &\quad \left. - 16 \frac{(s - M^2)(M^2 - u) - M^2(s - u)}{t(M^2 - u)} \right] . \end{aligned} \quad (3.12)$$

The first term is the contribution from the t channel and exactly the same result we obtained in Equation (3.11).

To calculate the interaction probability in BAMPS simulations (see Chapter 4), the total cross section is needed. First, the MANDELSTAM relation $s + t + u = \sum_i m_i^2 = 2M^2$ (cf. Appendix A.2) can be used to substitute u . Consequently, the total cross section for $gQ \rightarrow gQ$ is obtained by integrating the differential cross section from Equation (3.6) over t ,

$$\sigma_{gQ \rightarrow gQ}(s) = \int_{t_{\min}}^{t_{\max}} \frac{d\sigma}{dt} dt . \quad (3.13)$$

The boundaries of the integral can be derived from kinematic considerations. From the definition of the MANDELSTAM variable

$$t = (p_1 - p_3)^2 = 2E_1 E_3 (\cos \theta - 1) \quad (3.14)$$

one gets from forward ($\theta = 0^\circ$) and backward ($\theta = 180^\circ$) scattering the boundaries

$$\begin{aligned} t_{\max} &= 0 \\ t_{\min} &= -\frac{(s - M^2)^2}{s} . \end{aligned} \quad (3.15)$$

However, $t_{\max} = 0$ leads to a singularity in the t channel, which causes a diverging cross section. The reason for this is the gluon propagator in the left diagram of Figure 3.1. This propagator diverges for small momentum transfers (small t) since gluons are massless. In a medium, however, the internal gluon acquires an effective mass that cures the divergence.

3.1.2. Debye screening in a medium

In thermal field theory long-range interactions (which correspond to small t) are screened by the medium. Formally, the gluon propagator must be screened with its self-energy $\Pi_T(\omega, q)$

$$\frac{1}{t} \rightarrow \frac{1}{t - \Pi_T(\omega, q)} \quad (3.16)$$

with $(\omega, \mathbf{q}) = p_1^\mu - p_3^\mu$ and $t = \omega^2 - q^2$. Nevertheless, calculations with the self-energy are tedious. Therefore, we approximate the self-energy with a screening mass $\mu_t = \kappa_t m_D^2$ that is proportional to the DEBYE mass,

$$\frac{1}{t} \rightarrow \frac{1}{t - \mu_t} . \quad (3.17)$$

The prefactor κ_t is mostly set to 1 in the literature without a sophisticated reason. However, one can fix this factor to $\kappa_t \approx 0.2$ by comparing the dE/dx of the BORN cross section with κ_t to the energy loss within the hard-thermal-loop approach (see Section 5.1.5).

The DEBYE mass for gluons is defined by [XG05, Won96a]

$$m_D^2 = \pi \alpha_s d_g \int \frac{d^3 p}{(2\pi)^3} \frac{1}{p} (N_c f_g + n_f f_q) , \quad (3.18)$$

and for light quarks by

$$m_q^2 = 4\pi\alpha_s \frac{N_c^2 - 1}{2N_c} \int \frac{d^3p}{(2\pi)^3} \frac{1}{p} (f_g + f_q), \quad (3.19)$$

where $N_c = 3$ is the number of colors for $SU(3)$ symmetry of QCD, $d_g = 2 \cdot 8 = 16$ the degeneracy factor of gluons, n_f the number of flavors, and f the distribution of gluons and quarks. It has been assumed that local equilibrium is present and df/dp can be written as f/p . In the transport model BAMPS (see Chapter 4) the integral in (3.18) is evaluated as a sum over all particles i in a cell with volume V , which is chosen small enough to ensure local homogeneity,

$$d_i \int \frac{d^3p}{(2\pi)^3} \frac{f_i}{p} \rightarrow \frac{1}{VN_{\text{test}}} \sum_i \frac{1}{p_i}, \quad (3.20)$$

where i stands for g (gluons) or q (quarks). N_{test} is the number of test particles in BAMPS (see Section 4.1). The degeneracy factor of light quarks is $d_q = 2N_c 2n_f$.

For a medium in equilibrium the integrals can be easily performed. With quantum statistics (BOSE-EINSTEIN and FERMI-DIRAC distributions for gluons and quarks, respectively) the DEBYE mass is

$$m_{D,\text{eq},QS}^2 = \frac{4\pi\alpha_s}{3} \left(N_c + \frac{n_f}{2} \right) T^2. \quad (3.21)$$

Assuming classical BOLTZMANN statistics for gluons and quarks² the DEBYE mass reads

$$m_{D,\text{eq},CS}^2 = \frac{8\alpha_s}{\pi} (N_c + n_f) T^2. \quad (3.22)$$

3.1.3. Running coupling

An effective description of the running coupling can be obtained from measurements of e^+e^- annihilation as well as non-strange hadronic decays of τ leptons and continued to the time-like region [DMW96, GA08, Pes12],

$$\alpha_s(Q^2) = \frac{4\pi}{\beta_0} \begin{cases} L_-^{-1} & Q^2 < 0 \\ \frac{1}{2} - \pi^{-1} \text{atn}(L_+/\pi) & Q^2 > 0 \end{cases} \quad (3.23)$$

with $\beta_0 = 11 - \frac{2}{3}n_f$ and $L_{\pm} = \ln(\pm Q^2/\Lambda^2)$ with $\Lambda = 200$ MeV. For the space like part ($Q^2 < 0$) this is exactly the same as Equation (2.2). If $\alpha_s(Q^2)$ is larger than $\alpha_s^{\text{max}} = 1.0$ it is set to α_s^{max} . This cut-off procedure can be justified by universality arguments [Pes12, Dok02]. We checked that our results of the energy loss in Chapter 5 are not very dependent on the exact value of Λ or α_s^{max} since the contribution of the soft part is very small. Figure 3.4 shows the Q^2 dependence of α_s for zero and three active flavors.

The renormalization scale $\mu_R = Q$, at which the running coupling $\alpha_s(\mu_R)$ in the matrix element (3.12) or DEBYE mass definition is evaluated, is arbitrary due to renormalization flow equations. However, if one chooses a characteristic scale suitable to the physical problem,

²In the semi-classical transport model BAMPS all particles are treated as BOLTZMANN particles.

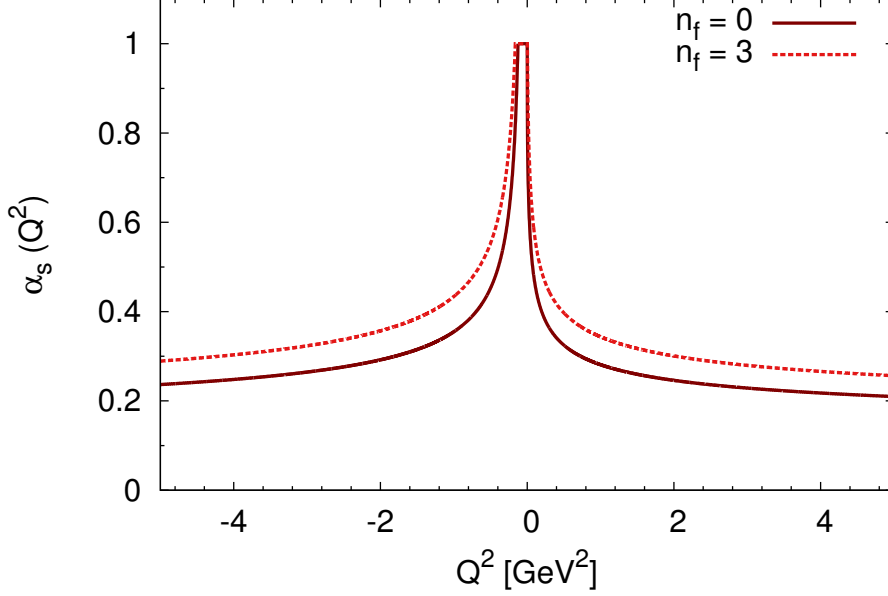


Figure 3.4.: Running coupling α_s as a function of the momentum scale Q^2 for n_f active flavors.

the contribution of higher orders can be reduced and the uncertainty of considering only the leading order can be decreased. In the t channel, for instance, large logarithms of t occur in next-to-leading order (NLO) due to vacuum contributions to the self-energy and vertex corrections, which can be absorbed via renormalization by fixing the scale, at which α_s is evaluated in the leading order result, to t . Therefore, we evaluate $\alpha_s(\mu_R)$ at the virtuality of the respective channel, that is, $s - M^2$, t , and $u - M^2$ for the s , t , and u channel, respectively. The coupling in the definitions of the gluon and quark DEBYE masses from Equations (3.18) and (3.19), respectively, is also evaluated at the characteristic scale of the corresponding channel. For instance, in the t channel we employ the substitution

$$\frac{\alpha_s^2}{t^2} \rightarrow \frac{\alpha_s^2(t)}{[t - \kappa_t m_D^2(\alpha_s(t))]^2}. \quad (3.24)$$

The u channel internal line of $gQ \rightarrow gQ$ is a heavy quark (see left diagram in Figure 3.1) and, therefore, the propagator is screened with the quark DEBYE mass,

$$\frac{\alpha_s^2}{(u - M^2)^2} \rightarrow \frac{\alpha_s^2(u - M^2)}{[u - M^2 - \kappa_u m_q^2(\alpha_s(u - M^2))]^2}. \quad (3.25)$$

Due to the heavy quark mass M in the denominator, the propagator is screened anyhow and the additional quark DEBYE mass has only minor importance for screening the divergence. However, to treat heavy and light partons (see Appendix A.3 for the latter) on the same footing, we keep the DEBYE mass here, but set $\kappa_u = 1$ for simplicity. The same applies to the s channel.

Interference terms, e.g., of s and t channel, go with one α_s from each channel and every propagator has its own DEBYE mass evaluated at the corresponding scale,

$$\frac{\alpha_s^2}{(s-M^2)t} \rightarrow \frac{\alpha_s(s-M^2)\alpha_s(t)}{[s-M^2+m_q^2(\alpha_s(s-M^2))][t-\kappa_t m_D^2(\alpha_s(t))]} . \quad (3.26)$$

3.1.4. Elastic heavy quark scattering with a gluon in medium

With the considerations from the previous sections the matrix element for $gQ \rightarrow gQ$ with running coupling and DEBYE screening reads for all channels and their interference terms

$$\begin{aligned} |\overline{\mathcal{M}}_{gQ \rightarrow gQ}|^2 = & 16\pi^2 \left[2\alpha_s^2(t) \frac{(s-M^2)(M^2-u)}{[t-\kappa_t m_D^2(\alpha_s(t))]^2} \right. \\ & + \frac{4}{9}\alpha_s^2(s-M^2) \frac{(s-M^2)(M^2-u) + 2M^2(s+M^2)}{[s-M^2+m_q^2(\alpha_s(s-M^2))]^2} \\ & + \frac{4}{9}\alpha_s^2(u-M^2) \frac{(s-M^2)(M^2-u) + 2M^2(u+M^2)}{[M^2-u+m_q^2(\alpha_s(u-M^2))]^2} \\ & + \frac{1}{9}\alpha_s(s-M^2)\alpha_s(u-M^2) \\ & \quad \times \frac{M^2(4M^2-t)}{[s-M^2+m_q^2(\alpha_s(s-M^2))][M^2-u+m_q^2(\alpha_s(u-M^2))]} \\ & + \alpha_s(t)\alpha_s(s-M^2) \frac{(s-M^2)(M^2-u) + M^2(s-u)}{[t-\kappa_t m_D^2(\alpha_s(t))][s-M^2+m_q^2(\alpha_s(s-M^2))]} \\ & \left. - \alpha_s(t)\alpha_s(u-M^2) \frac{(s-M^2)(M^2-u) - M^2(s-u)}{[t-\kappa_t m_D^2(\alpha_s(t))][M^2-u+m_q^2(\alpha_s(u-M^2))]} \right] . \quad (3.27) \end{aligned}$$

The same matrix element can also be employed for light quarks if M is set to zero (cf. Equation (A.10d) in Appendix A.3).

Figures 3.5 and 3.6 show the total (Equation (3.13)) and differential (Equation (3.6)) cross sections, respectively, for different κ_t and constant as well as running coupling.

3.1.5. Elastic heavy quark scattering with a light quark in medium

For light and heavy quark scattering the differential cross section reads

$$\frac{d\sigma}{dt} = \frac{|\overline{\mathcal{M}}_{qQ \rightarrow qQ}|^2}{16\pi(s-M^2)^2} \quad (3.28)$$

with the matrix element

$$|\overline{\mathcal{M}}_{qQ \rightarrow qQ}|^2 = \frac{64}{9}\pi^2\alpha_s^2(t) \frac{(M^2-u)^2 + (s-M^2)^2 + 2M^2t}{[t-\kappa_t m_D^2(\alpha_s(t))]^2} , \quad (3.29)$$

where we also employed the running coupling and DEBYE screening analogously to Equation (3.27).

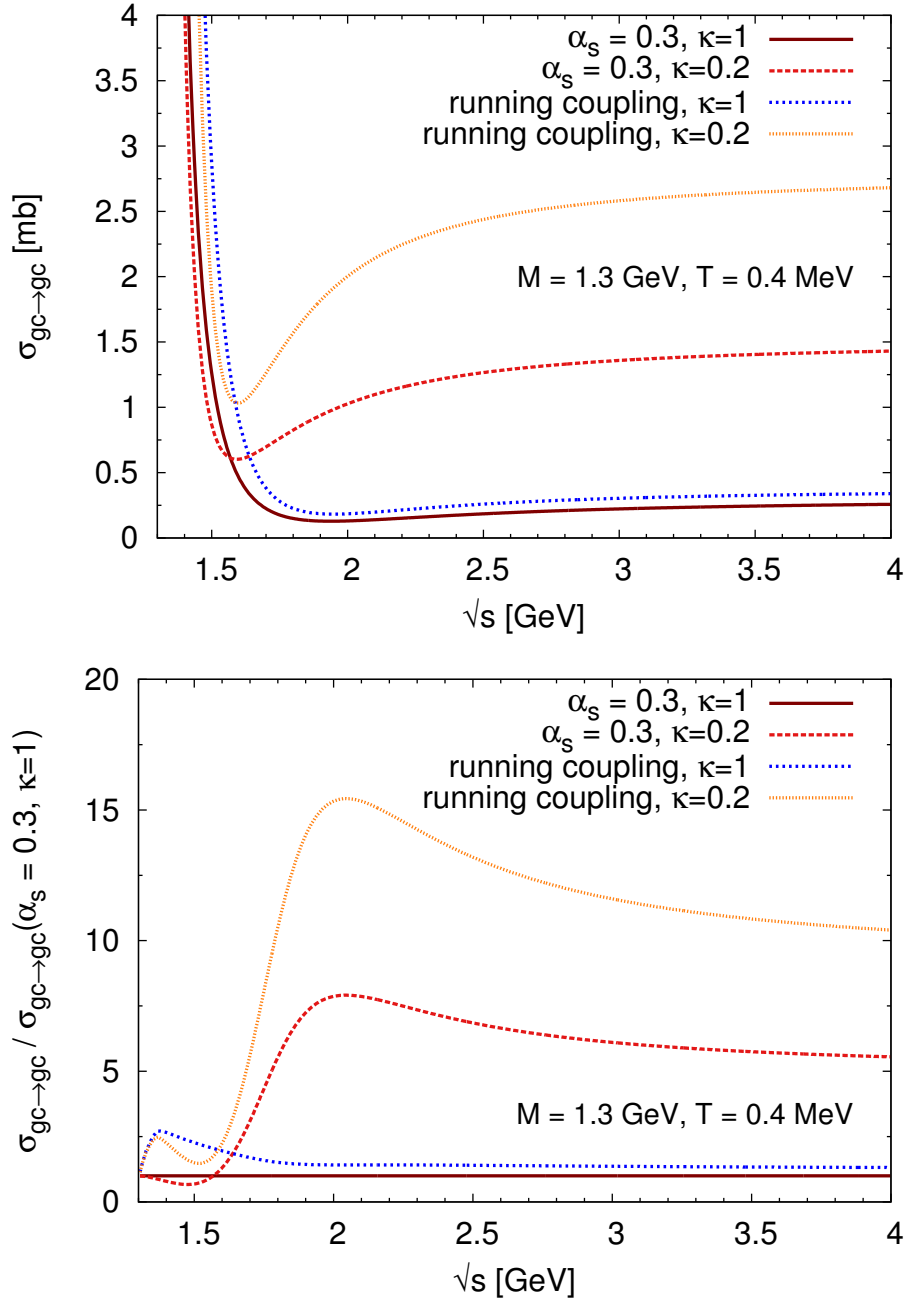


Figure 3.5.: Total cross section of $gc \rightarrow gc$ for $M = 1.3 \text{ GeV}$ and a DEBYE mass according to a medium with temperature $T = 400 \text{ MeV}$. Running or fixed coupling $\alpha_s = 0.3$ and κ_t are varied. In addition, the ratios to the curve with $\alpha_s = 0.3$ and $\kappa_t = 1$ are shown in the lower plot.

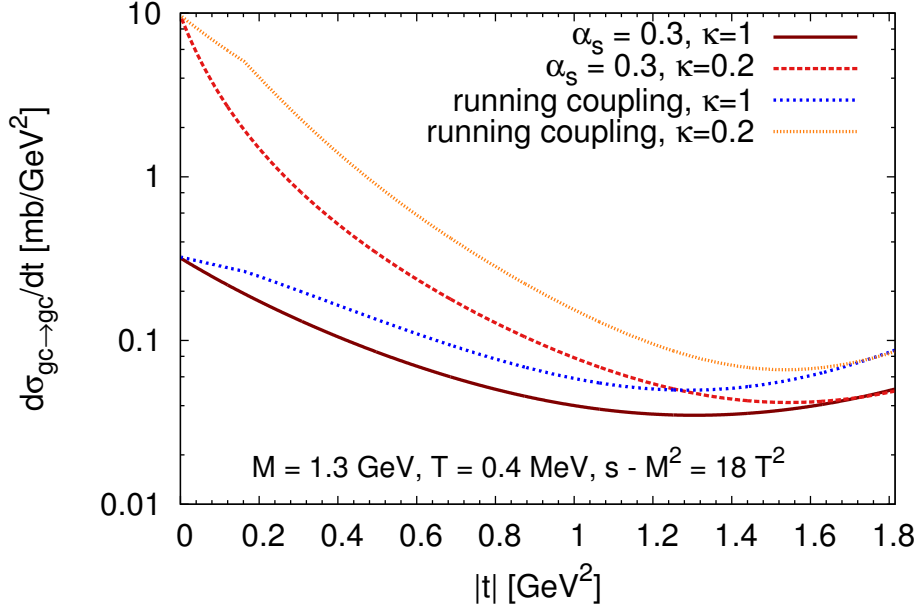


Figure 3.6.: Differential cross section $d\sigma/dt$ of $gc \rightarrow gc$ for $M = 1.3$ GeV, a DEBYE mass for a medium temperature of $T = 400$ MeV, and different κ_t as well as coupling schemes. The squared center-of-mass energy is fixed to $18T^2 + M^2$.

3.1.6. Average value of the running coupling in a thermal medium

Due to the explicit consideration of the running coupling and the phenomenon of asymptotic freedom, the effective coupling strength of a heavy quark jet with small energy is larger than that of a high-energy heavy quark. The same is true for light partons, for which we have also implemented the running coupling as part of this work and whose binary cross sections are given in Appendix A.3.

It is intriguing to study the average value of the coupling in a thermal medium and how it changes with the temperature of the medium. To this end, we consider with BAMPS (see Chapter 4) a thermal medium of light partons with temperature T and allow only binary interactions. As can be seen from the formulas listed in Appendix A.3 for light quarks (and also Equations (3.27) and (3.29) for heavy quarks), the binary cross sections depend on the coupling α_s through the prefactor proportional to α_s^2 and through the squared DEBYE mass in the internal gluon propagators, which is linear in α_s (cf. Equation (3.18)),

$$\sigma_{22} = \sigma_{22}(\alpha_s, m_D^2(\alpha_s)) . \quad (3.30)$$

We now define an effective average value of the running coupling by averaging over all cross sections of all particle pairs in the static medium,

$$\langle \alpha_s^{\text{eff}} \rangle = \left\langle \sqrt{\frac{\sigma_{22}(\alpha_s, m_D^2(\alpha_s))}{\sigma_{22}(\alpha_s^{\text{fixed}}, m_D^2(\alpha_s^{\text{fixed}})) / (\alpha_s^{\text{fixed}})^2}} \right\rangle , \quad (3.31)$$

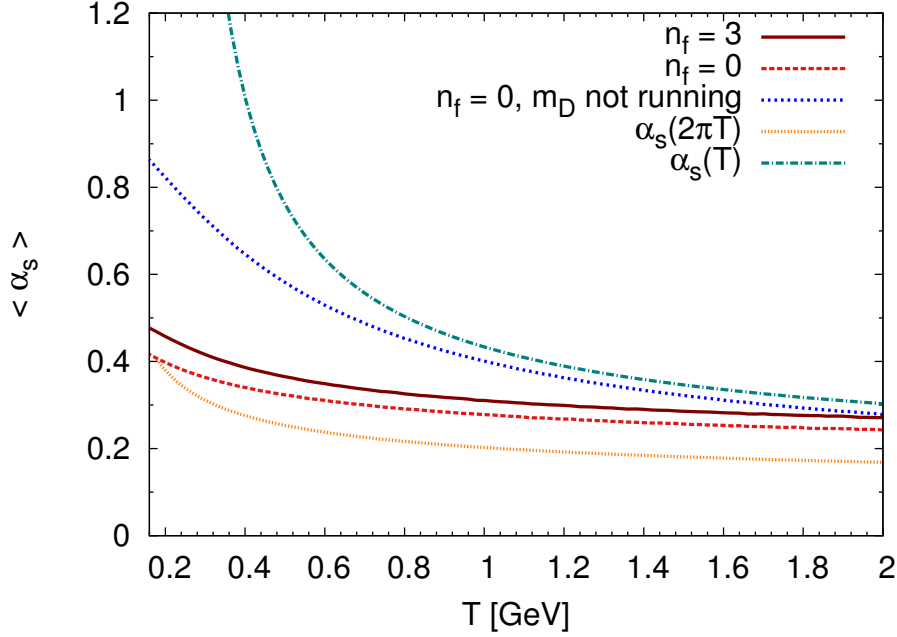


Figure 3.7.: Effective average value of the running coupling in a thermal medium of temperature T for light partons with number of flavors n_f and only binary interactions. Furthermore, the standard parametrization of $\alpha_s(Q)$ (see Equation (2.2) or the space-like part of Equation (3.23)) is shown with setting the scale Q to the first MATSUBARA frequency $2\pi T$ [Bel00] or the temperature T .

where $\alpha_s^{\text{fixed}} = 0.3$ is set. As a note, the average over the particle pairs is weighted with the probability for a collision of the pair taking place. The factor $(\alpha_s^{\text{fixed}})^2$ cancels the coupling prefactor in the cross section in the denominator since it is constant. Thus, schematically written, Equation (3.31) is for t channel processes

$$\langle \alpha_s^{\text{eff}} \rangle = \left\langle \sqrt{\frac{\int(\text{phase space}) \frac{1}{[t - m_D^2(\alpha_s(t))]^2} \alpha_s^2(t)}{\int(\text{phase space}) \frac{1}{[t - m_D^2(\alpha_s^{\text{fixed}})]^2}}} \right\rangle, \quad (3.32)$$

If the DEBYE mass were not α_s dependent, the result in the square root would be, therefore, the cross section with a squared running coupling divided by the cross section without a coupling. Hence, the square root would be just the average value of the running α_s weighted with the cross section. However, since the coupling also enters in the DEBYE mass, we call the left hand side of Equation (3.31) the effective average value of the running coupling.

Figure 3.7 depicts the effective average value of the running coupling as a function of the temperature of the medium for $n_f = 3$ and $n_f = 0$. The curves are only moderately temperature dependent and the effective values of the coupling are between 0.3 and 0.5. In addition, the third curve is obtained for a DEBYE mass that is calculated with α_s^{fixed} while the coupling from the prefactor still runs. Thus, it really is the average of the running coupling prefactor and not only an effective value since the DEBYE mass dependent terms in Equation (3.31) cancel out. For this configuration the coupling depends stronger on the temperature, but is

significantly smaller than one due to the cut with α_s^{\max} in Equation (3.23).

For comparison, we also depict the standard running coupling formula from Equation (2.2) (or, equivalently, the space-like part of Equation (3.23)), which we evaluate at the first MATSUBARA frequency $2\pi T$ [Bel00] or the temperature T . These curves depend stronger on the temperature. The values of $\alpha_s(T)$ are always larger than in BAMPS, whereas the values of $\alpha_s(2\pi T)$ are slightly smaller. In conclusion, the effective average values of the running coupling in BAMPS assume comparable values as for macroscopic thermal quantum field theory estimations [Bel00], although the running coupling in BAMPS is employed on a microscopic level by evaluating the coupling at the momentum transfer of each collision.

3.2. Inelastic heavy quark scattering

The most important higher order contribution to heavy quark scattering with a gluon or a light quark is the radiative correction to the binary scattering with an additional gluon in the final state:

$$\begin{aligned} g + Q &\rightarrow g + Q + g \\ q + Q &\rightarrow q + Q + g . \end{aligned} \tag{3.33}$$

Parts of the following sections are based on our work for light parton radiative scatterings, which was published in Ref. [FUXG13], while it is extended to the heavy flavor sector.

A commonly used approximation for the leading order pQCD matrix element of partonic $2 \leftrightarrow 3$ processes is a result derived by GUNION and BERTSCH (GB) in 1981 [GB82] for light quark scattering $qq' \rightarrow qq'g$. This approximation gives a comparatively simple expression for the gluon radiation amplitude in terms of the transverse momentum of the radiated gluon k_\perp and the transverse exchanged momentum q_\perp . It has been widely employed for solving transport problems [XS94, BvDM⁺93, SMM97, MPST98, Won96b, CDOW10, CDDW11, GAGG10], for instance, via rate equations or via microscopic transport approaches. In particular, the GB matrix element is implemented in the partonic transport model BAMPS, which is subject of this work and in detail introduced in Chapter 4. In Ref. [DA10, AGMM11, BMDA12] some efforts are made to go beyond the soft GB approximation, while still obtaining a relatively compact form.

Recently, the results obtained within the BAMPS framework, especially with respect to the computed shear viscosity [XG08], have been challenged in a paper by CHEN et al. [CDDW13], who claim that a mis- or double-counting of symmetry factors when applying the GB matrix element to inelastic processes might lead to an overestimation of interaction rates in BAMPS by a factor of six. Furthermore, a recent work by ZHANG [Zha13] has addressed this issue and finds numerical discrepancies between cross sections based on the GB approximation compared to full leading order results for the $2 \rightarrow 3$ amplitudes, which have also been known since the early 1980s [BKDC⁺81, ES86]. The numerical discrepancy found in Ref. [Zha13] is much less pronounced than the one claimed in Ref. [CDDW13]. However, it is not fully clear how the results of these two works compare since both use different screening schemes.

In Ref. [FUXG13] we addressed these issues in great detail by providing extensive numerical comparisons between the GB approximation and the exact leading order pQCD result for light partons. We showed that the approximation by GUNION and BERTSCH needs to be carefully corrected in certain phase space regions when being employed to the computation of cross

sections or rates from the matrix element. To this end, we proposed an improved version of the GB matrix element that is valid in all regions of phase space. However, we want to emphasize that the deviations of rates computed in the original GB approximation compared to rates computed from the improved GB and the exact matrix element are caused deep within the approximations made by GUNION and BERTSCH and are not given by simple symmetry factors as argued in Ref. [CDDW13].

In the next section we outline the calculation of the improved GB matrix element as it was presented in Ref. [FUXG13], but generalize it to include also the scattering of a heavy quark. In Section 3.2.9 we will compare the original GB, the improved GB, and the exact matrix element numerically for differential and total cross sections considering light parton as well as heavy quark processes.

3.2.1. Gunion-Bertsch calculation for heavy quark scattering with a light quark

In this section we argue that the approximation to the leading order pQCD matrix element for $qQ \rightarrow qQg$ processes (and more generally for other gluon radiation processes as well) as computed by GUNION and BERTSCH (for light quarks) [GB82] needs to be carefully corrected when being applied to the computation of cross sections or rates. This correction consists of two parts:

1. Keeping a kinematic factor $(1 - x)^2$, where x is the fraction of light cone momentum carried by the radiated gluon.
2. Respecting the symmetry of the process by explicitly combining results from $A^+ = 0$ and $A^- = 0$ gauges, restricting the emission of gluons to the respective forward direction.

Kinematics, light cone coordinates, and Feynman diagrams

The FEYNMAN diagrams for the process $qQ \rightarrow qQg$ are given in Figure 3.8. In the following we label the four-momentum of the incoming heavy quark with p_1 . The incoming light quark is p_2 . The outgoing heavy and light quarks are p_3 and p_4 , respectively. The radiated gluon is denoted with k and the momentum transfer of the process or, equivalently, the momentum of the internal gluon propagator is q . This notation is shown in Figure 3.9 for the example of diagram 1.

In the present section we use light cone coordinates because these are better suited to this particular problem than the standard MINKOWSKI coordinates. An arbitrary vector $v^\mu = (v^0, v^1, v^2, v^3)$ is written in light cone coordinates as

$$v^\mu = (v^+, v^-, v^1, v^2) = (v^+, v^-, \mathbf{v}_\perp) \quad (3.34)$$

with $v^\pm = v^0 \pm v^3$ and $\mathbf{v}_\perp = (v^1, v^2)$. The inner product, which is $v_\mu w^\mu = v^0 w^0 - v^1 w^1 - v^2 w^2 - v^3 w^3$ in MINKOWSKI coordinates, then reads

$$v_\mu w^\mu = \frac{v^+ w^-}{2} + \frac{v^- w^+}{2} - v^1 w^1 - v^2 w^2 \quad (3.35)$$

in light cone coordinates.

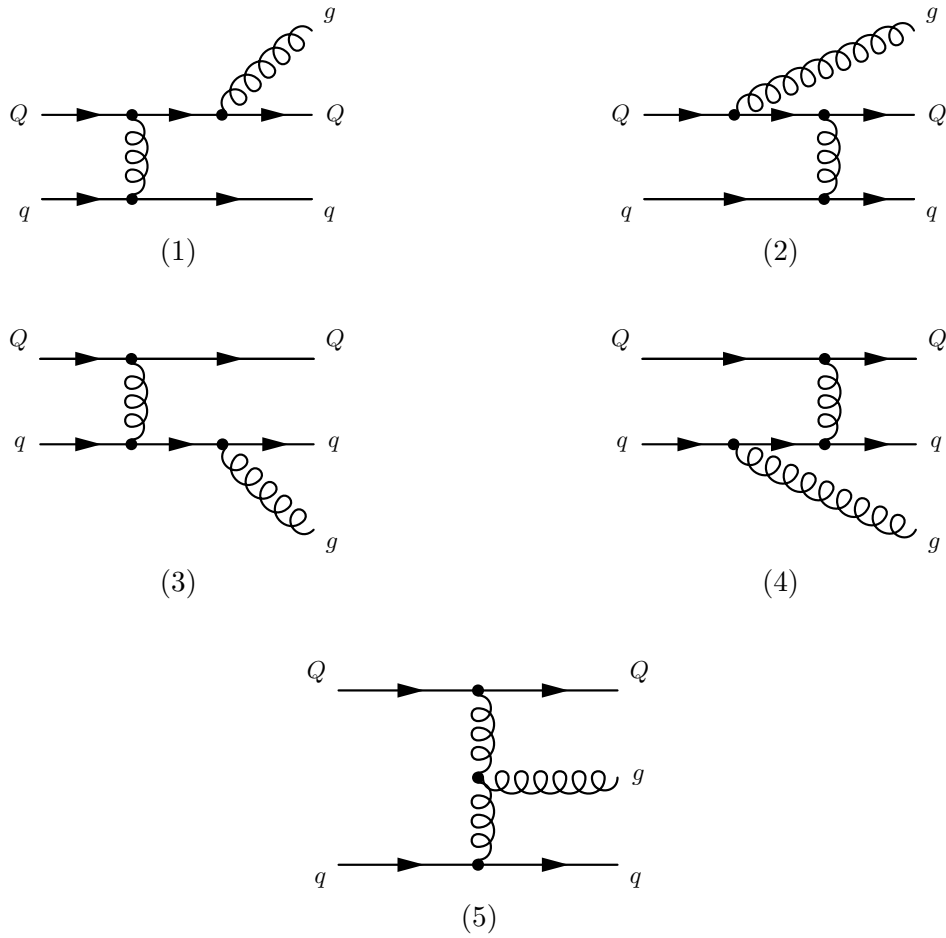


Figure 3.8.: FEYNMAN diagrams for $q + Q \rightarrow q + Q + g$.

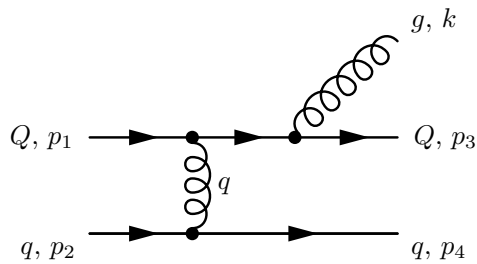


Figure 3.9.: FEYNMAN diagram (1) for $qQ \rightarrow qQg$ with notation for momenta. The label q at the internal gluon line denotes the momentum of the exchanged gluon and should not to be confused with the symbol a light quark.

In the center-of-mass frame, the momenta of the incoming particles in light cone coordinates are given by

$$\begin{aligned} p_1^\mu &= \left(\sqrt{s}, \frac{M^2}{\sqrt{s}}, 0, 0 \right) \\ p_2^\mu &= \left(0, \frac{s - M^2}{\sqrt{s}}, 0, 0 \right) . \end{aligned} \quad (3.36)$$

The Lorentz-invariant quantity

$$x = \frac{k^+}{p_1^+} \quad (3.37)$$

characterizes the fraction of light cone momentum carried away by the radiated gluon. It can be related to the rapidity y of the emitted gluon via

$$x = \frac{k_\perp}{\sqrt{s}} e^y . \quad (3.38)$$

The GUNION and BERTSCH matrix element is derived in the high-energy limit. This means that the radiated gluon and the momentum transfer of the process are soft,

$$\begin{aligned} k_\perp &\ll \sqrt{s} \\ q_\perp &\ll \sqrt{s} . \end{aligned} \quad (3.39)$$

The third approximation relates k_\perp , q_\perp , and x ,

$$xq_\perp \ll k_\perp . \quad (3.40)$$

These approximations are explicitly stated by GB in their paper. However, as we will see later we need in our calculation three additional approximations, that is, $x(1-x)s \gg k_\perp^2$ and all components of q and k being soft, $q^\mu, k^\mu \ll \sqrt{s}$, to end up with the same result as GB. With the approximations (3.39) as well as (3.40) and from the constraint that all external particles are on-shell one can explicitly specify k and q in light cone coordinates

$$\begin{aligned} k^\mu &= \left(x\sqrt{s}, \frac{k_\perp^2}{x\sqrt{s}}, \mathbf{k}_\perp \right) \\ q^\mu &= \left(-q_\perp^2 \frac{\sqrt{s}}{s - M^2}, \frac{(\mathbf{q}_\perp - \mathbf{k}_\perp)^2}{(1-x)\sqrt{s}} + \frac{k_\perp^2}{x\sqrt{s}} + \frac{x}{1-x} \frac{M^2}{\sqrt{s}}, \mathbf{q}_\perp \right) . \end{aligned} \quad (3.41)$$

The outgoing momenta are determined by momentum conservation,³

$$\begin{aligned} p_3 &= p_1 + q - k \\ p_4 &= p_2 - q . \end{aligned} \quad (3.42)$$

The original computation of the GB matrix element has been carried out in light cone gauge, $A^+ = 0$. This implies that the $+$ component of the polarization vector $\epsilon(k)$ is also zero. The

³For the two diagrams where a gluon is radiated by the light quark line, the kinematics look slightly different. We will address this in more detail when calculating these diagrams.

physical polarizations of the emitted gluon must be transverse to its momentum, $\epsilon(k) \cdot k = 0$. With these two constraints the two physical polarization vectors, $i = 1, 2$, are given by

$$\epsilon_{(i)}^\mu(k) = \left(0, \frac{2\epsilon_\perp^{(i)} \cdot \mathbf{k}_\perp}{x\sqrt{s}}, \epsilon_\perp^{(i)} \right), \quad (3.43)$$

where $\epsilon_\perp^{(1)} = (1, 0)$ and $\epsilon_\perp^{(2)} = (0, 1)$ are possible choices. For brevity we will suppress the polarization index (i) in the following, keeping in mind that the final polarization sum will simply amount to the replacement $\sum_\epsilon |\mathbf{p} \cdot \epsilon_\perp|^2 = \mathbf{p}^2$.

Before calculating the matrix element of the process $qQ \rightarrow qQg$, we first start with the diagram of binary scattering without an emitted gluon and evaluate this in the high-energy limit.

Diagram 0: Elastic scattering

Analogous to Section 3.1.1, the matrix element for $qQ \rightarrow qQ$ can be obtained employing the FEYNMAN rules,

$$\begin{aligned} i\mathcal{M}_0^{qQ} &= \bar{u}(p_3) ig\gamma^\nu \lambda_{ki}^b u(p_1) \frac{-ig_{\nu\sigma} \delta^{bc}}{q^2} \bar{u}(p_4) ig\gamma^\sigma \lambda_{nm}^c u(p_2) \\ &= \frac{ig^2}{q^2} \lambda_{ki}^b \lambda_{nm}^b J_\nu(p_3, p_1) J^\nu(p_4, p_2) =: \lambda_{ki}^b \lambda_{nm}^b iM_0^{qQ}, \end{aligned} \quad (3.44)$$

where we suppressed the spinor indices and defined the matrix element without color factors,

$$iM_0^{qQ} = \frac{ig^2}{q^2} J_\nu(p_3, p_1) J^\nu(p_4, p_2). \quad (3.45)$$

Please note that the full matrix element with color factors is denoted with a stylized \mathcal{M} , while the matrix element without color factors is written as a standard M . Furthermore, we define the source

$$J^\mu(p, p') := \bar{u}(p) \gamma^\mu u(p') = \bar{u}(p) \left[\frac{(p+p')^\mu}{2m} + \frac{i\sigma^{\mu\nu}(p-p')_\nu}{2m} \right] u(p'). \quad (3.46)$$

The second relation is called the GORDON identity [PS95]. The mass of the particle is denoted with m and the tensor $\sigma^{\mu\nu} = \frac{i}{2}[\gamma^\mu, \gamma^\nu]$ is a composition of the DIRAC matrices γ . Setting $p' = p + q$ and assuming that $q \ll p$ (which means that all components of q are soft, $q^\mu \ll \sqrt{s}$), which is basically the *eikonal approximation* [BP02], the second term is much smaller than the first and the expression simplifies to

$$J^\mu(p, p+q) \simeq \bar{u}(p) \frac{(2p+q)^\mu}{2m} u(p+q). \quad (3.47)$$

In this limit the complicated matrix structure of the quark-gluon vertex disappears. Since $q \ll p$, the normalization of the DIRAC spinors, that is $\bar{u}_r(p) u_s(p) = 2m\delta_{rs}$ (r and s are the spin indices that have been suppressed before), can be inserted and one obtains

$$J^\mu(p, p+q) \simeq (2p+q)^\mu. \quad (3.48)$$

Here, we suppressed the spin indices again while keeping in mind that the δ_{rs} from the normalization becomes important when summing over the initial and final states. This eikonal approximation essentially amounts to describing the problem in scalar QCD and is responsible for the fact that the amplitudes of different gluon and quark processes only differ by the color factor in the high-energy limit.

With this identity the two sources from Equation (3.44) are given by

$$\begin{aligned} J^\nu(p_3, p_1) &\simeq (2p_1 + q)^\nu \\ J^\nu(p_4, p_2) &\simeq (2p_2 - q)^\nu . \end{aligned} \quad (3.49)$$

After employing these relations and taking the high-energy limit given by the GB approximations from (3.39), the matrix element (3.44) reads

$$i\mathcal{M}_0^{qQ} \simeq 2ig^2 \lambda_{ki}^b \lambda_{nm}^b \frac{s - M^2}{t} . \quad (3.50)$$

For the squared matrix element of the elastic process, which is averaged (summed) over initial (final) states, one obtains with $g^2 = 4\pi\alpha_s$

$$|\overline{\mathcal{M}}_{qQ \rightarrow qQ}|^2 := |\overline{\mathcal{M}}_0^{qQ}|^2 = \frac{128}{9} \pi^2 \alpha_s^2 \frac{(s - M^2)^2}{t^2} , \quad (3.51)$$

which is the same result as Equation (3.29) for $t \ll s$ and, therefore, $u = 2M^2 - s - t \simeq 2M^2 - s$ (cf. Appendix A.2).

For future reference we note the connection to the matrix element iM_0^{qQ} without color factor from Equation (3.45):

$$|\overline{\mathcal{M}}_0^{qQ}|^2 = \frac{C(N)^2(N^2 - 1)}{N^2} |\overline{M}_0^{qQ}|^2 = \frac{2}{9} |\overline{M}_0^{qQ}|^2 \quad (3.52)$$

with the number of colors $N = 3$ and the invariant $C(N = 3) = 1/2$ of the fundamental representation of the $SU(N = 3)$ group associated with QCD.

Having done most of the preparatory work already with computing the elastic matrix element, the calculation of the bremsstrahlung diagrams will be relatively straightforward.

Diagram 1

The FEYNMAN rules give for diagram 1

$$\begin{aligned} i\mathcal{M}_1^{qQ} &= \bar{u}(p_3) \epsilon_\mu^*(k) ig\gamma^\mu \lambda_{kj}^a \frac{i(\not{p}_3 + \not{k} + M)}{(p_3 + k)^2 - M^2} ig\gamma^\nu \lambda_{ji}^b u(p_1) \frac{-ig_{\nu\sigma} \delta^{bc}}{q^2} \bar{u}(p_4) ig\gamma^\sigma \lambda_{nm}^c u(p_2) \\ &= -i\frac{g^3}{q^2} \lambda_{kj}^a \lambda_{ji}^b \lambda_{nm}^b \frac{1}{(p_3 + k)^2 - M^2} \epsilon_\mu^*(k) \Gamma^{\mu\nu}(p_3, p_3 + k, p_1) J_\nu(p_4, p_2) , \end{aligned} \quad (3.53)$$

where we defined

$$\Gamma_{rs}^{\mu\nu}(p, k, p') = \bar{u}^r(p) \gamma^\mu (\not{k} + m) \gamma^\nu u^s(p') = \sum_t J_{rt}^\mu(p, k) J_{ts}^\nu(k, p') , \quad (3.54)$$

but again suppressed the spin indices in Equation (3.53). With $(p_3 + k)^2 = M^2 + 2p_3 \cdot k$ and employing the relation (3.48) for the sources the matrix element reads

$$\begin{aligned} i\mathcal{M}_1^{qQ} &\simeq -i\frac{g^3}{q^2} \lambda_{kj}^a \lambda_{ji}^b \lambda_{nm}^b \frac{1}{2p_3 \cdot k} \epsilon_\mu^*(k) (2p_1 + 2q - k)^\mu (2p_1 + q)^\nu (2p_2 - q)_\nu \\ &\simeq -g \lambda_{kj}^a \lambda_{ji}^b \lambda_{nm}^b iM_0^{qQ} (1-x) \frac{2\epsilon_\perp \cdot \mathbf{k}_\perp}{k_\perp^2 + x^2 M^2} . \end{aligned} \quad (3.55)$$

In the last step we inserted the matrix element for the elastic scattering without color factor iM_0^{qQ} from Equation (3.45). To end up at the GB result when calculating the term $(2p_1 + q)^\nu (2p_2 - q)_\nu$ the restriction $x(1-x)s \gg k_\perp^2$ is required in addition to the standard GB approximations (3.39) and (3.40). The implication of this additional constraint will be discussed at the end of this section, around Equation (3.66).

Diagram 2

Diagram 2 is given by

$$i\mathcal{M}_2^{qQ} = \bar{u}(p_3) i g \gamma^\nu \lambda_{kj}^b \frac{i(\not{p}_1 - \not{k} + M)}{(p_1 - k)^2 - M^2} \epsilon_\mu^*(k) i g \gamma^\mu \lambda_{ji}^a u(p_1) \frac{-i g_{\nu\sigma} \delta^{bc}}{q^2} \bar{u}(p_4) i g \gamma^\sigma \lambda_{nm}^c u(p_2) . \quad (3.56)$$

With $(p_1 - k)^2 = M^2 - 2p_1 \cdot k$ and the relations (3.54) and (3.48) the matrix element reads

$$\begin{aligned} i\mathcal{M}_2^{qQ} &\simeq i\frac{g^3}{q^2} \lambda_{kj}^b \lambda_{ji}^a \lambda_{nm}^b \frac{1}{2p_1 \cdot k} \epsilon_\mu^*(k) (2p_1 - k)^\mu (2p_1 + q - 2k)^\nu (2p_2 - q)_\nu \\ &\simeq g \lambda_{kj}^b \lambda_{ji}^a \lambda_{nm}^b iM_0^{qQ} (1-x) \frac{2\epsilon_\perp \cdot \mathbf{k}_\perp}{k_\perp^2 + x^2 M^2} . \end{aligned} \quad (3.57)$$

Again the constraint $x(1-x)s \gg k_\perp^2$ needs to be used.

Diagram 3

For diagrams 3 and 4 the kinematics are slightly different than for the other diagrams since the gluon is emitted from the lower line. Therefore, the components of the momentum transfer q need to be redetermined from the on-shell conditions ($p_3^2 = (p_1 + q)^2 = 0$ and $p_4^2 = (p_2 - q - k)^2 = 0$). With the choice of keeping k in the form given in Equation (3.41), the momentum transfer reads

$$q^\mu \simeq \left(-x\sqrt{s}, \frac{q_\perp^2 - M^2}{\sqrt{s}}, \mathbf{q}_\perp \right) . \quad (3.58)$$

Employing the FEYNMAN rules and performing similar simplifications as for the aforementioned diagrams give for diagram 3

$$\begin{aligned} i\mathcal{M}_3^{qQ} &= \bar{u}(p_3) i g \gamma^\sigma \lambda_{ki}^b u(p_1) \frac{-i g_{\nu\sigma} \delta^{bc}}{q^2} \bar{u}(p_4) \epsilon_\mu^*(k) i g \gamma^\mu \lambda_{nj}^a \frac{i(\not{p}_4 + \not{k} + M)}{(p_4 + k)^2} i g \gamma^\nu \lambda_{jm}^c u(p_2) \\ &\simeq -i\frac{g^3}{q^2} \lambda_{nj}^a \lambda_{jm}^b \lambda_{ki}^b \frac{1}{2p_4 \cdot k} \epsilon_\mu^*(k) (2p_2 - 2q - k)^\mu (2p_1 + q)_\nu (2p_2 - q)^\nu \\ &\simeq -g \lambda_{nj}^a \lambda_{jm}^b \lambda_{ki}^b iM_0^{qQ} (2-x) \frac{\epsilon_\perp \cdot (\mathbf{q}_\perp + \mathbf{k}_\perp)}{s - M^2} . \end{aligned} \quad (3.59)$$

In the light cone gauge A^+ and the high-energy limit, the contribution from this diagram is much smaller than that of diagrams 1 and 2 due to the s term in the denominator. Therefore, we can neglect it in the following.

Diagram 4

For diagram 4 we get

$$\begin{aligned}
 i\mathcal{M}_4^{qQ} &= \bar{u}(p_3) i g \gamma^\sigma \lambda_{ki}^b u(p_1) \frac{-i g_{\nu\sigma} \delta^{bc}}{q^2} \bar{u}(p_4) i g \gamma^\nu \lambda_{nj}^c \frac{i(\not{p}_2 - \not{k} + M)}{(p_2 - k)^2} i g \gamma^\mu \lambda_{jm}^a \epsilon_\mu^*(k) u(p_2) \\
 &\simeq i \frac{g^3}{q^2} \lambda_{ki}^b \lambda_{nj}^b \lambda_{jm}^a \frac{1}{2p_2 \cdot k} \epsilon_\mu^*(k) (2p_2 - k)^\mu (2p_1 + q)_\nu (2p_2 - 2k - q)^\nu \\
 &= 0,
 \end{aligned} \tag{3.60}$$

since $\epsilon_\mu^*(k)(2p_2 - k)^\mu = 0$.

Diagram 5

The last diagram is the most interesting one due to its three-gluon vertex. With help of the FEYNMAN rules the matrix element can be written as

$$\begin{aligned}
 i\mathcal{M}_5^{qQ} &= \bar{u}(p_3) i g \gamma^\nu \lambda_{ki}^c u(p_1) \frac{-i}{(q - k)^2} g f^{cba} [g_{\nu\sigma}(k - 2q)^\mu + g_{\sigma\mu}(q + k)^\nu + g_{\mu\nu}(q - 2k)^\nu] \\
 &\quad \times \epsilon_\mu^*(k) \frac{-i}{q^2} \bar{u}(p_4) i g \gamma^\sigma \lambda_{nm}^b u(p_2) \\
 &= \frac{g^3}{q^2(q - k)^2} f^{cba} \lambda_{ki}^c \lambda_{nm}^b \epsilon_\mu^*(k) [J_\nu(p_3, p_1) J^\nu(p_4, p_2)(k - 2q)^\mu \\
 &\quad + J_\nu(p_3, p_1) J^\mu(p_4, p_2)(q + k)^\nu + J^\mu(p_3, p_1) J_\nu(p_4, p_2)(q - 2k)^\nu] \\
 &\simeq -i g f^{abc} \lambda_{ki}^c \lambda_{nm}^b i M_0^{qQ} (1 - x) \frac{2 \epsilon_\perp \cdot (\mathbf{q}_\perp - \mathbf{k}_\perp)}{(\mathbf{q}_\perp - \mathbf{k}_\perp)^2 + x^2 M^2}.
 \end{aligned} \tag{3.61}$$

Also for diagram 5 it was necessary to employ the constraint $x(1 - x)s \gg k_\perp^2$ in addition to the standard GB approximations.

Total matrix element

The total matrix element is the sum of all the five diagrams where we can neglect diagram 3 and diagram 4 does not contribute. Using $([\lambda^a, \lambda^b])_{ki} = i f^{abc} \lambda_{ki}^c$ for the sum of diagrams 1 and 2 yields for the total matrix element

$$i\mathcal{M}_{qQ \rightarrow qQg} \simeq -i g f^{abc} \lambda_{ki}^c \lambda_{nm}^b i M_0^{qQ} (1 - x) 2 \epsilon_\perp \cdot \left[\frac{\mathbf{k}_\perp}{k_\perp^2 + x^2 M^2} + \frac{\mathbf{q}_\perp - \mathbf{k}_\perp}{(\mathbf{q}_\perp - \mathbf{k}_\perp)^2 + x^2 M^2} \right]. \tag{3.62}$$

The total squared matrix element summed and averaged over spin, polarization, and color

states can then be computed to

$$\begin{aligned}
 |\overline{\mathcal{M}}_{qQ \rightarrow qQg}|^2 &= 4g^2 \frac{C(N)^2 C_2(G) (N^2 - 1)}{N^2} |\overline{M}_0^{qQ}|^2 (1-x)^2 \\
 &\quad \times \left[\frac{\mathbf{k}_\perp}{k_\perp^2 + x^2 M^2} + \frac{\mathbf{q}_\perp - \mathbf{k}_\perp}{(\mathbf{q}_\perp - \mathbf{k}_\perp)^2 + x^2 M^2} \right]^2 \\
 &= 12g^2 |\overline{\mathcal{M}}_{qQ \rightarrow qQ}|^2 (1-x)^2 \left[\frac{\mathbf{k}_\perp}{k_\perp^2 + x^2 M^2} + \frac{\mathbf{q}_\perp - \mathbf{k}_\perp}{(\mathbf{q}_\perp - \mathbf{k}_\perp)^2 + x^2 M^2} \right]^2
 \end{aligned} \tag{3.63}$$

with $C_2(G) = N = 3$. $|\overline{\mathcal{M}}_{qQ \rightarrow qQ}|^2 := |\overline{M}_0^{qQ}|^2$ denotes the averaged squared matrix element for $qQ \rightarrow qQ$. This result explicitly demonstrates that in the high-energy limit the matrix element of the $2 \rightarrow 3$ process factorizes into an elastic $2 \rightarrow 2$ part and a gluon emission amplitude.

For the massless case, $M = 0$, Equation (3.63) reduces to

$$|\overline{\mathcal{M}}_{qq' \rightarrow qq'g}|^2 = 12g^2 |\overline{\mathcal{M}}_{qq' \rightarrow qq'}|^2 (1-x)^2 \frac{q_\perp^2}{k_\perp^2 (\mathbf{q}_\perp - \mathbf{k}_\perp)^2}. \tag{3.64}$$

Note that the algebraic simplification employed for the term in the bracket in Equation (3.63) is strictly only valid if the propagator terms $1/k_\perp^2$ and $1/(\mathbf{q}_\perp - \mathbf{k}_\perp)^2$ are not screened with a DEBYE mass, cf. Section 3.2.9.

The factor $(1-x)^2$ in Equation (3.63) or (3.64) leads to a sizeable suppression of the amplitude at forward rapidity, where $x > k_\perp/\sqrt{s}$, which is immediately evident from Equation (3.38). At the maximal rapidity that is kinematically allowed for a given transverse momentum, $y_{\max} = \ln(k_\perp/\sqrt{s})$, x is 1 and the factor $(1-x)^2$ completely suppresses the matrix element. While GUNION and BERTSCH have the $(1-x)$ terms in their intermediate results for the single diagrams, they were mostly interested in emission spectra in the mid-rapidity region, $x \simeq k_\perp/\sqrt{s} \ll 1$, and, thus, omitted the $(1-x)$ terms from their final results. The amplitude then simplifies to

$$|\overline{\mathcal{M}}_{qq' \rightarrow qq'g}|^2 \simeq 12g^2 |\overline{\mathcal{M}}_{qq' \rightarrow qq'}|^2 \frac{q_\perp^2}{k_\perp^2 (\mathbf{q}_\perp - \mathbf{k}_\perp)^2}, \tag{3.65}$$

which is the formula that has been mostly used in the literature as the GB matrix element since then [XS94, BvDM⁺93, SMM97, Won96b, MPST98, CDOW10, CDDW11] and that has also been implemented in the transport model BAMPS [XG05]. When computing cross sections or rates from Equation (3.64), however, the phase space integration covers the entire rapidity region and factors $(1-x)$ must not be omitted. Hence, Equation (3.64), rather than Equation (3.65), need to be employed when computing rates for $2 \rightarrow 3$ processes in the GB approximation.

The second modification that has been mentioned at the beginning of this section is somewhat more subtle. In order to arrive at the simple results for the single diagrams, the approximation

$$x(1-x)s \gg k_\perp^2 \tag{3.66}$$

is needed. It is instructive to study this constraint for the two extreme cases of large and small x .

1. Large x ($x \lesssim 1$): Equation (3.66) then reads $(1-x)s \gg k_\perp^2$, which is equivalent to $y \ll \ln \sqrt{s}/k_\perp$ for $k_\perp^2 \ll s$, where the definition of x from Equation (3.38) has been used. From kinematic considerations (see text after Equation (3.108)) one obtains that this is not a very strong constraint since the rapidity is always smaller than $\ln \sqrt{s}/k_\perp$ anyhow,

$$y \leq y_{\max} = \operatorname{arccosh} \frac{s - M^2}{2\sqrt{s}k_\perp} \simeq \ln \frac{s - M^2}{\sqrt{s}k_\perp} < \ln \frac{\sqrt{s}}{k_\perp}. \quad (3.67)$$

Furthermore, the matrix element itself is small for large x due to the $1-x$ factor. Consequently, Equation (3.66) is not really relevant in this regime.

2. Small x ($x \ll 1$): Equation (3.66) then simplifies to $xs \gg k_\perp^2$. Using Equation (3.38) again, this is equivalent to $y \gg \ln k_\perp/\sqrt{s}$. Since $k_\perp^2 \ll s$, the approximation includes the mid-rapidity region, but not the backward rapidity region where $y \sim \ln k_\perp/\sqrt{s}$.

Hence, the results (3.63) and (3.64) are only valid at mid-rapidity, where x is small, and for forward emitted gluons, but not in the backward rapidity region. The constraint (3.66) goes beyond the approximations (3.39) and (3.40) and has not been mentioned in the original GB publication [GB82].

Qualitatively, the need for a restriction such as Equation (3.66) can be understood when noting that the process $qq' \rightarrow qq'g$ is symmetric in interchanging q and q' and, therefore, the resulting amplitude should be symmetric in the rapidity of the emitted gluon. Terms including x , however, are evidently not symmetric in y , cf. Equation (3.38), and, thus, the result (3.64) does not obey the symmetry that should be present. This consideration nicely matches the analytic finding that Equation (3.64) is valid only in the forward and mid-rapidity region.

One can, however, carry out the same calculation in the $A^- = 0$ gauge. In this gauge, diagrams 3, 4 and 5 have sizeable contributions, while diagrams 1 and 2 do not contribute to the final amplitude. Setting

$$x' = \frac{k_\perp}{\sqrt{s}} e^{-y}, \quad (3.68)$$

the final result for the averaged squared matrix element in $A^- = 0$ gauge reads

$$|\overline{\mathcal{M}}_{qQ \rightarrow qQg}|^2 = 12g^2 |\overline{\mathcal{M}}_{qQ \rightarrow qQ}|^2 (1-x')^2 \left[\frac{\mathbf{k}_\perp}{k_\perp^2} + \frac{\mathbf{q}_\perp - \mathbf{k}_\perp}{(\mathbf{q}_\perp - \mathbf{k}_\perp)^2} \right]^2. \quad (3.69)$$

Note that no mass terms are present in the denominators of the bracket since the gluon is now emitted off the light quark line. Apart from this, Equation (3.69) is simply the result obtained from the $A^+ = 0$ gauge, cf. (3.63), with x being replaced by x' . Since both results are also valid at mid-rapidity it is self-evident to combine Equations (3.63) and (3.69) to

$$\begin{aligned} |\overline{\mathcal{M}}_{qQ \rightarrow qQg}|^2 &= 12g^2 |\overline{\mathcal{M}}_{qQ \rightarrow qQ}|^2 \left[\Theta(y)(1-x)^2 \left[\frac{\mathbf{k}_\perp}{k_\perp^2 + x^2 M^2} + \frac{\mathbf{q}_\perp - \mathbf{k}_\perp}{(\mathbf{q}_\perp - \mathbf{k}_\perp)^2 + x^2 M^2} \right]^2 \right. \\ &\quad \left. + \Theta(-y)(1-x')^2 \left[\frac{\mathbf{k}_\perp}{k_\perp^2} + \frac{\mathbf{q}_\perp - \mathbf{k}_\perp}{(\mathbf{q}_\perp - \mathbf{k}_\perp)^2} \right]^2 \right] \\ &\simeq 12g^2 |\overline{\mathcal{M}}_{qQ \rightarrow qQ}|^2 (1-\bar{x})^2 \left[\frac{\mathbf{k}_\perp}{k_\perp^2 + x^2 M^2} + \frac{\mathbf{q}_\perp - \mathbf{k}_\perp}{(\mathbf{q}_\perp - \mathbf{k}_\perp)^2 + x^2 M^2} \right]^2, \quad (3.70) \end{aligned}$$

where we have defined

$$\bar{x} = \frac{k_{\perp}}{\sqrt{s}} e^{|y|} . \quad (3.71)$$

Going from the first to the second line we added the terms $x^2 M^2$ also in the denominators of the backward rapidity terms proportional to $\Theta(-y)$. This is valid within the approximations since x (not x' or \bar{x}) is small at backward rapidity according to its definition (3.38). In the following we refer to this result as the improved GB matrix element since it is not only valid at mid-rapidity, but also at forward and backward rapidity. In Section 3.2.9 we compare this result to the exact matrix element without any approximations.

As a note, the idea of decomposing the phase space in forward and backward rapidities was also used in Ref. [Gui06] for the inelastic scattering of a light and heavy quark in the GB approximation, although the $(1 - \bar{x})^2$ factor was neglected.

The observed factorization of the GB matrix element into an elastic part and a gluon emission amplitude in the high-energy limit, cf. for instance Equation (3.70), immediately implies that the GB calculation is also valid for other $2 \rightarrow 3$ processes, such as $Qg \rightarrow Qgg$ or for light partons $qg \rightarrow qgg$ or $gg \rightarrow ggg$. In the high-energy limit of the GB approximations the specific nature of the scattering particles becomes irrelevant for the structure of the resulting matrix elements. Therefore, Equation (3.70) also holds for processes other than the one explicitly considered here if one takes into account the different color prefactors of the corresponding $2 \rightarrow 2$ small angle amplitudes,

$$|\overline{\mathcal{M}}_{gQ \rightarrow gQ}|^2 \simeq \frac{9}{4} |\overline{\mathcal{M}}_{qQ \rightarrow qQ}|^2 , \quad (3.72)$$

and for light partons,

$$|\overline{\mathcal{M}}_{gg \rightarrow gg}|^2 \simeq \frac{9}{4} |\overline{\mathcal{M}}_{qg \rightarrow qg}|^2 \simeq \left(\frac{9}{4}\right)^2 |\overline{\mathcal{M}}_{qq' \rightarrow qq'}|^2 . \quad (3.73)$$

For the case of a heavy quark scattering with a gluon we verify this explicitly in the next section.

3.2.2. Gunion-Bertsch calculation for heavy quark scattering with a gluon

The process $g + Q \rightarrow g + Q + g$ has 16 diagrams, much more than for the heavy quark scattering with a light quark, due to the self-coupling of the gluon. However, in the approximation of a soft momentum transfer, the MANDELSTAM variable t is small and, therefore, the t channel dominates the total cross section. As a consequence, we can neglect the other channels and consider only the t channel, which has—besides one additional diagram—the same diagrams as in the previous section if one substitutes the light quark by a gluon, see Figure 3.10. Nevertheless, the calculation gets considerably more complicated due to the three-gluon vertices. The additional diagram 6 in Figure 3.10, is suppressed by the kinematics of the four-gluon vertex and can be neglected.

We start calculating the elastic scattering of a heavy quark and a gluon with the GUNION and BERTSCH approximations.

Diagram 0: Elastic scattering

The matrix element for $gQ \rightarrow gQ$ reads

$$\begin{aligned}
 i\mathcal{M}_0^{gQ} &= \bar{u}(p_3) ig\gamma^\nu \lambda_{ki}^b u(p_1) \frac{-ig_{\nu\rho}\delta^{bc}}{q^2} \epsilon_\delta^*(p_4) \epsilon_\sigma(p_2) \\
 &\quad \times g f^{cmn} \left[g^{\rho\sigma}(-q-p_2)^\delta + g^{\sigma\delta}(p_2+p_4)^\rho + g^{\delta\rho}(-p_4+q)^\sigma \right] \\
 &= \frac{g^2}{q^2} \lambda_{ki}^b f^{bmn} J_\nu(p_3, p_1) F^\nu(p_4, p_2, -q) =: \lambda_{ki}^b f^{bmn} iM_0^{gQ} .
 \end{aligned} \tag{3.74}$$

The source $J_\nu(p_3, p_1)$ describes the quark-gluon vertex and is defined in Equation (3.46). We denote the contribution of the three-gluon vertex with

$$\begin{aligned}
 F^\nu(p', p, q) &= \epsilon_\delta^*(p') \epsilon_\sigma(p) \left[g^{\nu\sigma}(q-p)^\delta + g^{\sigma\delta}(p+p')^\nu + g^{\delta\nu}(-p'-q)^\sigma \right] \\
 &= \epsilon_\delta^*(p') \epsilon_\sigma(p) \left[g^{\nu\sigma}(-p'+2q)^\delta + g^{\sigma\delta}(2p+q)^\nu + g^{\delta\nu}(-p-2q)^\sigma \right] \\
 &= \epsilon_\delta^*(p') \epsilon_\sigma(p) \left[g^{\nu\sigma}(2q)^\delta + g^{\sigma\delta}(2p+q)^\nu + g^{\delta\nu}(-2q)^\sigma \right] \\
 &\simeq \epsilon_\delta^*(p) \epsilon_\sigma(p) g^{\sigma\delta}(2p+q)^\nu ,
 \end{aligned} \tag{3.75}$$

where we made use of the transverse polarization of the gluons, $\epsilon(k) \cdot k = 0$, and employed the eikonal approximation ($p' = p + q$ with $q \ll p$) in the second to last and last step, respectively. The polarization states in Equation (3.75) vanish when the summing and averaging of the squared matrix element is performed (cf. Equation (3.8)).⁴ Therefore, we adopt a somewhat sloppy notation and just write

$$F^\nu(p+q, p, q) \simeq (2p+q)^\nu . \tag{3.76}$$

Comparing this result to Equation (3.48) shows that in the eikonal approximation the three-gluon vertex has the same kinematics as the quark-gluon vertex—only the color factor is different.

The matrix element without color factor is defined analogously to iM_0^{gQ} from Equation (3.45) as

$$iM_0^{gQ} = \frac{g^2}{q^2} J_\nu(p_3, p_1) F^\nu(p_4, p_2, -q) , \tag{3.77}$$

which is equal to iM_0^{qQ} in the eikonal approximation since $F^\nu(p_4, p_2, -q) \simeq J_\nu(p_4, p_2)$. This is a remarkable result that simplifies the calculation substantially because we can adopt nearly every result of the previous section and only have to worry about the color factor.

Doing the color algebra, the squared and averaged matrix element is

$$\begin{aligned}
 |\overline{\mathcal{M}}_0^{gQ}|^2 &= \frac{C(N)C_2(G)(N^2-1)}{N(N^2-1)} |\overline{M}_0^{gQ}|^2 = \frac{1}{2} |\overline{M}_0^{gQ}|^2 \\
 &= \frac{C_2(G)N}{C(N)(N^2-1)} |\mathcal{M}_0^{qQ}|^2 = \frac{9}{4} |\mathcal{M}_0^{qQ}|^2 \\
 &\simeq 32\pi^2 \alpha_s^2 \frac{(s-M^2)^2}{t^2} .
 \end{aligned} \tag{3.78}$$

⁴This is related to the sum of the spin states for the quark-gluon vertex. The result in both procedures is the same: The spin/polarization states do not contribute to the result.

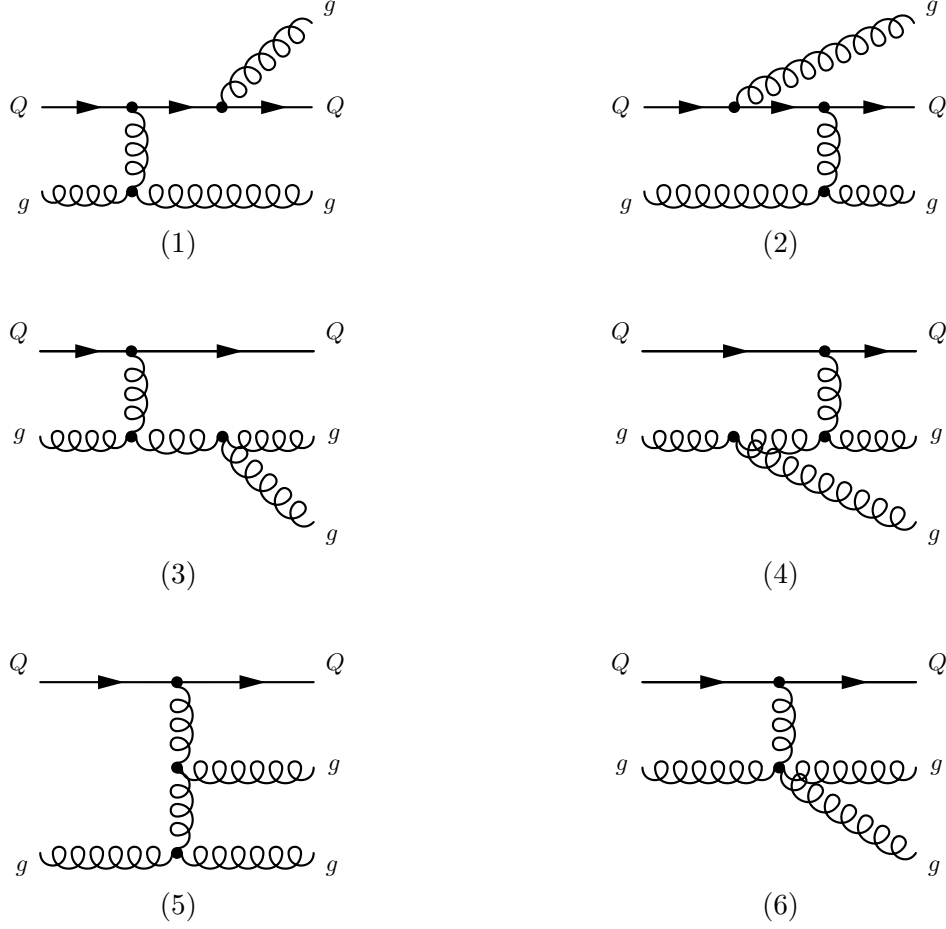


Figure 3.10.: FEYNMAN diagrams for the t channel of the process $g + Q \rightarrow g + Q + g$ in lowest order.

This is the same result as Equation (3.11) for the eikonal approximation $t \ll s$, as one would expect.

Neglecting diagram 6 in Figure 3.10, we now turn to the calculation of the radiative diagrams.

Diagrams 1 to 5

Since the three-gluon vertex has the same kinematics as the quark-gluon vertex in the high-energy limit, the results of all diagrams are the same as in Section 3.2.1 apart from the color factor.

Therefore, we can copy the result from Equation (3.62) with the adjusted color factor, which gives

$$i\mathcal{M}_{gQ \rightarrow gQg} \simeq -igf^{abc}f^{bmn}\lambda_{ki}^c iM_0^{gQ} (1-x) 2\epsilon_{\perp} \cdot \left[\frac{\mathbf{k}_{\perp}}{k_{\perp}^2 + x^2M^2} + \frac{\mathbf{q}_{\perp} - \mathbf{k}_{\perp}}{(\mathbf{q}_{\perp} - \mathbf{k}_{\perp})^2 + x^2M^2} \right]. \quad (3.79)$$

The squared and averaged matrix element is then

$$\begin{aligned} |\overline{\mathcal{M}}_{gQ \rightarrow gQg}|^2 &= 4g^2 \frac{C(N)C_2(G)^2}{N} |\overline{M}_0^{gQ}|^2 (1-x)^2 \left[\frac{\mathbf{k}_\perp}{k_\perp^2 + x^2 M^2} + \frac{\mathbf{q}_\perp - \mathbf{k}_\perp}{(\mathbf{q}_\perp - \mathbf{k}_\perp)^2 + x^2 M^2} \right]^2 \\ &= 12g^2 |\overline{\mathcal{M}}_{gQ \rightarrow gQ}|^2 (1-x)^2 \left[\frac{\mathbf{k}_\perp}{k_\perp^2 + x^2 M^2} + \frac{\mathbf{q}_\perp - \mathbf{k}_\perp}{(\mathbf{q}_\perp - \mathbf{k}_\perp)^2 + x^2 M^2} \right]^2. \end{aligned} \quad (3.80)$$

As it was the case for $qQ \rightarrow qQg$, the result is only valid at forward and mid-rapidity. Along the same line of argumentation (cf. Equation (3.70) and surrounding text), it can be generalized to the improved version of the GB matrix element by substituting $(1-x) \rightarrow (1-\bar{x})$,

$$|\overline{\mathcal{M}}_{gQ \rightarrow gQg}|^2 = 12g^2 |\overline{\mathcal{M}}_{gQ \rightarrow gQ}|^2 (1-\bar{x})^2 \left[\frac{\mathbf{k}_\perp}{k_\perp^2 + x^2 M^2} + \frac{\mathbf{q}_\perp - \mathbf{k}_\perp}{(\mathbf{q}_\perp - \mathbf{k}_\perp)^2 + x^2 M^2} \right]^2. \quad (3.81)$$

To sum this and the previous section up, one can split the squared matrix element of the QCD bremsstrahlung process into the contribution from the elastic scattering plus a radiative factor P_M^g in the high-energy limit

$$|\overline{\mathcal{M}}_{g(q)+Q \rightarrow g(q)+Q+g}|^2 = |\overline{\mathcal{M}}_{g(q)+Q \rightarrow g(q)+Q}|^2 P_M^g \quad (3.82)$$

with

$$P_M^g = 12g^2 (1-\bar{x})^2 \left[\frac{\mathbf{k}_\perp}{k_\perp^2 + x^2 M^2} + \frac{\mathbf{q}_\perp - \mathbf{k}_\perp}{(\mathbf{q}_\perp - \mathbf{k}_\perp)^2 + x^2 M^2} \right]^2, \quad (3.83)$$

which depends on the mass M of the heavy quark.

The final result (3.82) is proportional to g^6 or α_s^3 due to the three vertices, two associated with the $2 \rightarrow 2$ part and one with the emitted gluon. Explicitly considering the running of the coupling, it is sensible to choose proper scales since this reduces the influence of higher orders (cf. also the discussion before Equation (3.27)). The relevant scale for the binary part is the momentum transfer t , the same as for the $2 \rightarrow 2$ matrix element, see Equation (3.29). The only scale associated with the vertex of the emitted gluon is its transverse momentum k_\perp . Hence, the coupling of the $2 \rightarrow 3$ matrix element goes with $\alpha_s^2(t) \alpha_s(k_\perp^2)$. For the binary part of the matrix element one can insert the results from Section 3.1, Equations (3.27) and (3.29). In the presence of a medium and a running coupling, the radiation factor from Equation (3.83) modifies to

$$P_M^g = 48\pi\alpha_s(k_\perp^2) (1-\bar{x})^2 \left[\frac{\mathbf{k}_\perp}{k_\perp^2 + x^2 M^2} + \frac{\mathbf{q}_\perp - \mathbf{k}_\perp}{(\mathbf{q}_\perp - \mathbf{k}_\perp)^2 + m_D^2 (\alpha_s(k_\perp^2)) + x^2 M^2} \right]^2. \quad (3.84)$$

The first term in the bracket does not need to be screened by a screening mass since the infrared divergence is cured by the LPM effect, as shown in Section 3.2.7. The second term stems from diagram 5 in Figure 3.8 and resembles the propagator from one of the internal gluon lines. Hence, it must be screened with the gluon DEBYE mass.

3.2.3. Radiative heavy quark processes in Feynman gauge

In this section we rederive the matrix element for the process $q + Q \rightarrow q + Q + g$ in FEYNMAN gauge [AGM⁺12]. Of course, a matrix element should be gauge independent if no approximations are employed. However, using approximations can break the gauge invariance or at least restrict the region of validity, as we have seen in the previous two sections. Although we do the calculation in FEYNMAN gauge with slightly different approximations than in the GB case in light cone gauge (see Section 3.2.1), we show that both calculations agree within their approximations, which is an independent check that our calculations are correct. Furthermore, we compare the GB result to the exact matrix element in Section 3.2.9 to also verify that the employed approximations are reasonable.

In Figure 3.8 the five FEYNMAN diagrams for the process $qQ \rightarrow qQg$ are shown. We assume very soft gluon emission ($k \rightarrow 0$) [BKDC⁺81], which implies for the MANDELSTAM variables defined in Appendix A.2 that $t' \rightarrow t$, $s' \rightarrow s$, $u' \rightarrow u$ and for the longitudinal momentum fraction from Equations (3.38) and (3.71) $x, \bar{x} \rightarrow 0$, respectively. In the center of momentum frame we consider the case where the energy of the emitted gluon ω is much smaller than the momentum transfer $\sqrt{|t|} \approx q_\perp$ from the projectile (heavy quark) to the target (light quark) which again is small compared to the energy E of the heavy quark. This leads to the hierarchy

$$E \gg \sqrt{|t|} \gg \omega. \quad (3.85)$$

This hierarchy is very similar to (3.39) and (3.40) used in the GUNION-BERTSCH calculation, but is stricter in the sense that the emitted gluon must be also soft compared to the momentum transfer t . This significantly simplifies the calculation in FEYNMAN gauge. It is important to note that—like in the GUNION-BERTSCH calculation—the scaled mass of the heavy quark with its energy M/E and the gluon emission angle θ are free from any constraints.

The gauge invariant amplitude for the process $qQ \rightarrow qQg$ can be written as the sum of the squared matrix elements from the diagrams of Figure 3.8, including their interference terms,

$$|\overline{\mathcal{M}}_{qQ \rightarrow qQg}|^2 = \sum_{i \geq j} \mathcal{M}_{ij}^2, \quad (3.86)$$

where i and j run from 1 to 5 and $\mathcal{M}_{ij}^2 = \mathcal{M}_i \mathcal{M}_j^*$ with \mathcal{M}_i being the matrix element of diagram i (see Figure 3.8).

With the hierarchy indicated in (3.85) the different squared matrix elements are obtained in FEYNMAN gauge as

$$\begin{aligned} \mathcal{M}_{11}^2 &= \mathcal{M}_{22}^2 = \frac{128}{27} g^6 \frac{s^2}{t^2} \frac{1}{k_\perp^2} \left[\frac{M^2}{s} - 1 + \mathcal{J} \right] \mathcal{J} \\ \mathcal{M}_{33}^2 &= \mathcal{M}_{44}^2 = \mathcal{M}_{55}^2 = 0 \\ \mathcal{M}_{12}^2 &= \frac{128}{27} g^6 \frac{s^2}{t^2} \frac{1}{k_\perp^2} \left[\frac{1}{4} \left(\frac{M^2}{s} - 1 + \mathcal{J} \right) \right] \mathcal{J} \\ \mathcal{M}_{14}^2 &= \mathcal{M}_{23}^2 = \frac{128}{27} g^6 \frac{s^2}{t^2} \frac{1}{k_\perp^2} \left[\frac{7}{8} \left(1 - \frac{M^2}{s} \right) \right] \mathcal{J} \\ \mathcal{M}_{13}^2 &= \mathcal{M}_{24}^2 = \frac{128}{27} g^6 \frac{s^2}{t^2} \frac{1}{k_\perp^2} \left[\frac{1}{4} \left(1 - \frac{M^2}{s} \right) \right] \mathcal{J} \\ \mathcal{M}_{34}^2 &= \mathcal{M}_{15}^2 = \mathcal{M}_{25}^2 = \mathcal{M}_{35}^2 = \mathcal{M}_{45}^2 = 0 \end{aligned} \quad (3.87)$$

with

$$\mathcal{J} = 1 - \left[\left(\frac{s}{M^2} - 1 \right) \sin^2(\theta/2) + 1 \right]^{-1} \quad (3.88)$$

and $k_\perp = \omega \sin \theta$, the transverse momentum of the emitted gluon. For the calculation of the matrix elements the programs REDUCE and CalcHep [Sem09] have been used. We note that the results are in accordance with the matrix elements obtained from the process $q\bar{q} \rightarrow Q\bar{Q}g$ from Ref. [KPR80] by crossing the light anti-quark and the heavy anti-quark.

The gauge invariant amplitude for the process $qQ \rightarrow qQg$ can now be obtained by summing all the sub-amplitudes given in Equation (3.87),

$$\begin{aligned} |\overline{\mathcal{M}}_{qQ \rightarrow qQg}|^2 &= 12g^2 |\overline{\mathcal{M}}_{qQ \rightarrow qQ}|^2 \frac{1}{k_\perp^2} \frac{\mathcal{J}^2}{\left(1 - \frac{M^2}{s}\right)^2} \\ &= 12g^2 |\overline{\mathcal{M}}_{qQ \rightarrow qQ}|^2 \frac{1}{k_\perp^2} \left(1 + \frac{M^2}{s \tan^2(\frac{\theta}{2})}\right)^{-2} \\ &= 12g^2 |\overline{\mathcal{M}}_{qQ \rightarrow qQ}|^2 \frac{1}{k_\perp^2} \left(1 + \frac{M^2}{s} e^{2y}\right)^{-2}, \end{aligned} \quad (3.89)$$

where $y = \eta = -\ln[\tan(\theta/2)]$ is the rapidity of the emitted massless gluon. The two body amplitude $|\overline{\mathcal{M}}_{qQ \rightarrow qQ}|^2$ is given in this limit in Equation (3.51).

It is the same matrix element as obtained from the GB calculation in Section 3.2.1 if one applies there the same limit as in this section, that is, the emitted gluon being much softer as the momentum transfer t . This constraint, given in Equation (3.85) implies for light-cone coordinates that $q_\perp \gg k_\perp$ and $x, \bar{x} \rightarrow 0$. The GUNION-BERTSCH result from Equation (3.70) then reduces to

$$|\overline{\mathcal{M}}_{qQ \rightarrow qQg}|^2 \simeq 12g^2 |\overline{\mathcal{M}}_{qQ \rightarrow qQ}|^2 \left[\frac{\mathbf{k}_\perp}{k_\perp^2 + x^2 M^2} \right]^2 = 12g^2 |\overline{\mathcal{M}}_{qQ \rightarrow qQ}|^2 \frac{1}{k_\perp^2} \left(1 + \frac{x^2 M^2}{k_\perp^2}\right)^{-2}. \quad (3.90)$$

As a note, the $x^2 M^2$ term in the denominator cannot be neglected with respect to k_\perp^2 , although $x \rightarrow 0$, since also $k_\perp \rightarrow 0$. Plugging in the definition of the longitudinal momentum fraction from Equation (3.38), $x = k_\perp e^y / \sqrt{s}$, yields the same result as Equation (3.89). Therefore, we find that within the approximations (3.85) of a very soft emitted gluon the result in light cone gauge and FEYNMAN gauge agree with each other, which indicates that our result is gauge invariant—at least in the phase space region where the emitted gluon is very soft.

As we saw in the previous paragraph, in the limit $q_\perp \gg k_\perp$ the second term of the GB result from Equation (3.70) vanishes. This is the contribution that stems from diagram 5 in Figure 3.8. Consistently, also in Equation (3.87) in FEYNMAN gauge all terms that have contributions from diagram 5 vanish. Hence, in other words, the approximations employed in this section highlight the QED-like diagrams of the process and neglect the emission from the internal gluon line, which is unique to QCD.

3.2.4. Dead cone effect

The dead cone effect, that is, the suppression of gluon emission off a heavy quark at small angles, should be also visible in our results from the previous sections, which is shown in this

section and compared to the original result of DOKSHITZER and KHARZEEV [DK01]. They calculated the radiation spectrum of a gluon emitted off a heavy quark for a large heavy quark energy, $E \gg M$, and small angle θ of the gluon with respect to the outgoing heavy quark. In addition, they neglected the diagram in which the gluon can also be emitted off the exchanged gluon between the heavy quark and the medium particle (diagram (5) in Figure 3.8), which corresponds to the limit $q_\perp \gg k_\perp$.

First, we derive the dead cone effect for these approximations to find the same result as DOKSHITZER and KHARZEEV. Consequently, we show that the dead cone suppression factor is also present in our results—and that it even has a larger level of validity than the one from Ref. [DK01]. More specifically, our result is valid for all heavy quark masses as well as all angles of the emitted gluon and reduces to the result of Ref. [DK01] for small masses and small angles.

As we saw in the last section, for $q_\perp \gg k_\perp$ the matrix element for $qQ \rightarrow qQg$ from Equation (3.70) is dominated by the first term in the bracket going basically with $1/k_\perp^2$ (cf. Equation (3.89)),

$$|\overline{\mathcal{M}}_{qQ \rightarrow qQg}|^2 \simeq 12g^2 |\overline{\mathcal{M}}_{qQ \rightarrow qQ}|^2 (1 - \bar{x})^2 \left[\frac{\mathbf{k}_\perp}{k_\perp^2 + x^2 M^2} \right]^2. \quad (3.91)$$

For small angles θ the components of the momentum of the emitted gluon can be approximated by $k_z \simeq \omega$ and $k_\perp = \omega \sin \theta \simeq \omega \theta$. The momentum fraction x of the gluon with respect to the incoming heavy quark is then given by

$$x = \frac{k^+}{p^+} \simeq \frac{2\omega}{\sqrt{s}} \simeq \frac{2\omega}{2E} = \frac{\omega}{E} \simeq \frac{k_\perp}{\theta E}, \quad (3.92)$$

where we used in the third step $E \gg M$. If we insert this in Equation (3.91), we end up with

$$\begin{aligned} |\overline{\mathcal{M}}_{qQ \rightarrow qQg}|^2 &\simeq 12g^2 |\overline{\mathcal{M}}_{qQ \rightarrow qQ}|^2 (1 - \bar{x})^2 \frac{k_\perp^2}{(k_\perp^2 + x^2 M^2)^2} \\ &\simeq 12g^2 |\overline{\mathcal{M}}_{qQ \rightarrow qQ}|^2 (1 - \bar{x})^2 \frac{1}{k_\perp^2} \mathcal{D}_{\text{DK}}, \end{aligned} \quad (3.93)$$

where we defined the dead cone factor as

$$\mathcal{D}_{\text{DK}} = \frac{1}{\left(1 + \frac{M^2}{\theta^2 E^2}\right)^2} = \frac{1}{\left(1 + \frac{\theta_D^2}{\theta^2}\right)^2} \quad (3.94)$$

with the dead cone angle $\theta_D = M/E$. This is exactly the same expression that was found in Ref. [DK01] and named the dead cone suppression factor.

In Figure 3.11 the dead cone factor \mathcal{D}_{DK} is depicted as a function of θ . For a massless quark, the suppression vanishes and $\mathcal{D}_{\text{DK}} = 1$ for all angles. For finite masses, small angles are suppressed, which is the manifestation of the dead cone effect. With increasing mass the suppression gets more pronounced. The dead cone angle $\theta_D = M/E$ is an indicator where the transition between suppression and standard radiation occurs, although this transition is actually smeared out over a rather broad range for larger masses. More precisely, θ_D labels the angle at which the radiation off a heavy quark is only 25% ($\mathcal{D}_{\text{DK}} = 1/4$) of the radiation off a

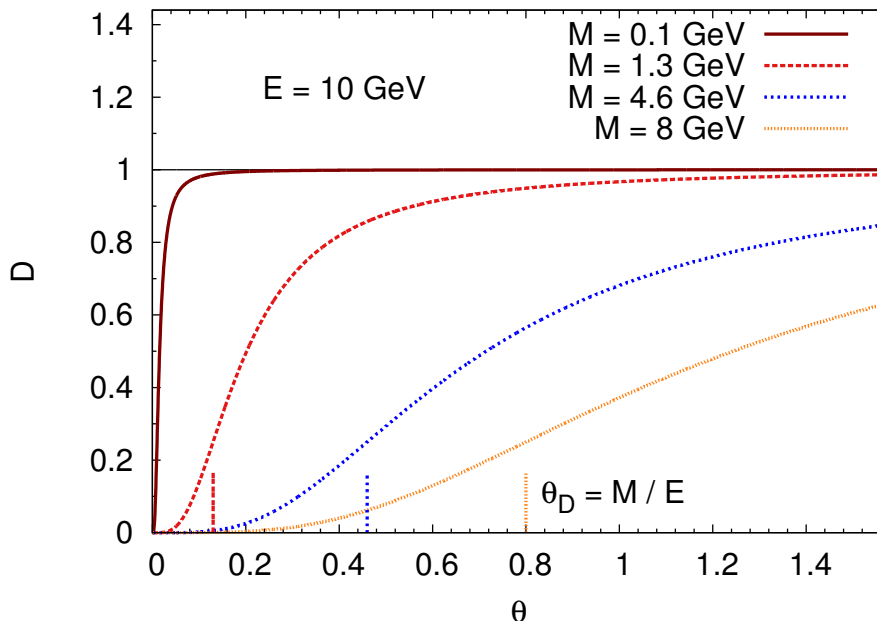


Figure 3.11.: The dead cone factor \mathcal{D}_{DK} as a function of the angle θ between the emitted gluon and the heavy quark for an incoming heavy quark with an energy of 10 GeV and different masses. The vertical lines indicate where the dead cone angle $\theta_D = M/E$ is located for the respective masses.

massless quark (cf. Equation (3.94)). Therefore, the angle θ_D can be interpreted as the angle of a dead cone around a heavy quark. Within this cone the radiation is suppressed, but—in principle—still allowed with a small probability.

In general, without employing the approximations given above, the dead cone factor can be defined as the radiation spectrum of a gluon emitted off a heavy quark as given in Equation (3.83) divided by the spectrum for the massless case,

$$\mathcal{D}_{\text{GB}} = \frac{P_M^g}{P_0^g}. \quad (3.95)$$

In contrast to \mathcal{D}_{DK} an explicit dependence on k_\perp , q_\perp , and the angle between both, ϕ , remains. For $E \gg M$, a small angle θ , and $q_\perp \gg k_\perp$ the more general dead cone factor \mathcal{D}_{GB} simplifies to \mathcal{D}_{DK} .

Figure 3.12 shows the dead cone factor \mathcal{D}_{GB} as a function of θ for $M/\sqrt{s} = 0.1$ and $\phi = 1.0$ as well as different parameter sets for k_\perp and q_\perp . Especially for large θ , the suppression factor \mathcal{D}_{GB} deviates from \mathcal{D}_{DK} since the latter is only applicable for small angles. While \mathcal{D}_{DK} goes back to zero for large angles—thus, creating a second artificial dead cone around the light parton— \mathcal{D}_{GB} saturates at one, as it is expected. If k_\perp and q_\perp are of the same order, the dead cone is even more pronounced than that of DOKSHITZER and KHARZEEV. The dead cone factor is also strongly dependent on the angle ϕ and the mass M . For small ϕ the suppression is considerably larger than \mathcal{D}_{DK} , whereas for $\phi = \pi/2$ the suppression factor \mathcal{D}_{GB} does not depend on k_\perp and q_\perp anymore (both not plotted). For large masses M the suppression of

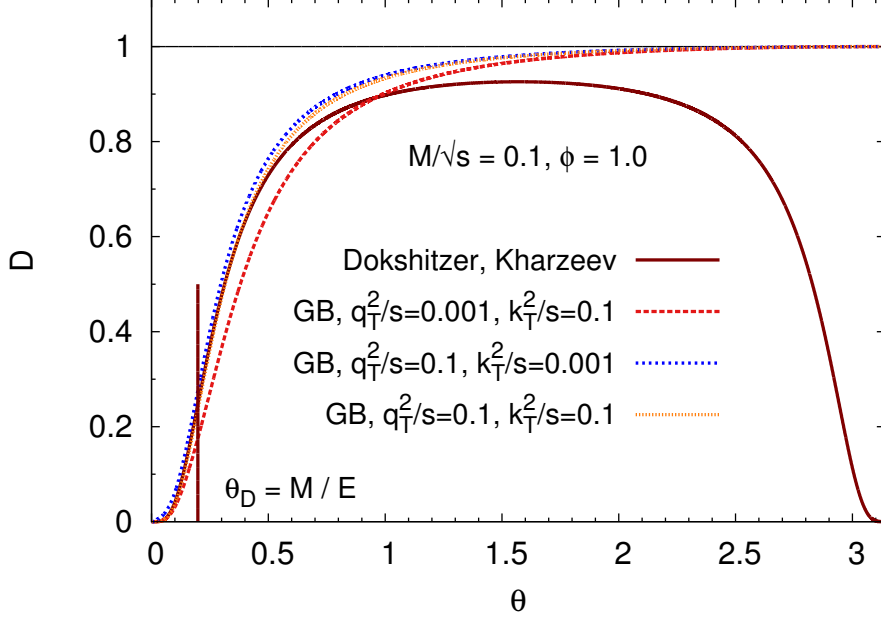


Figure 3.12.: The dead cone factor \mathcal{D}_{GB} as a function of the angle θ between the emitted gluon and the heavy quark for $M/\sqrt{s} = 0.1$ and $\phi = 1.0$ (the angle between \mathbf{k}_\perp and \mathbf{q}_\perp). The curves are for different values of k_\perp^2/s and q_\perp^2/s . In addition, the result of Ref. [DK01] is shown. The vertical line indicates the dead cone angle $\theta_D = M/E$.

\mathcal{D}_{GB} is also significantly larger than \mathcal{D}_{DK} for the same mass, as shown in Figure 3.13 for $M/\sqrt{s} = 0.8$. This difference comes due to the approximation $E \gg M$ employed for \mathcal{D}_{DK} .

To study the suppression factor \mathcal{D}_{GB} in more detail we once again employ the approximation $q_\perp \gg k_\perp$, but do not put any constraints on the heavy quark mass or the angle of the emitted gluon as has been done by DOKSHITZER and KHARZEEV. The suppression factor then reads

$$\mathcal{D}_{\text{GB}} = \frac{P_M^g}{P_0^g} \simeq \frac{\left[\frac{\mathbf{k}_\perp}{k_\perp^2 + x^2 M^2} \right]^2}{\left[\frac{\mathbf{k}_\perp}{k_\perp^2} \right]^2} = \left(1 + \frac{x^2 M^2}{k_\perp^2} \right)^{-2} = \left(1 + \frac{M^2}{s \tan^2(\frac{\theta}{2})} \right)^{-2} =: \mathcal{D}_{\text{AGMMU}} \quad (3.96)$$

and does not depend on k_\perp or q_\perp anymore. As a note, this is also the result that one would directly obtain from our result in FEYNMAN gauge, see Equation (3.89), due to the given hierarchy (3.85) [AGM⁺12]. Therefore, we name this suppression factor in the very soft gluon approximation in the following $\mathcal{D}_{\text{AGMMU}}$ after the authors of our paper [AGM⁺12]. It is valid in the full range of θ —or rapidity of the emitted gluon—(i.e., $-\pi < \theta < +\pi$) and in the full range of $m = M/\sqrt{s}$ (i.e., $0 < m < 1$). As can be seen in Figure 3.14 the suppression is rather narrow in θ for small m , but becomes very wide for large masses. The valley around $\theta \simeq 0$ clearly indicates the presence of the dead cone in the forward direction with respect to the propagating heavy quark. In the backward region, $\theta \simeq \pm\pi$, the suppression factor saturates to unity. This suggests that the quark mass plays only a role in the forward direction where the energy of the quark becomes of the order of its mass.

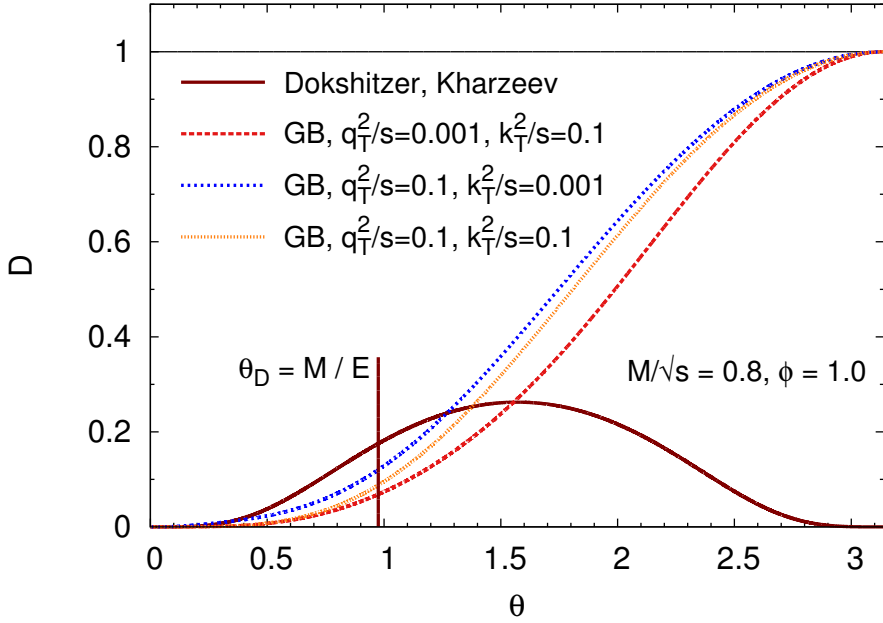


Figure 3.13.: As Figure 3.12 but for $M/\sqrt{s} = 0.8$

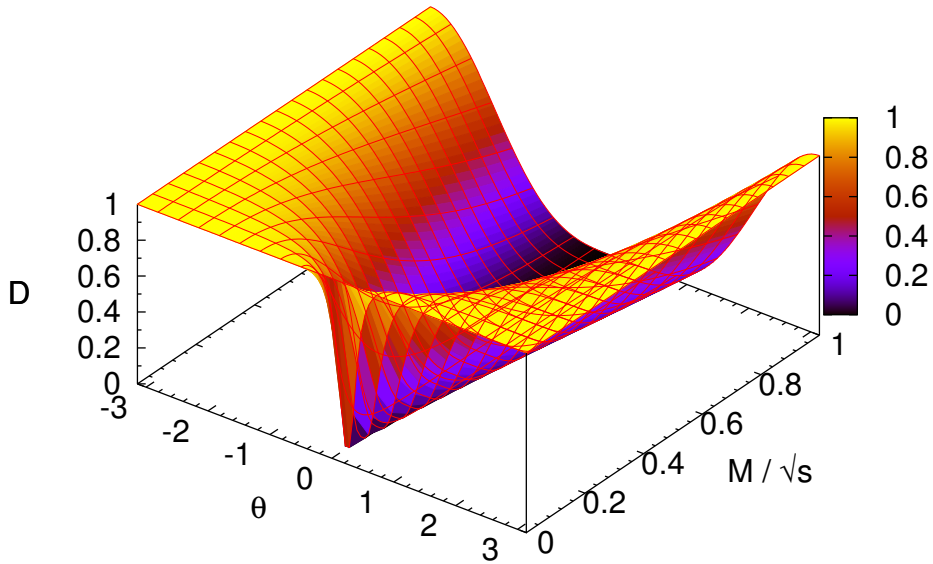


Figure 3.14.: The suppression factor $\mathcal{D}_{\text{AGMMU}}$ from Equation (3.96) as a function of θ and M/\sqrt{s} .

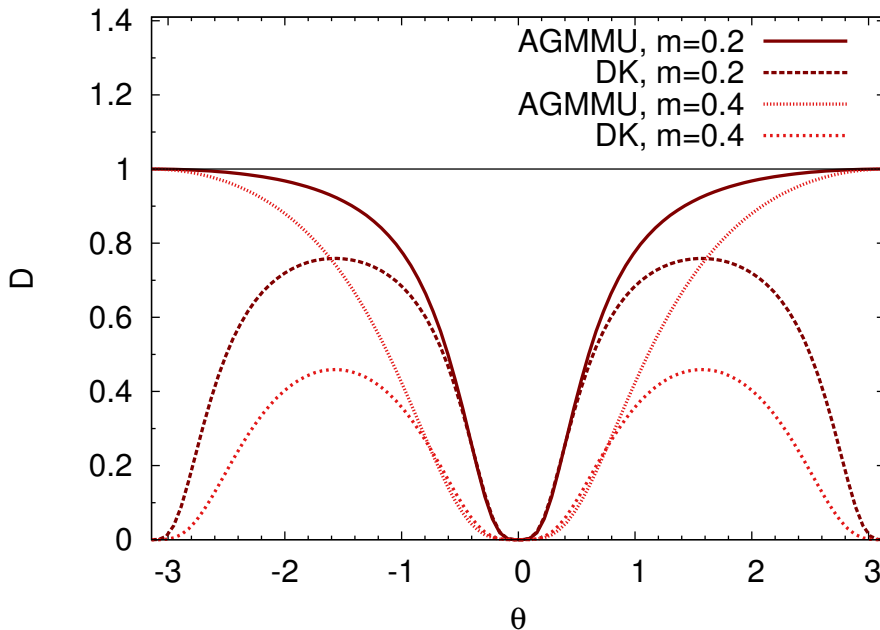


Figure 3.15.: The suppression factor (3.96) as a function of θ (labeled as AGMMU) compared to the result of DOKSHITZER and KHARZEEV [DK01] (DK) for different $m = M/\sqrt{s}$. Note that the latter is only valid at small angles.

In the limit $M \ll \sqrt{s}$ and $\theta \simeq 0$, it is $\sqrt{s} \simeq 2E$ and $\tan(\theta/2) \simeq \theta/2$ and Equation (3.96) reduces to the result of DOKSHITZER and KHARZEEV from Equation (3.94). Figure 3.15 compares the suppression factor (3.96) to that given in Equation (3.94) as a function of the emission angle θ for two values of the mass, $m = 0.2$ and 0.4 . The result of DOKSHITZER and KHARZEEV [DK01] agrees with our result in the domain of a small emission angle. However, the little variation in this region is due to the constraint $M \ll \sqrt{s}$ employed in Ref. [DK01], whereas no such constraint is set in our calculation. For large emission angles the suppression factor $\mathcal{D}_{\text{AGMMU}}$ approaches unity. This indicates that the backward emission is as strong as for light quarks. In this domain the result of Ref. [DK01] is not valid.

To summarize this section, our results contain a generalized suppression factor for gluon emission off a heavy quark through the scattering with a light parton. In the appropriate limit this expression reduces to the usually known dead cone factor. Our analysis shows that there is a suppression of soft gluon emission due to the mass of the heavy quark in the forward direction. On the other hand, the present findings also indicate that a heavy quark emits a soft gluon almost similar to that of a light quark in the backward rapidity region. This is an important aspect for gluon emission off a heavy quark which was not explored earlier [MPST98, DK01, DAM10, KPS10]. Instead, some models [TKS05, XDZ05, ZZ07, DAM10, MBAD11] employ the simplified dead cone formula (3.94) from Ref. [DK01] for all angles, which gives an additional suppression in the backward region that should not be there.

The impact of the improved GB matrix element, which gives the correct suppression pattern, on the energy loss of heavy quarks in a static medium and on heavy flavor observables in heavy-ion collisions is studied in Sections 5.3 and 6.2, respectively.

3.2.5. Total cross section

In Sections 3.2.1, 3.2.2, and 3.2.3 the matrix elements for radiative processes involving a heavy quark have been calculated. To carry out collisions one needs the total cross section, which is obtained by integrating over the available phase space.

According to Equation (3.1) the total cross section of a $2 \rightarrow 3$ process ($p_1 + p_2 \rightarrow p_3 + p_4 + k$, where k is the radiated gluon) is defined by

$$\sigma_{23} = \frac{1}{2E_1 2E_2 v_{\text{rel}}} \frac{1}{\nu} \int \frac{d^3 p_3}{(2\pi)^3 2E_3} \frac{d^3 p_4}{(2\pi)^3 2E_4} \frac{d^3 k}{(2\pi)^3 2k^0} \times (2\pi)^4 \delta^{(4)}(p_1 + p_2 - (p_3 + p_4 + k)) |\overline{\mathcal{M}}_{2 \rightarrow 3}|^2, \quad (3.97)$$

where we used the same notation as in Section 3.2.1. Note that the symmetry factor $\nu = n!$, which accounts for n identical particles in the final state, is not needed when computing cross sections from the (improved) GB matrix element. In this case the specific choice and identification of the outgoing momenta, where k is the momentum of the radiated gluon, selects a specific configuration and, thus, obviates the need for a symmetry factor $1/\nu$. This is taken into account for *all* calculations involving the original or improved GB matrix elements in this work and has also been correctly implemented in BAMPS from the beginning [XG05]. However, when we compare to the exact matrix elements in Section 3.2.9 the symmetry factors must be explicitly considered when calculating the cross section of the exact matrix elements since gluons are treated as indistinguishable particles in these matrix elements.

To obtain the total cross section of radiative heavy quark processes we want to insert the GUNION-BERTSCH cross section from the previous sections. However, this is not given in terms of the four-momenta p_3 , p_4 , and k but in terms of \mathbf{q}_\perp , \mathbf{k}_\perp , and \bar{x} in the center-of-mass frame (cf. Equation (3.82)). More precisely, it only depends on the scalars \bar{x} , q_\perp^2 , and k_\perp^2 as well as on the angle ϕ between \mathbf{q}_\perp and \mathbf{k}_\perp through the terms $\mathbf{q}_\perp \cdot \mathbf{k}_\perp = q_\perp k_\perp \cos \phi$. Consequently, we rewrite the integrals in Equation (3.97) as integrals over q_\perp^2 , k_\perp^2 , ϕ and the rapidity of the emitted gluon y , which is related to \bar{x} via Equation (3.71). Along this way we generalize previous considerations [XG05, Foc11] to quarks with finite masses. Another advantage of changing to these variables is the numerical efficiency. Instead of performing the nine-dimensional integration in Equation (3.97) one can analytically integrate out the delta function to end up with only a five dimensional integral, which can be reduced to a four dimensional integral by performing one angle integration directly.

Employing for p_4 the general relation

$$\int \frac{d^3 p}{2E} = \int d^4 p \delta(p^2 - m^2) \Theta(p^0), \quad (3.98)$$

which follows from a property of the delta function,

$$\delta(f(x)) = \sum_i \frac{1}{|f'(x_i)|} \delta(x - x_i), \quad (3.99)$$

where x_i are the roots of $f(x)$, and performing the integral over p_4 yields

$$\sigma_{23} = \frac{1}{128 \pi^5} \frac{1}{\nu} \frac{1}{2E_1 2E_2 v_{\text{rel}}} \int \frac{d^3 p_3}{E_3} \frac{d^3 k}{k^0} \delta(F) |\overline{\mathcal{M}}_{2 \rightarrow 3}|^2. \quad (3.100)$$

The argument of the δ function $F = (p_1 + p_2 - p_3 - k)^2 - m_4^2$ can also be expressed in terms of the new variables,

$$F = s - 2\sqrt{s} \left(\sqrt{q_\perp^2 + m_3^2} \cosh y_3 + k_\perp \cosh y \right) + 2q_\perp k_\perp \cos \phi + m_3^2 - m_4^2 + 2\sqrt{q_\perp^2 + m_3^2} k_\perp (\cosh y_3 \cosh y - \sinh y_3 \sinh y) , \quad (3.101)$$

where y (y_3) denotes the rapidity of the particle with momentum k (p_3) and m_i is the mass corresponding to p_i .

For a particle with momentum p the derivative of the rapidity with respect to p_z is $dy/dp_z = 1/E$ and, thus, $d^3p/E = d^2p_\perp dy = \frac{1}{2} dp_\perp^2 d\phi dy$. Employing this relation for p_3 and k , respectively, performing one of the ϕ' integration (e.g., ϕ'_{p_3} from d^3p_3), and choosing the coordinate system such that the other ϕ' (e.g., ϕ'_k from d^3k) corresponds to ϕ , one ends up with

$$\sigma_{23} = \frac{1}{128 \pi^4} \frac{1}{\nu} \frac{1}{2E_1 2E_2 v_{\text{rel}}} \int dq_\perp^2 dy_3 dk_\perp^2 dy d\phi \delta(F) |\overline{\mathcal{M}}_{2 \rightarrow 3}|^2 . \quad (3.102)$$

By performing the y_3 integration and making use of Equation (3.99) the final result of the total cross section of a $2 \rightarrow 3$ process is given by

$$\sigma_{23} = \frac{1}{128 \pi^4} \frac{1}{\nu} \frac{1}{2E_1 2E_2 v_{\text{rel}}} \int dq_\perp^2 dk_\perp^2 dy d\phi |\overline{\mathcal{M}}_{2 \rightarrow 3}|^2 \sum \left(\frac{\partial F}{\partial y_3} \Big|_{F=0} \right)^{-1} . \quad (3.103)$$

The derivative of F reads

$$\frac{\partial F}{\partial y_3} = -2 \left[(\sqrt{s} - k_\perp \cosh y) p_3^z + \sqrt{q_\perp^2 + p_3^{z2} + m_3^2} k_\perp \sinh y \right] \quad (3.104)$$

and the solutions for $F = 0$ are

$$p_3^z = \frac{-b \pm \sqrt{b^2 - 4ac}}{2a} , \quad (3.105)$$

with

$$\begin{aligned} a &= (\sqrt{s} - k^0)^2 - k_z^2 \\ b &= k_z (s - 2\sqrt{s} k_0 + 2q_\perp k_\perp \cos \phi + m_3^2 - m_4^2) \\ c &= (\sqrt{s} - k^0)^2 (q_\perp^2 + m_3^2) - \frac{1}{4} (s - 2\sqrt{s} k_0 + 2q_\perp k_\perp \cos \phi + m_3^2 - m_4^2)^2 . \end{aligned} \quad (3.106)$$

Furthermore, the solutions have to satisfy the additional constraint

$$s - 2\sqrt{s} k^0 + 2q_\perp k_\perp \cos \phi - 2p_3^z k_z + m_3^2 - m_4^2 \geq 0 . \quad (3.107)$$

As a check, we have confirmed numerically that both formulas for the total $2 \rightarrow 3$ cross section, (3.97) and (3.103), give the same results.

So far the derivation applies to all $2 \rightarrow 2 + g$ processes, regardless of the mass of the particles (only the emitted gluon must be massless). For a scattering of a heavy quark with mass M

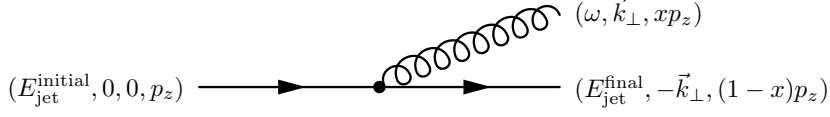


Figure 3.16.: Kinematics of gluon radiation off a heavy quark jet. The four-momenta of the individual particles are shown.

and a light parton, Equation (3.103) reads

$$\sigma_{g(q)+Q \rightarrow g(q)+Q+g} = \frac{1}{256} \frac{1}{\pi^4} \frac{1}{\nu} \frac{1}{s-M^2} \int_0^{\frac{(s-M^2)^2}{4s}} dq_{\perp}^2 \int_0^{\frac{(s-M^2)^2}{4s}} dk_{\perp}^2 \int_{y_{\min}}^{y_{\max}} dy \int_0^{\pi} d\phi \times |\overline{\mathcal{M}}_{g(q)+Q \rightarrow g(q)+Q+g}|^2 \sum \left(\left. \frac{\partial F}{\partial y_3} \right|_{F=0} \right)^{-1}, \quad (3.108)$$

where we used Equation (3.3) and restored the boundaries of the integrals, which are determined from kinematics. The available phase space limits the rapidity range to $y_{\max/\min} = \pm \text{arccosh} [(s-M^2)/2\sqrt{s}k_{\perp}]$. However, as we will see in Section 3.2.8 an additional constraint due to the LANDAU-POMERANCHUK-MIGDAL (LPM) effect also restricts the rapidity range. For massless particles the LPM effect also introduces a lower cut-off for k_{\perp} , which is not present for massive particles. However, the interplay between the LPM effect and the dead cone effect prevents also for heavy quarks a divergence of the total cross section (see Figure 3.19 and surrounding text).

3.2.6. Formation time of a gluon emitted off a heavy quark

The radiation of a gluon off a heavy quark jet is a quantum mechanical process that does not happen instantaneously, but has a certain formation time. According to the uncertainty principle the formation time τ is of the order of the inverse of the virtuality ΔE of the process,

$$\tau \simeq \frac{1}{\Delta E}. \quad (3.109)$$

The virtuality of the process can be determined by adding up all energies of the involved particles. If all the particles were on-shell, the sum would be zero. A finite value gives the off-shellness or virtuality of the process.

We consider a fast heavy quark jet in the lab frame that radiates a soft gluon. Due to the boost the gluon is emitted at small angles even if the angle in the center-of-mass frame can be large (cf. Section 3.2.4). With the notation from Figure 3.16, the virtuality of the process is

$$\begin{aligned} \Delta E &= E_{\text{jet}}^{\text{final}} + \omega - E_{\text{jet}}^{\text{initial}} \\ &= \sqrt{(1-x)^2 p_z^2 + k_{\perp}^2 + M^2} + \sqrt{x^2 p_z^2 + k_{\perp}^2} - \sqrt{p_z^2 + M^2}, \end{aligned} \quad (3.110)$$

where M is the mass of the heavy quark and $x = k_z/p_z$ the longitudinal momentum fraction of the emitted gluon.⁵ Soft small angle radiation implies $p_z \gg k_z$ as well as $x \ll 1$ and for a

⁵Note that x here is slightly differently defined than in Equation (3.37). However, in the present scenario we assume that the gluon is emitted at small angles and in this case both definitions are the same.

fast heavy quark jet it is $p_z \gg M$. With these assumptions ΔE is

$$\Delta E \simeq \frac{k_\perp^2 + x^2 M^2}{2k_z} \simeq \frac{k_\perp^2 + x^2 M^2}{2\omega}, \quad (3.111)$$

since for small angles the energy of the gluon is $\omega \simeq k_z$. Thus, the formation time of a gluon that is emitted off a heavy quark jet is given in the lab frame by

$$\tau \simeq \frac{2\omega}{k_\perp^2 + x^2 M^2}. \quad (3.112)$$

This result agrees with the finding of Ref. [ZWW04] within the approximations. For a massless case it simplifies to the well-known result $\tau \simeq 2\omega/k_\perp^2$.

This formation time was calculated for an off-shell $1 \rightarrow 2$ process in the lab frame. A complimentary derivation of the formation time of the gluon in the center-of-mass frame of an on-shell $2 \rightarrow 3$ process is the following. Consider a reference frame Σ_{trans} in which the emitted gluon is purely transverse. In this frame the formation time is given by the uncertainty principle as $\tau_{\text{trans}} \simeq 1/k_\perp$. To obtain the value in the center-of-mass system one has to boost with the factor $\gamma_{\text{trans}} = \cosh y$ where y is the rapidity of the emitted gluon in the center-of-mass frame. Hence, with $\omega = k_\perp \cosh y$ the formation time of a gluon for a $2 \rightarrow 3$ processes in the center-of-mass frame is

$$\tau \simeq \frac{\omega}{k_\perp^2}. \quad (3.113)$$

This value differs from the formation time of a $1 \rightarrow 2$ processes in the lab frame in Equation (3.112) by a prefactor of 2 and by the missing mass term in the denominator.

Since within the BAMPS model we are mainly interested in $2 \rightarrow 3$ on-shell processes and because Equation (3.113) has been applied for massless particles, we also use this formula, but extend it to the heavy flavor sector by adding the mass term in the denominator. Thus, we employ for the formation time in the frame Σ_{trans}

$$\tau_{\text{trans}} = \frac{k_\perp}{k_\perp^2 + x^2 M^2}. \quad (3.114)$$

Furthermore, we will study the effect of varying the prefactor of the formula on our results.

3.2.7. Landau-Pomeranchuk-Migdal effect

The LANDAU-POMERANCHUK-MIGDAL (LPM) effect [LP53, Mig56] describes the suppression of medium-induced bremsstrahlung processes due to coherence effects of multiple scatterings.

For a jet traversing a medium radiation processes are induced by the medium. If the wavelengths, or equivalently the formation times, of the radiated particles (gluons in QCD or photons in QED) are large compared to the time between subsequent interactions with the medium constituents, interference effects lead to a suppression of the radiation. In the QED case the time between two scattering processes is given by the mean free path of the jet. However, in QCD also the emitted gluon carries color charge and interacts (cf. Figure 3.17), leading to a modification of its formation time and a more complicated suppression procedure [GW94, BDPS95, BDM⁺97b].

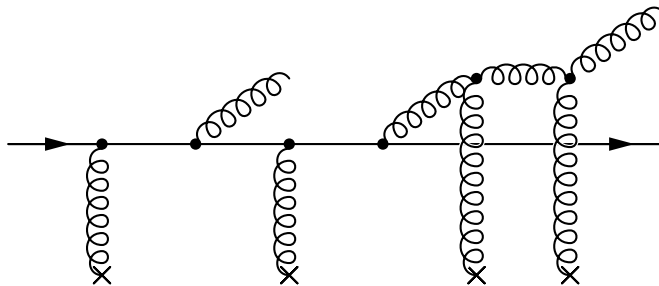


Figure 3.17.: Illustration of multiple medium-induced gluon radiation from a high-energy parton and rescatterings of the emitted gluons.

The implementation of such a coherence effect is rather involved in a semi-classical transport model like BAMPS. To keep things simple we allow only radiation processes that are independent from subsequent interactions and discard all interfering processes during the formation of the emitted gluon. In other words radiation is only allowed if the formation time of the emitted gluon is smaller than the time until the next interaction happens. We assume that this time is given by the mean free path of the jet, which is inspired by the QED case. However, to be more in line with the QCD case one should in principle compare to either the jet mean free path or the mean free path of the emitted gluon—whichever is smaller. Nevertheless, this is currently not implemented in BAMPS due to numerical limitations. One would have to carry out the full sampling of the final momenta for a potential scattering to determine the mean free path of the emitted gluon that is needed to calculate the actual cross section of the process and determine if the scattering actually happens in the first place.

The constraint that the formation time τ of the emitted gluon is smaller than the mean free path λ of the jet can be ensured by multiplying the integrand in Equation (3.108) with the step function

$$\Theta(\lambda - \tau) \quad (3.115)$$

before calculating the cross section. This makes the cross section—and thus also the rate—dependent on the mean free path, which in turn influences the mean free path. Hence, the actual mean free path of the jet must be determined in an iterative procedure,

$$\lambda = \lim_{i \rightarrow \infty} \lambda_i = \lim_{i \rightarrow \infty} \frac{v}{R_{22} + R_{23}(\lambda_{i-1}) + R_{32}(\lambda_{i-1})}, \quad (3.116)$$

where v is the velocity of the jet in the rest frame of the medium and R_n the rate for process n . The rates for $2 \leftrightarrow 3$ are influenced by the LPM effect and, therefore, depend on the mean free path itself. However, for heavy quarks we will neglect $3 \rightarrow 2$ processes since their rates are much smaller than the other processes.

It is important to consider the formation time and the mean free path in the same frame of reference. To compare to the formation time from Equation (3.114), which is given in the frame Σ_{trans} where the emitted gluon is entirely transverse, the mean free path, calculated in the rest frame of the medium Σ_{lab} , must be first boosted to the center-of-mass system Σ_{cms} and then to Σ_{trans} . This leads to an overall boost of

$$\gamma = \gamma_{\text{cms}} \gamma_{\text{trans}} (1 + \boldsymbol{\beta}_{\text{cms}} \cdot \boldsymbol{\beta}_{\text{trans}}) = \frac{\cosh y}{\sqrt{1 - \beta_{\text{cms}}^2}} (1 + \beta_{\text{cms}} |\tanh y| \cos \theta), \quad (3.117)$$

where the definition of $\gamma = 1/\sqrt{1-\beta^2}$ has been used. γ_{cms} denotes the boost from Σ_{lab} to Σ_{cms} and γ_{trans} the boost from Σ_{cms} to Σ_{trans} . The latter is specified by the gluon's rapidity in the center-of-mass system via $\gamma_{\text{trans}} = \cosh y$ and $\beta_{\text{trans}} = |\tanh y|$ since the boost is along the z axis in the center-of-mass frame. The angle between β_{cms} and β_{trans} is denoted with θ . The situation of the two boosts is illustrated in Figure 3.18.

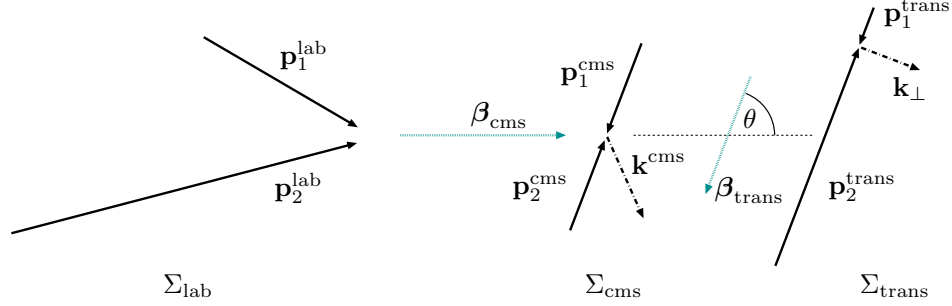


Figure 3.18.: Illustration of the reference frames involved when comparing the mean free path λ measured in the frame Σ_{lab} to the formation time of the emitted gluon τ_{trans} measured in the frame Σ_{trans} . $\mathbf{p}_i^{\text{lab}}$, $\mathbf{p}_i^{\text{cms}}$ and $\mathbf{p}_i^{\text{trans}}$ are the momenta of the incoming particles 1 and 2 in the respective frame. The thick dashed arrow (labeled \mathbf{k}) depicts the radiated gluon. See text for more details. In this example $|\mathbf{p}_2^{\text{lab}}| = 2|\mathbf{p}_1^{\text{lab}}|$ and $\angle(\mathbf{p}_1^{\text{lab}}, \mathbf{p}_2^{\text{lab}}) = 45^\circ$ are chosen, leading to $\beta_{\text{cms}} \approx 0.933$ and $\theta \approx 69^\circ$. The gluon in this example is emitted with $\cosh y = \gamma_{\text{trans}} = \sqrt{2}$. Taken from Ref. [Foc11].

Hence, the step function that is employed in BAMPS for the $2 \leftrightarrow 3$ processes reads

$$\Theta(\lambda - \tau) = \Theta\left(\frac{\lambda}{\gamma} - \tau_{\text{trans}}\right), \quad (3.118)$$

where τ_{trans} from Equation (3.114) is used.

Approximating the LPM effect with a cut-off introduced by the step function is rather crude and leads to stronger suppression compared to more realistic scenarios since the interference domain is not only suppressed but completely discarded. Recently, more sophisticated implementations of the LPM effect in Monte Carlo simulations have been introduced [ZSW09, ZSW11, CSBS11, CSM12] and it would be interesting to study the impact of those on the BAMPS simulations. We leave this as a future project.

3.2.8. Phase space constraints due to kinematics and the Landau-Pomeranchuk-Migdal effect

The allowed phase space of the emitted gluon is constrained by the LPM effect and by kinematics. The constraint from kinematics due to energy and momentum conservation has already been introduced in Equation (3.108) as the integral boundary for the rapidity y of the gluon and demands

$$k_{\perp} < \frac{\sqrt{s}(1-m^2)}{2 \cosh y}, \quad (3.119)$$

where we defined $m = M/\sqrt{s}$ as the heavy quark mass M scaled by the center-of-mass energy \sqrt{s} .

The implementation of the LPM effect allows only interactions if $\lambda/\gamma > \tau_{\text{trans}}$ through the Θ function from Equation (3.118). By employing Equation (3.37) this constraint can be rewritten in terms of y and k_{\perp} ,

$$k_{\perp} > \frac{\cosh y + A \sinh y}{B(1 + m^2 e^{2y})} \quad (3.120)$$

with $A = \beta' \cos \theta$ and $B = \lambda \sqrt{1 - \beta'^2}$. This relation only holds if the heavy quark is the incoming particle number 1 that flies in the positive z direction (cf. notation in Figure 3.9). If the heavy quark is particle 2, all the findings of this section must be substituted with $y \rightarrow -y$ due to the symmetry of the process.

For the numerical sampling of the outgoing momenta after a collision via the rejection method (see Appendix A.6), the maximum of the total phase space volume is needed. The maximum kinematically allowed rapidity range independent of k_{\perp} can be obtained by finding the intersection points of the functions

$$f_{\text{kin}}(y) = \frac{\sqrt{s}(1 - m^2)}{2 \cosh y} \quad \text{and} \quad f_{\text{lpm}}(y) = \frac{\cosh y + A \sinh y}{B(1 + m^2 e^{2y})}, \quad (3.121)$$

which stem from Equations (3.119) and (3.120), respectively. This results in

$$y_{\text{left/right}} = \frac{1}{2} \ln \left(\frac{b \mp \sqrt{\Delta}}{2a} \right) \quad (3.122)$$

with $a = 1 + A - 2B(m^2 - m^4)$, $b = 2[1 - B(1 - m^2)]$, $c = 1 - A$, and $\Delta = b^2 - 4ac$. If the argument of the square root Δ is negative, no solution exists since no phase space region fulfills both Equations (3.119) and (3.120). If the term $b \mp \sqrt{\Delta}/2a$ is negative, $y_{\text{left/right}}$ is $\mp \infty$, respectively.

The values for $y_{\text{left/right}}$ give the maximum rapidity range independent of k_{\perp} . In contrast, to evaluate the integral in Equation (3.108), the rapidity range for a given k_{\perp} must be known, which is smaller than (or equal to) $y_{\text{left/right}}$. For the kinematic constraint one has to solve $f_{\text{kin}}(y) = k_{\perp}$, which gives $y_{\text{max/min}}^{\text{kin}}(k_{\perp}) = \pm \text{arccosh} [(s - M^2)/2\sqrt{s}k_{\perp}]$. Determining the limits of the LPM constraint is more complex. The equation $f_{\text{lpm}}(y) = k_{\perp}$ can be reduced to a cubic equation that is solved in BAMPS numerically. The function $f_{\text{lpm}}(y)$ goes asymptotically to $0 (+\infty)$ for $y \rightarrow +\infty (-\infty)$. Therefore, the smallest solution of $f_{\text{lpm}}(y) = k_{\perp}$ is the lower limit $y_{\text{min}}^{\text{lpm}}(k_{\perp})$ and the upper limit has always to be $y_{\text{max}}^{\text{lpm}}(k_{\perp}) = \infty$ due to the asymptotic behavior. Finally, the allowed y range is then given by the more restricting constraint of both cases,

$$y_{\text{min}}(k_{\perp}) = \max \left(y_{\text{min}}^{\text{kin}}(k_{\perp}), y_{\text{min}}^{\text{lpm}}(k_{\perp}) \right) \quad \text{and} \quad y_{\text{max}}(k_{\perp}) = y_{\text{max}}^{\text{kin}}(k_{\perp}). \quad (3.123)$$

In Figure 3.19 the available phase space in the y - k_{\perp} -plane is illustrated. The drawn curves show the envelope functions $f_{\text{kin}}(y)$ and $f_{\text{lpm}}(y)$. The dashed line represents for comparison the LPM constraint for a massless quark. In this case the LPM effect serves as a lower cut-off in k_{\perp} . In contrast, the emission from a massive quark with very small k_{\perp} is allowed at very forward

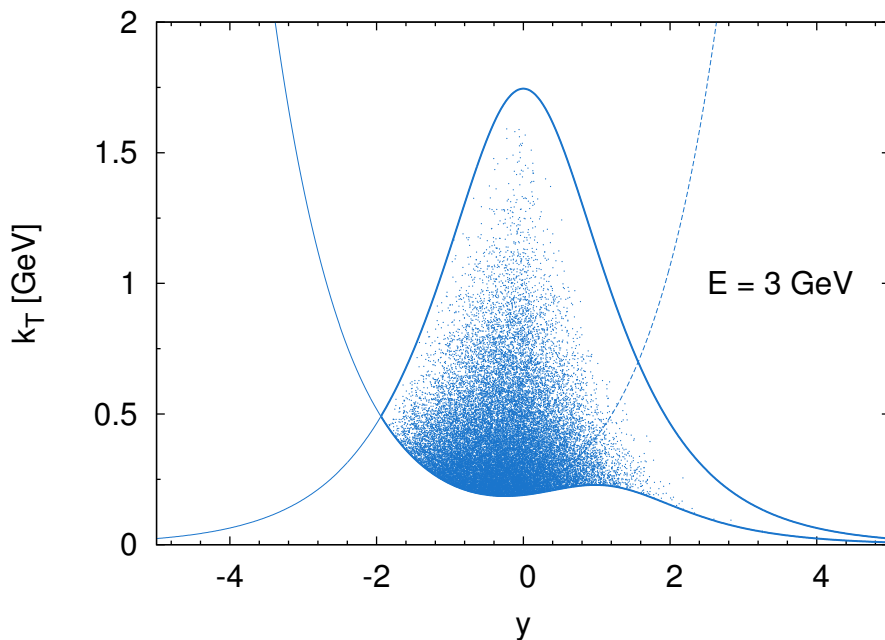


Figure 3.19.: Phase space sampling in the y - k_{\perp} -plane of the emitted gluon for a heavy quark with $E = 3$ GeV and mass $M = 1.3$ GeV. The heavy quark comes from the left and has a momentum of $p_1 = (E, 0, 0, \sqrt{E^2 - M^2})$. The medium particle is taken as $p_2 = (3T, 0, 0, -3T)$ with $T = 0.4$ GeV. The upper envelope curve is the constraint due to kinematics, $f_{\text{kin}}(y)$, while the lower line is the LPM constraint, $f_{\text{LPM}}(y)$. Allowed phase space is the area between these two curves. For comparison, the dashed line shows the LPM constraint for a massless quark. Each of the 100 000 dots represents one sampled phase space point from BAMPS. The mean free path is taken to be $\lambda = 1$ fm.

rapidity because of the mass dependence of the formation time, although the cross section in this region is very small due to the $(1 - \bar{x})$ factor and the $x^2 M^2$ term in the denominator of the matrix element from Equation (3.83) (dead cone effect). This interplay between the LPM and dead cone effect prevents a divergence of the cross section for small k_{\perp} in the case of heavy quark scatterings.

Each dot depicts a sampled phase space point from BAMPS for the given parameters. It can be nicely seen that all sampled phase space points obey the phase space constraints from Equations (3.119) and (3.120). The density of the points is a measure for the value of the matrix element in this phase space region. The density increases with smaller k_{\perp} and is largest around mid-rapidity. At positive rapidities the density is lower than at negative rapidities, which is due to the dead cone effect (see Section 3.2.4).

Figure 3.20 shows the phase space distribution for different heavy quark energies. The constraint from kinematics is always symmetric in rapidity and rises with larger heavy quark energy. In contrast, the LPM constraint is asymmetric in rapidity. For a small heavy quark energy it suppresses the backward region more than the forward direction. However, this changes for larger heavy quark energy. At $E = 50$ GeV backward rapidities are hardly

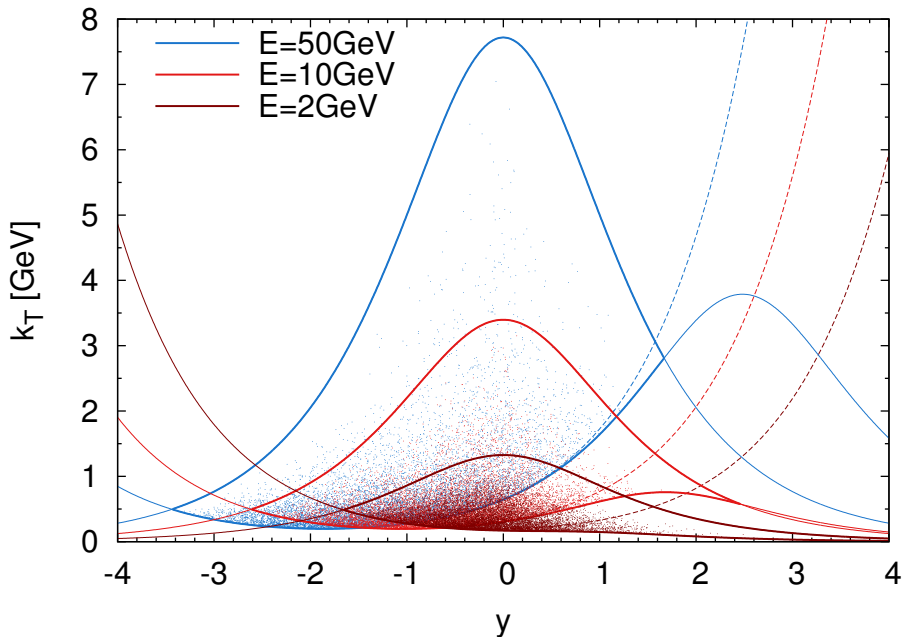


Figure 3.20.: As Figure 3.19 for different heavy quark energies E .

suppressed and the most suppression is in the forward region, creating basically a second dead cone due to the LPM effect. This overlays the standard heavy quark dead cone due to the matrix element and, thus, reduces its effect. Since such an LPM dead cone is also present for light particles (see dashed lines in Figure 3.20), it could be an explanation why the experimentally observed energy loss of light and heavy quarks is rather comparable. In other words, the dead cone due to the mass of the heavy quark is hidden behind the dead cone of the LPM effect. We will discuss this in more detail in Section 5.3. With increasing heavy quark energy the LPM constraint gets more and more independent of the heavy quark mass and resembles the dashed LPM curve for a massless particle. It would be interesting to study whether this effect is also present in a more sophisticated Monte Carlo implementation of the LPM effect, which is planned for the future.

The whole treatment of the LPM effect for heavy quarks is in line with the implementation for light partons [XG05, FXG10, Foc11] and reduces to the latter if the heavy quark mass M is set to zero.

3.2.9. Comparison of Gunion-Bertsch and exact cross sections

In this section we compare the original and improved GB matrix elements, see Equations (3.65) and (3.70), respectively, with the exact matrix elements for different processes [FUXG13]. For the sake of simplification, most comparisons are done for massless quarks, setting $M = 0$. However, at the end of this section we compare explicitly also the radiative heavy quark process $qQ \rightarrow qQg$.

Exact matrix elements

The exact matrix elements for the $2 \rightarrow 3$ processes involving light partons have been calculated in Refs. [BKDC⁺81, ES86]. For $qq' \rightarrow qq'g$ the result is relatively simple, [BKDC⁺81]

$$\begin{aligned}
 |\overline{\mathcal{M}}_{qq' \rightarrow qq'g}|^2 &= \frac{g^6}{8} [(s^2 + s'^2 + u^2 + u'^2) / tt'] [(p_1 k) (p_2 k) (p_3 k) (p_4 k)]^{-1} \\
 &\quad \times \{ C_1 [(u + u') (ss' + tt' - uu') + u(st + s't') + u'(st' + s't)] \\
 &\quad - C_2 [(s + s') (ss' - tt' - uu') + 2tt'(u + u') + 2uu'(t + t')] \} , \quad (3.124)
 \end{aligned}$$

with the constants $C_1 = (N^2 - 1)^2 / 4N^3$ and $C_2 = (N^2 - 1) / 4N^3$ where $N = 3$ is the number of colors. The MANDELSTAM variables for the $2 \rightarrow 3$ process are defined in Equation (A.6) in Appendix A.2. However, the expression for the matrix element has been simplified to such an extent that it is not obvious anymore how to identify the internal propagators, which are usually screened with a mass of the order of the DEBYE mass in thermal QCD.

The matrix element for $qg \rightarrow qgg$ is also given in Ref. [BKDC⁺81]. The expression for $gg \rightarrow ggg$ is considerably more complicated than the other two processes, but can still be expressed in a relatively compact form due to its symmetry [BKDC⁺81],

$$\begin{aligned}
 |\overline{\mathcal{M}}_{gg \rightarrow ggg}|^2 &= \frac{g^6}{2} [N^3 / (N^2 - 1)] [(12345) + (12354) + (12435) + (12453) + (12534) \\
 &\quad + (12543) + (13245) + (13254) + (13425) + (13524) + (14235) + (14325)] \\
 &\quad \times \left[\frac{[(p_1 p_2)^4 + (p_1 p_3)^4 + (p_1 p_4)^4 + (p_1 p_5)^4 + (p_2 p_3)^4]}{(p_1 p_2)(p_1 p_3)(p_1 p_4)(p_1 p_5)(p_2 p_3)(p_2 p_4)(p_2 p_5)(p_3 p_4)(p_3 p_5)(p_4 p_5)} \right. \\
 &\quad \left. + \frac{[(p_2 p_4)^4 + (p_2 p_5)^4 + (p_3 p_4)^4 + (p_3 p_5)^4 + (p_4 p_5)^4]}{(p_1 p_2)(p_1 p_3)(p_1 p_4)(p_1 p_5)(p_2 p_3)(p_2 p_4)(p_2 p_5)(p_3 p_4)(p_3 p_5)(p_4 p_5)} \right] \quad (3.125)
 \end{aligned}$$

with $(ijklm) = (p_i p_j)(p_j p_k)(p_k p_l)(p_l p_m)(p_m p_i)$ and p_5 being the momentum of the third outgoing gluon—in our notation $p_5 = k$. As for the other matrix elements, it is not a priori obvious how one would screen this matrix element. For the purpose of this work we introduce a cut-off prescription in the next section that regulates the divergencies when calculating the total cross section and allows for consistent comparisons to the GB result.

The exact matrix element for $qQ \rightarrow qQg$ is rather lengthy. It can be obtained from the process $q\bar{q} \rightarrow Q\bar{Q}g$, which has been calculated in Ref. [KPR80], by crossing the two anti-quarks. We checked numerically that it agrees with Equation (3.124) if the mass of the heavy quark is set to zero.

Numerical comparison

We have carried out extensive numerical comparisons between the exact matrix element and the matrix element calculated in the GB approximation (for both the original and improved GB matrix element) [FUXG13]. In order to obtain a picture as complete as possible we have investigated differential cross sections such as $d\sigma/dy$, $d\sigma/dx$, $d\sigma/dk_\perp dq_\perp$ in addition to the total cross section. All calculations take into account the full kinematics according to Equation (3.97) or (3.103), ensuring energy and momentum conservation.

Both the exact and GB matrix elements are divergent for infrared and collinear configurations. In thermal quantum field theory these divergencies can be cured by loop resummations of the propagator, which leads to an extra term with the self energy in the propagator. Phenomenologically, this self energy can be mimicked with a DEBYE mass m_D that modifies the propagator terms and makes them infrared-safe (cf. Section 3.1),⁶

$$\frac{1}{q_{\perp}^2} \rightarrow \frac{1}{q_{\perp}^2 + m_D^2} . \quad (3.126)$$

However, it is not straightforward to identify the propagator terms in the exact matrix elements due to their compact notation. Therefore, for all numerical calculations of total or differential cross sections from both the exact and the GB matrix elements we choose a simple cut-off procedure to cure the divergencies. The integrand is set to zero if the scalar product of any incoming or outgoing four-momenta is smaller than a cut-off Λ^2 , $p_i \cdot p_j < \Lambda^2$ with $i, j = 1 \dots 5$. Formally, this is expressed by multiplying the integrand in Equation (3.97) with

$$\prod_{i \neq j} \Theta(p_i \cdot p_j - \Lambda^2) , \quad (3.127)$$

where Λ^2 is chosen to be proportional to the DEBYE mass,

$$\Lambda^2 = \epsilon m_D^2 . \quad (3.128)$$

It is immediately obvious from Equation (3.125) that this prevents divergencies of the integrand. For propagator terms this scheme acts similar to the DEBYE screening, but the restrictions to the phase space potentially go beyond DEBYE screening only propagator terms. The resulting numerical values for the total or differential cross sections need thus not be the physically correct values and are, consequently, given in arbitrary units where necessary. Still, this cut-off prescription allows for consistent and well-defined comparisons between the GB approximation and the exact leading order matrix elements, which is the focus of this study. If not mentioned otherwise, we set $\epsilon = 0.001$ to reduce the screening effect as much as possible. In the last part of the section we will discuss the impact of different ϵ and compare this cut-off prescription to the standard DEBYE screening procedure for more physical scenarios.

The calculations in the remainder of the section are done for a temperature of $T = 400$ MeV. The coupling is set constant, $\alpha_s = 0.3$. If not stated otherwise, we use the average thermal value for massless particles for the squared center-of-mass energy, $s = 18T^2 \simeq 2.88 \text{ GeV}^2$, and determine Λ from the usual gluon DEBYE mass for BOLTZMANN statistics from Equation (3.18). For $n_f = 3$ at the given temperature and coupling, the DEBYE mass is $m_D^2 \simeq 0.73 \text{ GeV}^2$.

Figure 3.21 compares the rapidity spectrum of the emitted gluon as given by different approximations of the matrix element by depicting the differential cross section $d\sigma/dy$ for the process $qq' \rightarrow qq'g$. This process is the clearest to study since only one (the emitted) gluon is involved. Furthermore, it is the process that has been studied in the original GB publication, cf. Section 3.2.1. The plot nicely demonstrates the shortcomings of the standard GB matrix element, Equation (3.65), in the forward and backward region.

The exact matrix element, Equation (3.124), only peaks at mid-rapidity and does not have any sizeable contribution at forward or backward rapidity. The gluon emission into the forward

⁶For simplicity we omit here the κ prefactor for the screening mass that was introduced in Section 3.1 for heavy quarks to match hard-thermal-loop calculations.

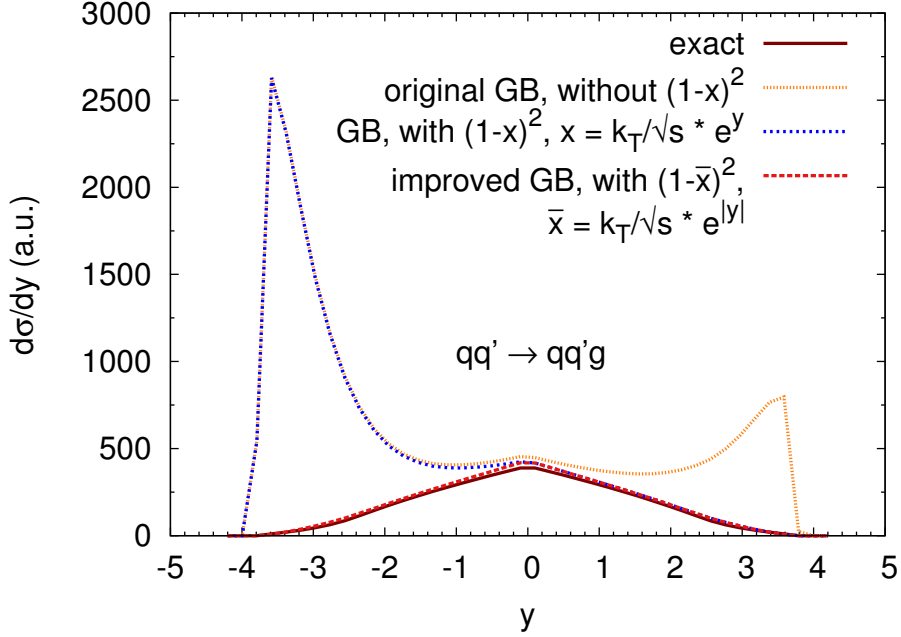


Figure 3.21.: Differential cross section $d\sigma/dy$ for the process $qq' \rightarrow qq'g$ calculated with the exact (Equation (3.124)), GB (3.65), GB with $(1-x)^2$ (3.64), and improved GB with $(1-\bar{x})^2$ (3.70) matrix element.

and backward region is suppressed since the phase space is occupied by the two quarks which just scatter off with a small angle. Furthermore, the cross section is symmetric in the rapidity of the emitted gluon as it must be for this process. The standard GB matrix element without the $(1-x)^2$ term (Equation (3.65)) is very similar at mid-rapidity, but has two additional large contributions at forward and backward rapidity. Thus, this matrix element would allow that, for instance, the gluon is emitted into the backward region and that one of the quarks is located at mid-rapidity. Although the matrix element itself is symmetric in y , the curve is not, since in our implementation the p_z of particle 3 is restricted to positive values to ensure that the particle only scatters off with a small angle.⁷

The matrix element with the GB approximation and the term $(1-x)^2$, Equation (3.64), has the same value at mid-rapidity as the other matrix elements since x is small in this region. However, at forward rapidity the $(1-x)^2$ factor leads to a significant reduction compared to the pure GB result. Here, the curve lies right on top of the curve from the exact matrix element. Nevertheless, as discussed in Section 3.2.1, the curve with $(1-x)^2$ is not symmetric anymore due to the asymmetric y dependence contained in x .

The last curve in Figure 3.21 shows the cross section of our proposed improvement of the GB matrix element, Equation (3.70). At forward and mid-rapidity it agrees with the previously mentioned curve. At backward rapidity the modified $(1-\bar{x})^2$ term removes the excess and

⁷This constraint is necessary if one transforms from MANDELSTAM t to q_{\perp}^2 for such a small angle favoring process since q_{\perp}^2 can be small for an outgoing particle that moves exactly in the other direction than it moved before the reaction. But in this case the scattering angle is not small anymore. Thus, t becomes large and $t \simeq -q_{\perp}^2$ does not hold anymore.

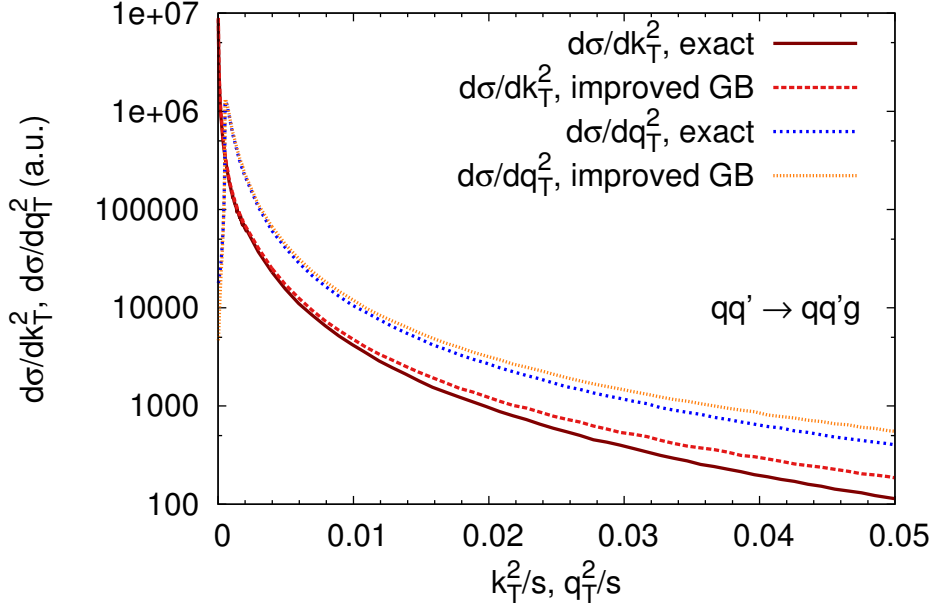


Figure 3.22.: Differential cross sections $d\sigma/dk_{\perp}^2$ and $d\sigma/dq_{\perp}^2$ as a function of k_{\perp}^2/s and q_{\perp}^2/s , respectively, for the process $qq' \rightarrow qq'g$ calculated with the exact (Equation (3.124)) and improved GB (Equation (3.70)) matrix element.

reconciles the shape of the GB approximation with the symmetry of the process. The overall agreement between the differential cross sections from the improved matrix element and from the exact result is remarkably good. The difference between the approximation and the exact result is on the level of a few percent over the entire y -range. This striking agreement is also visible in other differential cross sections such as $d\sigma/dq_{\perp}^2 dk_{\perp}^2$ and $d\sigma/dx$. In Figure 3.22 the transverse momentum distributions $d\sigma/dk_{\perp}^2$ and $d\sigma/dq_{\perp}^2$ are depicted. At small k_{\perp}^2 and q_{\perp}^2 , where the contribution to the cross section is largest, the deviation between the improved GB and the exact result is less than 5%. The asymmetry between the k_{\perp}^2 and q_{\perp}^2 distributions is due to an interplay between the cut-offs and the $(1-x)$ factor for the GB matrix element. The presence of this asymmetry in the exact curves is a further indicator that the $(1-x)$ factor is essential in describing the exact result.

Figure 3.21 was done for the simplest process, $qq' \rightarrow qq'g$, where only one gluon is involved. However, the findings also hold for $qg \rightarrow qgg$ and $gg \rightarrow ggg$. Since gluons are indistinguishable particles we plot the $d\sigma/dy$ for $qg \rightarrow qgg$ of all outgoing gluons in Figure 3.23. Since we choose the incoming gluon to be particle 1 and the process favors small angle scattering, there is a peak at forward rapidity in addition to the gluon peak at mid-rapidity. Again, the curve from the improved GB matrix element reproduces the curve from the exact one very well. This also holds for $gg \rightarrow ggg$, where one gets an additional gluon peak in the backward region that corresponds to the third outgoing gluon.

Since all differential cross sections for the improved GB and exact matrix elements agree nicely, it is not a surprise that this is also true for the total cross sections. In Figure 3.24 the ratios of the total cross sections $\sigma_{2 \rightarrow 3}$ for different processes from the improved GB to

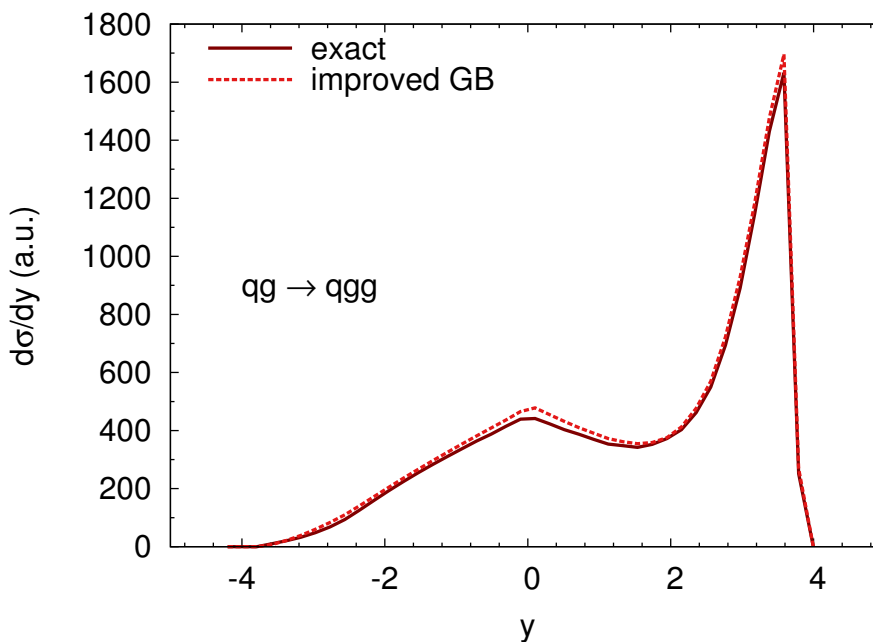


Figure 3.23.: Differential cross section $d\sigma/dy$ for all outgoing gluons for the process $qq \rightarrow qgg$ calculated with the exact and improved GB matrix element.

those obtained from the exact matrix elements are depicted as a function of the squared center-of-mass energy s . The exact and improved cross sections agree very well for all processes and virtually all s . Only at very small s , below the thermal average $s = 18T^2 \simeq 2.88 \text{ GeV}^2$, there is a slight discrepancy up to about 40%. The original GB cross section for $gg \rightarrow ggg$ as it was previously implemented in BAMPS is about a factor of three larger than the exact cross section. The same is true for the other processes (not plotted).

Figure 3.25 shows the dependence of the total cross section on the cut-off $\epsilon = \Lambda^2/m_D^2$. The improved GB matrix element works best for small ϵ , where the matrix elements are dominated by small k_\perp and q_\perp . At larger ϵ most of the phase space at small k_\perp and q_\perp is cut away and other phase space regions, in which the GB approximation is not as good, play the dominant role. Hence, the ratio rises. At $\epsilon \gtrsim 0.6$ (indicated by the gray band in the figure) the cut-off is so large that the entire available phase space is cut away and the GB as well as exact cross sections are zero. For such severe cut-offs the comparison scheme is not reliable anymore and the previously introduced DEBYE screening would be more realistic. However, the comparison to the exact matrix element with standard DEBYE screening is not done in this paper since the identification of the propagators in the compact results of the exact matrix elements is not known. Also note that Figure 3.25 is made for thermal $s = 18T^2$. For larger values of s the cut-off parameter ϵ , at which the ratio deviates from unity, becomes significantly larger. Thus, in summary, the improved GB approximation works best for larger s and/or smaller screening cut-offs ϵ .

Our improved GB result is, therefore, an especially good approximation for studying jet effects in heavy-ion collisions. For bulk dynamics, where the mean s is smaller, it is important how strong the screening effects actually are and if one is already in the regime of large ϵ where

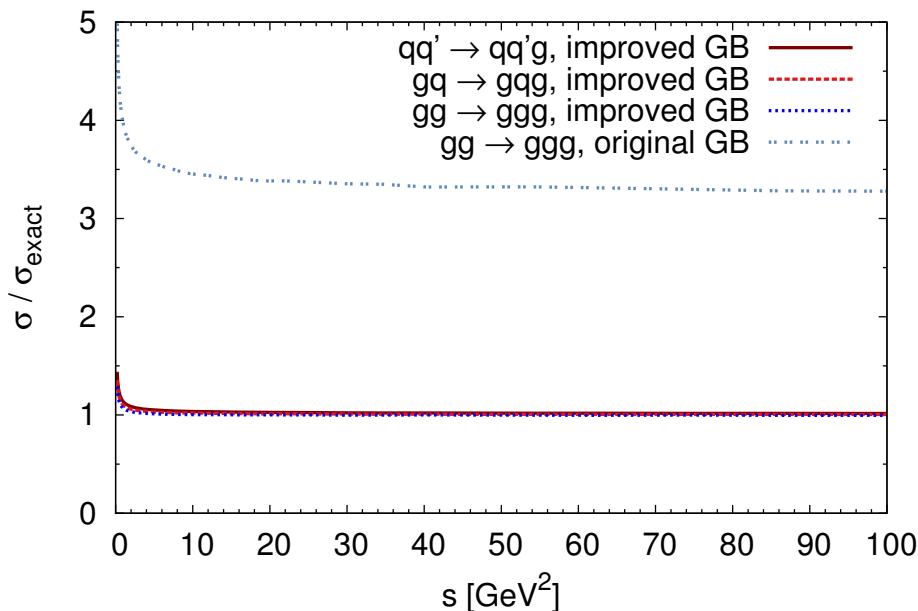


Figure 3.24.: Ratio of the total cross section $\sigma_{2 \rightarrow 3}$ of the improved GB matrix element (Equation (3.70)) to the exact one as a function of s for $qq' \rightarrow qq'g$, $gg \rightarrow ggg$, and $gg \rightarrow ggg$. In addition, the ratio of the original GB cross section (3.65) as it was previously implemented in BAMPS to the exact cross section is plotted for $gg \rightarrow ggg$.

the improved GB matrix element might deviate from the exact matrix element. To explore this in more detail, Figure 3.26 explicitly compares the improved GB differential cross section obtained from the cut-off procedure⁸ to the one obtained using the standard DEBYE screening according to Equation (3.126), which is for $qq' \rightarrow qq'g$ (cf. Equations (3.64) and (3.70))⁹

$$|\overline{\mathcal{M}}_{qq' \rightarrow qq'g}|^2 = \frac{32}{3} g^6 \frac{s^2}{(q_{\perp}^2 + m_D^2)^2} (1 - \bar{x})^2 \left[\frac{\mathbf{k}_{\perp}}{k_{\perp}^2 + m_D^2} + \frac{\mathbf{q}_{\perp} - \mathbf{k}_{\perp}}{(\mathbf{q}_{\perp} - \mathbf{k}_{\perp})^2 + m_D^2} \right]^2. \quad (3.129)$$

Now, to get a feeling for the quality of the improved GB approximation for DEBYE screened thermal processes one can either try to match the total cross sections σ or the differential cross sections $d\sigma/dy$ at mid-rapidity. Doing this, the necessary parameter ϵ can be determined to be of the order of $\epsilon \approx 0.4$ to 0.5 . As can be seen from Figure 3.25 the deviations between the improved GB and exact result in this ϵ region vary roughly between $\sigma/\sigma_{\text{exact}} \approx 4$ and $\sigma/\sigma_{\text{exact}} \approx 9$. However, Figure 3.26 also clearly demonstrates the distortion of the phase space due to extreme choices of the cut-off. Large rapidities are cut away entirely, while the standard DEBYE screening procedure leaves the whole phase space available. It is questionable whether

⁸Note that in contrast to the previous figures, the differential cross section in Figure 3.26 is not given in arbitrary units since we are now in a regime where the cross sections (especially with DEBYE screening) have a physical meaning.

⁹The implementation in BAMPS does not screen the $1/k_{\perp}^2$ term in the bracket since small k_{\perp} are regularized by the LPM effect [FXG10]. However, since the LPM effect is not employed in this study for the sake of simplicity, we regularize also this term with the DEBYE mass.

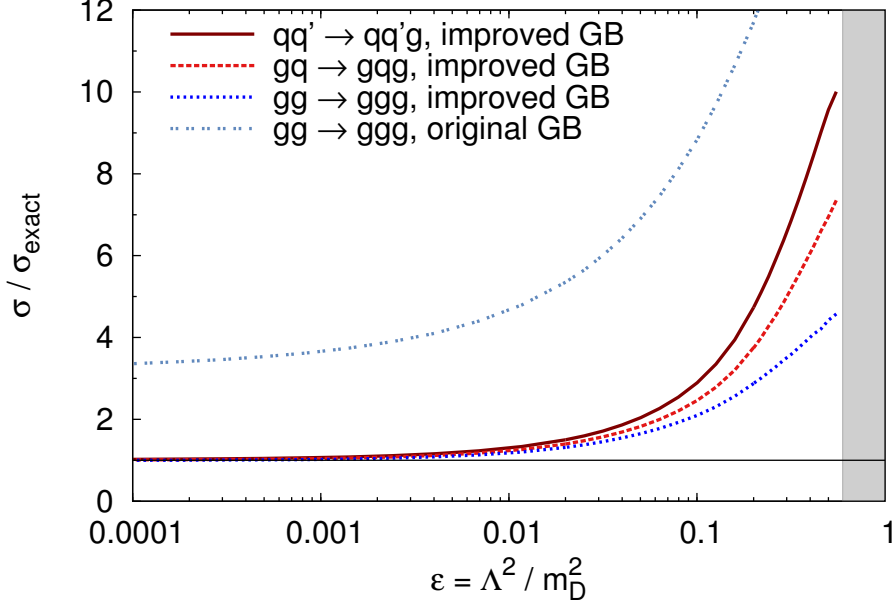


Figure 3.25.: Ratio of the total cross section σ of the improved GB matrix element to the exact result for $qq' \rightarrow qq'g$, $qq \rightarrow qgg$, and $gg \rightarrow ggg$ as a function of the screening cut-off ϵ from Equation (3.128). In addition, the ratio of the original GB cross section of $gg \rightarrow ggg$ as it was previously implemented in BAMPS to the exact is depicted.

the strong cuts in the cut-off procedure make physical sense. The comparison is thus a rather qualitative one and should be regarded as a first estimate of the quality of the (improved) GB approximation in the region of thermal processes with a standard DEBYE screening.

The factorization of the GB matrix element into an elastic $2 \rightarrow 2$ part and a radiation amplitude features an elastic amplitude that is in the small angle approximation and GB coordinates given by $|\overline{\mathcal{M}}_{2 \rightarrow 2}|^2 \propto 1/q_{\perp}^4$. If one, however, instead employs the exact binary matrix element for the t channel, which is

$$|\overline{\mathcal{M}}_{2 \rightarrow 2}|^2 \propto \frac{1}{t^2}, \quad (3.130)$$

the agreement between the exact and the improved GB result becomes much better at large ϵ , which is illustrated in Figure 3.27. The ratio is of the order of 1 over the entire ϵ range and the deviation is at most 50% for all processes. In contrast to the previous result with the approximated $2 \rightarrow 2$ matrix element (cf. Figure 3.25), the ratio for small ϵ is not 1 anymore but 0.9. This is probably due to the fact that different approximations are employed for the $2 \rightarrow 2$ and the radiative parts of the matrix element. However, since the numerical agreement is so good also in the region of thermal processes at larger ϵ , the combination of the improved GB approximation (3.70) for the radiation amplitude with the exact $2 \rightarrow 2$ part (3.130) is implemented in our transport model BAMPS.

Also for heavy quarks, the good agreement between the improved GB and exact results holds. Figure 3.28 compares the rapidity spectrum of the emitted gluon for the scattering of

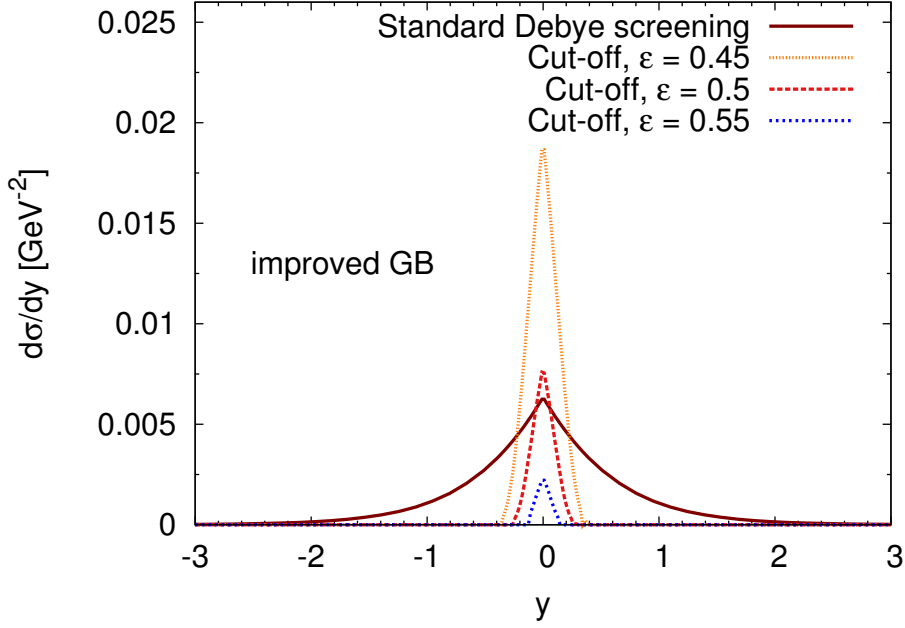


Figure 3.26.: Differential cross section $d\sigma/dy$ for the process $qq' \rightarrow qq'g$ calculated with the improved GB matrix element with the standard DEBYE screening and the cut-off procedure for different ϵ .

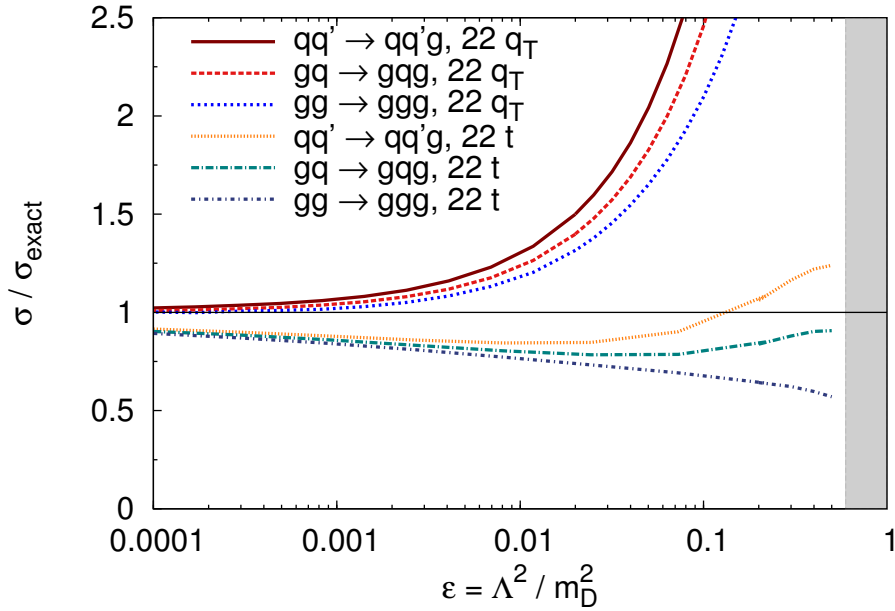


Figure 3.27.: As Figure 3.25 but, in addition, the improved GB cross section with the exact $2 \rightarrow 2$ gluon propagator ($22 t$) instead of the small angle approximation ($22 q_{\perp}$) is also shown.

a heavy quark with a light quark, $qQ \rightarrow qQg$. For a heavy quark mass of $M = 0 \text{ GeV}$, the process is in fact a scattering of two light quarks and, thus, symmetric. The exact curve is the same as in Figure 3.21. For the improved GB curve we employed the exact gluon propagator proportional to $1/t^2$ instead of the small angle approximation. Therefore, it deviates slightly from the curve in Figure 3.21. Furthermore, the gluon emission spectra for massive heavy quark scatterings are depicted for the charm and bottom masses. At forward rapidities—or small emission angles—the gluon emission spectrum is suppressed, which is a consequence of the dead cone effect (cf. Section 3.2.4). Independent of the heavy quark mass, the agreement between the improved GB and exact matrix element is remarkably good.

In Figure 3.29 the dependence of this agreement on the cut-off parameter ϵ is shown. Using the exact gluon propagator for the $2 \rightarrow 2$ part in the GB matrix element, the deviation for all ϵ is rather small for both light and heavy quarks. Note that the threshold, above which the whole phase space is cut away, is smaller for heavy quarks. Thus, these curves go back to zero for smaller ϵ compared to the light quark case where the gray box depicts the region with zero cross section.

Results with these improved GB cross sections are presented in Sections 5.3 and 6.2, where we show the radiative energy loss of light and heavy partons in a static medium and their suppression in ultra-relativistic heavy-ion collisions, respectively.

3.3. J/ψ dissociation and regeneration

In the medium, J/ψ can dissociate via the process $J/\psi + g \rightarrow c + \bar{c}$. The cross section of this interaction has been calculated in Ref. [Pes79, BP79] by expanding the matrix element as operator products and applying QCD sum rules. To this end, a coulombic-bound meson state with a large mass is considered with a soft, short-distance dominated perturbation from the gluon. The cross section is then given to leading order in the coupling α_s and leading order in $1/N_c^2$ (large N_c limit with N_c being the number of colors) as [Pes79, BP79]

$$\sigma_{J/\psi g \rightarrow c\bar{c}}(s) = \frac{2^{11}\pi}{3N_c^2} \frac{1}{\sqrt{M_c^3 \epsilon_{J/\psi}}} \frac{\left(\frac{w}{\epsilon_{J/\psi}} - 1\right)^{3/2}}{\left(\frac{w}{\epsilon_{J/\psi}}\right)^5}, \quad (3.131)$$

where $w = P_{J/\psi}^\mu P_{g\mu} / M_{J/\psi} = (s - M_{J/\psi}^2) / 2M_{J/\psi}$ is the gluon energy in the rest frame of the J/ψ and $\epsilon_{J/\psi} = 2M_D - M_{J/\psi}$ is the binding energy of the J/ψ . M_c , M_D , and $M_{J/\psi}$ denote the charm quark, D meson, and J/ψ mass, respectively. The kinematic prefactor $(M_c^3 \epsilon_{J/\psi})^{-1/2}$ is proportional to $\alpha_s a_0^2$ [AGGA02], where $a_0 = 16\pi/3g^2 M_c$ is the BOHR radius of the coulombic-bound $c\bar{c}$ system. This makes the leading order nature of Equation (3.131) for an interaction of a color dipole of size a_0 apparent [AGGA02]. The leading order result corresponds to a chromoelectric dipole interaction, while the (repulsive) octet potential—or, equivalently, the final state interaction—is neglected [BEGV11]. A rederivation of Equation (3.131) within the BETHE-SALPETER formalism can be found in Ref. [BAG11]. Recently, the BHANOT-PESKIN cross section was extended to finite temperatures in an effective field theory approach [BEGV11], resulting only in small modifications of the thermal width compared to the BHANOT-PESKIN formula.

The cross section of the back reaction, $c + \bar{c} \rightarrow J/\psi + g$, that is, the regeneration of J/ψ via charm and anti-charm annihilation, can be obtained from Equation (3.131) via detailed

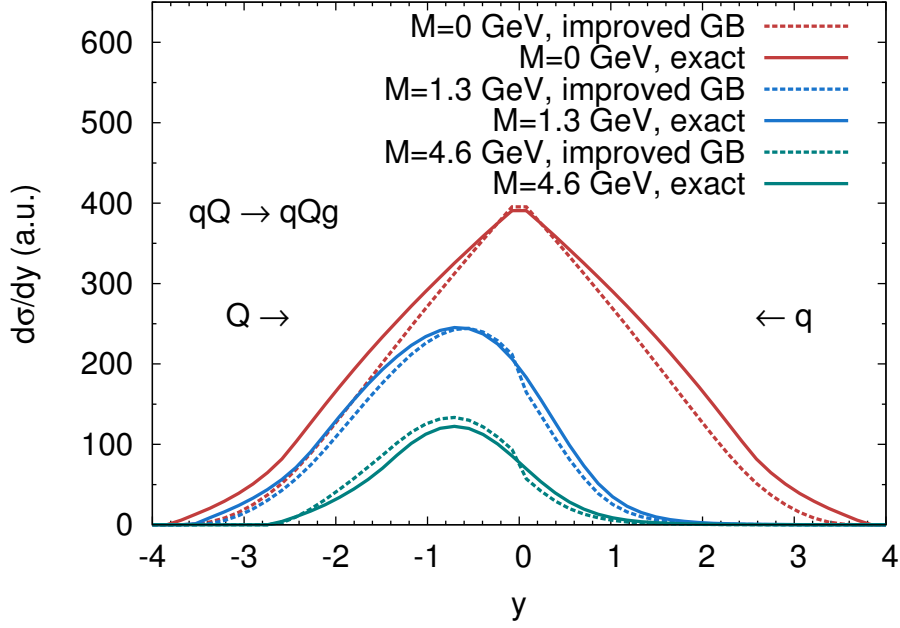


Figure 3.28.: Differential cross section $d\sigma/dy$ for $qQ \rightarrow qQg$ calculated with the exact [KPR80] and improved GB (3.70) matrix element for different heavy quark masses M . For the $2 \rightarrow 2$ part of the GB matrix element the exact expression for the gluon propagator is used, which is proportional to $1/t^2$ instead of $1/q_{\perp}^4$. The calculations are done for $s - M^2 = 18T^2$.

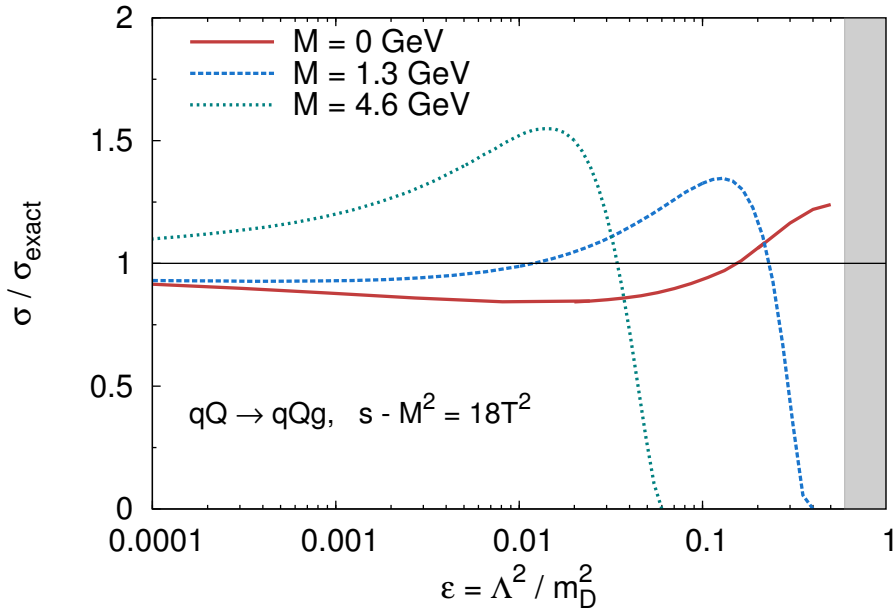


Figure 3.29.: As Figures 3.25 or 3.27 with the exact $2 \rightarrow 2$ gluon propagator (22 t) for different heavy quark masses M .

balance (cf. Appendix A.4),

$$\sigma_{c\bar{c} \rightarrow J/\psi g}(s) = \frac{4}{3} \frac{(s - M_{J/\psi}^2)^2}{s(s - 4M_c^2)} \sigma_{J/\psi g \rightarrow c\bar{c}}(s) . \quad (3.132)$$

In Chapter 7 we employ these cross sections to study the dissociation and regeneration of J/ψ in heavy-ion collisions.

4. Parton cascade BAMPS

We know very little, and yet it is astonishing that we know so much, and still more astonishing that so little knowledge can give us so much power.

ABC of Relativity
BERTRAND RUSSELL

In the following we outline some details of the partonic transport model BAMPS with a focus on the treatment on heavy flavor particles. In particular, initial distributions of open heavy flavor (Section 4.3) and J/ψ (Section 4.4) are highlighted, but also the initial conditions of light partons are addressed in Section 4.5. Furthermore, in Section 4.6 we give a brief overview of BAMPS results not associated with heavy flavor.

4.1. The framework

The partonic transport model BAMPS [XG05, XG07], which stands for *Boltzmann Approach to MultiParton Scatterings*, simulates the full 3 + 1 dimensional space-time evolution of the QGP in heavy-ion collisions by solving the BOLTZMANN equation [Rei76, Hau05, Sch06],

$$\left(\frac{\partial}{\partial t} + \frac{\mathbf{p}}{E} \frac{\partial}{\partial \mathbf{r}} \right) f_i(\mathbf{r}, \mathbf{p}, t) = \mathcal{C}_i^{2 \rightarrow 2} + \mathcal{C}_i^{2 \leftrightarrow 3} + \dots, \quad (4.1)$$

dynamically for on-shell partons with a stochastic transport algorithm and pQCD interactions. The left hand side describes the dynamics and evolution of the one-particle distribution function $f_i(\mathbf{r}, \mathbf{p}, t)$ of species $i = g, q, Q, J/\psi$. If the right hand side were zero, no collisions would take place and the solution of the BOLTZMANN equation would be just freely streaming particles. Thus, the interactions between the particles are described by the collision terms \mathcal{C}_i . For instance, for $2 \rightarrow 2$ processes it is given by [XG05]

$$\begin{aligned} \mathcal{C}_i^{2 \rightarrow 2} = & \sum_{j,k,l} \frac{1}{2E_i} \frac{1}{\nu_{ij}} \int \frac{d^3 p_j}{(2\pi)^3 2E_j} \frac{d^3 p_k}{(2\pi)^3 2E_k} \frac{d^3 p_l}{(2\pi)^3 2E_l} f_k f_l |\overline{\mathcal{M}}_{kl \rightarrow ij}|^2 \\ & \times (2\pi)^4 \delta^{(4)}(p_k + p_l - p_i - p_j) \\ & - \sum_{j,k,l} \frac{1}{2E_i} \frac{1}{\nu_{kl}} \int \frac{d^3 p_j}{(2\pi)^3 2E_j} \frac{d^3 p_k}{(2\pi)^3 2E_k} \frac{d^3 p_l}{(2\pi)^3 2E_l} f_i f_j |\overline{\mathcal{M}}_{ij \rightarrow kl}|^2 \\ & \times (2\pi)^4 \delta^{(4)}(p_i + p_j - p_k - p_l), \quad (4.2) \end{aligned}$$

where i denotes the considered species from the BOLTZMANN equation (4.1) and j, k , and l each stand for one of the implemented species $g, q, Q, J/\psi$. If k and l are identical particles, it is $\nu_{kl} = 2$, otherwise $\nu_{kl} = 1$.

Within the stochastic method, the probability for a collision of two particles during a time step Δt in a volume element ΔV can be obtained from these collision integrals [XG05],

$$P_{2 \rightarrow n} = v_{\text{rel}} \frac{\sigma_{2 \rightarrow n}}{N_{\text{test}}} \frac{\Delta t}{\Delta V}, \quad (4.3)$$

where v_{rel} stands for the relative velocity (see Equation (3.2)), and $\sigma_{2 \rightarrow n}$ for the two body cross sections.

To enhance statistics the test particle method is used. That is, a real particle is substituted by N_{test} virtual particles. This implies that the particle density scales like $n \rightarrow n N_{\text{test}}$. To keep the physical mean free path for each particle the same, the cross section has to be scaled like $\sigma \rightarrow \sigma / N_{\text{test}}$, which is the reason why this factor is present in Equation (4.3).

The following binary processes are implemented in BAMPS in the light and heavy flavor sector:

light flavor	heavy flavor	
$g g \leftrightarrow q \bar{q}$	$g g \leftrightarrow Q \bar{Q}$	
$q \bar{q} \rightarrow q' \bar{q}'$	$q \bar{q} \leftrightarrow Q \bar{Q}$	
$g q \rightarrow g q$	$g Q \rightarrow g Q$	
$q q' \rightarrow q q'$	$q Q \rightarrow q Q$	
$g g \rightarrow g g$	$J/\psi g \leftrightarrow c \bar{c}$	
$q q \rightarrow q q$		
$q \bar{q} \rightarrow q \bar{q}$		

(4.4)

The light parton cross sections are discussed in Section A.3 for both a fixed and running coupling. The heavy quark cross sections are given in Section 3.1 and the J/ψ cross section in Section 3.3. Details on the heavy quark production cross sections can be found in Refs. [UFXG10a, Uph09]. Elastic heavy quark processes among each other are neglected since the number of produced heavy quarks in heavy-ion collisions is small.

In addition to the binary collisions, BAMPS incorporates also the following $2 \leftrightarrow 3$ scatterings:

light flavor	heavy flavor	
$g q \leftrightarrow g q g$	$g Q \rightarrow g Q g$	
$q q' \leftrightarrow q q' g$	$q Q \rightarrow q Q g$	
$g g \leftrightarrow g g g$		
$q \bar{q} \leftrightarrow q \bar{q} g$		
$q q \leftrightarrow q q g$		

(4.5)

The cross sections for these processes are implemented in the GUNION-BERTSCH approximation, which has been explicitly calculated in Section 3.2.1 for heavy quarks. The light parton results can be obtained by setting the heavy quark mass to zero. All processes that are dominated by the s channel have been neglected since their cross section is much smaller and the GUNION-BERTSCH cross section is only calculated for the t channel. Details on the implementation of the light parton $3 \rightarrow 2$ processes can be found in Ref. [XG05, Foc11]. For heavy quarks, $3 \rightarrow 2$ processes are not implemented since their cross section is rather small and does not have a significant impact on the heavy quark energy loss.

The initial particle distributions can be obtained, for instance, from event generators or other initial models for the momentum space and geometric considerations of the collision overlap region for the particle positions. But also other initial configurations and geometries such as a thermal static medium are possible for more theoretical studies. BAMPS divides then the system into small cells of volume ΔV such that the mean free paths of the particles are larger than the cell size to prevent acausal behavior. In each cell, all particles can scatter with each other, no matter where exactly they are in the cell. The probability of an interaction is given by Equation (4.3). Of course, it must always be smaller than one, which is ensured by reasonable choices for Δt and ΔV . In one considered time step, BAMPS goes through all cells and carries out the interactions by comparing the probability for a process to a random number between zero and one. If the random number is smaller than the probability, a scattering takes place and the momenta of the outgoing particles are determined according to the differential cross section, e.g., $d\sigma/dt$ for binary processes. If it is larger, the particles do not scatter. After the collisions took place, all particles are propagated to the next time step. If the energy density in a cell falls below a threshold of $\epsilon_c = 0.6 \text{ GeV}/\text{fm}^3$, a phase transition to a hadron gas should occur and the partons should hadronize. However, since hadronization of the bulk medium has not been implemented in BAMPS yet, the particles just do not interact anymore.¹ Algorithm 1 illustrates the procedure of a BAMPS simulation.

Algorithm 1: Schematic view of the stochastic collision algorithm used in BAMPS.
Taken from Ref. [Foc11].

```

t = 0
while t < tfinal do
  foreach cell  $\Delta V$  do
    foreach particle pair (triplet) in the current cell do
      Compute collision probability  $P$ 
      Generate random number  $x \in [0, 1)$ 
      if  $x < P$  then // collision takes place
        Sample new momenta of outgoing particles
        Assign new momenta to outgoing particles
    t = t +  $\Delta t$ 
  Propagate particles to time t

```

In Figure 4.1 the evolution of the particles is shown for a BAMPS simulation of a heavy-ion collision at the LHC. The beam axis runs horizontally. Each dot depicts a single particle. The color is chosen according to its rapidity, where blue means small and yellow large. The number of test particles is $N_{\text{test}} = 7$. Consequently, there are seven times more particles than in reality. The pictures are taken from a movie [Uph12] that has been produced with *ParaView*², an open source application for visualizing data. A tool to transfer heavy-ion data into a suitable input format for ParaView was provided by XUNLEI WU (Renci³) and STEFFEN BASS (Duke

¹Heavy quarks, however, are fragmented to heavy mesons to compare to data (see below).

²<http://www.paraview.org>

³*Renaissance Computing Institute*, founded by Duke University, North Carolina State University, and University of North Carolina.

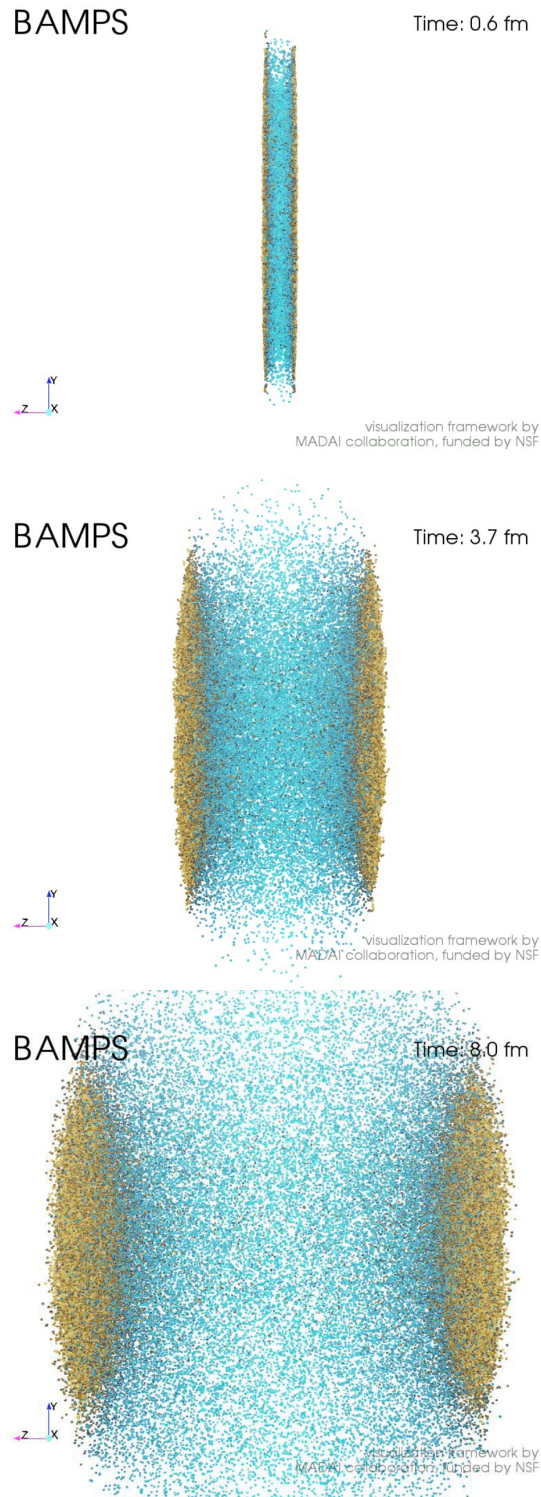


Figure 4.1.: Screenshots from a movie picturing the evolution of a central heavy-ion collision at $\sqrt{s} = 2.76$ TeV in a BAMPS simulation. The movie can be found in Ref. [Uph12].

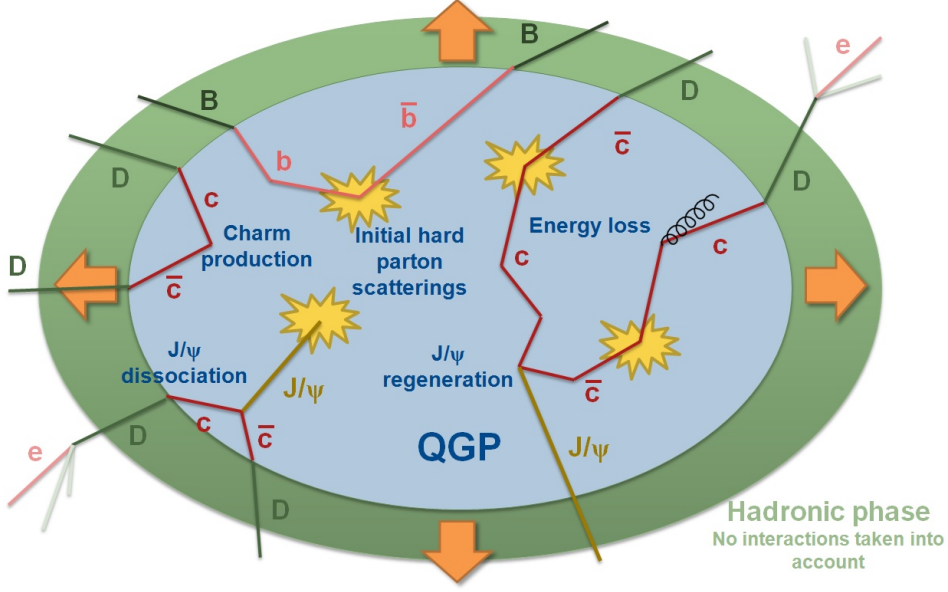


Figure 4.2.: Sketch of heavy flavor in BAMPS.

University) from a project of the MADAI collaboration⁴.

Figure 4.2 displays a sketch of heavy flavor in BAMPS. Heavy quarks are primarily produced in initial hard parton scatterings. To have a proper initial input we employ the next-to-leading order (NLO) event generator MC@NLO to sample the initial heavy quark momenta—the details are given in Section 4.3. Since MC@NLO focuses only on heavy quarks, PYTHIA [SMS06, SMS08] is used for the light parton initial production, which is outlined in Section 4.5. The initial positions of the particles are sampled according to the geometry of the overlap region [XG05]. After their production, heavy quarks traverse the medium, lose energy, and participate in the collective flow. During the medium evolution, additional heavy quark production can take place. Furthermore, unrelated charm and anti-charm quarks can bound together and regenerate a J/ψ . Also the complimentary interaction of J/ψ melting in the medium or dissociation due to an interaction with a gluon can occur (see Section 3.3).

After the energy density in the surrounding of a heavy quark in BAMPS has dropped below $\epsilon_c = 0.6 \text{ GeV}/\text{fm}^3$ it is fragmented to a D or B meson. The model we use for the hadronization process is PETERSON fragmentation. The PETERSON fragmentation function of a heavy quark to a heavy meson H is given by [PSSZ83]

$$D_{H/Q}(z) = \frac{N}{z \left(1 - \frac{1}{z} - \frac{\epsilon_Q}{1-z}\right)^2}. \quad (4.6)$$

N is a normalization constant, $z = |\mathbf{p}_H|/|\mathbf{p}_Q|$ the ratio of the meson and quark momenta, and $\epsilon_Q = 0.05$ (0.005) for charm (bottom) quarks, which are the default values in PYTHIA [SMS06] and in agreement with leading log fits to heavy quark production data [NO00, ZEUS03]. In Figure 4.3 the PETERSON fragmentation function is depicted for charm and bottom quarks. Since the average z in both distributions is relatively large, D and B mesons carry

⁴funded by the NSF under grant # NSF-PHY-09-41373

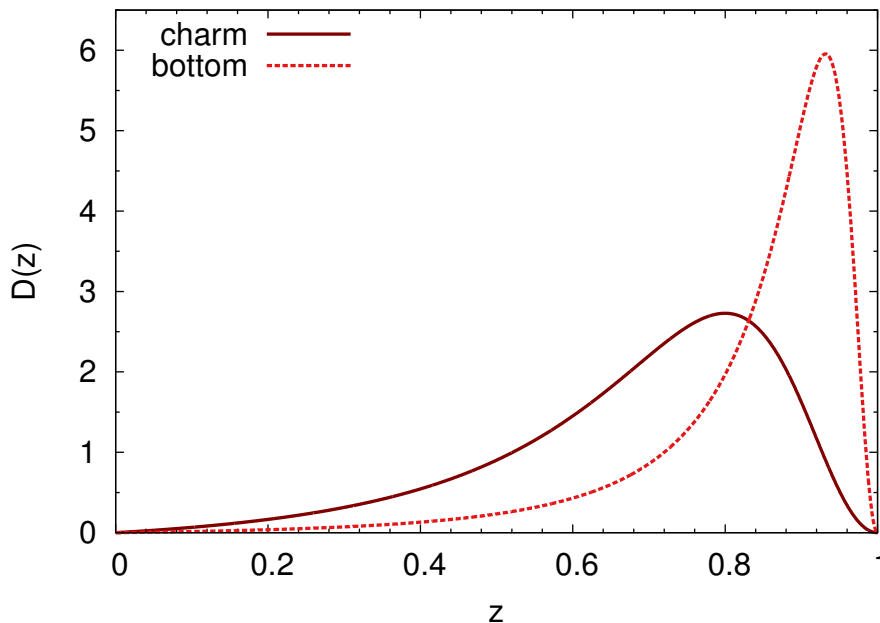


Figure 4.3.: PETERSON fragmentation function as a function of $z = |\mathbf{p}_H|/|\mathbf{p}_Q|$ with $\epsilon_Q = 0.05$ (0.005) for charm (bottom) quarks.

most of the momenta of their mother quark, as one would expect for such a heavy particle. Some models even assume that heavy mesons have still the same momenta as heavy quarks before hadronization, which is often named *parton hadron duality* and corresponds to a delta function $\delta(z - 1)$ for $D_{H/Q}(z)$. PETERSON fragmentation, however, is only applicable at large transverse momenta of the particles. At smaller p_T one expects that other hadronization models like coalescence become more dominant.

The produced D mesons can then directly be compared to the experimental data. To yield non-prompt J/ψ , that is, a J/ψ stemming from a B meson, we carry out the decay of B mesons with PYTHIA 8.1 [SMS06, SMS08] by switching on the relevant decay channels. PYTHIA is also used to perform the decay of D and B mesons to electrons and muons, which can then also be compared to experimental data. In these decays, heavy flavor electrons—or muons—carry approximately half of the transverse momentum of the parent meson if one considers a realistic meson p_T spectrum from p+p events, as is shown in the left panel of Figure 4.4.

The direction of a heavy flavor electron points in the same direction as its parent heavy flavor meson if the transverse momentum of the electron is not too small. From the right panel of Figure 4.4 it can be concluded that electrons from D (B) mesons have the same direction for $p_T \gtrsim 1$ GeV (4 GeV). Hence, they are a good probe to study open heavy flavor if the mesons themselves are not accessible.

Since charm and bottom quarks are very rare probes (there are about four heavy quark pairs at mid-rapidity in a central Au+Au collision at RHIC compared to about 800 gluons [UFXG10a]), one needs to simulate several million events to yield sufficient statistics to obtain their spectra and elliptic flow. However, the most time consuming part of these event simulations is the computation of the interactions among the sizeable number of gluons (and

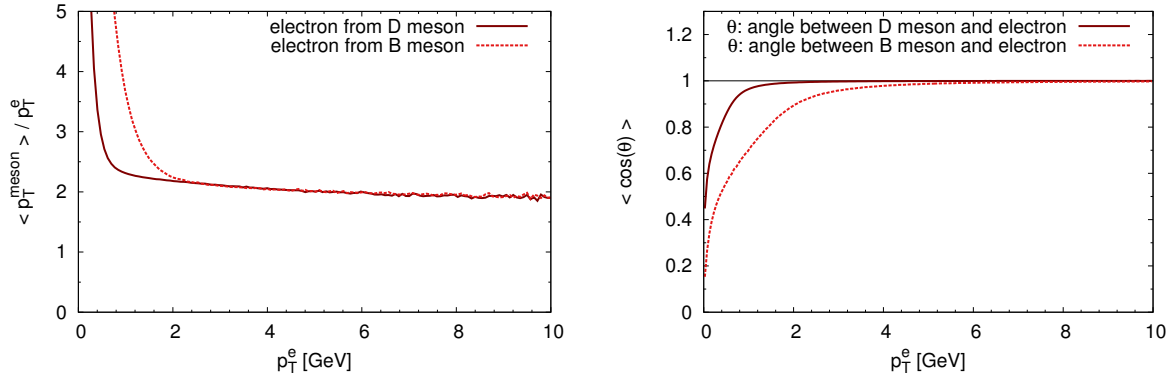


Figure 4.4.: Left: Ratio of mean parent heavy meson transverse momentum p_T^{meson} and daughter electron transverse momentum p_T^e as a function of the latter. Right: Average cosine of the angle between the heavy flavor meson and electron $\langle \cos \theta \rangle$. Both distributions are obtained from MC@NLO simulations of heavy quark production in p+p events at $\sqrt{s} = 2.76$ TeV, consecutive PETERSON fragmentation to heavy mesons, and the decay to heavy flavor electrons performed with PYTHIA.

light quarks), for which we do not need as much statistics. Therefore, we generate a smaller sample of pure light partonic events and use them several times as a background medium, in which heavy quarks generated with MC@NLO are placed. This treatment is in perfect accordance with the conventional BAMPS model. The only difference to full simulations is the neglect of medium modifications induced by the heavy quarks, which is a very good approximation given the small number of heavy quarks in a heavy-ion collision.

4.2. Details of the numerical implementation of the cross sections

To calculate the probabilities according to Equation (4.3) for $2 \rightarrow 2$ and $2 \rightarrow 3$ processes the total cross sections are needed. Due to the complexity of the matrix elements and especially when employing a running coupling, it is necessary to perform the integration for the total cross sections numerically. For this, the VEGAS routines [Lep78, PTVF07] are used. However, an online integration for the cross sections of all possible scattering pairs is rather time consuming. Therefore, the integration has been done only once and tabularized as a function of the needed parameters. In the BAMPS simulations the value for the cross section of each scattering pair is then interpolated from these tables.

For $2 \rightarrow 2$ processes (see Section 3.1 for heavy quarks and Section A.3 for light partons), the total cross sections are usually dependent on the squared center-of-mass energy s and the DEBYE mass m_D^2 , for some processes also on the quark DEBYE mass m_q^2 . For $2 \rightarrow 3$ processes (see Section 3.2), there are more parameters due to the LPM effect. The following choice of parameters is implemented in BAMPS (see Section 3.2.7 for the definitions): the DEBYE mass scaled by the squared center-of-mass energy m_D^2/s , the scaled mean free path $\lambda\sqrt{s}$, the boost γ , the angle $\cos \theta$, and the squared center-of-mass energy s (the latter is only necessary if a running coupling or a heavy quark is considered since both introduce an additional scale that breaks the scale invariance of the matrix element with respect to s).

The momenta of the outgoing particles are sampled according to differential cross sections. For binary scatterings, t is sampled from $d\sigma/dt$, see Equation (3.5), with the METROPOLIS algorithm (cf. Appendix A.6). Knowing t and the azimuthal angle, which is sampled uniformly, determines all the outgoing momenta. The sampling of q_\perp , k_\perp , y , and ϕ for $2 \rightarrow 3$ scatterings is done with the rejection method (see Appendix A.6) according to

$$\frac{d\sigma_{23}}{dq_\perp^2 dk_\perp^2 dy d\phi} = \frac{1}{128 \pi^4} \frac{1}{\nu} \frac{1}{2E_1} \frac{1}{2E_2} \frac{1}{v_{\text{rel}}} |\overline{\mathcal{M}}_{2 \rightarrow 3}|^2 \sum \left(\left. \frac{\partial F}{\partial y_3} \right|_{F=0} \right)^{-1}, \quad (4.7)$$

which is obtained from Equation (3.103). All the kinematics of the three outgoing particles can be determined from these four variables and an additional azimuthal angle that is uniformly distributed.

4.3. Initial heavy quark distribution—MC@NLO

The initial heavy quarks for BAMPS simulations of heavy-ion collisions are sampled with the Monte Carlo event generator for next-to-leading order (NLO) calculations MC@NLO [FW02, FNW03]. This framework is linked to the *Les Houches Accord Parton Density Function* (LHAPDF) program [WBG05], which conveniently allows switching between different parton distribution function parameterizations such as CTEQ [P⁺02, KLOT04], MRST [MRST02, MRST05], GRV [GRV98], and many more. For the results in this section we employ CTEQ6m, which is suitable for NLO matrix elements. To compare the initial distributions to the experimental data from p+p collisions, the heavy quarks are fragmented to D and B mesons, which subsequently decay into heavy flavor electrons.

Figure 4.5 compares the measured heavy flavor electrons in p+p collisions at RHIC to the initial distributions obtained with MC@NLO. The factorization and renormalization scales, μ_F and μ_R , respectively, are in principle arbitrary when considering all orders of the cross section. However, for the leading order cross section uncertainties due to neglecting higher order terms can be reduced if the two scales are of the order of the relevant scale of the process,

$$\sqrt{p_T^2 + M^2}, \quad (4.8)$$

p_T being the transverse momentum and M the mass of the produced heavy quarks. The exact value of the scale is fixed by giving a good agreement with the experimental data, which results in

$$\mu_F = \mu_R = 0.65 \sqrt{p_T^2 + M_c^2} \quad (4.9)$$

for charm ($M_c = 1.3 \text{ GeV}$) and

$$\mu_F = \mu_R = 0.4 \sqrt{p_T^2 + M_b^2} \quad (4.10)$$

for bottom quarks ($M_b = 4.6 \text{ GeV}$). The agreement of the fit and the data is very good, as can be seen in Figure 4.5.

As a note, large theoretical uncertainties in the heavy quark distributions exist due to uncertainties in the parton distribution functions, renormalization and factorization scales, and

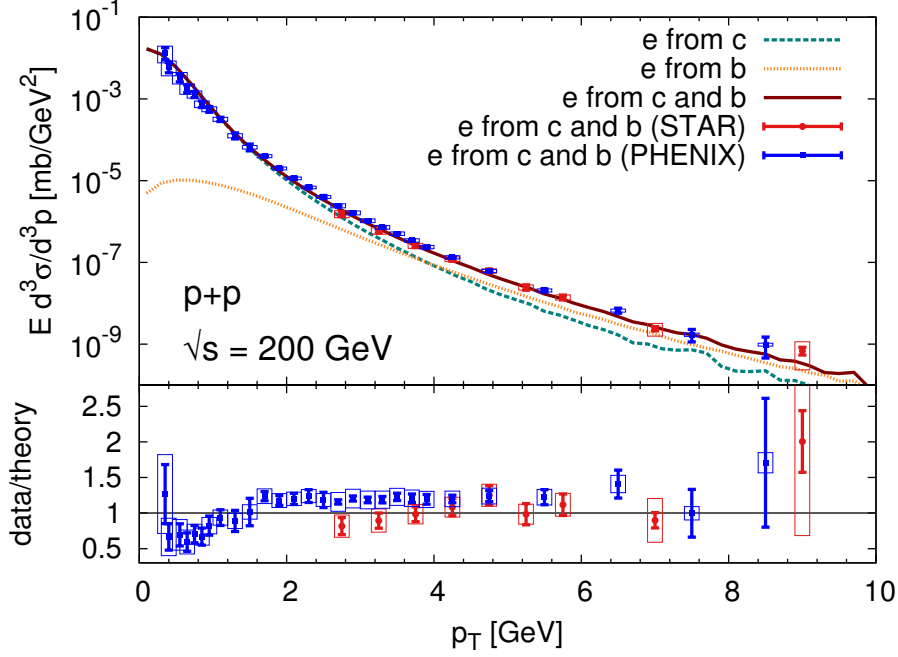


Figure 4.5.: Differential invariant cross section of heavy flavor electrons at mid-rapidity $|y| < 0.35$ as a function of transverse momentum for p+p collisions with $\sqrt{s} = 200$ GeV simulated with MC@NLO. For comparison experimental data [PHENIX11b, STAR11a] is also shown.

heavy quark masses [UFXG10a, CNV05]. In particular, the relative contributions of charm and bottom quarks to the electron spectrum have not been fully settled yet, although there are first measurements to distinguish both [STAR10, ALICE13d].

In contrast, at the LHC charm and bottom can be separated by measuring D mesons and non-prompt J/ψ from B mesons directly. Therefore, it is even more important to have the correct reference for the initial heavy quark distribution. As for RHIC we employ MC@NLO with a factorization and renormalization scale of

$$\mu_F = \mu_R = 1 \sqrt{p_T^2 + M_c^2} \quad (4.11)$$

for charm and

$$\mu_F = \mu_R = 0.4 \sqrt{p_T^2 + M_b^2} \quad (4.12)$$

for bottom quarks, which have been fitted to experimental data. The scales for charm differ slightly from those used for RHIC simulations, reflecting the uncertainties of the underlying theoretical calculations. It should be emphasized that fitting these scales to data does not provide any additional physical insight, but is necessary to obtain a proper initial heavy quark distribution, which is crucial when comparing to experimental data of the nuclear modification factor (cf. Chapter 6).

In Figure 4.6 the invariant differential cross sections of D mesons and heavy flavor electrons as well as muons are compared to experimental data from ALICE at $\sqrt{s} = 7$ TeV. The D mesons and heavy flavor electrons at mid-rapidity are well described by MC@NLO. At

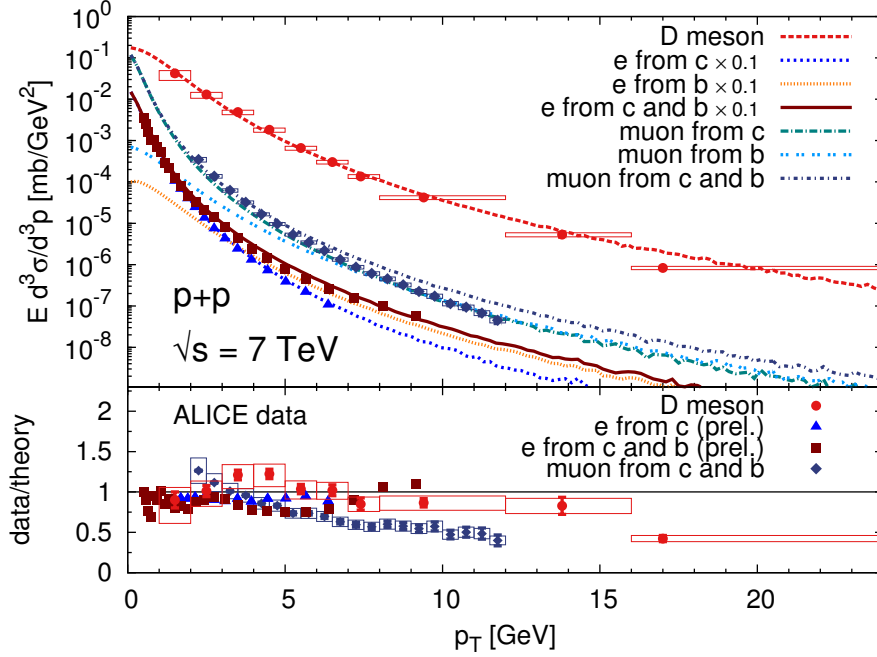


Figure 4.6.: Differential invariant cross section of D mesons with $|y| < 0.5$ and heavy flavor electrons with $|y| < 0.8$ at mid-rapidity as well as muons at forward rapidity $2.5 < y < 4$ as a function of the transverse momentum for p+p collisions with $\sqrt{s} = 7$ TeV simulated with MC@NLO. For comparison experimental data [ALICE12b, ALICE11e, ALICE12c] with the same kinematic cuts is also shown. In the upper plot the electron curves and the corresponding data points have been scaled with the factor 0.1 to distinguish them from the muon curves. Since the data for electrons is preliminary, we do not have access to the errors and plot those data points without any errors as obtained from Ref. [ALICE11e].

forward rapidity, however, the slope of the muons at larger p_T is slightly different. Such a disagreement has also been observed by CMS in a more detailed study of inclusive bottom jets in Ref. [CMS12a] by comparing MC@NLO to data for larger p_T and various rapidities. Nevertheless, we checked that the muon R_{AA} is not very sensitive to the exact slope in this p_T range.

To obtain the initial heavy quark distribution as an input for BAMPS we run MC@NLO with the same parameters for a center-of-mass energy of $\sqrt{s} = 2.76$ TeV, the energy of the recent heavy-ion runs.

The initial distributions for nucleus-nucleus collisions are obtained by scaling proton-proton collisions according to the GLAUBER model (see Appendix A.5). Thus, the p+p events from MC@NLO are scaled with the number of binary collisions, see Equation (A.21). In the present work nuclear effects for the parton distribution functions, for instance, shadowing or the CRONIN effect, are not taken into account for heavy quark production since the impact on the heavy quark distributions at intermediate and high transverse momentum p_T is rather small [ACD⁺06].

MC@NLO samples both charm and anti-charm quarks from NLO matrix elements in a single p+p scattering. Thus, it provides a realistic angle distribution of correlated heavy quarks,

which is necessary for correlation studies. It would be interesting to study those in a future project. In contrast, *fixed-order-next-to-leading-log* (FONLL) calculations [CNV05, CFH⁺12], which are theoretically more advanced than NLO calculations, only have access to inclusive heavy quark distributions and are, therefore, not suitable for studying correlations of heavy quarks.

4.4. Initial J/ψ production

To study J/ψ suppression in ultra-relativistic heavy-ion collisions it is important to have the proper initial production as a baseline. In contrast to open heavy flavor, cold nuclear matter effects have a large impact on the J/ψ yield and can already explain part of the observed suppression.⁵ Therefore, we convolve in this section the initial J/ψ distribution scaled from p+p events with parameterizations of cold nuclear matter effects to obtain a physical initial J/ψ input for BAMPS [UZF⁺11]. The influence of the medium on J/ψ mesons, that is, the hot nuclear matter effect, is discussed in Chapter 7.

The dominant process of initial J/ψ production is gluon fusion, $g + g \rightarrow J/\psi + g$. Therefore, the differential cross section for J/ψ production in p+p collisions is given by

$$\frac{d\sigma_{\text{pp}}^{J/\psi}}{dp_T dy_{J/\psi} dy_g} = x_1 x_2 f_g(x_1, \mu_F) f_g(x_2, \mu_F) \frac{d\sigma_{gg \rightarrow J/\psi g}}{dt}, \quad (4.13)$$

which is related to the heavy quark production cross section from Equation (2.6)—only with other labels, slightly different kinematics, and without medium effects.

In this section we parameterize the measured J/ψ production cross section in p+p collisions and incorporate cold nuclear matter effects as outlined in the following to get the production cross section for A+A collisions. The implementation in BAMPS was done in collaboration with the Tsinghua group [LQXZ09, LQXZ10, ZXZ10, LXZ10, ZER13].

The most important contributions to cold nuclear matter effects are shadowing, nuclear absorption, and the CRONIN effect. Shadowing describes the phenomenon that the parton distribution functions of partons in a nucleus $f^A(x, \mu_F)$ are modified compared to parton distribution functions in a nucleon $f^p(x, \mu_F)$. The ratio of both for parton i ,

$$R_i^A(x, \mu_F) = \frac{f_i^A(x, \mu_F)}{f_i^p(x, \mu_F)}, \quad (4.14)$$

can be obtained, for instance, from deep inelastic scattering at nuclei and nucleons. In the present study we employ the shadowing parameterization EPS08 [EPS08] for $R_i^A(x, \mu_F)$ and set the factorization scale,

$$\mu_F = \sqrt{p_T^2 + M_{J/\psi}^2}, \quad (4.15)$$

⁵There are two reasons why cold nuclear matter effects are more important for J/ψ than for open heavy flavor: 1) nuclear absorption, which is an effect that only acts on the meson and not on the quark level, 2) shadowing, which is present for both, but is most important at small p_T . Open heavy flavor is usually studied at intermediate and large p_T where shadowing effects can be neglected, whereas J/ψ R_{AA} is usually p_T integrated because the total number is important. Hence, it crucially depends on the shadowing parameterization for low p_T .

to the transverse mass of the J/ψ . Furthermore, we use a shadowing function that also depends on the transverse position in the collision [KV03],

$$\mathcal{R}_i^A(\mathbf{x}_T, x, \mu_F) = 1 + N_{A,\rho} [R_i^A(x, \mu_F) - 1] \frac{T_A(\mathbf{x}_T)}{T_A(0)}. \quad (4.16)$$

$T_A(\mathbf{x}_T)$ denotes the nuclear thickness function from the GLAUBER model (see Appendix A.5) and $N_{A,\rho} = A T_A(0)/T_{AB}(0)$ is a normalization constant.

A produced J/ψ can also be absorbed by the remains of the collided nuclei shortly after its production. The nuclear absorption can be effectively described by a survival probability for J/ψ passing through nuclear matter,

$$S_{\text{abs}} = e^{-\sigma_{\text{abs}}[T_A(\mathbf{x}_T, z_A, +\infty) + T_A(\mathbf{x}_T - \mathbf{b}, -\infty, z_B)]}. \quad (4.17)$$

$T_A(\mathbf{x}_T, z_1, z_2)$ is the nuclear thickness function, but not integrated over the full z range $(-\infty, +\infty)$ but over the interval $[z_1, z_2]$. The limits in the formula above are chosen in such a way that it represents the path length that the produced J/ψ travels through the passing remains of the nuclei. For the absorption cross section we employ a value of $\sigma_{\text{abs}} = 2.8 \text{ mb}$ [PHENIX08a]. However, the exact value and whether nuclear absorption is still present at LHC energy is under debate.

The J/ψ production cross section in p+p collisions can be parameterized as [LQXZ10, PHENIX07b]

$$\frac{d\sigma_{\text{pp}}^{J/\psi}}{p_T dp_T dy} = \frac{2(n-1)}{D(y)} \left(1 + \frac{p_T^2}{D(y)}\right)^{-n} \frac{d\sigma_{\text{pp}}^{J/\psi}}{dy}. \quad (4.18)$$

The prefactor $2(n-1)/D(y)$ is a normalization constant and ensures that the integration over the transverse momentum yields indeed $d\sigma_{\text{pp}}^{J/\psi}/dy$. The function $D(y)$ can be determined by considering the mean transverse momentum squared for a given rapidity,

$$\langle p_T^2 \rangle_y^{\text{pp}} = \frac{\int dp_T^2 p_T^2 \left(1 + \frac{p_T^2}{D(y)}\right)^{-n}}{\int dp_T^2 \left(1 + \frac{p_T^2}{D(y)}\right)^{-n}} = \frac{D(y)}{n-2}. \quad (4.19)$$

Of course, the mean p_T^2 is zero for a J/ψ in beam direction, which has (the maximum allowed) rapidity $Y = \text{arccosh}(\sqrt{s_{\text{pp}}}/(2m_{J/\psi}))$ obtained from $\cosh y = E/M_T$. Taking into account that $\langle p_T^2 \rangle_y^{\text{pp}}$ should be the same for positive and negative y leads to the following educated guess for the rapidity dependence of mean transverse momentum squared

$$\langle p_T^2 \rangle_y^{\text{pp}} = \langle p_T^2 \rangle_{y=0}^{\text{pp}} (1 - y^2/Y^2). \quad (4.20)$$

With the measured mid-rapidity value at RHIC of $\langle p_T^2 \rangle_{y=0}^{\text{pp}} = 4.14 \text{ GeV}^2$ [PHENIX07b], Equation (4.20) is in good agreement with the measured value in forward rapidity [PHENIX07b].

For $d\sigma_{\text{pp}}^{J/\psi}/dy$ we employ a double Gaussian distribution [PHENIX07b, LQXZ10] to fit the data, which is depicted in Figure 4.7 (left) for RHIC energies. The best fit to the p_T distribution is obtained with $n = 6$ in Equation (4.18)—see Figure 4.7 (right). The fits to the LHC data are shown in Figure 4.8. The extracted parameters for the LHC fit are $n = 6$ and $\langle p_T^2 \rangle_{y=0}^{\text{pp}} = 8 \text{ GeV}^2$.

4.4. Initial J/ψ production

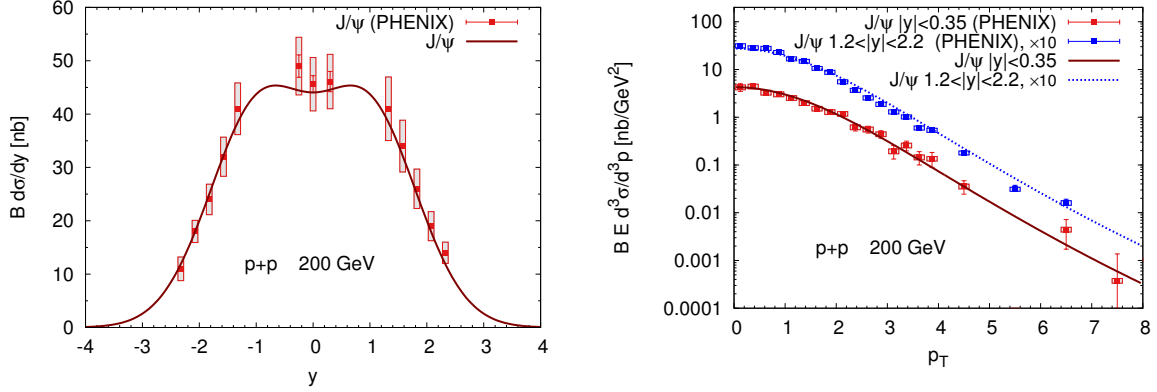


Figure 4.7.: Fits to the experimentally measured [PHENIX07b] differential J/ψ production cross section in p+p collisions at RHIC as a function of rapidity y (left) and transverse momentum p_T (right). The cross section is multiplied with the branching ratio B of $J/\psi \rightarrow e^+e^-$ [PDG12].

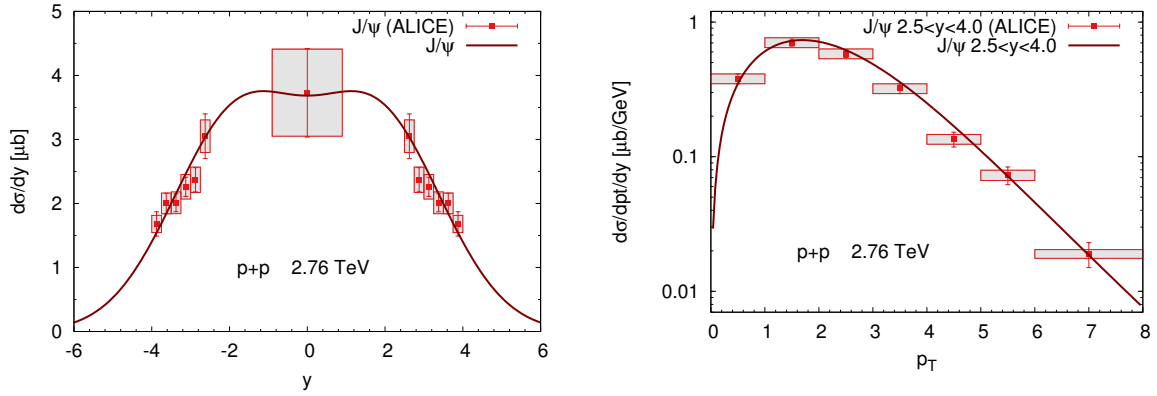


Figure 4.8.: As Figure 4.7 for LHC. Data is from Ref. [ALICE12a].

To account for the CRONIN effect, which describes the p_T broadening of the fusing gluons in the nuclei, we add an additional path length dependence to the mean p_T in the parameterization of the p+p cross section above,

$$\langle p_t^2 \rangle = \langle p_t^2 \rangle_{pp} + a_{gN} L \quad (4.21)$$

with $a_{gN} = 0.1 \text{ GeV}^2/\text{fm}$ [ZR08] and

$$L = \frac{1}{n_0} [T_A(\mathbf{x}_T, -\infty, z_A) + T_A(\mathbf{x}_T - \mathbf{b}, z_B, +\infty)] . \quad (4.22)$$

The latter is the path length of the two incoming gluons through the nuclear matter of the other nucleus. n_0 denotes the maximum nuclear density from the Woods-Saxon distribution (cf. Section A.5).

With all these cold nuclear matter effects the differential J/ψ production cross section in

heavy-ion collisions can be written as

$$\begin{aligned}
 \frac{dN_{AA}^{J/\psi}}{dp_T dy_{J/\psi} dy_g} &= \int d\mathbf{x}_T \int dz_A \int dz_B n_A(\mathbf{x}_T, z_A) n_A(\mathbf{x}_T - \mathbf{b}, z_B) \\
 &\quad \times \mathcal{R}_g^A(\mathbf{x}_T, x_1, \mu_F) \mathcal{R}_g^A(\mathbf{x}_T - \mathbf{b}, x_2, \mu_F) e^{-\sigma_{\text{abs}}[T_A(\mathbf{x}_T, z_A, +\infty) + T_A(\mathbf{x}_T - \mathbf{b}, -\infty, z_B)]} \\
 &\quad \times x_1 x_2 f_g(x_1, \mu_F) f_g(x_2, \mu_F) \frac{d\sigma_{gg \rightarrow J/\psi g}}{dt} \\
 &= \int d\mathbf{x}_T \int dz_A \int dz_B n_A(\mathbf{x}_T, z_A) n_A(\mathbf{x}_T - \mathbf{b}, z_B) \\
 &\quad \times \mathcal{R}_g^A(\mathbf{x}_T, x_1, \mu_F) \mathcal{R}_g^A(\mathbf{x}_T - \mathbf{b}, x_2, \mu_F) e^{-\sigma_{\text{abs}}[T_A(\mathbf{x}_T, z_A, +\infty) + T_A(\mathbf{x}_T - \mathbf{b}, -\infty, z_B)]} \\
 &\quad \times \frac{d\sigma_{pp}^{J/\psi}}{dp_T dy_{J/\psi} dy_g}, \tag{4.23}
 \end{aligned}$$

where Equation (4.13) was used. In the following we assume that the emitted outgoing gluon in the J/ψ production process $g + g \rightarrow J/\psi + g$ is soft. As a consequence, x_1 and x_2 are independent of its rapidity y_g and we can integrate it out:

$$\begin{aligned}
 \frac{dN_{AA}^{J/\psi}}{dp_T dy_{J/\psi}} &= \int d\mathbf{x}_T \int dz_A \int dz_B n_A(\mathbf{x}_T, z_A) n_A(\mathbf{x}_T - \mathbf{b}, z_B) \\
 &\quad \times \mathcal{R}_g^A(\mathbf{x}_T, x_1, \mu_F) \mathcal{R}_g^A(\mathbf{x}_T - \mathbf{b}, x_2, \mu_F) e^{-\sigma_{\text{abs}}[T_A(\mathbf{x}_T, z_A, +\infty) + T_A(\mathbf{x}_T - \mathbf{b}, -\infty, z_B)]} \\
 &\quad \times \frac{d\sigma_{pp}^{J/\psi}}{dp_T dy_{J/\psi}}. \tag{4.24}
 \end{aligned}$$

If there are no cold nuclear matter effects ($R_g^A = 1$, $a_{gN} = 0 \text{ GeV}^2/\text{fm}$, and $\sigma_{\text{abs}} = 0 \text{ mb}$) this formula simplifies to the well known binary scaling from p+p to A+A collisions,

$$\frac{dN_{AA}^{J/\psi}}{dp_T dy} = T_{AA}(\mathbf{b}) \frac{d\sigma_{pp}^{J/\psi}}{dp_T dy}. \tag{4.25}$$

In Figure 4.9 the initial J/ψ distributions for Au+Au collisions at RHIC with cold nuclear matter effects for different impact parameters are compared to the p+p reference. The nuclear matter effects in central Au+Au collisions are quite sizeable, although the shape itself is barely changed. In peripheral Au+Au collisions the suppression is smaller due to the impact parameter dependent nuclear absorption and shadowing parameterizations. It is also interesting to compare to the data from deuteron-gold (d+Au) collisions since here only cold nuclear matter effects are present. The suppression in the positive rapidity direction, which is the direction of the deuteron, is larger than in the negative direction since a produced J/ψ sees the passing nucleus and can be absorbed. Furthermore, a J/ψ in this direction is produced on average from gluons with a smaller x from the nucleus than from the deuteron. Hence, the small x regime is probed, where shadowing effects are strong. In the negative direction hardly any suppression compared to p+p is present. Interestingly, the curve for only cold nuclear matter effected J/ψ in peripheral heavy-ion collisions is rather close to the d+Au data at mid- and forward rapidity, which might not be too suprising given that ultra-peripheral heavy-ion collisions should not be too different from d+Au collisions at forward rapidity.

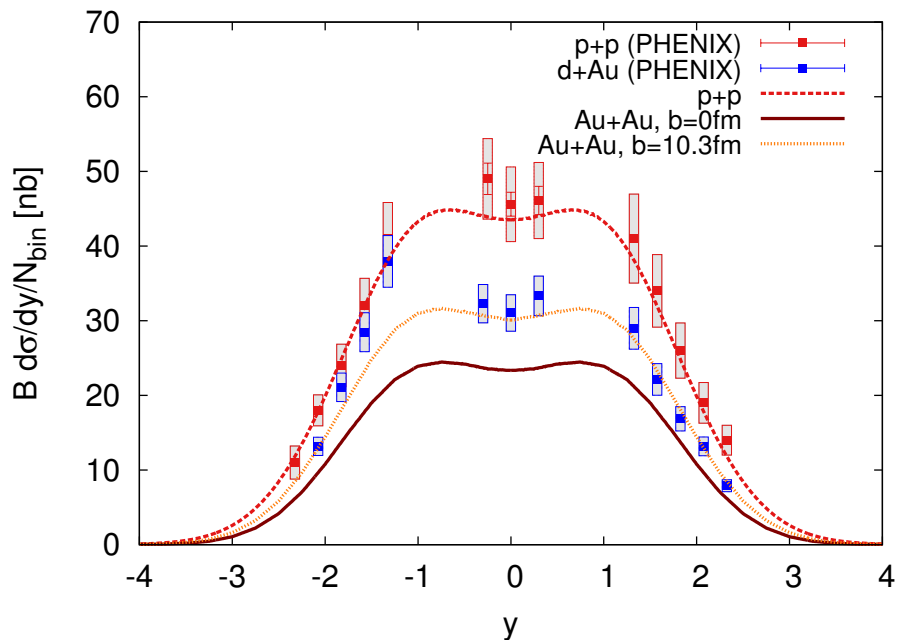


Figure 4.9.: Differential J/ψ cross section in Au+Au collisions with only cold nuclear matter effects for different impact parameters b and scaled by the number of binary collisions N_{bin} . As a reference the p+p curve is shown with data for p+p [PHENIX07b]. The data for d+Au [PHENIX11a] is measured with the deuteron going in the forward rapidity direction. B is the branching ratio of J/ψ to di-electrons.

Since Equation (4.24) describes the initial J/ψ distribution in heavy-ion collisions including cold nuclear matter effects, we employ it to sample the initial J/ψ input for BAMPS. The subsequent evolution and the effect of hot nuclear matter on J/ψ are presented in Chapter 7, where we also show results on J/ψ R_{AA} and v_2 .

4.5. Initial light parton distribution—PYTHIA and minijet model

The initial light parton distributions are obtained either from PYTHIA or the mini-jet model. For most calculations in this work, PYTHIA is employed since it gives a more realistic picture of the initial distribution. However, for studying highly energetic light partons in Section 6.2.1 we employ the mini-jet model since it is numerically easier to use for sampling rare probes such as jets and because it has been applied for studying light parton observables in the past [FXG09, FXG10].

For our simulation we use PYTHIA 6.4 [SMS06] with the parton distribution function CTEQ6l [P⁺02], allow all QCD interactions, and turn off the hadronization. PYTHIA distinguishes between soft and hard events. Since soft events are usually events without any hard parton interactions, we discard them and only scale the hard events with the number of binary collisions, see Equation (A.21), having in mind the picture of a heavy-ion collision consisting—according to the GLAUBER model (cf. Appendix A.5)—of a superposition of

independent nucleon-nucleon collisions.

Both at RHIC and LHC most of the initially produced particles are gluons. In contrast, the quark number is much smaller, resulting in an initial quark to gluon ratio at mid-rapidity of 0.15 at RHIC and 0.1 at LHC [UFXG10a].

In the mini-jet model [KLL87, EKL89], the initial parton distribution is given by several independent 2-jet events, which are sampled according to [WG91]

$$\frac{d\sigma_{\text{jet}}}{dp_T^2 dy_1 dy_2} = K \sum_{a,b} x_1 f_a(x_1, p_T^2) x_2 f_b(x_2, p_T^2) \frac{d\sigma_{ab}}{dt}, \quad (4.26)$$

where p_T denotes the transverse momentum, y the rapidity, and x the BJORKEN variable. The cross section σ_{ab} is calculated in leading order pQCD and a $K = 2$ factor is introduced to account for higher orders.

To avoid problems at low momenta where pQCD is not valid anymore, a momentum cut-off must be introduced. However, since we employ the mini-jet model only for high-energy particles the value of this cut-off is not important.⁶ The number of produced partons is given by

$$N_{\text{partons}}(b) = \sigma_{\text{jet}} T_{AB}(\mathbf{b}) \quad (4.27)$$

with $T_{AB}(\mathbf{b})$ being defined in Appendix A.5.

For more details on the two models and the particular implementation in BAMPS we refer to Refs. [XG05, Uph09, UFXG10a].

4.6. Non-heavy-flavor BAMPS studies

Apart from the heavy flavor results presented in this thesis, BAMPS has been applied to study a wide variety of phenomena related to heavy-ion collisions. The most important investigations are briefly summarized in the following.

It is important to note that for all previous pQCD based studies the original GUNION-BERTSCH (GB) matrix element has been employed. In Section 3.2 we identified several problems with the original GB version and proposed an improved matrix element. The applicability of the latter was verified by comparing to exact calculations. Hence, the previously obtained results with the original GB cross section must be revisited with the improved version that should describe the inelastic processes more accurately, which is planned for the near future. As a note, all hard probes studies presented in this thesis feature the improved GB cross section.

One of the first studies after establishing the BAMPS framework was the investigation of thermalization of a gluon plasma in both a static medium and an expanding fireball in a heavy-ion collision [XG05]. A very short thermalization time of about 1 fm was found, mainly driven by inelastic processes [XG05, XG07]. In addition, the thermalization within BAMPS with color glass condensate initial conditions was compared to the so called ‘‘bottom-up’’ scenario [EXG08].

For either a large coupling $\alpha_s = 0.6$ and a large freeze-out energy density $\epsilon_c = 1.0 \text{ GeV}/\text{fm}^3$ or a small coupling $\alpha_s = 0.3$ and later freeze-out ($\epsilon_c = 0.6 \text{ GeV}/\text{fm}^3$), the integrated elliptic

⁶If one is also interested in the soft parton sector, one can fix the value by comparing the final transverse energy distribution of the gluons with data [XG06].

flow at RHIC can be described by a purely gluonic plasma [XGS08, XG09]. More recent calculations of the elliptic flow include also light quark degrees of freedom, either effectively [XG10] or rigorously [FUXG11, Foc11] by actually implementing light quarks in BAMPS.

Calculations that reproduce the measured elliptic flow also exhibit a very small shear viscosity to entropy density ratio [XGS08], as it is also the case for hydrodynamic models (cf. Section 2.2.2). The shear viscosity in BAMPS has been calculated using different methods: from transport rates [XG08], from the GREEN-KUBO relation [WER⁺11], from the classical picture of the shear viscosity [RBE⁺12], and from the entropy principle as well as GRAD's approximation for the off-equilibrium distribution function [EMXG09, ELW⁺12], giving consistent results.

Within the same framework that describes the QGP with a large elliptic flow, a rapid thermalization, and a small shear viscosity to entropy density ratio, also the jet quenching of light partons was studied [FXG09, FXG10, CGW⁺10, FUXG11, Foc11]. This includes the calculation of the nuclear modification factor but also the extraction of the jet transport parameter \hat{q} . In addition, first calculations with reconstructed jets have been performed [SFU⁺13]. The suppression of highly energetic particles is much larger than the experimental data [FXG09, FXG10, FUXG11, Foc11] due to a strong radiative energy loss. As we will see in Section 6.2.1, the improved GB matrix element leads to a much smaller energy loss.

BAMPS was also employed in several more theoretical studies. For instance, the relativistic RIEMANN problem, which considers the propagation of a shock wave, was investigated in hot and dense matter with different viscosities [B⁺09]. Being in agreement with the analytic solution for vanishing viscosity, the BAMPS results for finite viscosity can serve as a benchmark for viscous hydrodynamic models [BMN⁺10]. Such comparisons are possible since BAMPS solves the BOLTZMANN equation very accurately. Therefore, it can be employed to verify dissipative hydrodynamic equations derived from kinetic theory, for instance, in the ISRAEL-STEWART procedure [EXG10, EMXG10, EBW⁺12] and beyond [DNB⁺12]. The latter result is in agreement with heat flow calculations in BAMPS [GRB⁺13].

Furthermore, BAMPS was used to study whether jets in heavy-ion collisions can produce shock waves in form of MACH cones and if they form a double peak in two-particle correlations [BEF⁺12]. In addition to heavy-ion collisions, BAMPS was extended to p+p collisions and the elliptic as well as triangular flow was calculated in these more elementary collisions [DXG12].

5. Energy loss of heavy quarks

One thing I have learned in a long life: that all our science, measured against reality, is primitive and childlike—and yet it is the most precious thing we have.

Letter to Hans Mühnsam dated July 9th, 1951

ALBERT EINSTEIN

In this chapter we study the elastic and radiative energy loss of heavy quarks. First, we outline a derivation of an analytic formula for elastic heavy quark energy loss from pQCD matrix elements and hard-thermal-loop resummations in a static medium [PP08b, PP08a] and recalculate it for BOLTZMANN statistics. By comparing to this result we can analytically fix the screening mass of the BORN cross section, which is implemented in BAMPS. To verify this matching we compare BAMPS simulations of a heavy quark traversing a static medium to the analytic result. In Section 5.2 we extend the analytic formula to a flowing medium and again compare to BAMPS simulations. Numerical results from BAMPS for the radiative energy loss are presented in Section 5.3 and compared to the elastic energy loss.

5.1. Elastic energy loss in a static medium

In this section we consider a high-energy heavy quark with mass M and large energy E traversing a static medium of thermally distributed light quarks and gluons with a temperature T . The energy loss per unit length of the heavy quark can be expressed as [BT91b, BT91a]

$$\frac{dE}{dx} = \sum_i \frac{1}{2Ev} \int \frac{d^3p_2}{(2\pi)^3 2E_2} \int \frac{d^3p_3}{(2\pi)^3 2E_3} \int \frac{d^3p_4}{(2\pi)^3 2E_4} n_i(p_2) \bar{n}_i(p_4) \times (2\pi)^4 \delta^{(4)}(p_1 + p_2 - p_3 - p_4) d_i |\overline{\mathcal{M}}_{i+Q \rightarrow i+Q}|^2 \omega. \quad (5.1)$$

The four-momenta of the incoming and outgoing heavy quark are $p_1 = (E, \mathbf{p}_1)$ and $p_3 = (E_3, \mathbf{p}_3)$. Thus, $\omega = E - E_3$ denotes the energy loss of the heavy quark in one interaction. The momenta of the incoming (outgoing) medium particle i is denoted with p_2 (p_4). v is the velocity of the heavy quark and $|\overline{\mathcal{M}}_{i+Q \rightarrow i+Q}|^2$ is the summed and averaged squared matrix element of one of the following elastic processes ($i = g, q$):

$$\begin{aligned} g + Q &\rightarrow g + Q \\ q + Q &\rightarrow q + Q. \end{aligned} \quad (5.2)$$

The matrix elements for the two processes are given in Equations (3.27) and (3.29), respectively. The degeneracy factor d_i of the thermal scattering particle is $d_g = 2 \cdot (N_c^2 - 1) = 16$ for gluons

and $d_q = 2 \cdot 2 \cdot N_c \cdot n_f = 12n_f$ for quarks. First, we calculate the general result for BOSE-EINSTEIN and FERMI-DIRAC statistics, $n_i(k) = (\exp(k/T) \mp 1)^{-1}$, for thermal gluons and light quarks, respectively, but later employ the assumption of BOLTZMANN statistics for both species, $n_i(k) = \exp(-k/T)$, in order to compare with BAMPS, in which all particles are treated as BOLTZMANN particles. The factor $\bar{n}_i = 1 \pm n_i$ takes the BOSE enhancement or PAULI blocking in the final state into account.

The following calculation is done analogously to Ref. [PP08b, PP08a]. Equation (5.1) can be rewritten after somewhat lengthy kinematical transformations [PP08b] in terms of the differential cross section $d\sigma/dt$ by neglecting quantum effects in the final state, $\bar{n}_i \rightarrow 1$, and assuming that E is very large,

$$\frac{dE}{dx} = \sum_i d_i \int \frac{d^3p_2}{(2\pi)^3 2E_2} n_i(p_2) \int_{t_{\min}}^{t_{\max}} dt (-t) \frac{d\sigma_{i+Q \rightarrow i+Q}}{dt}, \quad (5.3)$$

The differential cross sections of the processes in (5.2) are given in Section 3.1, in which also the limits of the t integration are calculated from the kinematics, see Equation (3.15).

The most important contribution to the differential cross section of both processes from (5.2) is the t channel, which is proportional to

$$\left. \frac{d\sigma_{i+Q \rightarrow i+Q}}{dt} \right|_{t \text{ channel}} \propto \frac{1}{t^2} + \dots \quad (5.4)$$

Consequently, the integral

$$\int_{t_{\min}}^{t_{\max}} dt (-t) \left. \frac{d\sigma_{i+Q \rightarrow i+Q}}{dt} \right|_{t \text{ channel}} \propto \ln \left| \frac{t_{\min}}{t_{\max}} \right| + \dots, \quad (5.5)$$

which enters in the energy loss calculation of Equation (5.3), is divergent for $t_{\max} = 0$. This is the same divergence that arose in Section 3.1, where we regularized the t channel with a screening mass. Here, however, we will go another way and calculate the energy loss of the soft diverging part within the hard-thermal-loop (HTL) approximation [BP90, Tho95], which is a more accurate description of medium effects on the propagator compared to the simple DEBYE screening.

To this end, following along the lines of the BRAATEN-YUAN prescription [BY91], we divide the t range with a cut-off t^* in a soft ($|t| < |t^*|$) and hard ($|t| > |t^*|$) part. The parameter t^* is chosen as an arbitrary intermediate scale that fulfills $m_D^2 \ll |t^*| \ll T^2$ with m_D being the DEBYE mass defined in Equation (3.18). This implies that $m_D^2 \ll T^2$, which is strictly only fulfilled if the coupling is very small. The issue is discussed in great detail in Ref. [GA08], where also another description is proposed that leads to very similar results as presented in this chapter. For the hard part, we can just proceed from here with the standard integration of Equation (5.3) since no divergence occurs. For the soft part, we calculate the energy loss within the HTL approximation, which also gives finite results.

As a note, it is not straightforward to employ the HTL approximation to calculate the total cross section directly instead of the more indirect energy loss because it would result in another divergence in the calculation of the interaction rate. In contrast, in the energy loss calculation

the additional explicit factor of $(-t)$ in Equation (5.3) (compared to the interaction rate) keeps the integrals finite.

In the next section we calculate not only the hard part of the t channel but also the contribution of the s and u channel, which are both infrared safe. The soft part of the t channel is calculated within the HTL approach in Section 5.1.2. We combine these results to the total energy loss in Section 5.1.3 and show that the final result does not depend on the separation scale t^* . Subsequently, in Section 5.1.4 the result for the energy loss with all particles obeying BOLTZMANN statistics is derived. In Section 5.1.5 we fix the screening mass of the BORN cross section by comparing to the HTL calculation and also compare the analytic formula to BAMPS simulations. Finally, we extend the analytic formula of the energy loss from a constant to a running coupling in Section 5.1.6.

5.1.1. s , t , and u channel—hard part

For the scattering process of a light and a heavy quark, only the t channel exists. Equations (3.29) and (3.28) can be rewritten (without any approximations) as¹

$$\frac{d\sigma_{qQ \rightarrow qQ}}{dt} = \frac{\pi\alpha_s^2}{16\tilde{s}^2} \frac{128}{9} \left(\frac{\tilde{s}^2}{t^2} + \frac{s}{t} + \frac{1}{2} \right), \quad (5.6)$$

where we introduced the abbreviation $\tilde{s} = s - M^2$ and, for later reference, also define $\tilde{u} = u - M^2$. The coupling α_s is assumed to be constant. In Section 5.1.6, however, we loosen this constraint and explicitly consider a running coupling. After plugging the differential cross section in Equation (5.3), one can perform the t integration up to $t_{\max} = t^*$ as well as the \mathbf{k} integration and gets

$$\frac{dE_q}{dx} \Big|_{|t| > |t^*|} = \frac{4\pi\alpha_s^2 T^2}{3} \frac{n_f}{6} \left[\ln \frac{8ET}{|t^*|} - \gamma_E - \frac{3}{4} + \frac{\zeta'(2)}{\zeta(2)} \right] \quad (5.7)$$

with $\gamma_E \approx 0.577$ being the EULER constant. ζ and ζ' denote the Riemann Zeta Function and its derivative, respectively.

In the limit of $E \rightarrow \infty$ the differential cross section of gluon-heavy-quark scattering from Equations (3.12) and (3.6) can be approximated as

$$\frac{d\sigma_{gQ \rightarrow gQ}}{dt} \simeq \frac{\pi\alpha_s^2}{16\tilde{s}^2} \left[32 \left(\frac{\tilde{s}^2}{t^2} + \frac{s}{t} + \frac{1}{2} \right) + \frac{64}{9} \left(\frac{-\tilde{u}}{\tilde{s}} + \frac{\tilde{s}}{-\tilde{u}} \right) \right], \quad (5.8)$$

The first inner bracket is the contribution from the t channel, the second from the s and u channels. The interference terms as well as some terms in the s and u channels vanish in this limit.

The t channel contribution is the same expression as for $q+Q$ scattering, just with a different prefactor. Taking this prefactor, the different degeneracy factors of gluons and light quarks, and the different integrals of BOSE and FERMI distributions (an extra factor of 2 as well as

¹Since we are here only interested in the hard part and $|t| > |t^*| \gg m_D^2$, we can neglect the screening masses. The soft part is computed in the next section from HTL calculations, which are theoretically more advanced than the DEBYE screening.

Distribution	$n(E)$	$\int_0^\infty dE n(E) E$	$\int_0^\infty dE n(E) E \ln(E/T)$
BOSE-EINSTEIN	$(\exp(E/T) - 1)^{-1}$	$\frac{\pi^2}{6} T^2$	$\frac{\pi^2}{6} T^2 \left[1 - \gamma_E + \frac{\zeta'(2)}{\zeta(2)} \right]$
FERMI-DIRAC	$(\exp(E/T) + 1)^{-1}$	$\frac{\pi^2}{12} T^2$	$\frac{\pi^2}{12} T^2 \left[1 - \gamma_E + \frac{\zeta'(2)}{\zeta(2)} + \ln 2 \right]$
BOLTZMANN	$\exp(-E/T)$	T^2	$T^2 [1 - \gamma_E]$

Table 5.1.: Useful integrals of the distribution functions of particles that obey BOSE-EINSTEIN, FERMI-DIRAC, or BOLTZMANN statistics.

the lack of a $\ln 2$ term, cf. Table 5.1) into account, yields the following result for the hard part of t channel contribution of $gQ \rightarrow gQ$:

$$\frac{dE_g}{dx} \Big|_{|t| > |t^*|}^{t \text{ channel}} = \frac{4\pi\alpha_s^2 T^2}{3} \left[\ln \frac{4ET}{|t^*|} - \gamma_E - \frac{3}{4} + \frac{\zeta'(2)}{\zeta(2)} \right]. \quad (5.9)$$

The s and u channels are not divergent for small t due to the finite heavy quark mass. Therefore, there is no need to introduce a cut-off t^* and the t integration in Equation (5.3) can be continued to zero. Consequently, in the next section we only have to consider the soft part of the t channel. Substituting t by \tilde{u} with the MANDELSTAM relation $\tilde{s} + t + \tilde{u} = 0$ (cf. Appendix A.2) and integration over the second term of Equation (5.8), yields the energy loss from the s and u channels:

$$\frac{dE_g}{dx} \Big|^{s,u \text{ channels}} = \frac{4\pi\alpha_s^2 T^2}{3} \frac{2}{9} \left[\ln \frac{4TE}{M^2} - \frac{5}{6} - \gamma_E + \frac{\zeta'(2)}{\zeta(2)} \right]. \quad (5.10)$$

5.1.2. t channel—soft part

In contrast to the previous section, the collisional energy loss of a heavy quark from the soft contribution is derived from its self-energy, which is calculated in the HTL approximation. The interaction rate Γ , which is closely related to the energy loss via

$$\frac{dE}{dx} = \frac{1}{v} \int d\omega \frac{\partial \Gamma}{\partial \omega} \omega, \quad (5.11)$$

can be calculated from the self-energy Σ of the heavy quark, [Bel00, PP08b]

$$\Gamma(E) = -\frac{1}{2E} (1 - n_F(E)) \text{tr} [(\not{P} + M) \text{Im} \Sigma(P)]. \quad (5.12)$$

Because of gauge invariance one can choose an arbitrary gauge (here COULOMB gauge) and evaluate the trace. Due to the assumption $M \gg T$, the FERMI distribution is $n_F(E) \ll 1$ and

the interaction rate becomes [PP08b]

$$\Gamma(E) = \frac{2\alpha_s}{v} \frac{4}{3} \int_0^\infty dq q \int_{\omega_-}^{\omega_+} d\omega (1 + n_B(\omega)) \left\{ \rho_L(\omega, q) \left[1 - \frac{\omega}{E} - \frac{t}{4E^2} \right] + \rho_T(\omega, q) \left[v^2 - \frac{\omega^2}{q^2} + \frac{t\omega}{Eq^2} - \frac{t}{2E^2} - \frac{t^2}{(2Eq)^2} \right] \right\}, \quad (5.13)$$

where \mathbf{q} is the gluon momentum, n_B the BOSE distribution and $\omega_\pm(q) = E - \sqrt{(p \mp q)^2 + M^2}$. The spectral functions of the longitudinal and transverse gluons are defined by [BT91a]

$$\rho_{L,T}(\omega, q) \equiv -\frac{1}{\pi} \text{Im} [\Delta_{L,T}(\omega + i\epsilon, q)] \quad (5.14)$$

with $\Delta_{L,T}$ being the longitudinal and transverse gluon propagators, which are in the HTL approximation given by

$$\Delta_L(\omega, q) = \frac{1}{q^2 + \Pi_L(x)}, \quad \Delta_T(\omega, q) = \frac{1}{\omega^2 - q^2 - \Pi_T(x)} \quad (5.15)$$

with the self-energies [BI02]

$$\begin{aligned} \Pi_L(x) &= m_D^2 [1 - Q(x)], \\ \Pi_T(x) &= \frac{m_D^2}{2} [x^2 + (1 - x^2)Q(x)] = \frac{m_D^2}{2} x(1 - x^2)Q'(x), \\ Q(x) &\equiv \frac{x}{2} \ln \frac{x+1}{x-1}, \end{aligned} \quad (5.16)$$

where m_D is the DEBYE mass.

To obtain the energy loss of a heavy quark one must weight—according to Equation (5.11)—the integral in Equation (5.13) with the factor ω/v . We also change variables to $t = \omega^2 - q^2$ and $x = \omega/q$, approximate the boundaries of the x integral to $\pm v$, and neglect terms of the order of $\mathcal{O}(|t|^{1/2}/E)$ since we only consider the soft region $|t| < |t^*|$ here. The energy loss then reads

$$\frac{dE_{g,q}}{dx} \Big|_{|t| < |t^*|}^{t \text{ channel}} = \frac{\alpha_s}{v^2} \frac{4}{3} \int_{-v}^v dx \frac{x}{(1-x^2)^2} \int_{t^*}^0 dt (-t) [\rho_L + (v^2 - x^2)\rho_T]. \quad (5.17)$$

As we have mentioned above, weighting the integral with ω is essential to avoid an infrared divergence. Thus, the energy loss is a well-defined quantity, whereas the interaction rate diverges due to soft transverse exchanges.

After evaluating the integrals, using $|t^*| \gg |\tilde{\Pi}_L(x)|, |\Pi_T(x)|$, and going to the limit $E \rightarrow \infty$ and, thus, $v \rightarrow 1$, we arrive at the result of the energy loss in the soft region of the t channel,

$$\frac{dE_{g,q}}{dx} \Big|_{|t| < |t^*|}^{t \text{ channel}} = \frac{\alpha_s m_D^2}{4} \frac{4}{3} \ln \frac{2|t^*|}{m_D^2} = \frac{4\pi\alpha_s^2 T^2}{3} \left(1 + \frac{n_f}{6}\right) \ln \frac{2|t^*|}{m_D^2}, \quad (5.18)$$

where the definition of the DEBYE mass $m_D^2 = 4\pi\alpha_s T^2(1 + n_f/6)$ for gluons with BOSE statistics from Equation (3.21) was used.

5.1.3. Total energy loss

In the previous sections we calculated the contributions of the s and u channel, Equation (5.10), the hard part of the t channel for scatterings with a light quark and a gluon, Equations (5.7) and (5.9), respectively, as well as the soft contribution of the t channel from the HTL approach, Equation (5.18). Adding all these results together, gives the total collisional energy loss of a heavy quark in a static and thermal quark-gluon plasma,

$$\frac{dE}{dx} = \frac{4\pi\alpha_s^2 T^2}{3} \left[\left(1 + \frac{n_f}{6}\right) \ln \frac{ET}{m_D^2} + \frac{2}{9} \ln \frac{ET}{M^2} + c(n_f) \right] \quad (5.19)$$

with

$$c(n_f) = a n_f + b \simeq 0.146 n_f + 0.050, \quad (5.20)$$

where the exact values of a and b are $a = (2/3) \ln 2 - 1/8 + (\zeta'(2)/\zeta(2) - \gamma_E)/6$ and $b = (31/9) \ln 2 - 101/108 + 11(\zeta'(2)/\zeta(2) - \gamma_E)/9$.

The first term in the bracket of Equation (5.19) has been first calculated by BJORKEN [Bjo82] and is called the COULOMB logarithm since it arises from the t channel. The second term is the COMPTON logarithm and stems from the s and u channels.

5.1.4. From quantum statistics to the classical Boltzmann limit

The parton cascade BAMPS treats the partons as BOLTZMANN particles. Therefore, to compare to numerical results from BAMPS, we must re-derive the analytic formula of the energy loss for particles that obey BOLTZMANN statistics. Table 5.1 on page 98 lists some integrals over the distribution functions that are used in the calculation. After performing these integrals, the contributions of the different channels from the light quark and gluon scatterings (see Equations (5.7), (5.9), (5.10), and (5.18)) are modified to

$$\begin{aligned} \frac{dE_q}{dx} \Big|_{|t| > |t^*|} &= \frac{8\alpha_s^2 T^2}{\pi} \frac{n_f}{3} \left[\ln \frac{4ET}{|t^*|} - \gamma_E - \frac{3}{4} \right] \\ \frac{dE_g}{dx} \Big|_{|t| > |t^*|}^{t \text{ channel}} &= \frac{8\alpha_s^2 T^2}{\pi} \left[\ln \frac{4ET}{|t^*|} - \gamma_E - \frac{3}{4} \right] \\ \frac{dE_g}{dx} \Big|_{|t| > |t^*|}^{s,u \text{ channels}} &= \frac{8\alpha_s^2 T^2}{\pi} \frac{2}{9} \left[\ln \frac{4ET}{M^2} - \gamma_E - \frac{5}{6} \right] \\ \frac{dE_{g,q}}{dx} \Big|_{|t| < |t^*|}^{t \text{ channel}} &= \frac{8\alpha_s^2 T^2}{\pi} \left(1 + \frac{n_f}{3}\right) \ln \frac{2|t^*|}{m_D^2}. \end{aligned} \quad (5.21)$$

Summing all these contributions up, yields the total collisional energy loss in the BOLTZMANN limit:

$$\frac{dE}{dx} = \frac{8\alpha_s^2 T^2}{\pi} \left[\left(1 + \frac{n_f}{3}\right) \ln \frac{ET}{m_D^2} + \frac{2}{9} \ln \frac{ET}{M^2} + f(n_f) \right] \quad (5.22)$$

with

$$f(n_f) = g n_f + h \simeq 0.251 n_f + 0.747, \quad (5.23)$$

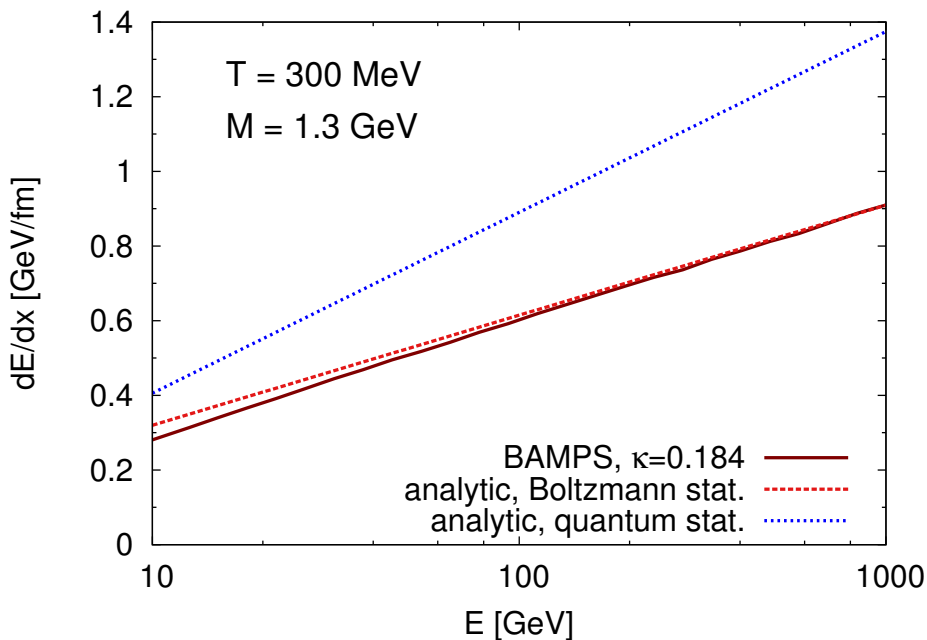


Figure 5.1.: Collisional energy loss per unit length dE/dx as a function of jet energy E of the heavy quark in a static and thermalized medium of gluons ($n_f = 0$) with temperature $T = 300$ MeV. The numerical result from BAMPS with the BORN cross section, a constant coupling $\alpha_s = 0.3$, and a screening mass with $\kappa_t = 0.184$ is compared to the analytical result from Equation (5.22) for BOLTZMANN statistics. In addition, the curve for quantum statistics is shown.

where $g = \ln 2 - 1/4 - \gamma_E/3$ and $h = (31/9) \ln 2 - 101/108 - 11\gamma_E/9$.

In Figure 5.1 both results for BOLTZMANN and quantum statistics are shown. The analytic curve for quantum statistics is about 25 % larger than the BOLTZMANN curve for $E \simeq 10$ GeV. In addition, the result from a BAMPS simulation with an improved DEBYE screening is depicted, which is discussed in the next section.

5.1.5. Comparison to Born cross section

We emphasized earlier that a full HTL calculation of the interaction rate or, equivalently, the cross section diverges. However, the cross section that is implemented in BAMPS must be finite. Accordingly, we approximated in Equation (3.16) the self-energy in the screened gluon propagator by a constant screening mass $\mu^2 = \kappa_t m_D^2$, which is proportional to the DEBYE mass, as discussed in Section 3.1. In this section we will fix the prefactor κ_t by comparing the energy loss obtained with the screened BORN cross section from Section 3.1 to the energy loss from the HTL calculation.

Therefore, we now perform the integration in Equation (5.3) for the different channels of the screened BORN matrix elements given in Equations (3.27) and (3.29) with the screening mass $\mu^2 = \kappa_t m_D^2$ in the t channel but for a constant coupling.² The result of the s and u

²Furthermore, we set the screening masses in the s and u channel to zero since both channels are screened by

channel is the same as in Equation (5.10) since they are not affected by the screening. The integration range for the hard part of the t channel is $|t| \in [|t^*|, \tilde{s}^2/s]$. By definition $|t^*| \gg m_D^2$ and, therefore, $|t| \gg m_D^2$ for the hard part. As a consequence, the screening of the gluon propagator can be neglected in this range, $1/(t - \mu^2)^2 \rightarrow 1/t^2$, and the energy loss of the hard part of the t channel is the same as in Equations (5.7) and (5.9) for scattering with a quark or gluon, respectively.

Consequently, the only difference arises from the soft t channel contribution, which we now calculate with the screened BORN matrix elements for scatterings with quarks and gluons instead from HTL calculations. To obtain the energy loss due to the soft part of the t channel, we insert the screened BORN cross section in Equation (5.3) and perform the integrations. Due to the screened gluon propagator the t integration does not diverge and we can integrate from $t_{\min} = t^*$ to $t_{\max} = 0$. For large s we obtain the result (quantum statistics)

$$\frac{dE_{g,q}}{dx} \Big|_{|t| < |t^*|}^{t \text{ channel}} = \frac{4\pi\alpha_s^2 T^2}{3} \left(1 + \frac{n_f}{6}\right) \left(\ln \frac{|t^*|}{\mu^2} - 1\right) = \frac{4\pi\alpha_s^2 T^2}{3} \left(1 + \frac{n_f}{6}\right) \ln \frac{|t^*|}{e \kappa_t m_D^2}. \quad (5.24)$$

Comparing this result to the energy loss of the soft t channel, computed in the HTL approximation in Equation (5.18), determines κ_t to be

$$\kappa_t = \frac{1}{2e} \approx 0.184. \quad (5.25)$$

The same result for κ_t is also obtained with BOLTZMANN statistics instead of quantum statistics. Hence, if we employ this κ_t in the screening mass μ in the BORN cross section, we reproduce the energy loss calculated in the theoretically more advanced HTL approach. One advantage is that we can use the screened BORN matrix element also to calculate the cross section, which does not diverge and can be implemented in BAMPS. However, although this approach leads to the correct overall energy loss dE/dx , it does not reveal whether the energy loss per collision ΔE and the mean free path Δx individually are correctly described. Due to the HTL resummations in the soft region, also long-range interactions are probed. This corresponds to an increase in the number of scattering centers and, hence, an increase of the rate compared to the standard BORN cross section, while the energy loss per collision is expected to decrease. And indeed the resulting cross sections seem to be rather large whereas the mean energy transfer per collision is rather small. Although this goes in the expected direction, the presented prescription does not make any statement whether the rates or energy loss per collision are the same as one would obtain from a more sophisticated HTL scheme. Thus, this approach may only be an effective description to obtain the correct overall energy loss but not the microscopic details of the underlying processes. We discuss this in more detail in Section 5.3.

In Figure 5.1 the numerical result with BAMPS and $\kappa_t = 0.184$ is compared to the analytic formula (5.22) for BOLTZMANN statistics. For large jet energies—the regime in which the analytic formula is valid—the agreement with the numerical result is very good.

This comparison has also been done in Refs. [GA08, Pes12]. Ref. [GA08] calculated the energy loss with the full QCD matrix element (3.12) and not only the approximation from Equation (5.8). In this case an explicit dependence on t^* remains in the final dE/dx result. This dependence can only be neglected if $|t^*| > T^2$, a domain in which the HTL approximation is not necessarily valid anymore. However, if one screens also the hard part of the t channel

the heavy quark mass and, therefore, do not diverge for small t or u .

with Equation (3.17), the final result depends only weakly on $|t^*|$. With this procedure the authors find $\kappa_t \approx 0.16$ for a constant coupling and $\kappa_t \approx 0.11$ for a running coupling.

5.1.6. Running coupling

The analytic result of the heavy quark collisional energy loss obtained for a constant coupling, Equation (5.19) or (5.22), can be extended to include a running coupling by examining some simple considerations without performing the tedious calculation from the last sections again. To this end, we first derive the leading COULOMB and COMPTON logarithms, $\ln ET/m_D^2$ and $\ln ET/M^2$, respectively, in a simpler picture for a constant coupling, which is then generalized to a running coupling.

For the COULOMB logarithm we consider the dominant part of t channel scattering $\propto 1/t^2$ (cf. Equations (5.6) and (5.8)). Up to leading logarithmic accuracy the boundaries of the t integration in Equation (5.3) can be replaced by $t_{\min} = -\tilde{s}^2/s \simeq -s \rightarrow -ET$ and $t_{\max} \rightarrow -m_D^2$ [PP08a]. The latter expresses the presence of medium effects and is equivalent to screening the gluon propagator with the DEBYE mass (up to leading logarithmic accuracy). For a fixed coupling α_s the t integration yields the leading logarithm (cf. Equation (5.5)):

$$\alpha_s^2 \int_{-ET}^{-m_D^2} dt (-t) \frac{1}{t^2} = \alpha_s^2 \ln \frac{ET}{m_D^2}. \quad (5.26)$$

The running coupling for this channel should be evaluated at t (see (3.27) and the surrounding text), which influences the integration,

$$\begin{aligned} \int_{-ET}^{-m_D^2} dt \alpha_s(t)^2 (-t) \frac{1}{t^2} &= \left(\frac{4\pi}{\beta_0} \right)^2 \left[\frac{1}{\ln(-t/\Lambda^2)} \right]_{-ET}^{-m_D^2} = \left(\frac{4\pi}{\beta_0} \right)^2 \frac{\ln(ET/\Lambda^2) - \ln(m_D^2/\Lambda^2)}{\ln(ET/\Lambda^2) \ln(m_D^2/\Lambda^2)} \\ &= \alpha_s(ET) \alpha_s(m_D^2) \ln \frac{ET}{m_D^2}, \end{aligned} \quad (5.27)$$

where the representation of α_s from Equation (3.23) has been used, which simplifies for space-like Q to $\alpha_s(Q^2) = 4\pi/[\beta_0 \ln(-Q^2/\Lambda^2)]$.

The COMPTON logarithm stems from the u channel. Here, the running coupling should be evaluated at \tilde{u} (cf. Equation (3.27)) and the t integration in Equation (5.3), which is substituted by \tilde{u} , looks like

$$\int_{-ET}^{-M^2} d\tilde{u} \alpha_s(\tilde{u})^2 \frac{1}{-\tilde{u}} = \alpha_s(ET) \alpha_s(M^2) \ln \frac{ET}{M^2}. \quad (5.28)$$

The contribution to the constant beyond leading logarithmic accuracy is dominated by $|t| \simeq m_D^2$ and $|t| \simeq ET$ for the t channel and $|\tilde{u}| \simeq ET$ for the u channel. Since there is no singularity in these integrals, the coupling of these terms can be evaluated at an arbitrary scale between m_D^2 and ET [PP08a]. Therefore, we can just choose $\alpha_s^2 = \alpha_s(ET)\alpha_s(m_D^2)$ and

write for the total energy loss of a heavy quark with running coupling [PP08a]

$$\begin{aligned} \frac{dE}{dx} = \frac{4\pi T^2}{3} & \left[\alpha_s(ET) \alpha_s(m_D^2) \left(1 + \frac{n_f}{6}\right) \ln \frac{ET}{m_D^2} + \alpha_s(ET) \alpha_s(M^2) \frac{2}{9} \ln \frac{ET}{M^2} \right. \\ & \left. + \alpha_s(ET) \alpha_s(m_D^2) c(n_f) + \mathcal{O} \left(\alpha_s(ET) \alpha_s^2(m_D^2) \ln \frac{ET}{m_D^2} \right) \right] \end{aligned} \quad (5.29)$$

with $c(n_f)$ given in Equation (5.20).

For the BOLTZMANN case the energy loss reads

$$\begin{aligned} \frac{dE}{dx} = \frac{8T^2}{\pi} & \left[\alpha_s(ET) \alpha_s(m_D^2) \left(1 + \frac{n_f}{3}\right) \ln \frac{ET}{m_D^2} + \alpha_s(ET) \alpha_s(M^2) \frac{2}{9} \ln \frac{ET}{M^2} \right. \\ & \left. + \alpha_s(ET) \alpha_s(m_D^2) f(n_f) + \mathcal{O} \left(\alpha_s(ET) \alpha_s^2(m_D^2) \ln \frac{ET}{m_D^2} \right) \right] \end{aligned} \quad (5.30)$$

with $f(n_f)$ from (5.23).

5.2. Elastic energy loss in a flowing medium

In heavy-ion collisions the medium is not static but expands, which is fully taken into account in BAMPS calculations since it simulates the medium on the particle level without the need of thermodynamic variables. Therefore, it is intriguing to study the energy loss of heavy quarks analytically in a flowing thermal medium and compare it to BAMPS simulations.

In this section, we consider BOLTZMANN statistics for the medium particles. More precisely, they obey a JÜTTNER distribution, which is a generalization of the BOLTZMANN distribution for a non-vanishing velocity u_μ of the medium,

$$n_J(k) = e^{-\frac{u_\mu k^\mu}{T}} \quad (5.31)$$

with $u_\mu = \gamma(1, \mathbf{u})$ and $\gamma = 1/\sqrt{1-u^2}$. For $\mathbf{u} = 0$ the JÜTTNER distribution reduces to the standard BOLTZMANN distribution.

If we insert the JÜTTNER distribution in Equation (5.3) for $n_i(p_2)$, the right hand side is manifestly covariant since every factor ($n_i(p_2)$, t , and $d\sigma/dt$) and both integration measures ($d^3p_2/2E_2$ and dt) are covariant. Consequently, one could expect, as an educated guess, that the energy loss of a flowing medium can be simply obtained from Equation (5.19) or (5.22) by substituting $E \rightarrow p_\mu u^\mu$ in the leading logarithms. This is indeed the case as we showed analytically in Ref. [MPUG13] for the COULOMB logarithm.

Since the integrals with the JÜTTNER distribution are rather complex, we consider here only the special case that the flow of the medium is parallel to the heavy quark direction and show that the modification of the result due to the flowing medium indeed boils down to the substitution $E \rightarrow p_\mu u^\mu$.

To calculate the energy loss for the s and u channel as well as the hard part of the t channel for a flowing medium, the JÜTTNER distribution from Equation (5.31) must be inserted in Equation (5.3) instead of the BOLTZMANN distribution for a static medium. Performing

the phase space integration for gluon and light quark scattering, which is considerably more complicated with the JÜTTNER distribution, the energy loss reads

$$\begin{aligned}
 \frac{dE_q}{dx} \Big|_{|t|>|t^*|} &= \frac{8\alpha_s^2 T^2}{\pi} \frac{n_f}{3} \left[\ln \frac{4T\gamma E(1-u)}{|t^*|} - \gamma_E - \frac{3}{4} \right], \\
 \frac{dE_g}{dx} \Big|_{|t|>|t^*|}^{t \text{ channel}} &= \frac{8\alpha_s^2 T^2}{\pi} \left[\ln \frac{4T\gamma E(1-u)}{|t^*|} - \gamma_E - \frac{3}{4} \right], \\
 \frac{dE_g}{dx} \Big|_{|t|>|t^*|}^{s,u \text{ channels}} &= \frac{8\alpha_s^2 T^2}{\pi} \frac{2}{9} \left[\ln \frac{4T\gamma E(1-u)}{M^2} - \gamma_E - \frac{5}{6} \right].
 \end{aligned} \tag{5.32}$$

Since we are only interested in the leading logarithms and not the exact value of the constant beyond logarithmic accuracy, we refrain from calculating the soft part of the t channel from HTL for a flowing medium.

For the parallel case, the four-product of the heavy quark momentum and the medium velocity is $\gamma E(1-u) = p_\mu u^\mu$. Inserting this in Equation (5.32) and summing up the contributions, gives for the energy loss of a heavy quark in a medium that flows parallel to the heavy quark propagation

$$\frac{dE}{dx} = \frac{8\alpha_s^2 T^2}{\pi} \left[\left(1 + \frac{n_f}{3}\right) \ln \frac{p_\mu u^\mu T}{m_D^2} + \frac{2}{9} \ln \frac{p_\mu u^\mu T}{M^2} + f_{u^\mu}(n_f) \right]. \tag{5.33}$$

Note, that this result is only derived for the special case of a medium flowing parallel to the heavy quark, although we have already inserted the general expression $p_\mu u^\mu$ to make a connection to the general result.

Comparing Equation (5.33) to the result of the static medium from Equation (5.22), the only modification is the substitution of E by $p_\mu u^\mu$. The simplicity of this result suggests that Equation (5.33) also holds for a medium flowing in an arbitrary direction. This has been explicitly verified for the COULOMB logarithm in Ref. [MPUG13] and also holds for the COMPTON logarithm.

Furthermore, Equation (5.33) can be interpreted as boosting the energy of the heavy quark in the rest frame of the medium and evaluating the energy loss there. The energy loss per unit length in the fluid rest frame is then the same as in the lab frame. This and covariant arguments would even suggest that the constant $f_{u^\mu}(n_f)$ is the same as for the static case $f(n_f)$, which can be numerically verified by comparing to BAMPS simulations (see below). However, to calculate the constant analytically, an HTL calculation for a flowing medium must be done, which is not subject of this work.

In Figure 5.2 the result from Equation (5.33) is tested numerically with BAMPS for parallel and perpendicular flow with respect to the heavy quark direction. If the medium flows in the opposite direction with respect to the heavy quark propagation, the energy loss of the latter is enhanced since it experiences an additional “headwind” from the medium. In contrast, the energy loss is reduced if the medium flows in the direction of the heavy quark jet. The agreement between the analytical and numerical result is very good. The small difference between both curves is also present for $v_z = 0$, which indicates that we are not fully in the regime $E \rightarrow \infty$, in which the analytic formula is valid—despite using a jet energy of $E = 500$ GeV (cf. also Figure 5.1). The independence of this difference on the velocity indicates that the constant beyond logarithmic accuracy is indeed independent of the flow, $f_{u^\mu}(n_f) = f(n_f)$.

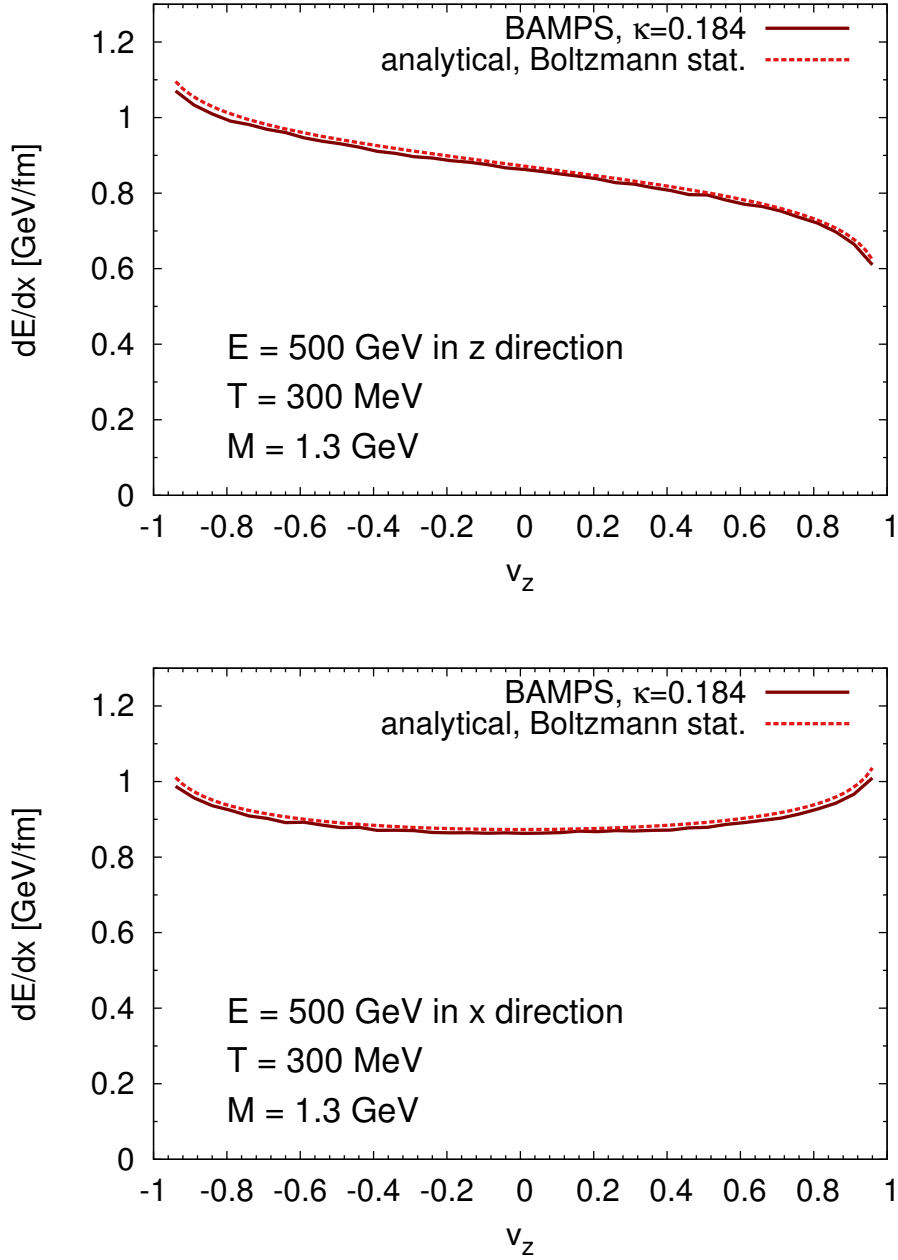


Figure 5.2.: Energy loss per unit length dE/dx as a function of the velocity v_z of a medium of gluons ($n_f = 0$) with temperature $T = 300$ MeV. In the upper plot the flow is parallel to the jet, which propagates in the positive z direction. In the lower plot the flow is transverse to a jet in x direction. The numerical results from BAMPS with the BORN cross section and a screening mass with $\kappa_t = 0.184$ are compared to the analytical results from Equation (5.33) for BOLTZMANN statistics.

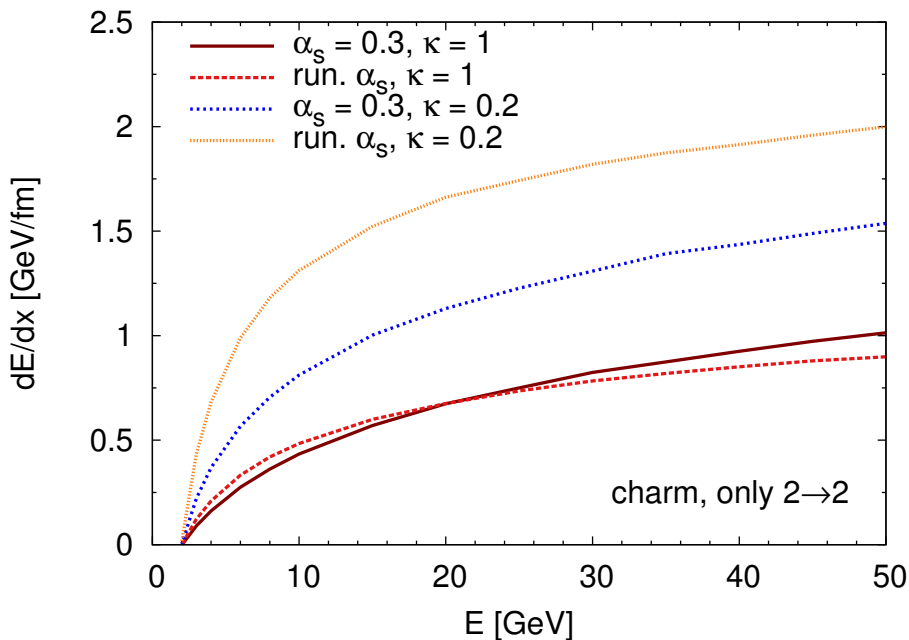


Figure 5.3.: Elastic energy loss per unit length of a charm quark ($M = 1.3$ GeV) with energy E traversing a static thermal medium with a temperature of $T = 0.4$ GeV. The curves are for constant or running coupling and DEBYE mass prefactor $\kappa_t = 1$ or $\kappa_t = 0.2$.

5.3. Elastic vs. radiative energy loss in a static medium

In Section 5.1 we calculated the elastic heavy quark energy loss analytically and made some first comparisons to simulations with BAMPS. Here, we take a closer look on the numerical calculations as well as address the differences between elastic and radiative energy loss.

First, to make a connection to the previous sections, we discuss BAMPS simulations of the elastic energy loss for constant and running coupling as well as different values for the DEBYE mass prefactor κ_t . The latter is defined in Equation (3.17) and is usually simply set to one. However, in Section 5.1.5 we derived an improved screening procedure that reproduces the energy loss derived from HTL calculations when setting the prefactor to $\kappa_t = 1/2e \simeq 0.184 \simeq 0.2$.

All the calculations in this section are done for a static thermal medium with a temperature of $T = 400$ MeV. The cross sections for the binary scatterings are given in Section 3.1, where also the idea of the κ_t factor and the running coupling is motivated in detail.

Figure 5.3 shows the energy loss per unit length of a charm quark in a static medium as a function of its energy. The first curve is the generally applied pQCD result employing a cross section with the standard DEBYE screening ($\kappa_t = 1$) and a constant coupling of $\alpha_s = 0.3$. The energy loss for this configuration is rather small. The curve for $\kappa_t = 1$, but with a running coupling has quite similar values but a slightly different energy dependence. As one would expect from the running coupling, the energy loss for small (large) E is stronger (weaker) than for the constant case.

Lowering the screening mass by the factor $\kappa_t = 0.2$ increases the cross section significantly

(cf. Figure 3.5). As a consequence, also the energy loss rises. For a running coupling, this effect is even more pronounced since the coupling also enters in the definition of the DEBYE mass (cf. Equations (3.18) and (3.27)). For a large jet energy, the momentum transfer is also sizeable and, hence, the coupling smaller than 0.3. Consequently, the DEBYE mass is smaller and the cross section as well as energy loss are larger than for a fixed $\alpha_s = 0.3$.³

We have compared the elastic energy loss of heavy quarks in BAMPS with two other models that also feature the improved screening procedure and the running coupling. A model developed by PESHIER [Pes12], which is based on transition probabilities, was extended by MEISTRENKO to include the same physics of elastic interactions. In detailed comparisons of the heavy quark energy loss in a static as well as flowing medium we found a perfect agreement between this model and BAMPS [MPUG13]. We also compared the energy loss in a static medium with results from the Nantes group [GA08, GBA09]. Due to different parameter choices, their energy loss is about 20% larger.⁴ In their model the maximum value of the coupling α_s^{\max} (see Section 3.1.3) is set to 1.117 instead of 1.0 as in BAMPS. The scale of the running coupling in the definition of the DEBYE mass from Equation (3.21) is not set to the momentum transfer t but to the DEBYE mass itself, $\alpha_s(-m_D^2)$, leading to an iterative determination of the DEBYE mass. If we implement their parameter choices in BAMPS, we find a perfect agreement in the energy loss (and also in more differential variables such as the rate, energy loss per collision, or transport coefficient).

As mentioned before, setting $\kappa_t = 0.2$ reproduces the HTL energy loss and is, thus, well motivated from the theory perspective. However, this matching holds primarily for the energy loss and does not make any statement about more differential variables like the energy loss per collision ΔE and the rate R (or the mean free path λ). These quantities are related to the energy loss per unit length in a static thermal medium via

$$\frac{dE}{dx} \simeq \frac{\Delta E}{\lambda} = \frac{R \Delta E}{v}, \quad (5.34)$$

where v is the velocity of the heavy quark.

In contrast to the analytic HTL calculation, these variables are accessible in BAMPS simulations. Figure 5.4 shows the collision rate and energy loss per collision for the same configurations as in Figure 5.3. Multiplying these curves for each E gives essentially the dE/dx curves from Figure 5.3 since the velocity for high-energy charm quarks is nearly one.

The increased energy loss for the improved screening $\kappa_t = 0.2$ is completely dominated by the increased rate. The energy loss per collision is even smaller for $\kappa_t = 0.2$ than for the standard DEBYE screening. The reason for the large rate is the sizeable cross section due to the small screening mass. On the other hand, a small screening mass leads to a stronger peak of the differential cross section $d\sigma/dt$ at small momentum transfers $|t|$ (see Figure 3.6). Consequently, the energy loss per collision decreases.

Although the energy loss per unit length of the improved screening scheme gives the correct result, as has been verified in Section 5.1.5, it is questionable whether the microscopic treatment

³Although this reasoning holds in principle also for $\kappa_t = 1$, the effect in that case is much less pronounced.

For the $\kappa_t = 0.2$ case the screening mass is significantly smaller, which renders the cross section to be very sensitive on its exact value. Furthermore, the energy loss is a complicated interplay between increased rates and decreased energy loss per collision for running coupling or $\kappa_t = 0.2$ compared to constant coupling and $\kappa_t = 1$, as we will discuss in the following and is shown in Figure 5.4.

⁴This also gives an indication why they need a smaller K factor to explain the open heavy flavor data with only binary interactions, cf. Section 6.1.

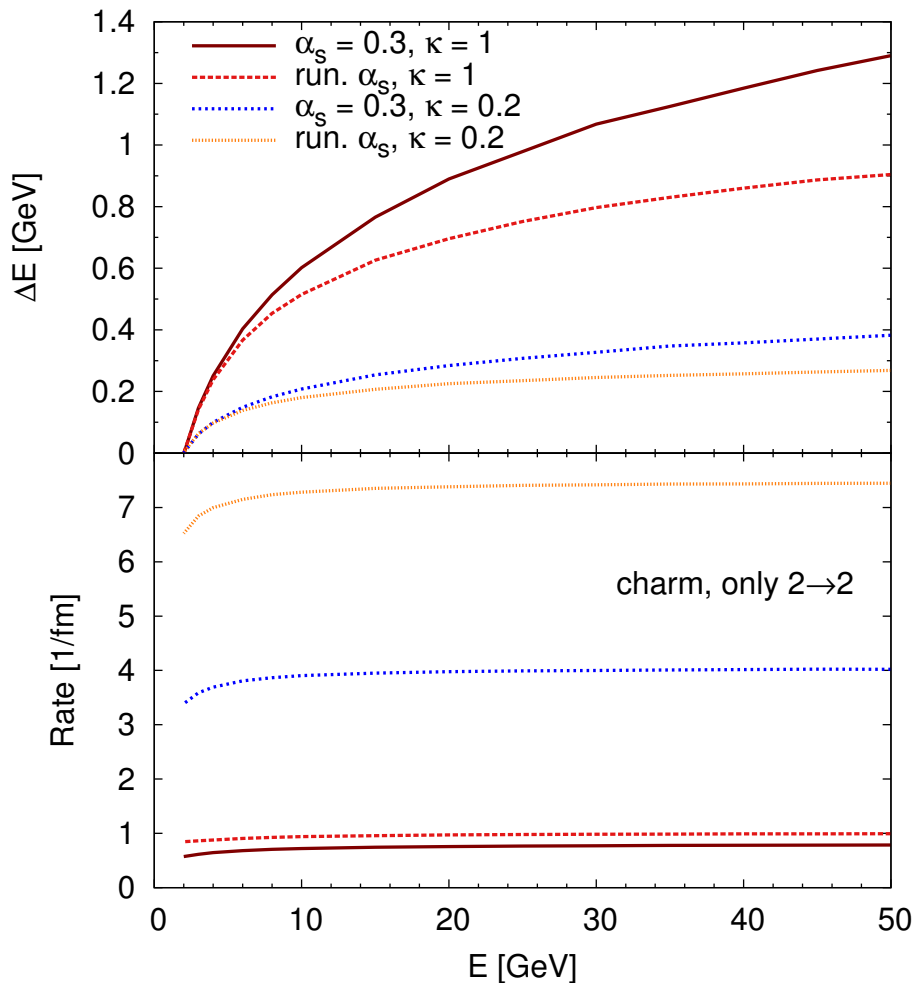


Figure 5.4.: Energy loss per collision and collision rate of a charm quark in a static thermal medium for the same configurations as in Figure 5.3.

of this effective procedure is accurate. The huge rate and small energy loss per collision raise at least some concerns regarding this treatment. However, we expect that the effective treatment gives correct results for observables that merely depend on the energy loss of the particles such as the nuclear modification factor. Nevertheless, as we will see below, problems occur on the microscopic level, for instance, when implementing the LPM effect (see Section 3.2.7) for radiative processes.

We now turn to the radiative energy loss. The cross sections of $2 \rightarrow 3$ processes are calculated in Section 3.2. Within the GUNION-BERTSCH approximation the radiative matrix element factorizes in the $2 \rightarrow 2$ matrix element and a factor for the emitted gluon, see Equation (3.82). For the binary part of the radiative process we employ the same matrix element as for the $2 \rightarrow 2$ process, including the running coupling and κ_t factor. The screened gluon emission factor is given in Equation (3.84).

Figure 5.5 depicts the elastic and radiative energy loss of light, charm, and bottom quarks for a constant coupling and standard DEBYE screening. The radiative energy loss is larger

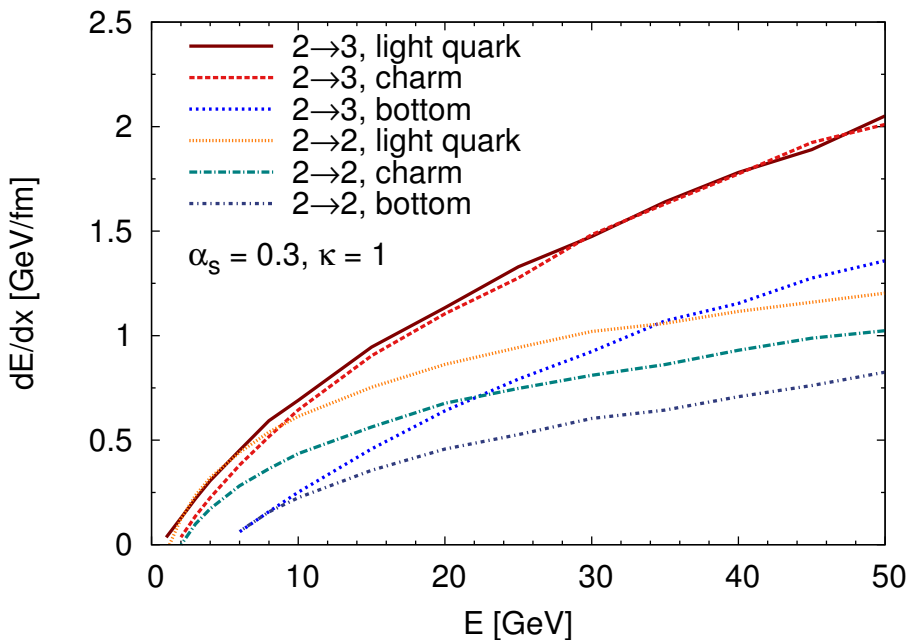


Figure 5.5.: Elastic and radiative energy loss per unit length of a light quark ($M = 0$ GeV), a charm quark ($M = 1.3$ GeV), and a bottom quark ($M = 4.6$ GeV) traversing a static thermal medium with temperature $T = 0.4$ GeV. The curves are calculated with constant coupling and DEBYE mass prefactor $\kappa_t = 1$.

than the elastic energy loss for all quark masses. While both have similar sizes at small energy, they differ by about a factor of two at larger energies for all flavors. The mass hierarchy is visible for both the elastic and radiative energy loss—heavy quarks lose less energy. However, between light and charm quarks the difference for the radiative energy loss is only marginal. As we have mentioned in Section 3.2.7, the LPM effect suppresses the gluon emission at small angles and partly overshadows the dead cone of heavy quarks. The charm quark dead cone is rather small at larger energies. Consequently, the energy loss is mostly influenced by the LPM suppression, which renders the charm and light quark curves to be rather similar.

This reasoning can be nicely verified by looking at the angular distribution of the gluon emitted off a light and charm quark jet. In the left panel of Figure 5.6 the differential cross section is depicted as a function of the gluon emission angle with respect to the jet for light, charm, and bottom quarks. The distributions of light and charm quarks are very similar. Small angles are suppressed due to the LPM effect, but no additional dead cone suppression for charm jets can be seen.

In the right panel of Figure 5.6 the mean free path that enters in the LPM effect is not determined iteratively (which is the default implementation in BAMPS), but set by hand to a large value of $\lambda = 10$ fm. Hence, the LPM suppression is reduced and smaller angles are allowed. Consequently, the suppression due to the dead cone effect becomes visible again, which results in a stronger suppression of charm quarks at small angles compared to light quarks. As a note, the total cross sections of all quarks are larger for $\lambda = 10$ fm compared to the default implementation since the LPM suppression is reduced.

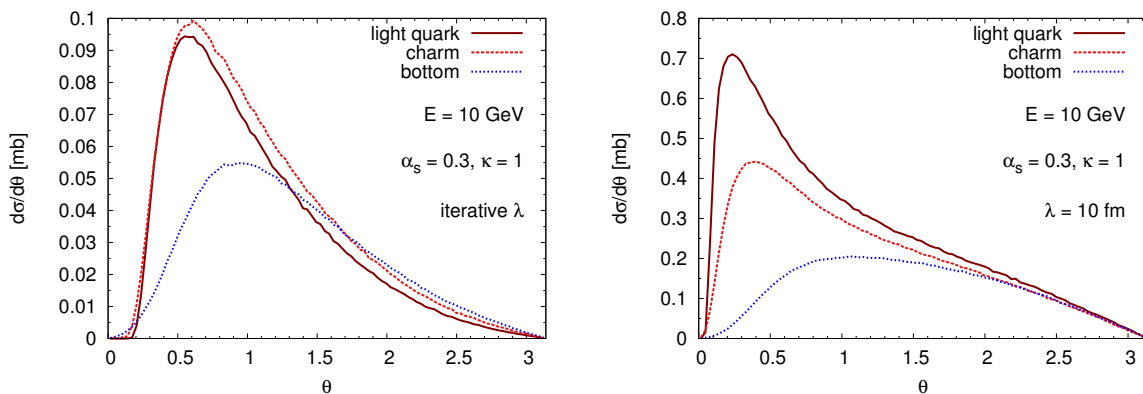


Figure 5.6.: Average differential cross section $d\sigma/d\theta$ of a light, charm, and bottom quark jet with energy $E = 10$ GeV as a function of the angle θ , at which the gluon is emitted in the lab frame with respect to the jet direction. For the left plot the mean free path that enters in the LPM effect is determined iteratively, while for the right plot it is set by hand to the large value of $\lambda = 10$ fm.

In contrast to charm quarks, the dead cone for bottom quarks is more pronounced and is even visible for an iteratively calculated mean free path. Hence, also the energy loss in Figure 5.5 is considerably smaller than for lighter quark flavors. The similar energy loss of light and charm quarks could be an explanation why the measured nuclear modification factors of charged hadrons and D mesons in heavy-ion collision have the same values. We discuss this in more detail in Section 6.2.

If we employ a running coupling, the findings change only modestly. As we saw in Figure 5.3 the elastic energy loss has a slightly different energy dependence but very similar values. However, Figure 5.7 shows that the radiative energy loss with a running coupling is significantly smaller than for a constant coupling at large energies. This is due to the LPM effect. The binary cross section for a running coupling is larger than for a constant coupling of $\alpha_s = 0.3$ (cf. rates in Figure 5.4). Hence, the mean free path is smaller, which leads to a stronger suppression. The mass hierarchy is barely present anymore. For a running coupling, the charm energy loss is slightly larger than for light quarks and even the bottom radiative energy loss is close to the light quark curve above $E = 30$ GeV. This is again a possible explanation for the similar suppression of light and heavy flavor in heavy-ion collisions.

The picture changes significantly if we consider not only a running coupling, but also the improved DEBYE screening. As we saw in Figure 5.4 the binary rate for $\kappa_t = 0.2$ is very large. Hence, the mean free path is small and we expect a considerable suppression of the radiative energy loss due to the LPM effect. Figure 5.8 confirms that this is indeed the case. The radiative contribution is so strongly suppressed that it can basically be neglected compared to the elastic energy loss. We only depict the curves for heavy quarks since the improved screening was solely derived for massive quarks in Section 5.1.

As discussed above, the huge binary rate is rather unphysical and also the small radiative contribution does not seem to be very sensible. The only way to circumvent this problem would be the implementation of a more accurate screening procedure, preferably by considering the gluon self energy in the HTL framework. However, this is a very complex task and seems nearly

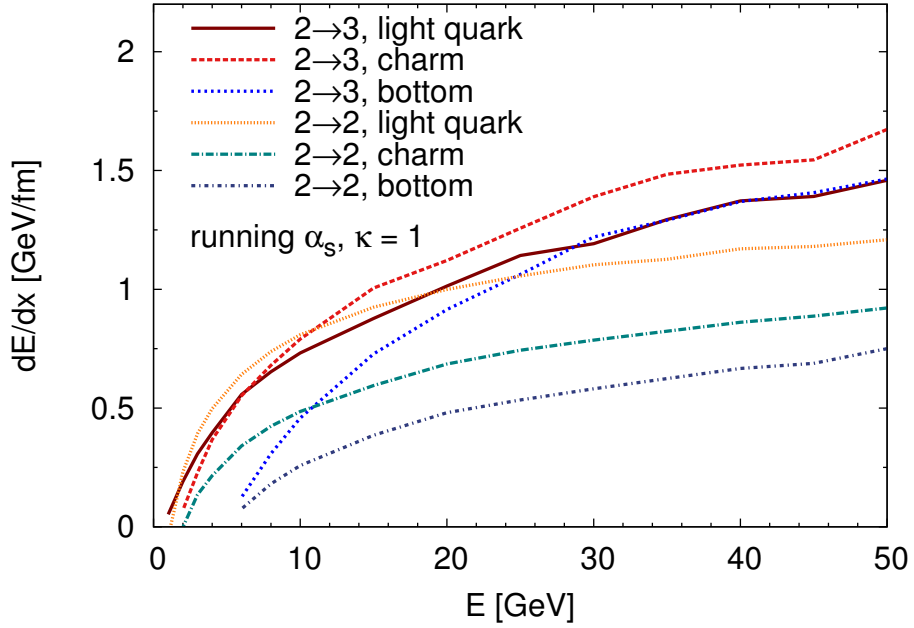


Figure 5.7.: As Figure 5.5 for a running coupling and DEBYE mass prefactor $\kappa_t = 1$.

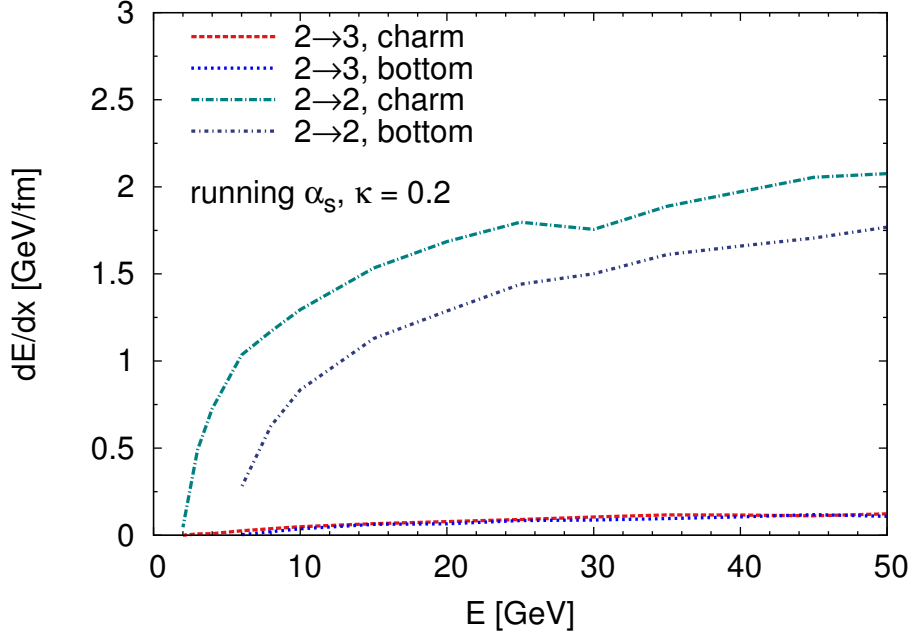


Figure 5.8.: As Figure 5.5 for a running coupling and DEBYE mass prefactor $\kappa_t = 0.2$. Light quarks are not shown since the κ_t parametrization has only been derived for heavy quarks (cf. previous sections).

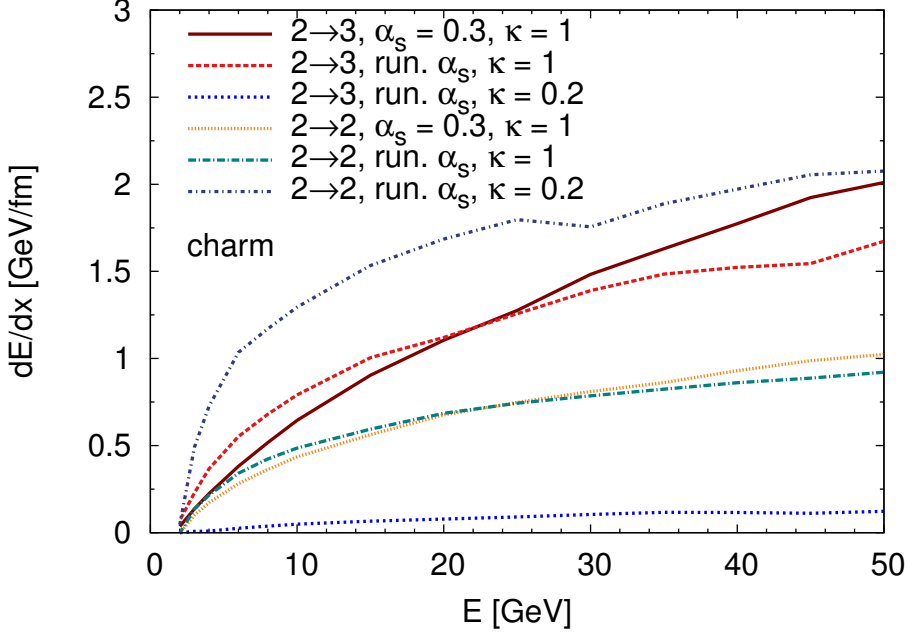


Figure 5.9.: Elastic and radiative energy loss per unit length of a charm quark in a static medium for constant or running coupling as well as $\kappa_t = 1$ or $\kappa_t = 0.2$.

impossible to be implemented in a transport model. Hence, we stick to the effective DEBYE screening and explore in this section as well as in Section 6.2 the limits of this prescription.

Figure 5.9 summarizes the energy loss scenarios from the previous figures for the case of a charm quark. The radiative energy loss for constant and running coupling with standard DEBYE screening is twice as large as the elastic energy loss. The improved DEBYE screening leads to a large elastic energy loss, but suppresses the radiative energy loss enormously due to the LPM effect.

For these configurations we also depict the energy loss per collision and the collision rate in Figures 5.10 and 5.11, respectively. The energy loss per collision is larger for radiative processes than for binary interactions due to the third particle in the final state. As we observed in Figure 5.4 already for the binary case, the energy loss per collision is largest for a constant coupling and standard DEBYE screening and smaller for running coupling and/or improved screening due to a stronger peaking of the differential cross section at small $|t|$. A difference from this hierarchy is only present for radiative processes with improved screening and running coupling because of the strong modification of the phase space due to the LPM suppression. The binary rate for $\kappa_t = 0.2$ and running coupling is again much larger than for the other configurations. As a result, the radiative rate for the same configuration is negligibly small because of the LPM effect.

We saw before that the radiative energy loss of light and heavy quarks only differs slightly, although the collisional energy loss has very different values. This is a consequence of the implementation of the LPM effect. Without any LPM suppression the radiative energy loss of light quarks would be larger than that of heavy quarks. But since the binary rate is also larger for light quarks, the LPM suppression is stronger for light quarks than for heavy quarks,

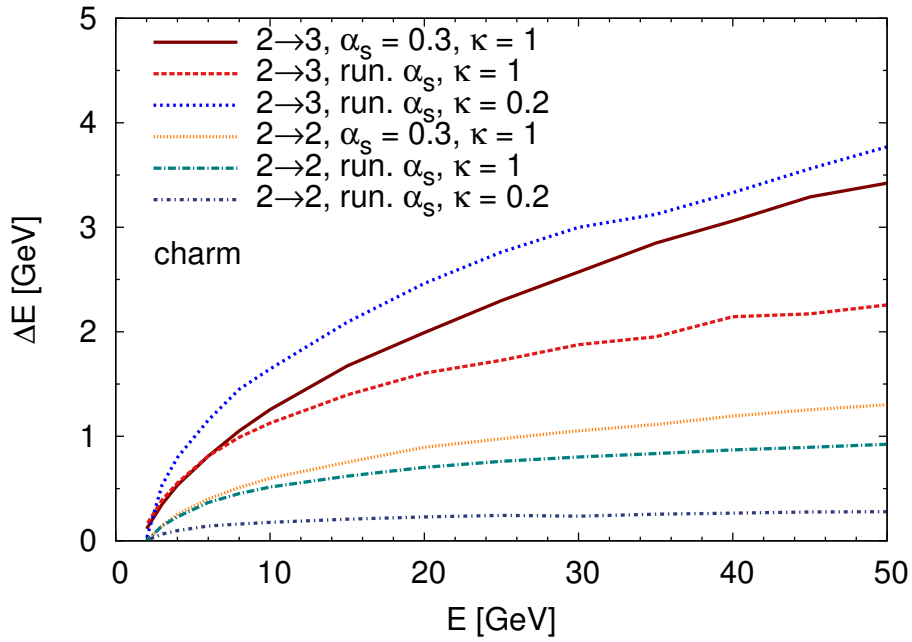


Figure 5.10.: Energy loss per collision of a charm quark for constant or running coupling and different choices of κ_t .

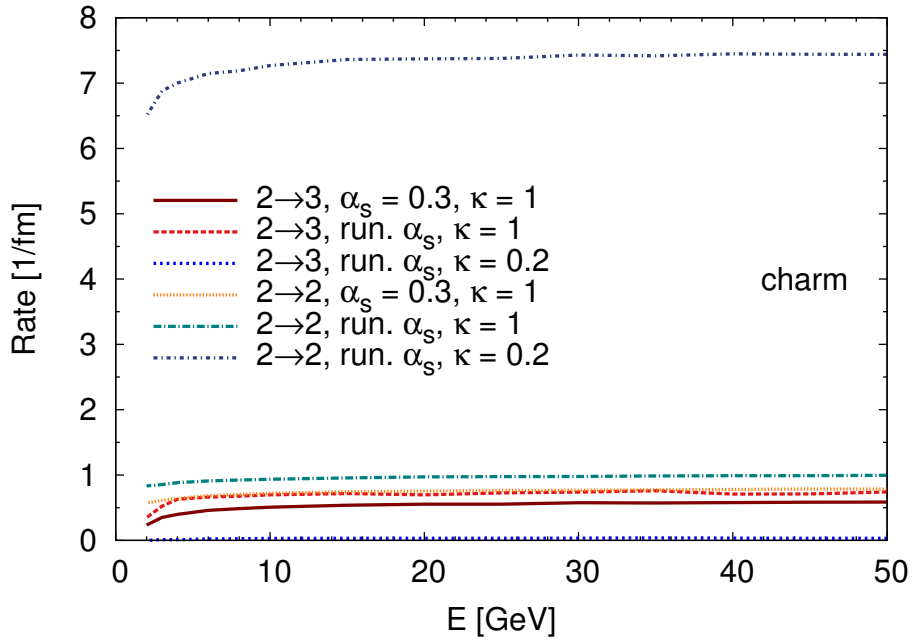


Figure 5.11.: Collision rate of a charm quark for constant or running coupling and different choices of κ_t .

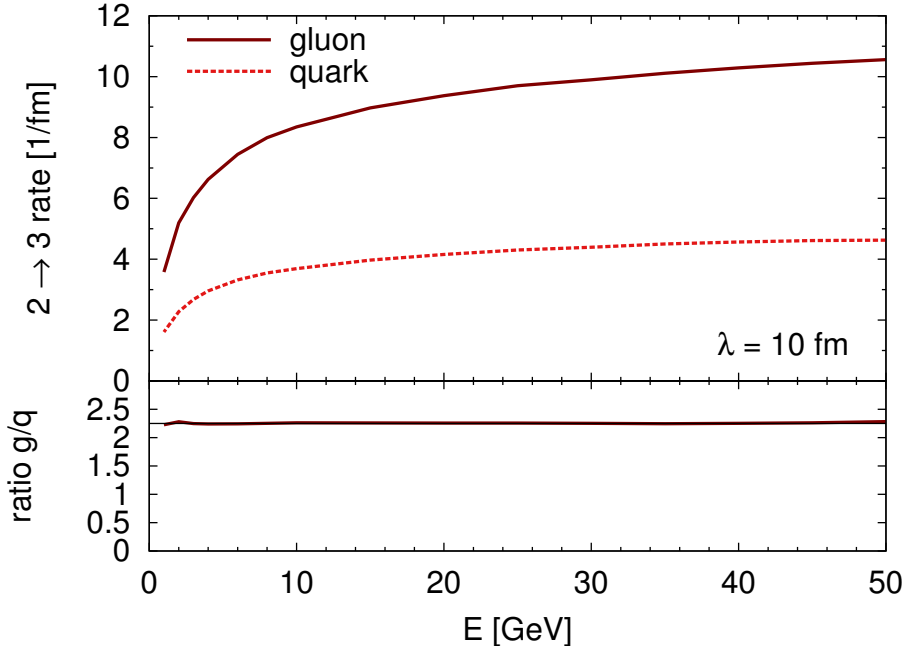


Figure 5.12.: Radiative collision rate of gluons and light quarks with a fixed value for the mean free path $\lambda = 10$ fm that enters in the LPM implementation.

which decreases the radiative energy loss of light quarks more than that of heavy quarks. This effect and the previously mentioned overshadowing of the dead cone effect by the LPM effect lead to the observation that the radiative energy loss of light and charm quarks takes very similar values.

The same effect can also be observed when comparing the radiative energy loss of gluons and light quarks. The ratio of the binary cross sections of energetic gluons and light quarks is the color factor $9/4$. This also holds for the radiative cross sections (cf. Section 3.2.1) if no LPM suppression is present or if we employ the same mean free path that enters in the LPM implementation for both species instead of calculating it iteratively according to Equation (3.116).

Figure 5.12 depicts the $2 \rightarrow 3$ rate for gluons and light quarks with setting a fixed mean free path of $\lambda = 10$ fm for the LPM effect by hand. And indeed, the ratio of both curves lies exactly at $9/4$. In contrast, Figure 5.13 shows the rates for gluons and light quarks with the default implementation that the mean free path for the LPM effect is calculated iteratively and, therefore, is actually the mean free path of the jet. As for the energy loss of massless and massive quarks, the difference due to the color factor is screened by the iterative computation of the mean free path. Gluons have a larger binary and radiative rate (without LPM), which leads to a stronger suppression of radiative processes compared to light quarks. This effect even overcompensates the difference due to the color factor and the radiative rate of light quarks becomes even slightly larger than that of gluons.

The LPM effect in BAMPS is implemented via a Θ function in the integrand of the $2 \rightarrow 3$ cross section, as discussed in Section 3.2.7. Since the prefactor of the formation time of the emitted gluon calculated in Section 3.2.6 is not rigorously defined and varies in the literature,

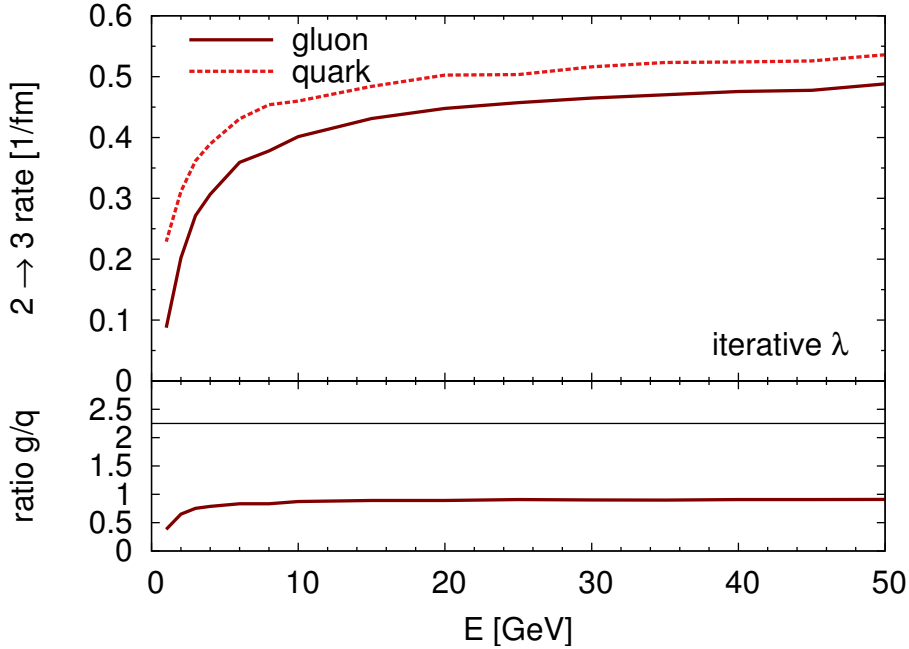


Figure 5.13.: Radiative collision rate of gluons and light quarks with the default implementation of the LPM effect, which calculates the mean free path iteratively. The expected ratio of $9/4$ of gluon and light quark rates without LPM effect is indicated by the solid thin line.

it is interesting to study the dependence of the radiative energy loss on this parameter. We include it in BAMPS by modifying the Θ function from Equation (3.118),

$$\Theta(\lambda - \tau) \rightarrow \Theta(\lambda - X\tau) . \quad (5.35)$$

Obviously, $X = 1$ corresponds to the default implementation and the previously presented results. An X smaller than one, effectively lowers the gluon formation time and reduces the suppression. Consequently, the energy loss increases, as depicted in Figure 5.14. Since our implementation resembles the BETHE-HEITLER regime of independent scatterings and completely suppresses interference effects, $X < 1$ is closer to the physical reality—LPM suppression is still present, but it is smaller than in the crude rejection of all possibly interfering processes. For completeness, we also show in Figure 5.14 the $X = 2$ case, which has a smaller energy loss very similar to the elastic one. Furthermore, the default implementation ($X = 1$) is depicted, but with setting a large mean free path ($\lambda = 10$ fm) by hand instead of calculating it iteratively from the rates. This case corresponds to a very small LPM suppression and, hence, the charm quark loses a lot of energy radiatively.

Figure 5.15 depicts the X dependence of the energy loss for light, charm, and bottom quarks with an energy of $E = 10$ GeV. The total cross section depends logarithmically on X . Since the energy loss per collision is only mildly influenced by X , the energy loss per unit length is also logarithmically dependent on X , $dE/dx \sim \ln 1/X$. As discussed above, the energy loss of light quarks and charm quarks is comparable for $X = 1$ (cf. Figure 5.5) because an LPM dead cone overshadows the mass dead cone of the charm quark. For $X < 1$ the impact of the

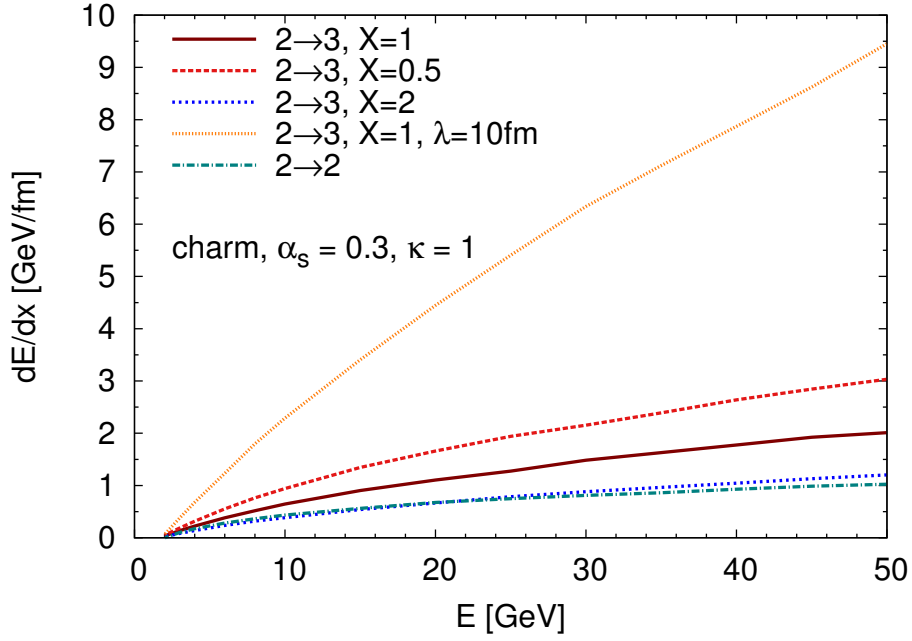


Figure 5.14.: Dependence of the radiative energy loss of a charm quark on the LPM effect. X denotes a prefactor in the LPM Θ function from Equation (3.118), which is modified to $\Theta(\lambda - X\tau)$. The $X = 1$ case is also shown for $\lambda = 10\text{fm}$, i.e., a small LPM suppression.

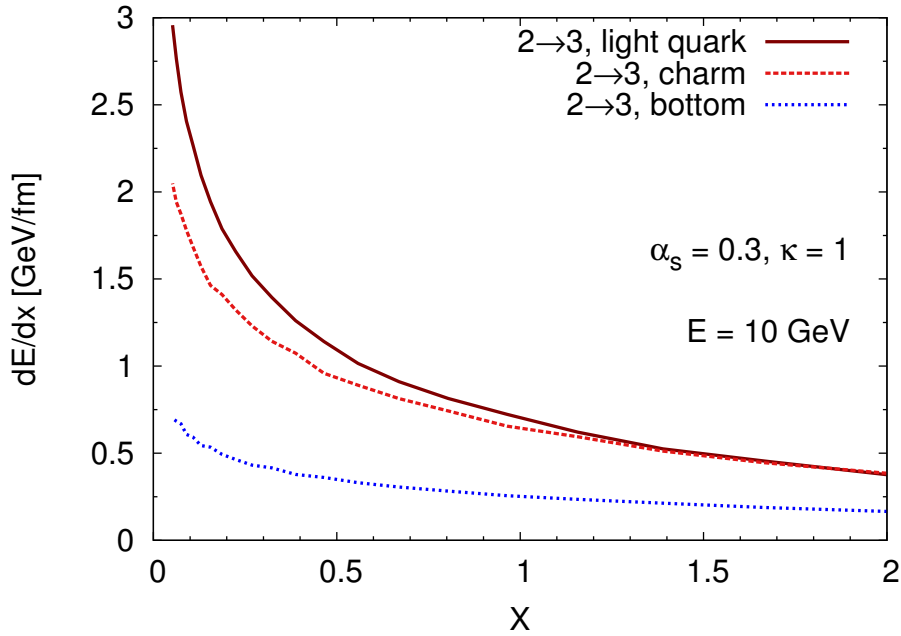


Figure 5.15.: Dependence of the radiative energy loss of light, charm, and bottom quarks with $E = 10\text{ GeV}$ on X , which denotes a prefactor in the LPM cut-off, $\Theta(\lambda - X\tau)$. $X = 1$ corresponds to the default value.

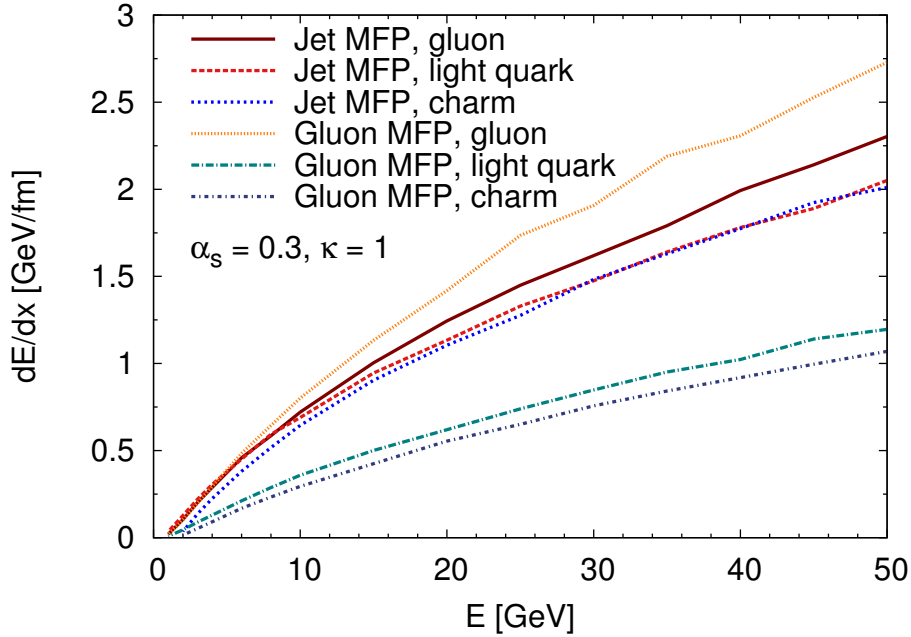


Figure 5.16.: Dependence of the radiative energy loss of a gluon, light quark, and charm quark on the choice of the mean free path (MFP) that enters as a parameter in the LPM implementation. “Jet MFP” means that the mean free path of the incoming jet particle is considered, which is the default choice in BAMPS (cf. Section 3.2.7). “Gluon MFP” compares the formation time to the mean free path of the emitted gluon. For simplicity, in this case the mean free path is set to the mean free path of a thermal gluon.

LPM effect is reduced and the energy loss of charm quarks becomes smaller than that of light quarks, which is in accordance with the expectations from the dead cone effect.

As discussed in Section 3.2.7, the mean free path of the jet is compared to the formation time of the gluon to determine whether the process is forbidden due to the LPM effect. This implementation corresponds to the QED picture of the LPM effect. In QCD, also the emitted gluon rescatters off other medium constituents. Therefore, comparing the mean free path of the emitted gluon to its formation time would be more in the spirit of QCD. However, this would be very demanding computational-wise since the collision dynamics have to be sampled before knowing if the scattering actually takes place. Consequently, to estimate the effect, we assume the emitted gluon to be thermal and just take the thermal mean free path of a gluon as an input for the LPM effect.

Figure 5.16 compares the radiative energy loss of gluons, light quarks, and charm quarks obtained with this procedure to the default LPM implementation where the mean free path of the jet particle is considered. As we saw before, the radiative energy loss of gluons, light quarks, and charm quarks is very similar for the default LPM implementation with the jet mean free path since the differences due to color factors or masses are screened by the LPM effect. If we now calculate the LPM suppression with the gluon mean free path, the gluon radiative energy loss changes only marginally since the thermal gluon mean free path differs only slightly from that of an energetic gluon. For light and charm quarks, however, the radiative energy loss

decreases significantly. This is due to the thermal gluon mean free path, which is dominated by elastic collisions and, therefore, about a factor of $9/4$ smaller than for highly energetic quarks. Since the gluon, light quark, and charm quark energy loss is calculated with the same mean free path of the emitted gluon entering in the LPM effect, also the radiative energy loss of gluons and quarks now differs by a factor of about $9/4$.

6. Open heavy flavor in heavy-ion collisions

The true mystery of the world is the visible, not the invisible.

The Picture of Dorian Gray
OSCAR WILDE

In this chapter we present BAMPS results on open heavy flavor observables such as the elliptic flow and nuclear modification factor and compare to the wealth of experimental data from RHIC and LHC. In Section 6.1 we first limit ourselves to include only elastic heavy quark processes while discussing their importance but also their problems in describing the data. In Section 6.2 radiative processes are then also included. We compare again to experimental data for different heavy flavor particles but also highlight differences compared to light particles.

As outlined in Section 4.1, heavy quarks and high-energy light partons studied in this section are set on top of fully simulated BAMPS background events to enhance the statistics of these rare probes. This treatment is in line with full BAMPS simulations, but neglects medium response effects. In this chapter we use solely background events calculated with the original GUNION-BERTSCH cross section, since they correctly reproduce bulk medium properties such as the measured elliptic flow of charged hadrons [XGS08, FUXG11, Foc11]. We checked that background events calculated with the improved GUNION-BERTSCH cross section, do not change the R_{AA} results presented in this section due to a similar number of scattering centers. However, the light parton elliptic flow with the improved GUNION-BERTSCH cross section might be reduced, which in turn would also decrease the elliptic flow of heavy quarks. Nevertheless, to determine this effect quantitatively, detailed calculations must be carried out, which is planned for the near future. In summary, the results in this section are calculated with a bulk medium that correctly features the experimentally measured properties and, thus, is appropriate to study the suppression and flow of hard probes.

6.1. Elliptic flow and nuclear modification factor from elastic collisions

6.1.1. RHIC

The leading order pQCD cross section for elastic heavy quark scatterings given in Section 3.1 with a constant coupling $\alpha_s = 0.3$ and the regular DEBYE screening mass for the t channel, i.e., $\kappa_t = 1$, is much too small to build up an elliptic flow that is in agreement with the experimental data of heavy flavor electrons at RHIC [UFXG10b, UFXG10c]. If we take the running of the coupling into account and determine the screening mass from comparison to hard-thermal-loop calculations, see Sections 3.1 and 5.1.5, we obtain an elliptic flow and R_{AA} that are much closer to the data [UFXG10c, UFXG11b]. However, since no radiative processes are included, it is

not surprising that the binary interactions alone—even with an improved DEBYE screening and running coupling—cannot explain the data.

In this section we summarize our findings from Refs. [UFXG12b, UFXG11a, UFXG10c, UFXG11b, UZF⁺11, UFXG12a, UFXG13a, UFXG13b], where we mimicked the lack of radiative or higher order contributions by scaling the binary cross section with an (artificial) K factor. To be compatible with the heavy flavor electron data for the elliptic flow measured by PHENIX [PHENIX11b], the elastic cross sections have to be multiplied with a factor $K = 4$ [UFXG11a, UFXG10c, UFXG11b, UZF⁺11, UFXG12a] if we consider heavy quarks in a purely gluonic plasma, and $K = 3.5$ [UFXG12b, UFXG13a, UFXG13b] if also light quarks are included (the reason for the deviation of the K factor is explained below).

As a note, for all calculations we assign the same kinematic acceptance cuts that are applied for the analysis of the experimental data (see labels in the plots for the values). The impact parameters used in BAMPS are matched with a GLAUBER calculation (cf. Appendix A.5) to the mean number of participants $\langle N_{\text{part}} \rangle$ given for each centrality class [PHENIX11b, ALICE11a].

First, we review the results for a pure gluonic plasma [UFXG11a], where we studied in particular the dependence of the heavy flavor observables on the initial model for the bulk medium. In Figure 6.1 we show the elliptic flow and nuclear modification factor of heavy quarks and heavy flavor electrons for a non-central Au+Au collision at RHIC obtained with BAMPS at the end of the QGP phase, that is, after the energy density of a given cell has dropped below $\epsilon_c = 0.6 \text{ GeV}/\text{fm}^3$ and interactions are not allowed any more (cf. Chapter 4).

One huge advantage of transport models is the direct access to all particles of the QGP during the whole time evolution. Therefore, we plot in addition to the heavy flavor electron curve the R_{AA} and v_2 of charm and bottom quarks. As can be seen in Figure 6.1 the curve of the heavy flavor electrons is shifted to smaller p_T compared to the parental heavy quarks due to fragmentation and decay processes (cf. also Section 4.1).

The binary cross section features the running coupling and an improved DEBYE screening (see Section 3.1). Since radiative contributions and quantum effects are missing, we try to determine the impact of those missing contributions by multiplying the cross section of $gQ \rightarrow gQ$ with an artificial factor $K = 4$, which is fitted to the elliptic flow data. BAMPS studies on the energy loss of light partons reveal that radiative contributions are dominant for light particles [FXG09, FXG10]. For heavy quarks these contributions are expected to be suppressed due to the dead cone effect (see Section 3.2.4), but as we saw in Section 5.3 the radiative energy loss is in most scenarios still considerably larger than the elastic energy loss. A larger contribution of radiative compared to elastic processes is also observed in other models [Mus05, WHDG07]. Consequently, we assume here that the implementation of radiative corrections like $gQ \rightarrow gQg$ could account for the missing factor of 4. In Section 6.2 we explicitly include the radiative processes and study whether these contributions have indeed the same effect as rescaling the binary cross section by a constant K factor. Furthermore, the consideration of quantum statistics would also enhance the cross section as is shown in Figure 5.1 for the energy loss and can, therefore, explain a part of the missing factor of 4.

Of course, a constant factor $K = 4$ is only an estimate for radiative contributions and quantum statistics. To explore the uncertainty of this factor the curves for $K = 3$ and 5 are also plotted in Figure 6.1 as gray bands for electrons and mini-jet initial conditions. Both observables v_2 and R_{AA} are not very sensitive on the exact value of K , although $K = 4$ gives the best agreement with the data.

Figure 6.1 compares the elliptic flow and heavy quark suppression obtained with two

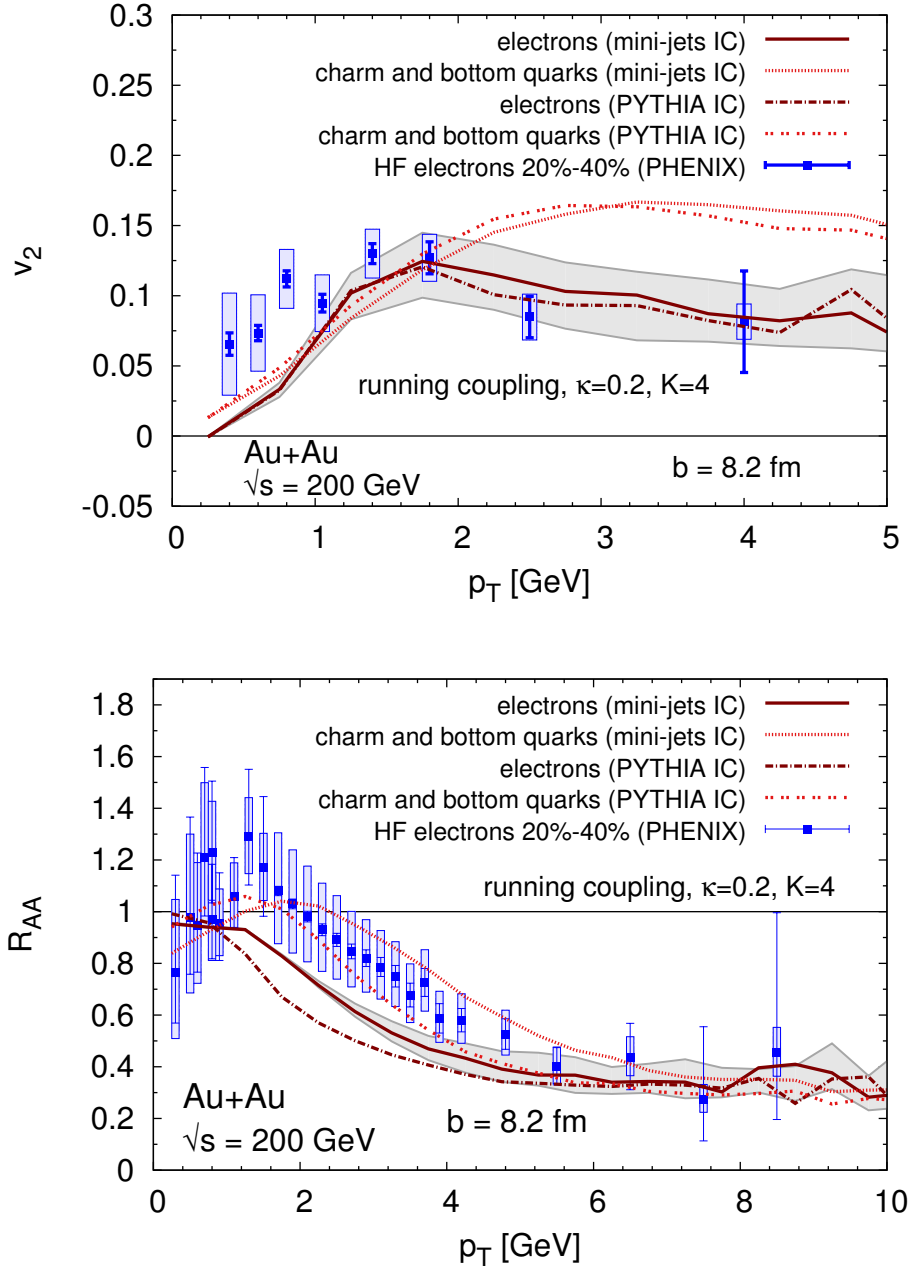


Figure 6.1.: Elliptic flow v_2 (top) and nuclear modification factor R_{AA} (bottom) of heavy quarks and heavy flavor electrons with pseudo-rapidity $|\eta| < 0.35$ as a function of transverse momentum for Au+Au collisions at RHIC with an impact parameter of $b = 8.2$ fm. The curves are obtained with PYTHIA and mini-jet initial conditions (IC) for a gluonic plasma ($n_f = 0+2$). The cross section of $gQ \rightarrow gQ$ is multiplied with the factor $K = 4$. To estimate the uncertainty of this K factor we plotted for mini-jet IC the electron curves for $K = 3$ and $K = 5$ as gray bands. For comparison, data of heavy flavor electrons for the centrality class of 20%–40% [PHENIX11b] are shown.

different initial conditions for the gluons. Both the PYTHIA and the mini-jet scenarios (see Section 4.5) lead to comparable curves, especially for larger p_T . This indicates that both heavy flavor observables are not very sensitive on the initial light parton distributions as long as the elliptic flow of light hadrons is reproduced, which has been shown for both mini-jet [XGS08, XG09, XG10] and PYTHIA [Foc11] initial conditions. However, in Ref. [GVvH⁺11] it was found that differences in the medium evolution can lead to modifications of the heavy quark suppression and elliptic flow up to a factor of two.

With $K = 4$ the agreement with the data is very good for large p_T . We emphasize that both v_2 and R_{AA} are described simultaneously within the same partonic transport model. For small p_T the employed hadronization scheme, namely, PETERSON fragmentation (see Section 4.1), is not suitable and coalescence might be the dominant process. It is expected that coalescence increases the elliptic flow at small transverse momenta since light quarks would also contribute to the flow of the heavy mesons. This could be an explanation why BAMPS underestimates the flow in Figure 6.1 for very small p_T . Neglecting cold nuclear matter effects such as the CRONIN effect or shadowing and also coalescence effects could be the reason for the deviation of the R_{AA} at small p_T . Recently, PHENIX measured the suppression factor R_{dAu} of heavy flavor electrons in deuteron-gold collisions to be larger than one at small p_T [PHENIX12], which points exactly in this direction.

These results are obtained with initial heavy quark distributions from MC@NLO. In addition, we employed heavy quark initial conditions from other NLO calculations [CNV05, Vog10] and found a good agreement with the curves shown in Figure 6.1. In contrast to PYTHIA, which we used in Refs. [UFXG10c, UFXG11b] for the initial heavy quark distributions, the electron spectrum from MC@NLO is slightly steeper for low p_T , which results in a less suppressed R_{AA} and, therefore, better agreement with the experimental data for $p_T < 3$ GeV.

To be compatible with the heavy flavor electron data for R_{AA} and v_2 at RHIC the elastic cross section had to be multiplied with a factor $K = 4$. Those calculations have been done without light quarks, $n_f = 0 + 2$ (number of light quarks + heavy quarks). In the following we present results from Refs. [UFXG12b, UFXG13a, UFXG13b], which feature a newer version of BAMPS that also includes light quark degrees of freedom ($n_f = 3 + 2$).

Figure 6.2 depicts the heavy flavor v_2 and R_{AA} for the pure gluonic calculations and the version including also light quarks. Comparing the $K = 4$ curves for $n_f = 0 + 2$ and $n_f = 3 + 2$ shows that both the suppression and elliptic flow are slightly higher for the latter. At first sight this seems counterintuitive since we use the same initial conditions from PYTHIA for both cases and, to get the same energy density, convert initial light quarks to gluons for $n_f = 0 + 2$, which are associated with a larger CASIMIR factor. However, the situation is more complex. The running coupling also depends on the number of flavors and is larger for $n_f = 3 + 2$ (see Figure 3.4). Furthermore, the chemistry of a purely gluonic plasma behaves slightly differently than a quark gluon plasma. This results in a larger number of scattering centers of the medium for $n_f = 3 + 2$. All influences combined lead to a slight increase of the suppression and elliptic flow for $n_f = 3 + 2$ compared to $n_f = 0 + 2$.

As can be seen in Figure 6.2 the best agreement with elliptic flow data for $n_f = 3 + 2$ is found with $K = 3.5$ in contrast to $n_f = 0 + 2$, where $K = 4$ yielded the best results. Again, we assume that this factor is necessary due to the lack of radiative processes and quantum statistics in our calculations, which we study in more detail in Section 6.2. As a note, the value of 3.5 is close to the needed K factor of Ref. [MPUG13], which—in an independent framework—included similar cross sections for $n_f = 3 + 2$ using ideal hydro as well as temperature and flow information

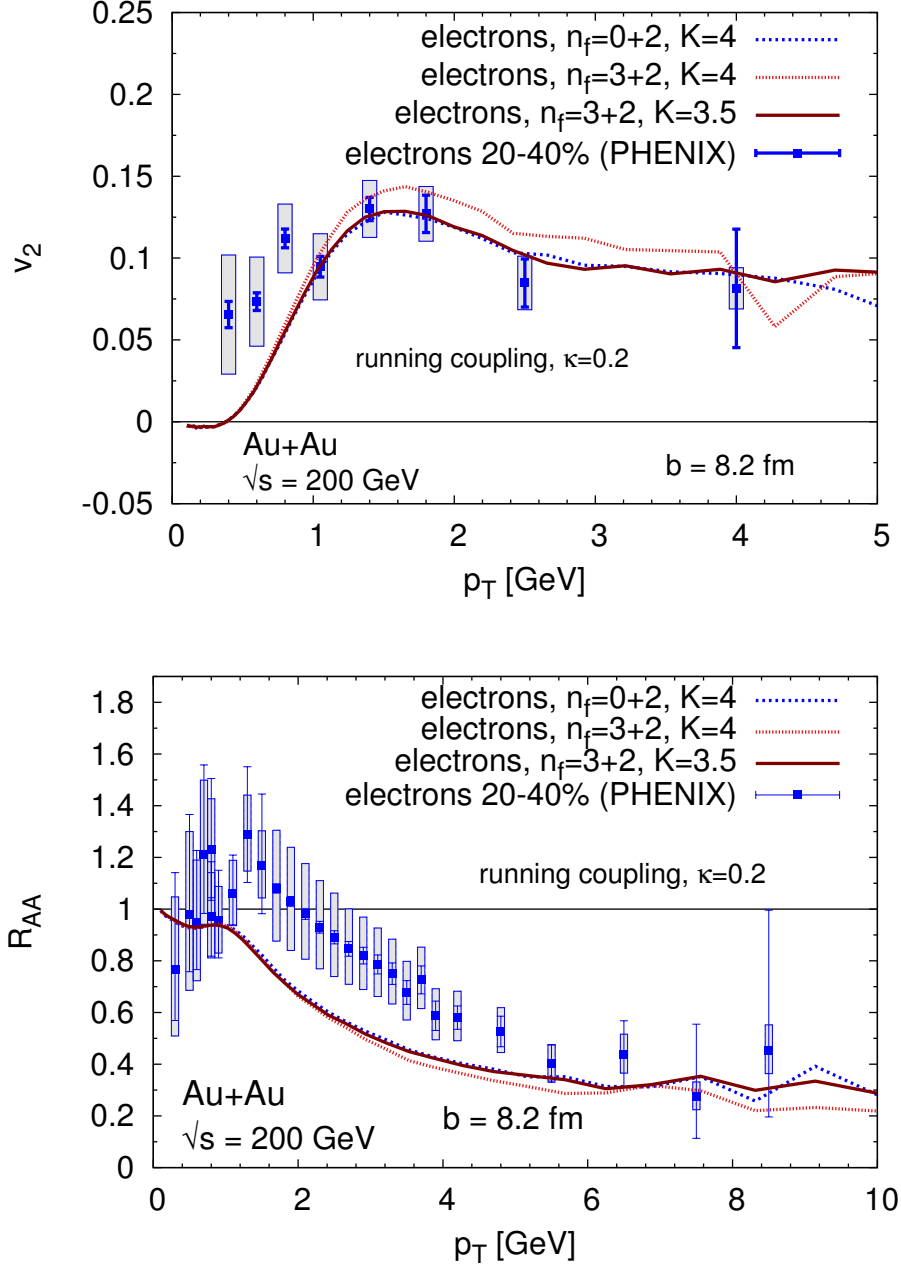


Figure 6.2.: As Figure 6.1, elliptic flow v_2 (top) and nuclear modification factor R_{AA} (bottom) of heavy flavor electrons at RHIC for different flavor configurations of the medium.

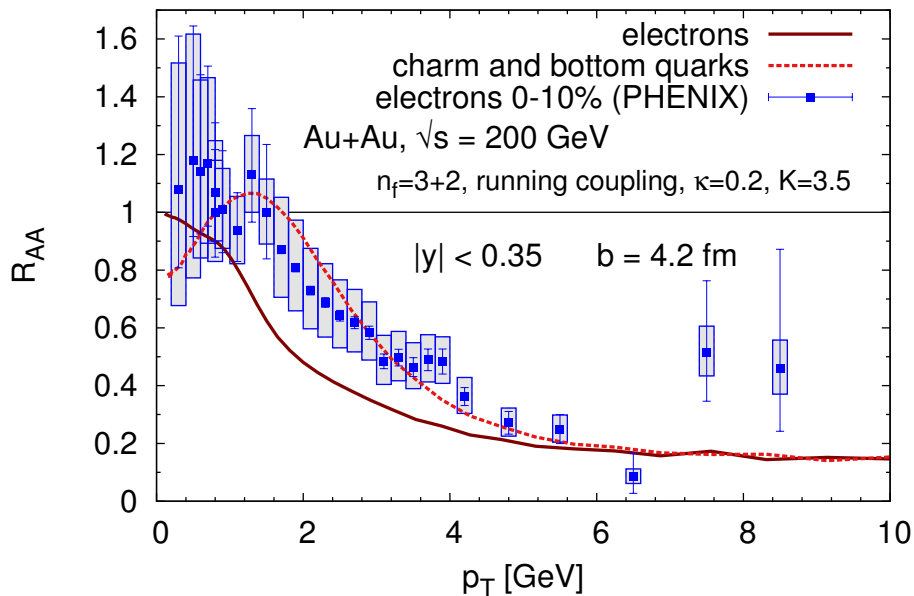


Figure 6.3.: Nuclear modification factor R_{AA} of heavy flavor electrons at RHIC for $b = 4.2$ fm with data [PHENIX11b].

from BAMPS for the medium evolution.

Although the agreement between the scaled BAMPS results and the data is very good for the elliptic flow, it slightly undershoots the R_{AA} data at small and intermediate p_T . This effect is also present in more central events, as is shown in Figure 6.3.

Since BAMPS solves the BOLTZMANN equation (cf. Section 4.1), which includes also non-equilibrium effects, BAMPS calculations explicitly consider the early phase of heavy-ion collisions where the medium is not thermalized yet. In contrast, many other models that rely on a hydrodynamic evolution of the background medium can only start after hydro is applicable, that is, after the medium is thermalized.

In Figure 6.4 the influence of such different treatments on the R_{AA} and v_2 is studied. To this end, we give heavy quarks different formation times, before which they are not allowed to interact with the rest of the medium. The first curve depicts the standard BAMPS implementation where the formation time of the heavy quark is set to the inverse of its transverse mass, $1/M_T$, which can be motivated from the uncertainty principle. For the second curve we give heavy quarks a formation time of 1 fm, which is often set as the starting time for hydrodynamic calculations. This mimics the implementation in many other models where the heavy quarks just stream freely before the hydrodynamic evolution starts. As can be seen from the figure, the suppression and elliptic flow gets considerably smaller if heavy quarks are not allowed to interact before 1 fm. Therefore, it is important to consider also the early non-equilibrium phase when studying the interactions of heavy quarks. In the following we thus set the formation time of heavy quarks again to the standard BAMPS choice of $1/M_T$.

A recent STAR upgrade makes it possible to reconstruct D mesons at small and intermediate transverse momenta also at RHIC [STAR13b]. In Figure 6.5 we compare our results for D

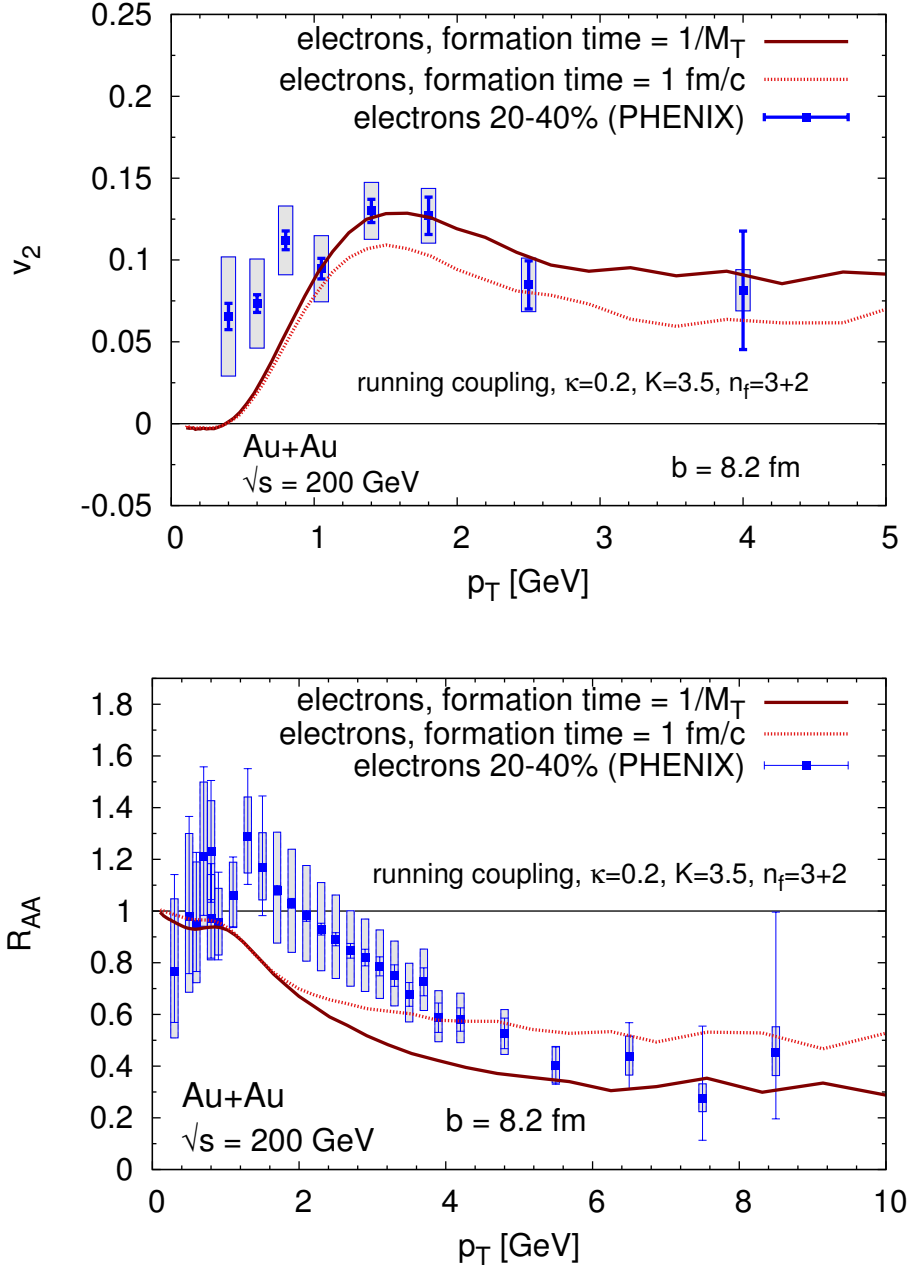


Figure 6.4.: As Figure 6.2, elliptic flow v_2 (top) and nuclear modification factor R_{AA} (bottom) of heavy flavor electrons at RHIC for the standard BAMPS formation time $1/M_T$ (M_T is the transverse mass) and a larger formation time of 1 fm.

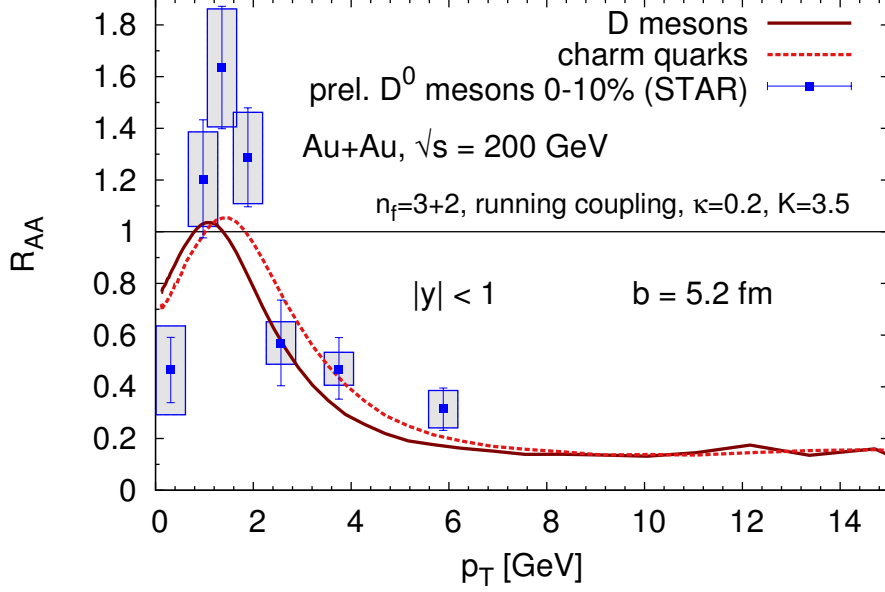


Figure 6.5.: Nuclear modification factor R_{AA} of D mesons at RHIC for $b = 5.2$ fm with data [STAR13b].

mesons, obtained with the same parameters as above, with the data. Again, the underestimation at small and intermediate p_T is visible. In addition, we cannot reproduce the bump around 1.5 GeV, which could be due to cold nuclear matter effects.

Above, we fitted the factor $K = 3.5$ to the heavy flavor electron elliptic flow data from PHENIX in the centrality class 20-40% [UFXG12b]. In Figure 6.6 we show our prediction for 0-60% centrality class for the same parameters, which is compared to new data from STAR [STAR13a]. Not surprisingly, the agreement is very good for small and intermediate transverse momenta. Even the bump around 1.7 GeV is nicely described. At large p_T , however, the data is significantly larger than our calculations. This could also be due to jet-like correlations, which are not considered in the analysis [STAR13a].

6.1.2. LHC

As is shown in the previous section, the effective description of the RHIC data with $K = 3.5$, which was fitted to the PHENIX heavy flavor v_2 data, agrees simultaneously also with the R_{AA} for intermediate and large p_T . Having the K factor fixed from RHIC data, one can make predictions with the exact same parameter for the LHC.

In this section we review our calculations at the LHC energy of $\sqrt{s} = 2.76$ TeV [UFXG12b], made at a time where only data for the R_{AA} of D mesons [ALICE12f], non-prompt J/ψ [CMS12f], and muons [ALICE12e] were available. Although preliminary data of the heavy flavor electron R_{AA} [ALICE11f] and D meson v_2 [ALICE11c] had also been presented, the errors were so large, that they were consistent with everything. In that sense our calculations for the electron R_{AA} , as well as the non-prompt J/ψ , D meson, electron, and muon v_2 from

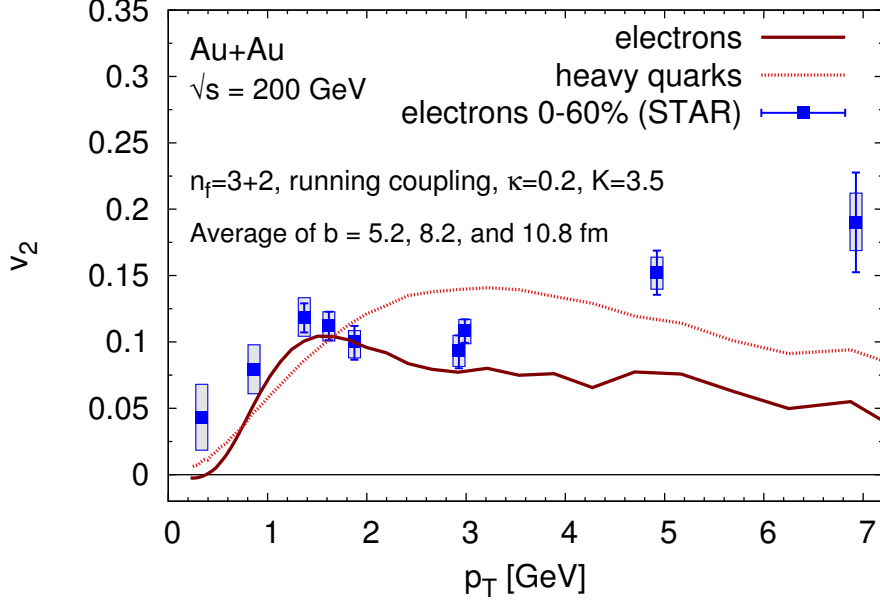


Figure 6.6.: Elliptic flow v_2 of heavy flavor electrons at RHIC for 0-60% centrality class with STAR data [STAR13a].

Ref. [UFXG12b] were predictions. In this section we compare these calculations, which have been published in Refs. [UFXG11a, FUXG11, UFXG12b, UFXG12a, UFXG13a, UFXG13b], with the newest available data.

In previous studies [UFXG10a, UFXG10b, UFXG11b, Uph09] we have found that at LHC energies a sizeable fraction of the produced charm quarks is created during the evolution of the QGP and not only in initial hard parton scatterings. These secondarily produced charm quarks can, of course, contribute to the v_2 and R_{AA} of heavy quarks. However, the impact on these observables is very small and could only affect the region of low p_T since secondary charm quarks are produced with small momenta. Due to their early production time, which is usually less than $1 \text{ fm}/c$ [UFXG10a], secondary charm quarks have enough time to interact with the medium, lose energy, and build up elliptic flow. Consequently, also in the low p_T region, v_2 is barely changed by secondary charm quarks. The fraction of bottom quarks produced in the medium is so small that the assumption that all of them are created in the initial hard parton scatterings is justified [UFXG10a]. In short, since the contribution of secondarily produced heavy quarks is insignificant, we neglect it in the following.

In Ref. [UFXG11a] we presented predictions for the electron R_{AA} and v_2 at LHC for $n_f = 0 + 2$. In Figure 6.7 an update on the predictions of the heavy flavor electron R_{AA} to $n_f = 3 + 2$ is shown [UFXG12b], employing again—as at RHIC—only collisional energy loss with a running coupling, improved DEBYE screening, and $K = 3.5$. Our calculation is slightly stronger suppressed than the preliminary experimental data. This is in accordance with the RHIC heavy flavor R_{AA} from last section, although at RHIC the deviation was even less pronounced. In addition to the electron curve, we show the R_{AA} on the heavy quark level directly, which is shifted to larger p_T as one would expect.

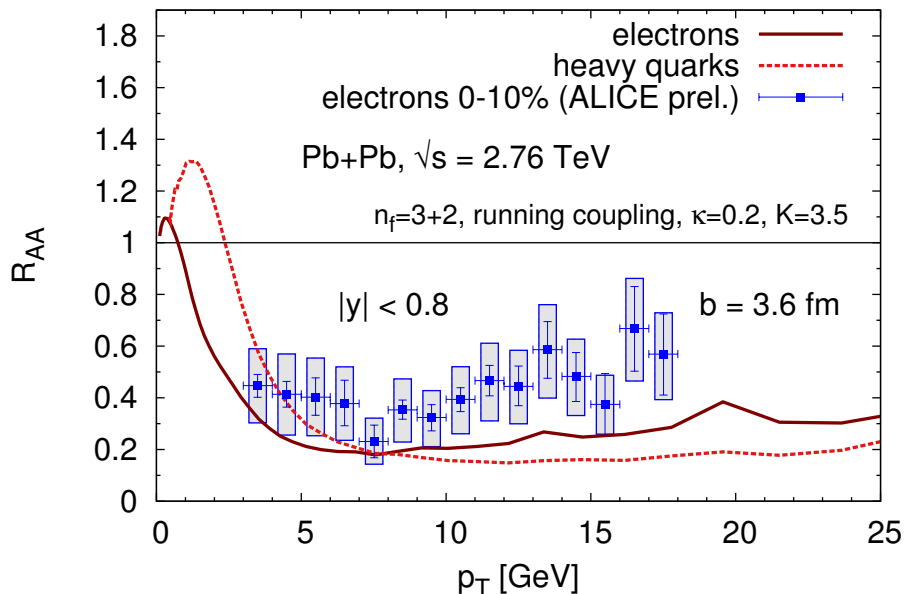


Figure 6.7.: Predictions for the nuclear modification factor R_{AA} of heavy flavor electrons at Pb+Pb collisions at LHC with an impact parameter $b = 3.6$ fm together with data [ALICE13e]. For heavy quarks only binary collisions are switched on, which are multiplied with $K = 3.5$.

ALICE can measure muons in forward rapidity stemming from heavy flavor decays. Figure 6.8 shows the BAMPS results in the same rapidity range as the experimental data. Comparing to Figure 6.7, it is obvious that the suppression of muons at forward rapidity is as strong as that of electrons at mid-rapidity since both nuclear modification factors assume very similar values. Again, a small deviation is visible between the data and our curve, which is calculated for the same parameters that describe the RHIC heavy flavor electron data.

By considering muons or electrons, the contributions from charm and bottom cannot be distinguished. However, at the LHC for the first time¹ one has access to charm and bottom quarks separately via D mesons and non-prompt J/ψ from B mesons.

The D meson R_{AA} from BAMPS for two impact parameters is compared to data in Figure 6.9. In addition to the D meson curve, we plot the charm quark R_{AA} . The difference between both curves is considerably smaller than it was the case for heavy flavor electrons or muons, which renders D mesons a very good indicator for actual charm quark quantities. Although the order of magnitude of the suppression is comparable, the experimental data tends to be slightly underestimated by our calculation. This is in accordance with the muon R_{AA} at forward rapidity in Figure 6.8 and the electron R_{AA} at mid-rapidity in Figure 6.7. Since the deviation is more pronounced at LHC than at RHIC, it could be a first hint that new effects compared to RHIC play a role at the LHC. An indication in this direction is also the fact that D meson suppression seems to be slightly smaller than that of charged hadrons [ALICE12f].

¹As is discussed in Section 6.1.1, recently, also STAR reconstructed D mesons directly at RHIC.

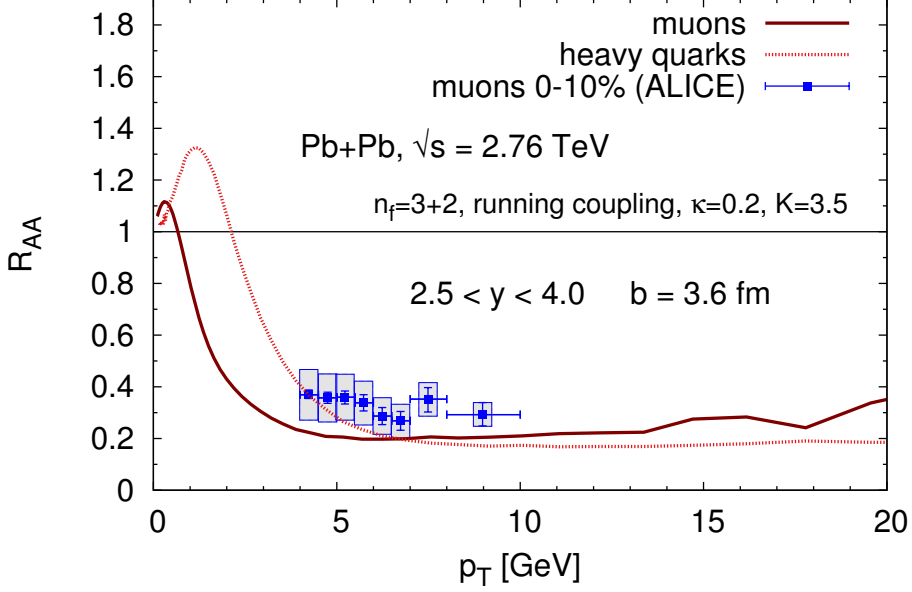


Figure 6.8.: R_{AA} of muons at forward rapidity at LHC with data [ALICE12e].

Possible explanations for the discrepancy of our R_{AA} calculations and the heavy flavor data could be cold nuclear matter effects, the normalization error of the data, which is not shown in the plot, or that we represent the rather large centrality classes by only one impact parameter (the agreement is better for 0–7.5% than 0–20% centrality class). Furthermore, a reason could be that the approximation of modeling the radiative energy loss by scaling the binary cross section with a constant factor is not justified. Although we do not expect that such a K factor is temperature dependent for a thermalized system,² non-thermal effects in the medium evolution could trigger different K factors for different collision energies at RHIC and LHC. However, this cannot be assessed without actually doing the calculation with higher order processes where the K factor is obsolete. We will investigate this in more detail in Section 6.2.

A complimentary measurement with respect to D mesons has been performed by the CMS collaboration, which has measured the suppression of non-prompt J/ψ from the decay of B mesons [CMS12f]. Although only one data point could be extracted, the suppression of non-prompt J/ψ is clearly visible in Figure 6.10 and the magnitude is in good agreement with our calculation. Analogously to the other R_{AA} comparisons at LHC, our curve is slightly smaller than the experimental value, although still within the errors. Again, the suppression of bottom quarks themselves is very similar to that of non-prompt J/ψ .

All these R_{AA} calculations have been done for central events at LHC. Figure 6.11 shows the integrated R_{AA} of highly energetic D mesons and non-prompt J/ψ as a function of the number of participants. As expected from the plots above, we also underestimate the integrated R_{AA} .

²In a thermal system the only relevant scale is the temperature T . Therefore, due to dimensional considerations both the average thermal binary cross section σ_{22} and the average (abstract) full cross section that includes all orders of the pQCD expansion $\sigma_{\text{all orders}}$ are proportional to $1/T^2$. Consequently, the ratio of both, which is the definition of the K factor, $K = \sigma_{\text{all orders}}/\sigma_{22}$ is not temperature dependent.

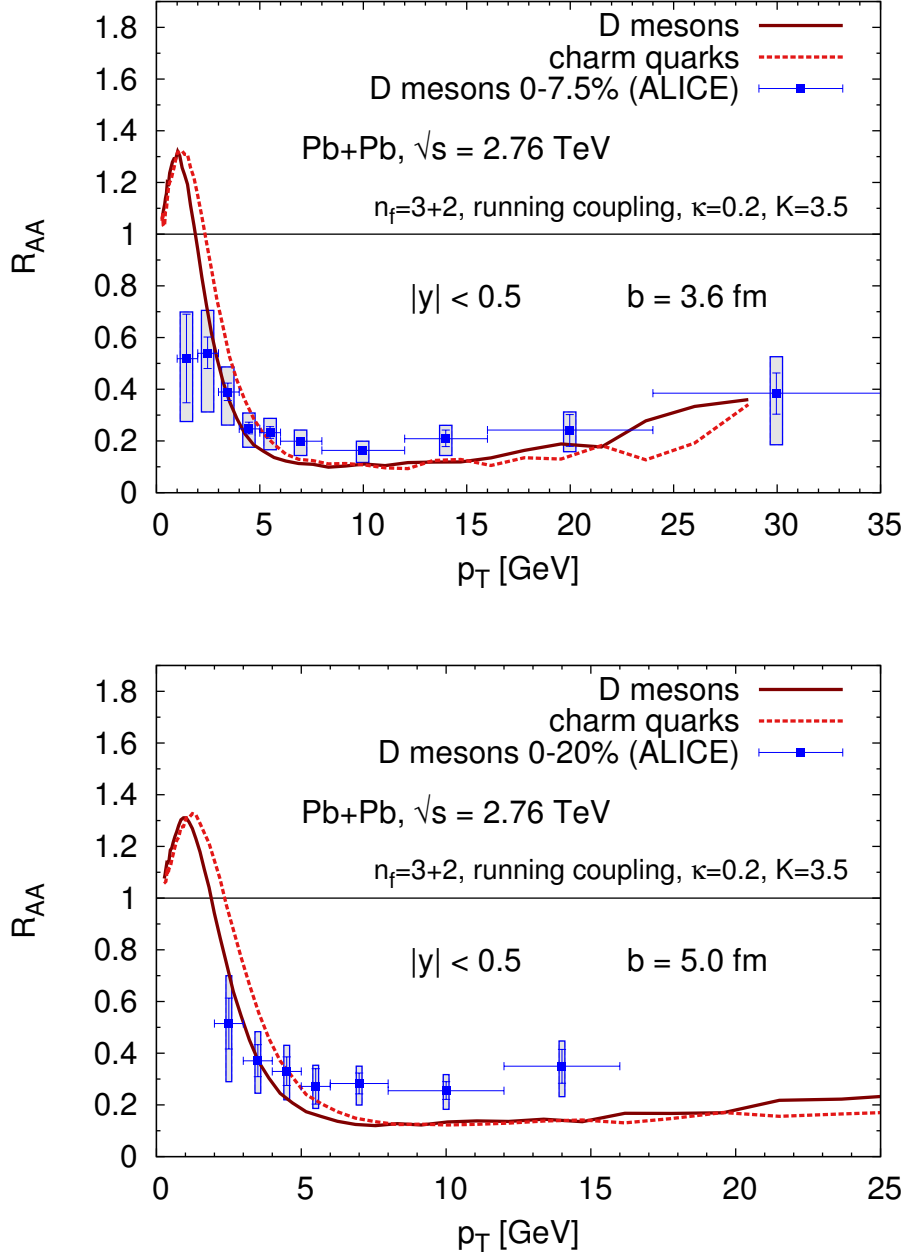
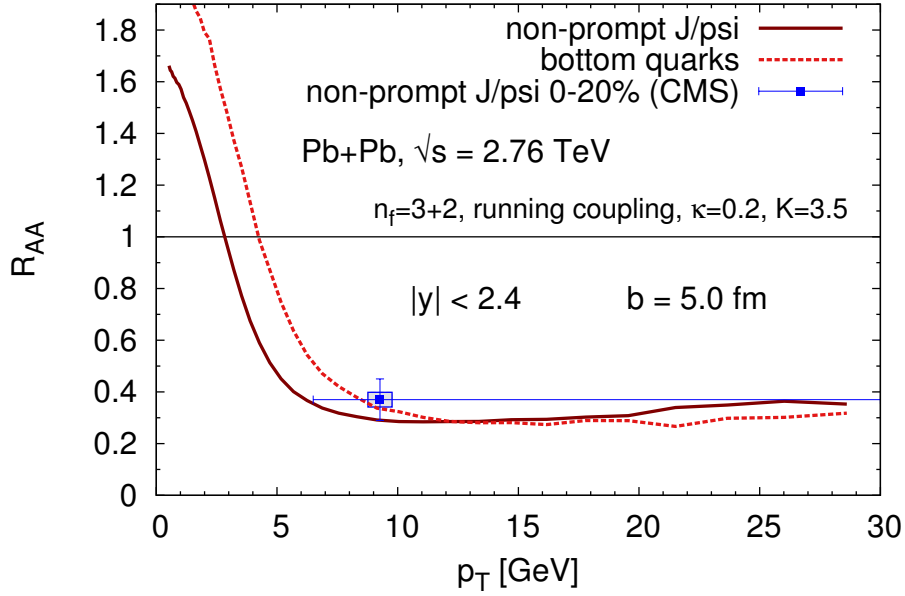
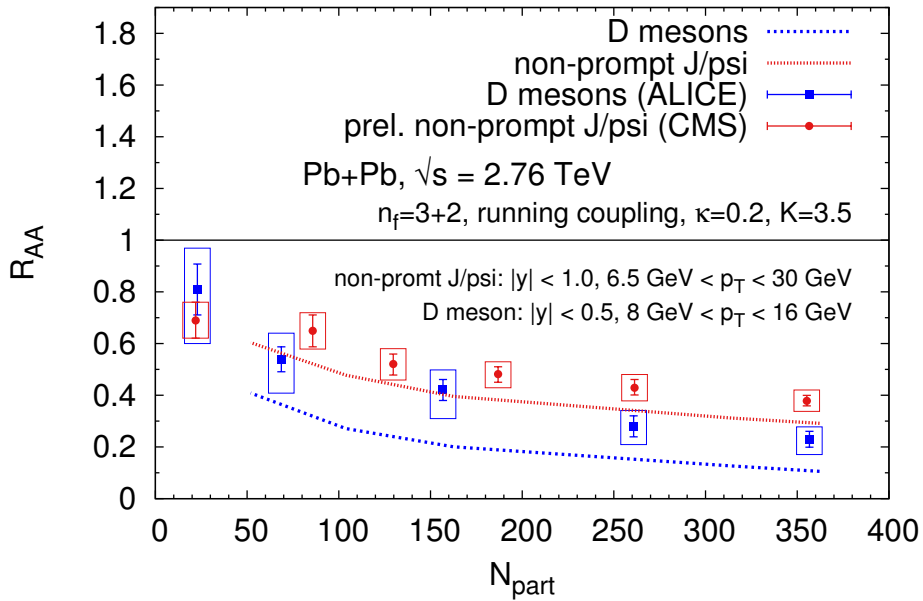


Figure 6.9.: Nuclear modification factor R_{AA} of D mesons at LHC for $b = 3.6$ fm (prediction, 0–7.5% centrality class) and $b = 5.0$ fm (postdiction, 0–20%) with data [ALICE13f, ALICE12f].


 Figure 6.10.: R_{AA} of non-prompt J/ψ at LHC with data [CMS12f].

 Figure 6.11.: R_{AA} of high-energy D mesons and non-prompt J/ψ at LHC as a function of the number of participants N_{part} together with data [CMS12i, CMS12h, ALICE12g, ALICE12f]. The R_{AA} of both the numerical simulation and the data is integrated over a p_T range of 8 – 16 GeV (6.5 – 30 GeV) for D mesons (non-prompt J/ψ).

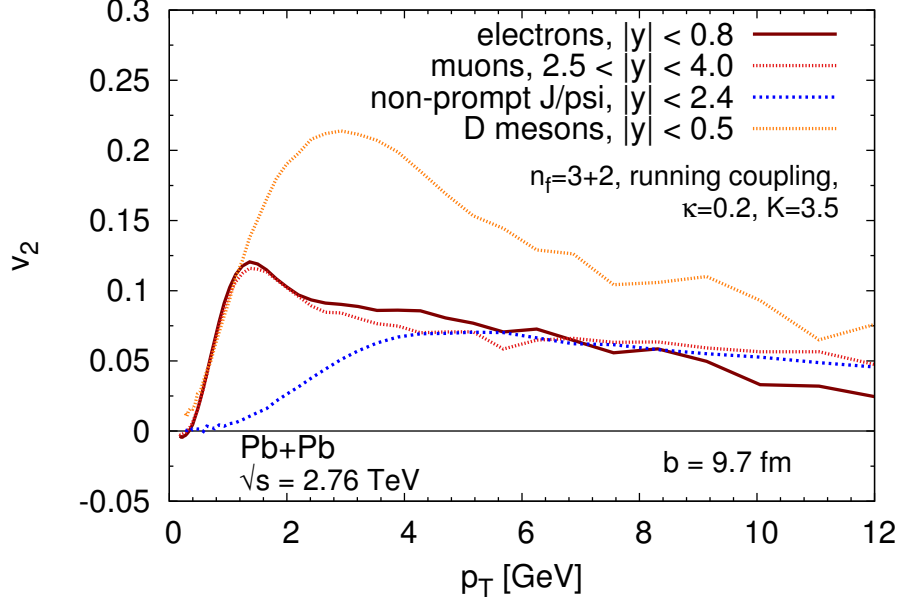


Figure 6.12.: Predictions for the elliptic flow v_2 of muons, electrons, non-prompt J/ψ , and D mesons.

However, it should be emphasized that the shape of the data and the difference between charm and bottom is very well reproduced, suggesting that if the employed K factor were smaller all data could be described.

In Figure 6.12 we show BAMPS predictions of the elliptic flow of muons, electrons, D mesons, and non-prompt J/ψ calculated with the same parameters used for the previous figures, which describe the RHIC data. The flow of non-prompt J/ψ is considerably smaller than the D meson flow due to the mass difference of charm and bottom quarks. While the elliptic flow of heavy flavor electrons is dominated for small p_T by the charm contribution, the v_2 at larger p_T resembles the v_2 of non-prompt J/ψ . The reason lies in the p_T dependence of the charm and bottom contributions to heavy flavor electrons resulting from different slopes of the charm and bottom production spectra (cf. Section 4.3). Muons at forward rapidity adopt the same elliptic flow as electrons at mid-rapidity. This is in accordance with the same R_{AA} of muons and electrons (cf. Figures 6.8 and 6.7). Since BAMPS is a 3+1 dimensional transport model, boost invariance of the system along the beam axis is not assumed, but—in first approximation—comes out naturally for not too large rapidity gaps, which is reflected in the same v_2 and R_{AA} of electrons and muons at mid- and forward rapidities, respectively. However, in Chapter 7 we will see that a residual temperature dependence in rapidity remains that causes different prompt J/ψ yields at mid- and forward rapidities.

Figure 6.13 compares the BAMPS calculations for D meson v_2 to recent data. The error bars of the preliminary data are too large to draw any definite conclusion, but our results are in good agreement within the errors. For the heavy flavor electron v_2 the errors of the data [ALICE13g] are much smaller and we find a very good agreement with our predictions, as can be seen in Figure 6.14.

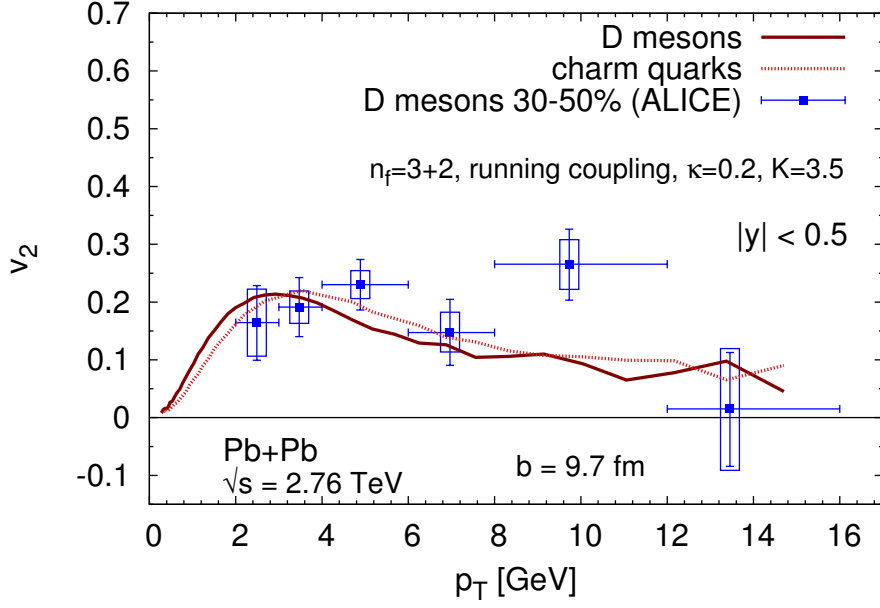


Figure 6.13.: Predictions for elliptic flow v_2 of D mesons at Pb+Pb collisions at LHC with an impact parameter $b = 9.7$ fm together with data [ALICE13b]. The D meson curve is the same as in Figure 6.12.

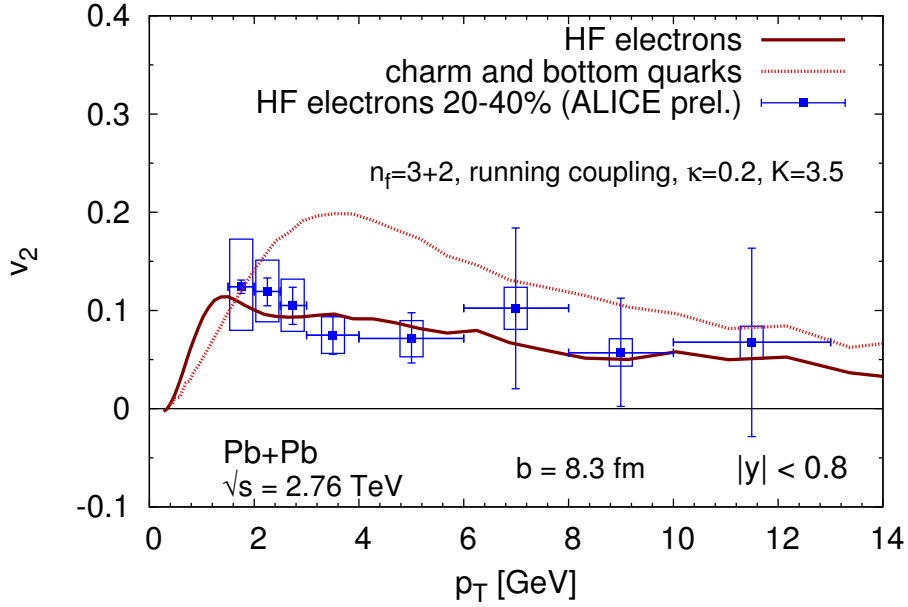


Figure 6.14.: Predictions for elliptic flow v_2 of electrons at LHC together with data [ALICE13g]. The electron curve is the same as in Figure 6.12.

In summary, both the nuclear modification factor and the elliptic flow at RHIC and LHC can be fairly well described with only elastic heavy quark collisions if a running coupling as well as an HTL inspired improved DEBYE screening are introduced and the cross sections are scaled with $K = 3.5$. A similar observation has been done by the authors of Refs. [GA08, GBA09], who need $K = 2$ to describe the R_{AA} and v_2 simultaneously. As is discussed in Section 5.3, the reason for the difference in the K factors lies in slightly different parameter choices, while the underlying physics is very similar. Refs. [ABDP⁺11, ABDP⁺13] consider also only binary interactions with a screening from HTL calculations within a LANGEVIN approach with a $2 + 1D$ hydrodynamic model for the background medium. However, while they get a rather good agreement with the R_{AA} data, the elliptic flow is much smaller than the data.

In Ref. [MPUG13] we included the same cross sections as in BAMPS in an independent model developed by PESHIER based on transition probabilities. For the medium evolution either ideal hydro or temperature and flow information extracted from BAMPS are employed. If also quantum statistics are considered, v_2 and R_{AA} can be fairly well described with only binary collisions and $K = 3$, which is consistent with the BAMPS results presented in this section with BOLTZMANN statistics.

MOORE and TEANEY [MT05] simulated the v_2 and R_{AA} in a LANGEVIN approach with a $2 + 1D$ hydrodynamic model. The diffusion coefficient is also calculated only with elastic collisions in LO pQCD. With $\alpha_s = 0.5$ they get the right magnitude of the R_{AA} , but the v_2 is much smaller than the data.

The authors of Refs. [HFR12a, HFR13] and [LvHSB12a, LvHSB12b] find that within the resonance scattering approach the R_{AA} and v_2 can be described simultaneously if coalescence is taken into account. The driving force behind this is the s channel process, which leads to large angle scatterings and, thus, large transport cross sections.

From these observations one can conclude that either resonance scattering or small-angle-peaked pQCD with the running coupling and the improved screening procedure as well as a K factor are needed to get an agreement with the experimental elliptic flow data. Or in other words, heavy quarks must have a large cross section—or at least a large transport cross section in the case of resonance scatterings—for interactions with the other medium constituents to pick up the elliptic flow of the medium. In the following we elaborate on this in more detail by addressing also the transport cross section and what we can learn from the comparison to experimental data.

Due to the transport character of BAMPS we have access to all the collision properties during the whole time evolution. Figure 6.15 sheds some light on why the experimental data can be fairly well described with the K factor.

For the elliptic flow isotropization is important and, hence, the transport cross section and transport rate are the relevant quantities since they weight the cross section and rate, respectively, with the angle of the diffracted particle. In the left plot of Figure 6.15 the time evolution of the mean transport cross section is shown in the central region of a heavy-ion collision at LHC. The value for charm quarks, including only $2 \rightarrow 2$ processes, is about 5 times larger than that for gluons, which interact also via $2 \leftrightarrow 3$ processes. As a note, the calculations with the $2 \rightarrow 2$ and $2 \leftrightarrow 3$ light parton processes employ the original GB matrix element (see Section 3.2.1) and can describe the elliptic flow data of light particles [XGS08, XG09, XG10]. Due to the large charm transport cross section also a sizeable elliptic flow for charm quarks builds up.

For comparison we show also the charm transport cross section under the assumption that

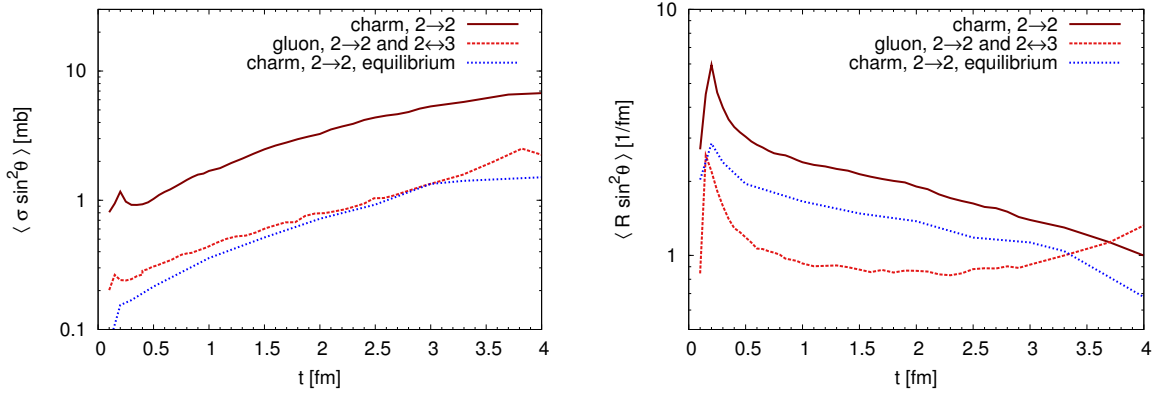


Figure 6.15.: Mean transport cross section $\langle \sigma \sin^2 \theta \rangle$ (left) and transport rate $\langle R \sin^2 \theta \rangle$ (right) of charm quarks and gluons as a function of time in the central region of a heavy-ion collision at LHC ($b = 9.7$ fm, $\sqrt{s} = 2.76$ TeV, $n_f = 3 + 2$, $K = 3.5$ for charm quarks). θ is the angle between the momenta of the considered charm quark (gluon) before and after the collision in the lab frame. The cross section is averaged over all particles in a tube with a radius of 1.5 fm and space-time rapidity $\eta \in [-0.5; 0.5]$. In addition, the charm transport cross section and rate in a thermally and chemically equilibrated medium is shown. That is, for each time we extract the medium energy density and mean charm energy from BAMPS in the central region and compute the transport cross section and rate of a charm quark with that energy in a static and equilibrated medium.

the medium is thermally and chemically equilibrated. These values are smaller compared to the full heavy-ion collision, where the gluon fugacity is below unity, which leads to a smaller DEBYE mass and, therefore, larger cross section. However, the sensitivity on the fugacity is reduced when considering the transport rates since the density also enters. The right hand side of Figure 6.15 shows that for the charm transport rate the equilibrium curve is only a factor of about 1.4 smaller than the values extracted from the full heavy-ion collision.

Gluons are calculated with a standard DEBYE screening and without a K factor, but with $2 \rightarrow 3$ interactions, leading to a smaller transport cross section compared to charm quarks. The reason for the large charm transport cross section is the effective treatment of the DEBYE screening on the heavy flavor sector and the additional multiplication of the factor $K = 3.5$. Since the binary pQCD cross section is dominated by small angles, the total cross section can be one order larger than the transport cross section, which is too large for partonic interactions. Therefore, we will investigate in Section 6.2 radiative processes, which can lead to an effective energy loss without the need of large cross sections, as it has been demonstrated in Section 5.3.

6.2. Elliptic flow and nuclear modification factor from elastic and radiative processes

In the previous section we saw that binary collisions alone cannot explain the experimental heavy flavor data, neither at RHIC nor at LHC. However, if the binary cross sections are scaled with a phenomenological K factor, both the elliptic flow and nuclear modification factor

of heavy flavor particles can be described at RHIC and LHC. We concluded that missing contributions such as radiative processes or quantum effects play an important role.

In this section we explicitly add the radiative contributions and study if binary and radiative processes together can explain the experimental data. In Section 6.2.1 the focus is put on the similarities and differences of light and heavy flavor particles. Furthermore, the influence of the dead cone effect is investigated. To treat light and heavy flavor partons on the same footing, we use for all species the standard DEBYE screening. In Section 6.2.2 we explicitly study the effect of the improved screening procedure and confront various heavy flavor calculations with experimental data.

6.2.1. Comparison between heavy and light flavor

The cross sections of binary processes are given in Appendix A.3 for light partons and in Section 3.1 for heavy flavor. As part of this work we implemented not only a running coupling for heavy flavor, but also applied it to the light parton sector. Since the improved screening procedure with setting the screening mass prefactor to $\kappa_t = 0.2$ (cf. Section 5.1.5) has only been derived for massive quarks and we want to treat heavy and light flavor on the same footing in order to make proper comparisons, we employ in this section the standard DEBYE screening for both light and heavy partons. Nevertheless, in the next section we investigate the influence of the improved screening procedure on heavy quark observables. It would be also interesting to extend the derivation of the improved screening procedure from comparisons to HTL calculations to the light parton sector and determine the value of κ_t for light particles. It is important to note that the same cross sections are employed for light and heavy partons. That is, if the mass in the heavy flavor cross sections is set to zero the cross sections of light quarks are obtained.

The same is true for the radiative processes. The cross sections calculated in Section 3.2 can be employed for heavy quarks and also for light partons if the mass is set to zero. Also the LPM effect and the treatment of all the kinematics are implemented in BAMPS consistently for massive and massless particles. Since $3 \rightarrow 2$ processes have only minor relevance for the energy loss of high-energy particles, we neglect those processes in the following study.

Figure 6.16 depicts the nuclear modification factor of gluons, light quarks, and charm quarks for central Pb+Pb collisions at the LHC. For each particle species the curves for fixed coupling $\alpha_s = 0.3$ and running coupling are shown. At large transverse momentum both curves for each species are very similar. While the light quark curves only differ slightly at smaller p_T , the suppression of charm quarks and gluons with running coupling becomes stronger than with constant coupling in this regime and a slight rise in the R_{AA} with p_T becomes visible, as it is also present in the data.

As could have been guessed from the rather similar energy loss in a static medium (see Figures 5.5 and 5.7), the suppression of light and charm quarks is very similar. The reason is the same; a dead cone at small angles of the radiated gluon stemming from the LPM effect overshadows the dead cone caused by the mass (cf. Section 5.3). Thus, effectively, the radiation pattern off a heavy quark in a medium is comparable to that off a light quark. The gluon R_{AA} is significantly smaller because of the larger elastic and also radiative energy loss due to the larger color factor.

For qualitative comparison, the experimental data of charged hadrons and D mesons are also depicted. The parton level R_{AA} seems to be slightly larger than the data. However, to make a

quantitative comparison to the data, the partons have to be first fragmented to hadrons.

The fragmentation of heavy quarks to D and B mesons with PETERSON fragmentation is outlined in Section 4.1. Light partons are fragmented to charged hadrons by using the AKK fragmentation functions [AKK08], which are obtained from global fits to data. In the following we briefly outline this procedure. The details can be found in Ref. [Foc11].

To reduce statistical fluctuations the fragmentation is not performed on the particle level but for the spectra. To this end, the spectra of all light parton species ($k = g, u, d, s$, and the light anti-quarks) are fitted with a power law

$$\frac{d^2 N_k}{dp_T dy}(p_T^k) = a \left[p_T^k \right]^{-b}, \quad (6.1)$$

where p_T^k is the transverse momentum of a parton of type k . Subsequently, the spectra are convoluted with the vacuum fragmentation function $D_{H/k}(z_k)$ to obtain the spectrum of hadrons of type H at momentum p_T^H (cf. Section 2.2.3),

$$\begin{aligned} \frac{d^2 N_H}{dp_T dy}(p_T^H) &= \sum_k \int_{z_k^{\min}}^1 dz_k \frac{d^2 N_k}{dp_T dy}\left(\frac{p_T^H}{z_k}\right) D_{H/k}(z_k, Q^2) \\ &\simeq \sum_k \int_{p_T^H}^{p_T^{k, \max}} dp_T^k \frac{p_T^H}{(p_T^k)^2} \frac{d^2 N_k}{dp_T dy}(p_T^k) D_{H/k}\left(\frac{p_T^H}{p_T^k}, Q^2\right), \end{aligned} \quad (6.2)$$

where $z_k = |\mathbf{p}_H|/|\mathbf{p}_k| \simeq p_T^H/p_T^k$ denotes the ratio of hadron and parton momenta.

Using in Equation (6.2) the vacuum fragmentation function instead of the medium modified fragmentation function is the appropriate choice since the medium modification is already contained in the BAMPS evolution and data on jet shower shapes suggest that high-energy particles fragment outside the medium produced in heavy-ion collisions [CMS12b].

In Figure 6.17 the nuclear modification factor R_{AA} of charged hadrons obtained after fragmentation is depicted for a running coupling and standard DEBYE screening. In addition, we plot also the corresponding gluon and light quark curves before fragmentation from Figure 6.16. The charged hadron curve lies mainly between the light quark and gluon curves, but is slightly larger than the light quark curve for large p_T , which is counter-intuitive at first sight. However, the average z of the fragmentation function is of the order of 0.5 [Foc11], that is, the charged hadron R_{AA} at a given p_T has approximately the same value as the parton R_{AA} at twice as large p_T . Due to the rise in the R_{AA} the hadron curve is shifted to larger values than the parton curve at same p_T .

Furthermore, the slope of the hadron curve is steeper than the parton curves. The reason lies again in the fragmentation process as well as in the different slopes of gluon and light quark spectra. Hadrons at large p_T are dominated by quark fragmentation, while hadrons at small p_T are dominated by gluon fragmentation [Foc11]. Since the light quark R_{AA} is larger than the gluon R_{AA} due to different color factors, the hadron curve increases stronger with p_T compared to the parton curves.

Whereas the heavy quark fragmentation to D and B mesons did not change the R_{AA} significantly due to the heavy quark mass and a peak of the fragmentation function at large z (cf. Figure 4.3), the light particle R_{AA} is significantly modified by the fragmentation process.

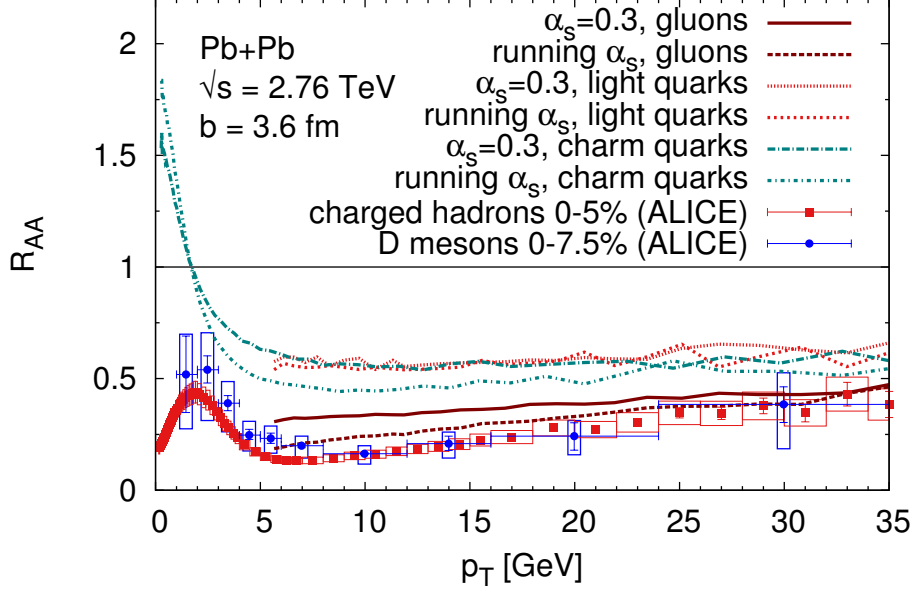


Figure 6.16.: Nuclear modification factor R_{AA} of gluons, light quarks, and charm quarks with a constant coupling $\alpha_s = 0.3$ and running coupling for central LHC events. To guide one's eye, the experimental data for charged hadrons [ALICE13c] and D mesons [ALICE13f] are also shown, although the parton curves have to be fragmented to hadrons for quantitative comparison with the data, see Figures 6.17 and 6.18.

The shape of the charged hadron R_{AA} from BAMPS is very similar to the data. However, the overall value is substantially larger. As discussed in Section 3.2.7, the way how the LPM effect is implemented in BAMPS forbids most of the radiative processes, leading to a destructive interference that is too strong. A more sophisticated treatment of the LPM effect should allow more processes, which would decrease the R_{AA} . We introduced a first step in this direction in Section 5.3 by lowering the formation time of the emitted gluon by a factor X , which effectively allows more radiative processes for $X < 1$. To this end, we modified the Θ function from Equation (3.118) according to

$$\Theta(\lambda - \tau) \rightarrow \Theta(\lambda - X\tau) . \quad (6.3)$$

In Figure 6.18 we tuned this parameter to get an agreement with the experimental data, which leads to $X = 0.3$. Not only the magnitude of the R_{AA} is nicely reproduced but also the shape and especially the rise with p_T . However, it is important to mention that the exact value of X is not theoretically motivated and, thus, a free parameter. Nevertheless, we expect that a more sophisticated LPM implementation boils effectively down to an $X < 1$. It is planned for the future to improve the implementation of the LPM effect in BAMPS and study the impact on observables such as the R_{AA} .

If we set the same value $X = 0.3$ also for heavy quarks, the experimental data of D mesons is also nicely reproduced. Since we employ the standard DEBYE screening in this section to heavy quark interactions as well, both heavy and light partons are treated consistently.

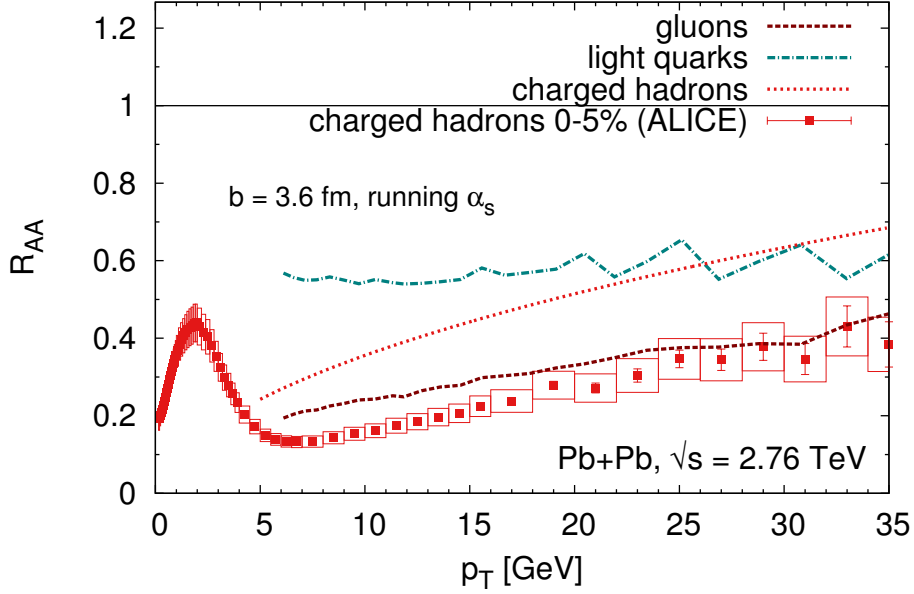


Figure 6.17.: Nuclear modification factor R_{AA} of gluons, light quarks, and charged hadrons at LHC for a running coupling and standard DEBYE screening together with data of charged hadrons [ALICE13c].

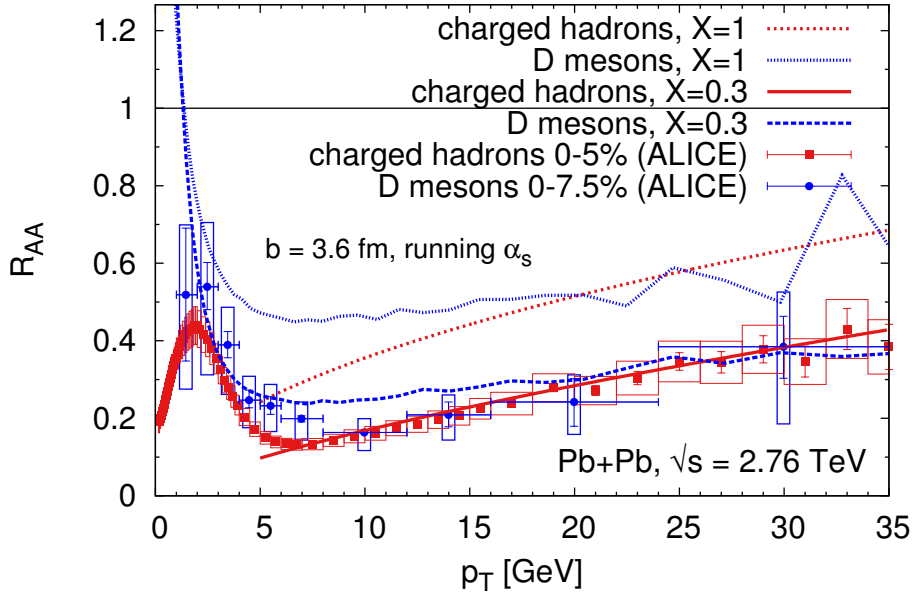


Figure 6.18.: Nuclear modification factor R_{AA} of charged hadrons and D mesons at LHC in comparison to data [ALICE13c, ALICE13f]. The LPM parameter X is set to 1 and 0.3 (see text).

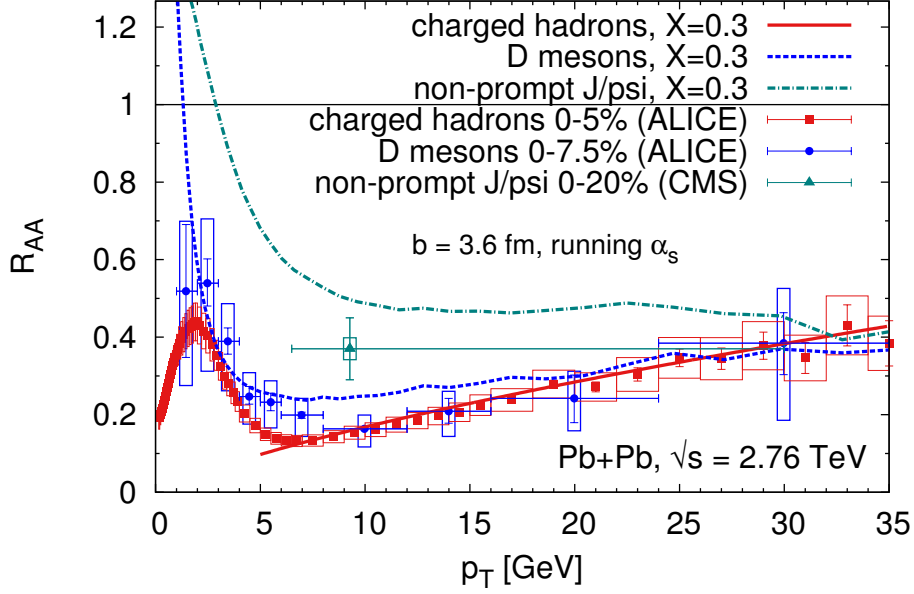


Figure 6.19.: Nuclear modification factor R_{AA} of charged hadrons, D mesons, and non-prompt J/ψ at LHC for $X = 0.3$ in comparison to data [ALICE13c, ALICE13f]. Note that the impact parameter $b = 3.6$ fm represents approximately a centrality class of 0-10%, while the data is only available for slightly different centrality classes.

Although the dead cone effect is present in our matrix element, the R_{AA} of D mesons and charged hadrons are comparable, as it is also the case for the data. There are two reasons for that: first, as described in detail in Section 5.3, the LPM effect produces a second dead cone that overlays the dead cone due to the heavy quark mass and effectively annihilates its influence. This leads to a similar suppression of light and heavy quarks. However, gluons are still stronger suppressed (see Figure 6.16). The second reason lies in the fragmentation process. The D meson R_{AA} is not really modified by the fragmentation, whereas the fragmentation of light quarks and gluons shifts the light hadron R_{AA} closer to the light quark curve and, thus, also to the D meson curve. Consequently, due to the interplay between these two effects, both the D meson and charged hadron R_{AA} take very similar values.

Very recently, the same observation was made by DJORDJEVIC [Djo13] within an extension of the WHDG framework. Also in her model, the suppression of light and charm quarks is comparable, whereas gluons are more suppressed. However, analogously to what we have observed, mass effects in the fragmentation function result in a similar suppression of charged hadrons and D mesons.

In Figure 6.19 we depict besides the charged hadron and D meson R_{AA} for $X = 0.3$ also the R_{AA} of non-prompt J/ψ for the same parameter. Non-prompt J/ψ , which stem from B mesons, are less suppressed than D mesons or charged hadrons. Because of the large mass of bottom quarks, the dead cone due to the mass is larger than the dead cone due to the LPM effect. This leads to a smaller suppression of bottom quarks compared to charm quarks. The experimental data of non-prompt J/ψ is slightly smaller than our curve but still larger than

the D meson data (however, note the slightly different centrality classes).

6.2.2. Open heavy flavor at RHIC and LHC with improved screening

In the previous section we employed the standard DEBYE screening to ensure a similar treatment of light and heavy partons. In contrast, we study in this section the effect of the improved screening procedure ($\kappa_t = 0.2$) on heavy flavor observables.

Figure 6.20 depicts the R_{AA} and v_2 of heavy flavor electrons in non-central RHIC collisions for various parameter sets. As we saw also in the previous section for D mesons at LHC, the suppression with standard DEBYE screening and $X = 1$ is smaller than the data both for a constant and running coupling.

Setting $\kappa_t = 0.2$ leads to a large binary cross section and a small mean free path of the heavy quark, as has been mentioned in Section 5.3. Due to our particular implementation of the LPM effect (see Section 3.2.7), most of the radiative processes are forbidden. Thus, the total rate or energy loss for running coupling and improved screening is completely dominated by the binary processes (cf. Figure 5.8). Since effectively no radiative processes are allowed, also the R_{AA} is above the data for large p_T .

In the previous section we lowered the effective formation time of the emitted gluon by setting $X = 0.3$ to get a reasonable agreement with the data for light and heavy particles with a standard DEBYE screening. If we employ the improved screening procedure, the best agreement with the R_{AA} data at large p_T is found for $X = 0.2$, which is depicted in Figure 6.20. It is worth noting that the value of X that gives a good agreement with the improved screening lies in the same range as that for the standard DEBYE screening. However, we want to emphasize again that the exact value of X is a free parameter, although a value smaller than one is expected from theoretical considerations (cf. Section 5.3). We expect that a more sophisticated treatment of the LPM effect makes such X factors obsolete.

For comparison, we also show the curve from Section 6.1, which was obtained by allowing only binary collisions and scaling the cross sections with $K = 3.5$. It gives a slightly stronger suppression than the curve with $X = 0.2$ at large p_T and a slightly weaker suppression at small p_T . This reflects the observation made for the energy loss in a static medium (see also Figure 6.21): including radiative processes is not the same as scaling the binary cross sections with a constant K factor since both energy loss distributions have distinguished energy dependencies.

For the elliptic flow, the picture looks very different (see lower panel of Figure 6.20). None of the curves that include radiative interactions can describe the elliptic flow data. In contrast, the scenario with the scaled binary interactions gives a sizeable v_2 , although its R_{AA} is comparable to the curve with $X = 0.2$. This similarity in the R_{AA} and the large deviation for the v_2 , simultaneously, are at first sight surprising. However, the mechanisms responsible for the two observables are very different. For the R_{AA} , the energy loss is the important quantity, while v_2 is most effectively build up by a large transport cross section.

In Figure 6.21 we depict the energy loss and transport cross section of charm quarks in a static medium for the two scenarios: only binary interactions scaled with $K = 3.5$ and binary as well as radiative processes with $X = 0.2$. Although the energy loss of both scenarios is on the same order,³ the transport cross section deviates strongly. This leads to a very similar

³The scaled binary cross section has a slightly larger energy loss, which is reflected in a slightly smaller R_{AA} at large transverse momentum in Figure 6.20.

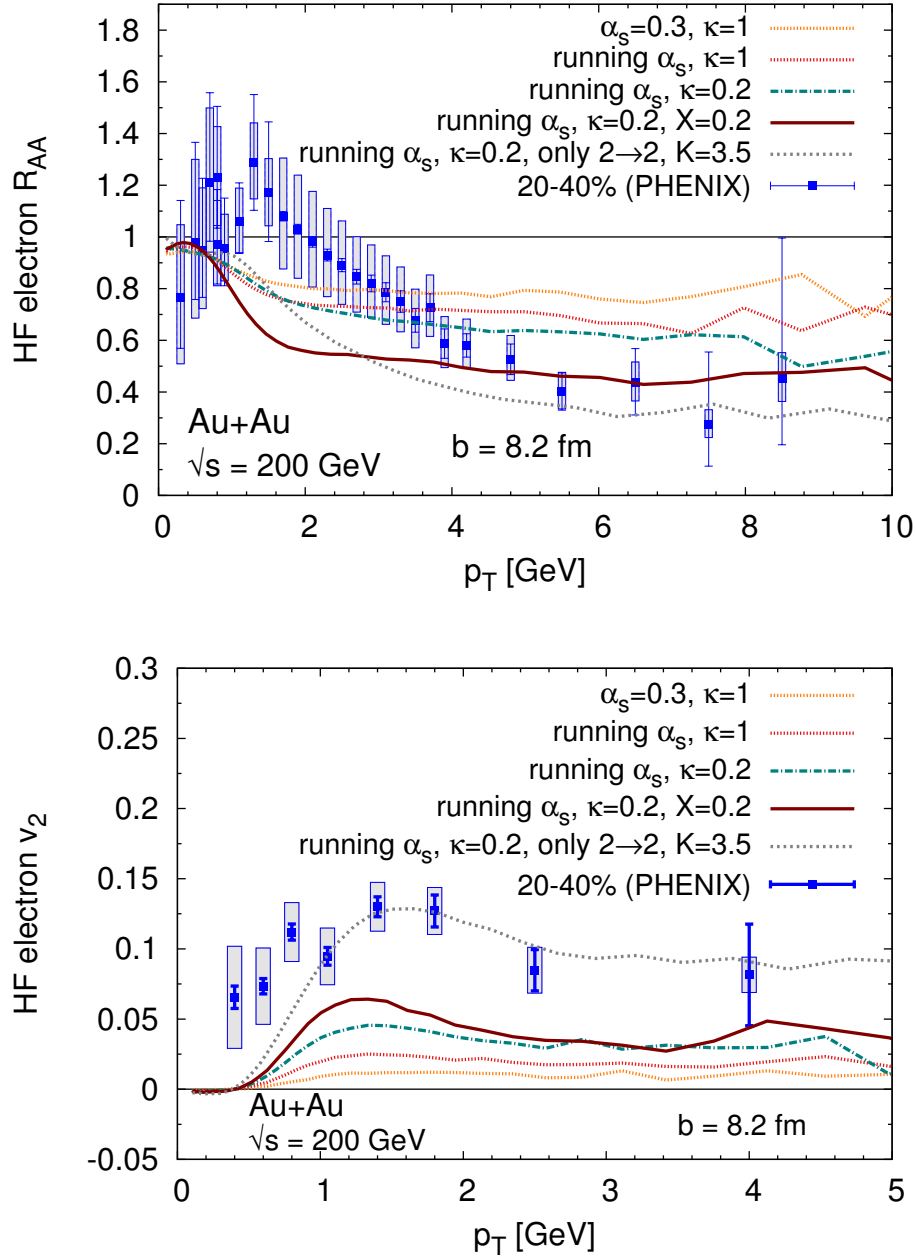


Figure 6.20.: Nuclear modification factor R_{AA} (top) and elliptic flow v_2 (bottom) of heavy flavor electrons in non-central events at RHIC for running and constant coupling as well as different values of the screening prefactor κ_t and the LPM parameter X . For comparison, data [PHENIX11b] and the curve with only scaled ($K = 3.5$) binary collisions (see Section 6.1) are shown.

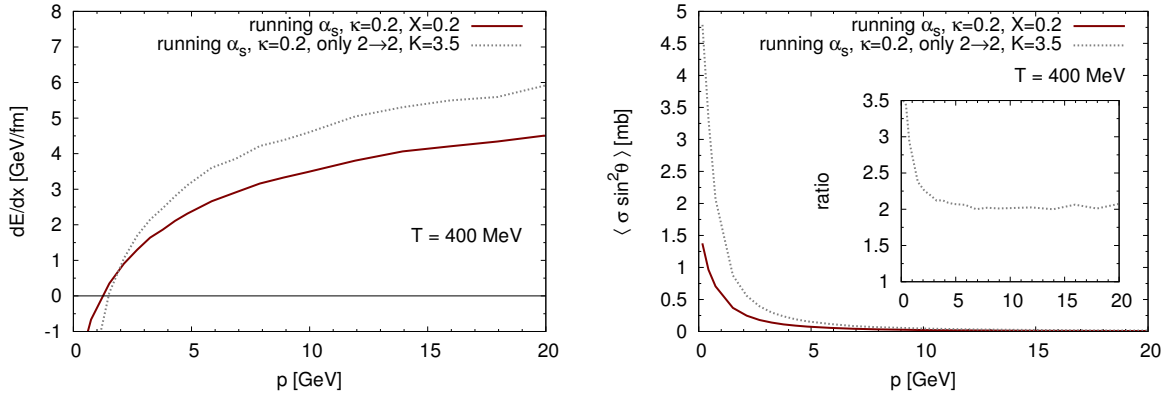


Figure 6.21.: Energy loss dE/dx (left) and transport cross section $\langle \sigma \sin^2 \theta \rangle$ (right) of charm quarks with momentum p in a static medium with a temperature $T = 400$ MeV. A running coupling and improved DEBYE screening are employed. The first curve includes binary and radiative collisions with $X = 0.2$ and the second curve only binary collisions with $K = 3.5$.

R_{AA} , but a large v_2 for the case with only binary interactions. However, a more detailed study (not shown here) reveals that the angular distribution is rather similar for elastic and radiative processes. Only the cross sections of both scenarios differ substantially. Due to the large $K = 3.5$ factor, the scenario with only scaled elastic collisions has a much larger cross section than the scenario with elastic and radiative processes. Since the energy loss per collision for radiative processes is significantly larger than for elastic interactions, the overall energy loss per unit length is similar. Nevertheless, the large cross section for the scenario with only scaled binary collisions produces a large v_2 that is in agreement with the data.

Figures 6.22 and 6.23 depict the nuclear modification factor of D mesons and non-prompt J/ψ , respectively, in Pb+Pb events at LHC. Again, the curves with elastic and radiative processes and $X = 1$ are significantly larger than the data, but the curves with $X = 0.2$ agree very well with the experimental results for both D mesons and non-prompt J/ψ . This indicates that the mass hierarchy of heavy quarks is accurately described within BAMPS if the improved screening procedure is employed. To this end, it is not surprising that one also finds a good agreement with heavy flavor electrons from D and B meson decays at LHC for $X = 0.2$, as shown in Figure 6.24.

Figures 6.25 and 6.26 display the elliptic flow of heavy flavor electrons and D mesons, respectively, in non-central events at LHC. Analogously to RHIC, the elliptic flow at LHC cannot be explained by elastic and radiative processes with $X = 0.2$, although the R_{AA} is described with this parameter. In contrast, the curve with only binary collisions scaled with $K = 3.5$ describes both the electron and D meson R_{AA} . The explanation for the discrepancy between the two curves is the same as mentioned in the discussion of the RHIC results: the transport cross sections of the scaled binary collisions are larger than for the scenario with binary and radiative processes and $X = 0.2$, although the energy loss is very similar. Hence, both have a rather similar R_{AA} (see Figures 6.22, 6.23, and 6.24) but a different v_2 .

A possible reason why we obtain a small elliptic flow with elastic and radiative processes might be that some effects are missing. We neglect initial stage fluctuations, apply only PETERSON fragmentation instead of coalescence at small transverse momenta, and do not take

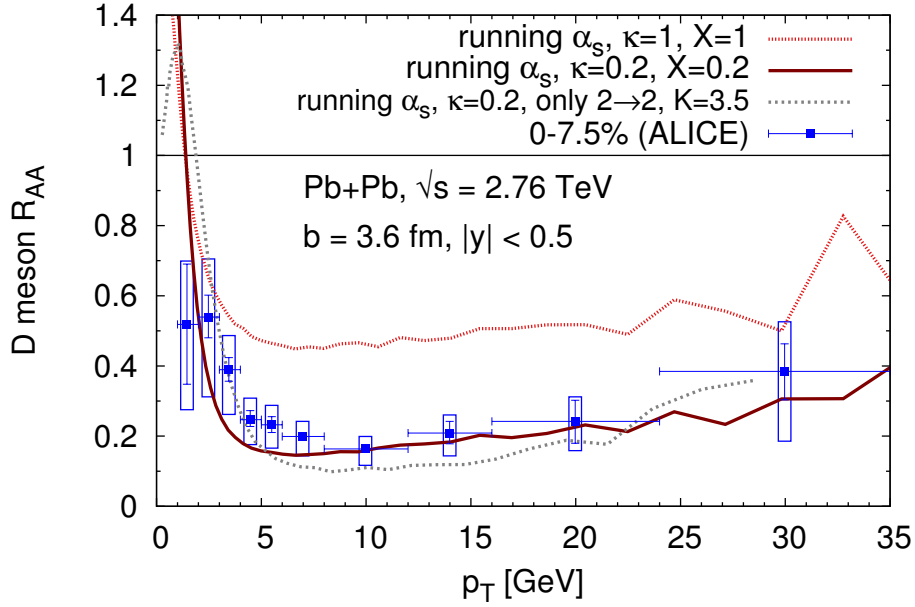


Figure 6.22.: Nuclear modification factor R_{AA} of D mesons at LHC for $b = 3.6$ fm with data [ALICE13f]. A running coupling is employed and either the parameter set $\kappa_t = 1$, $X = 1$ or $\kappa_t = 0.2$, $X = 0.2$. For comparison, the scaled binary collision curve from Section 6.1 is shown.

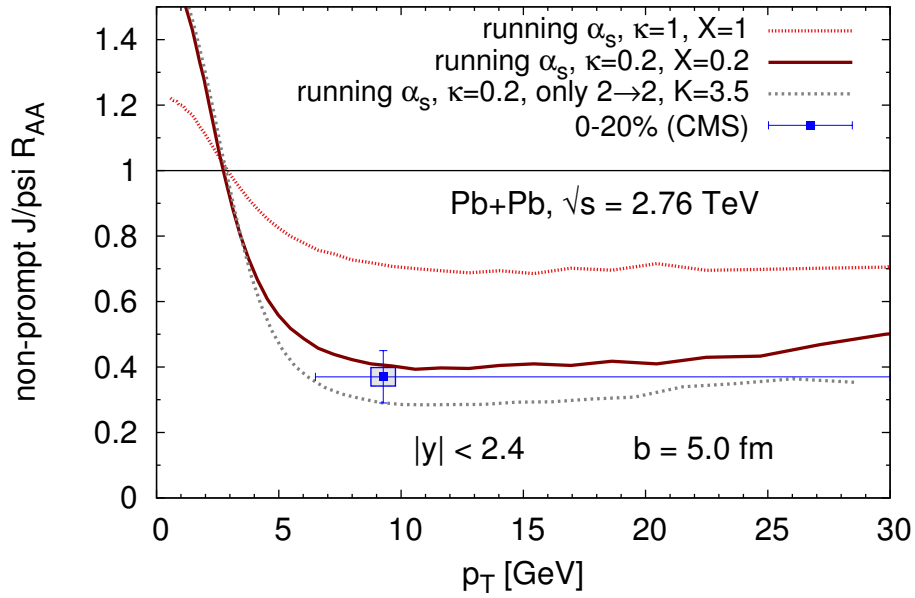


Figure 6.23.: R_{AA} of non-prompt J/ψ at LHC for $b = 5.0$ fm with data [CMS12f] for the same configurations as in Figure 6.22.

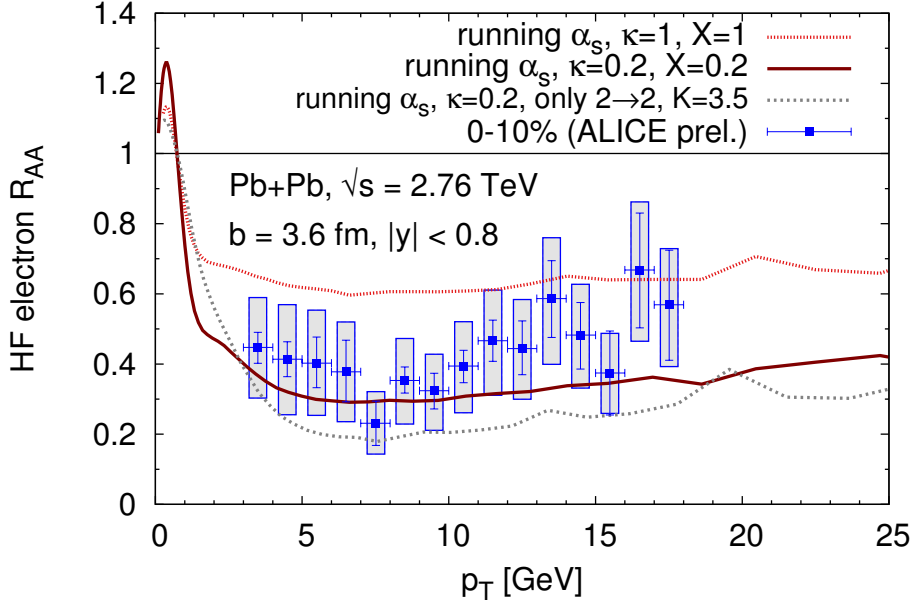


Figure 6.24.: R_{AA} of heavy flavor electrons at LHC for $b = 3.6$ fm with data [ALICE13e] for the same configurations as in Figure 6.22.

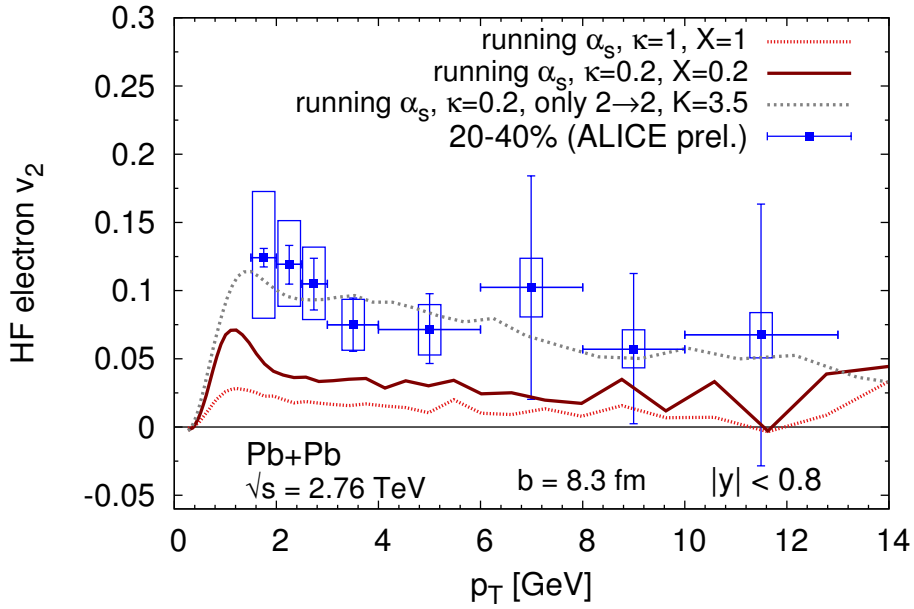


Figure 6.25.: Elliptic flow v_2 of electrons at LHC for $b = 8.3$ fm together with data [ALICE13g] for the same configurations as in Figure 6.22.

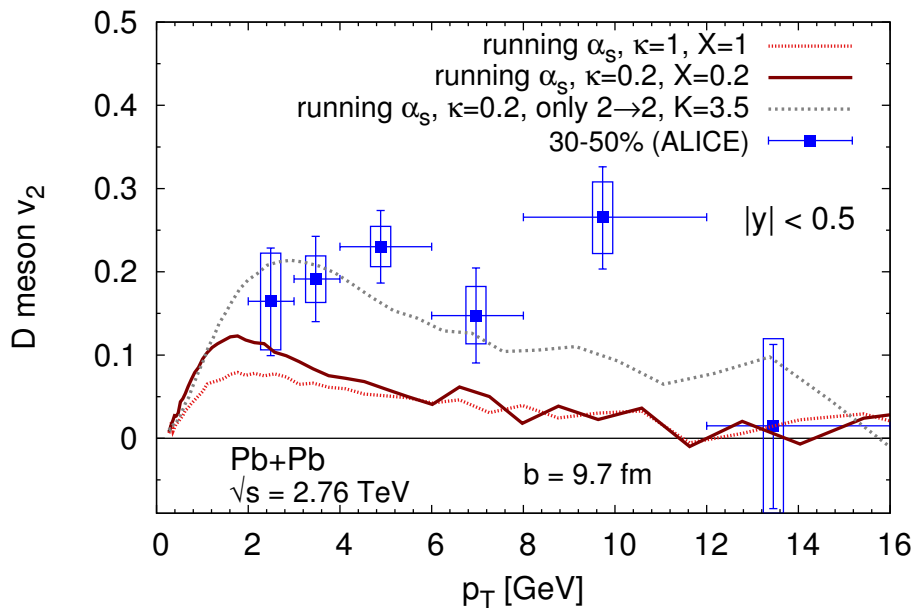


Figure 6.26.: Elliptic flow v_2 of D mesons at LHC with $b = 9.7$ fm together with data [ALICE13b] for the same configurations as in Figure 6.22.

hadronic interactions into account. All of these effects are expected to increase the elliptic flow, while the nuclear modification factor at large p_T is not strongly affected.

Most of the open heavy flavor models in the literature that include radiative interactions cannot describe the nuclear modification factor and elliptic flow simultaneously. Both in the ASW [ACD⁺06] and GLV (or the extended WHDG) [DGVW06, WHDG07, BG12b, BG12a] framework the R_{AA} is well described (also for light partons), but the calculated v_2 is significantly smaller than the data. The same is true for the results of Refs. [CB11, CQBM13], where radiative processes have been implemented in a LANGEVIN approach coupled to a 2 + 1D viscous hydrodynamic model.

Several models describe the R_{AA} data, but do not perform any elliptic flow calculations: Refs. [MBAD11, MBA13] and [AJMS12] conclude that radiative processes play the dominant role for the R_{AA} , whereas in Ref. [SVZ09] a combination of heavy quark quenching and inelastic heavy meson break-up processes lead to a strong suppression.

In contrast, the Nantes group explains the R_{AA} and v_2 data simultaneously fairly well if elastic and radiative interactions are rescaled with $K = 0.7$ [GNB⁺13, NAGW13]. This result is at first sight a little surprising, given that in BAMPS quite similar physics is implemented and—as we saw in this section—BAMPS cannot describe R_{AA} and v_2 simultaneously with radiative collisions. However, although the GUNION-BERTSCH matrix element is also employed in Refs. [GNB⁺13, NAGW13], two phenomena are treated differently compared to BAMPS. First, the emitted gluon acquires a finite mass from screening effects, whereas it is massless in BAMPS. Second, in contrast to BAMPS (see Section 3.2.7 for our implementation), the LPM effect is implemented through an interpolation between single and multiple scatterings [Gos12] that is matched to the BDMPS result [BDM⁺97b]. Both effects lead to very different

properties of radiative processes in BAMPS and the Nantes model [GA13], although the underlying matrix element is the same. Furthermore, differences in the background medium evolution might also lead to additional differences in the heavy quark observables.

7. J/ψ in heavy-ion collisions

Physics is really nothing more than a search for ultimate simplicity, but so far all we have is a kind of elegant messiness.

A Short History of Nearly Everything
BILL BRYSON

As discussed in Section 2.2.3, two classes of phenomena are important for studying J/ψ suppression in heavy-ion collisions: cold nuclear matter effects and hot nuclear matter effects. The former are all effects that would be present even if no QGP were formed and influence primarily the initial J/ψ production before the QGP is created. We discussed these effects, which include shadowing, nuclear absorption, and the CRONIN effect, in detail in Section 4.4. Hot nuclear matter effects, on the other hand, describe the modification of J/ψ mesons during the evolution of the QGP. In ultra-relativistic heavy-ion collisions, however, both effects are present and it is a challenge to disentangle them.

The J/ψ distribution obtained with cold nuclear matter effects according to Equation (4.24) is used as an input for the partonic transport model BAMPS (see Chapter 4), which we employ in this chapter to study hot nuclear matter effects. In the medium J/ψ can dissociate via the process $J/\psi + g \rightarrow c + \bar{c}$, whose cross section is given in Section 3.3. Furthermore, J/ψ regeneration from independent charm and anti-charm quarks is possible. Especially in view of the large charm production at the LHC, the process can be rather important. The cross section for the process $c + \bar{c} \rightarrow J/\psi + g$ is also given in Section 3.3.

Lattice results [AH04, MP07] indicate that a J/ψ can survive in the QGP up to the dissociation temperature T_d and melts at higher temperatures. In this study we use $T_d = 2T_c$ [RBC10, LQXZ09] with $T_c = 165$ MeV being the phase transition temperature. However, the exact value of T_d has not been determined yet and it is to some extent a parameter of the models. In BAMPS we implement the melting effect in the following way. If the temperature in a cell is larger than the dissociation temperature T_d , all the J/ψ in this cell decay to charm and anti-charm quarks. This is a rather crude and somehow artificial treatment of this phenomenon. However, it could be improved by considering—instead of Equation (3.131)—a more sophisticated cross section for J/ψ dissociation that leads to such a melting above T_d by itself without the need of an additional cut-off. A first attempt in this direction has been done, for instance, in Ref. [ZR08] with quasi-free scattering.

The main focus of this thesis is put on open heavy flavor. J/ψ production and suppression are studied, in a sense, as a side project, in particular, because of the unique opportunity to have with BAMPS a common framework that includes light as well as heavy flavor and that has access to all medium properties. In this chapter some first J/ψ results at RHIC energies are presented. We tried to incorporate all important effects in the most accurate way. However, more work on the details should be done and uncertainties of employed parameters need to

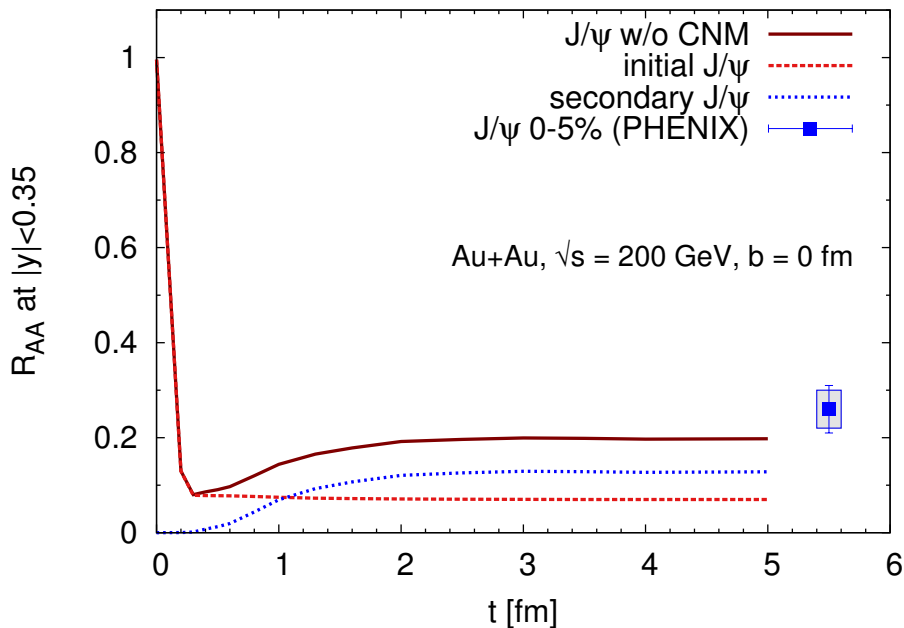


Figure 7.1.: R_{AA} of J/ψ at mid-rapidity $|y| < 0.35$ in central Au+Au collisions at RHIC as a function of time without cold nuclear matter effects. In addition, the contribution from initial and secondary J/ψ as well as experimental data [PHENIX07c] are shown.

be studied. For instance, any feed-down effects from higher $c\bar{c}$ states such as χ_c and ψ' on the J/ψ yield are neglected, which prevents detailed quantitative comparisons with data. It would be interesting to extend this study to cover a broader spectrum of J/ψ physics not only at RHIC but also at LHC energies. Nevertheless, the next sections show the wealth of J/ψ phenomena in heavy-ion collisions and demonstrate that BAMPS provides an unique framework to study them in detail.

7.1. J/ψ suppression

Figure 7.1 shows the nuclear modification factor R_{AA} of J/ψ without cold nuclear matter effects for central Au+Au collisions at RHIC as a function of time. The initial value is exactly one since cold nuclear matter effects are not included. Then right from the beginning, a lot of initially produced J/ψ melt due to the large temperature of the QGP at RHIC. After the rapid melting, the number of initial J/ψ stays nearly constant because most of the survived J/ψ are located at the edge of the heavy-ion collision. A counter-effect to the J/ψ dissociation is the regeneration, which enhances the total J/ψ number. Our final value at the end of the QGP phase is a bit smaller than the experimental data point.

In Figure 7.2 the same curve for the total J/ψ is shown and compared to the curve that also includes cold nuclear matter effects. Although the initial value of the yellow dashed curve is considerably smaller, the final J/ψ number is only slightly less since most of the J/ψ melt anyhow. The reason for the substantial melting in the first 0.5 fm is the large

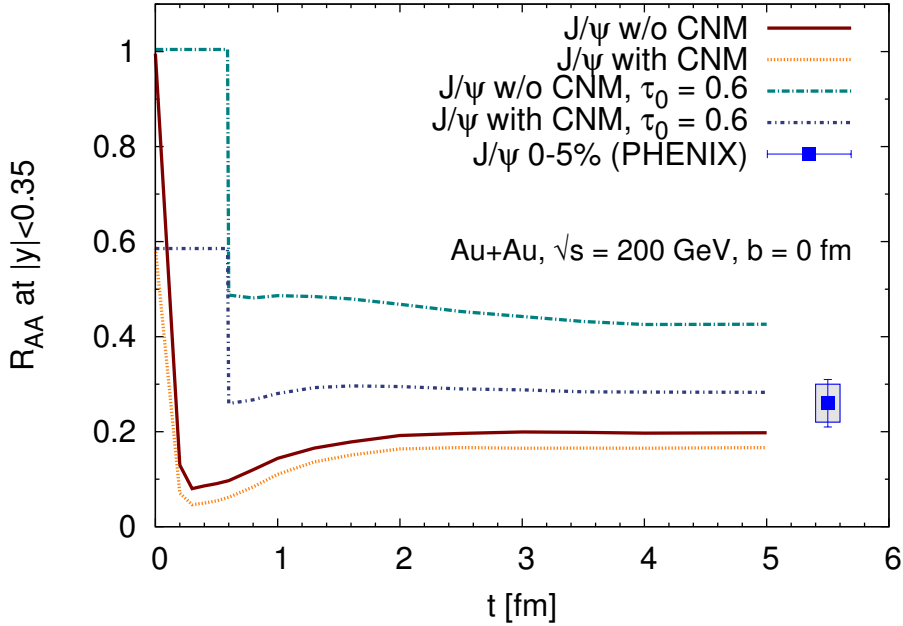


Figure 7.2.: As Figure 7.1 with and without cold nuclear matter (CNM) effects as well as J/ψ formation time $\tau_0 = 0.6$ fm.

medium temperature. However, since the medium is not thermalized yet, the physical meaning of defining a temperature is more than questionable. Therefore, we give the initial J/ψ a formation time of $\tau_0 = 0.6$ fm. During this time they cannot melt in the medium. Consequently, as shown in Figure 7.2, the J/ψ yield stays constant in this time span. Thereafter, the drop due to instantaneous melting is not as pronounced as without formation time, since the medium already cooled down and the temperature is properly defined. The value of τ_0 reflects the thermalization time of the QGP, but is to some extent a free parameter. It would be interesting to study the dependence of the R_{AA} on τ_0 in more detail, which we leave as a future project. The final value of the curve that includes cold nuclear matter effects and a formation time is in good agreement with the data point at mid-rapidity in central collisions.

In Figure 7.3 the curve with cold nuclear matter effects and a J/ψ formation time of $\tau_0 = 0.6$ fm is compared to the model calculation of the Tsinghua group [LQXZ09, LQXZ10, ZXZ10, LXZ10]. They study J/ψ dissociation and regeneration with a three dimensional transport equation and a 2 + 1D hydrodynamic model. As can be seen in the figure, they choose slightly different parameterizations of the cold nuclear matter effects than we do (cf. Section 4.4). The starting time of their hydrodynamical medium evolution is also $\tau_0 = 0.6$ fm, which leads to a similar drop in the J/ψ number at this time due to instantaneous melting. Because of different medium evolutions, the curves from BAMPS and Tsinghua differ slightly as a function of time. Moreover, their yield of secondarily produced J/ψ is higher than in BAMPS, although we implemented the same cross section for J/ψ regeneration. The reason for this difference lies in the treatment of open heavy flavor. While all charm quarks are taken to be thermalized in the Tsinghua model, BAMPS includes their full space-time evolution as well, which effectively reduces the J/ψ regeneration.

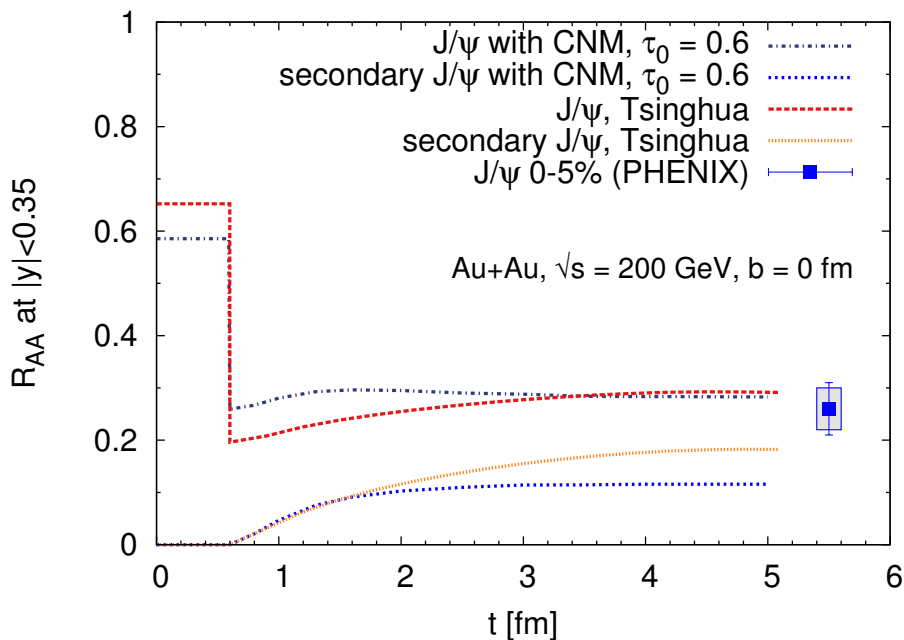


Figure 7.3.: R_{AA} of J/ψ at mid-rapidity at RHIC as a function of time with cold nuclear matter (CNM) effects and a J/ψ formation time of $\tau_0 = 0.6$ fm compared to the model of the Tsinghua group [LQXZ09, LQXZ10, ZXZ10, LXZ10]. The respective secondary J/ψ curves are also shown.

In Figure 7.4 the BAMPS calculations of the nuclear modification factor of J/ψ at RHIC for different rapidities are depicted as a function of the number of participants. Also for non-central collisions the agreement of our results and the data is very good at mid-rapidity. At forward rapidity the J/ψ suppression in BAMPS is less than at mid-rapidity, which is in contrast to the experimental data. The reason for the smaller suppression at forward rapidity lies in the smaller temperature in this region. In contrast to many other theoretical models, BAMPS does not assume boost invariance in the beam direction, and, hence, the temperature depends on the rapidity.

The generally assumed reason for the smaller suppression at mid-rapidity is the regeneration of secondary J/ψ , which is larger at mid-rapidity since more charm quarks are present. Although we observe a larger regeneration at mid-rapidity in BAMPS as well, the effect is not strong enough to counteract the larger suppression due to the larger temperature at mid-rapidity.

7.2. Elliptic flow of J/ψ

Experimental measurements at RHIC showed that the elliptic flow v_2 of J/ψ is very small [STAR11b]. This is in contradiction with the regeneration picture where the flow of the charm quarks should be transferred to the J/ψ . BAMPS is an ideal framework to study this in more detail since it reproduces the D meson flow (cf. Section 6.1) and also allows recombination of

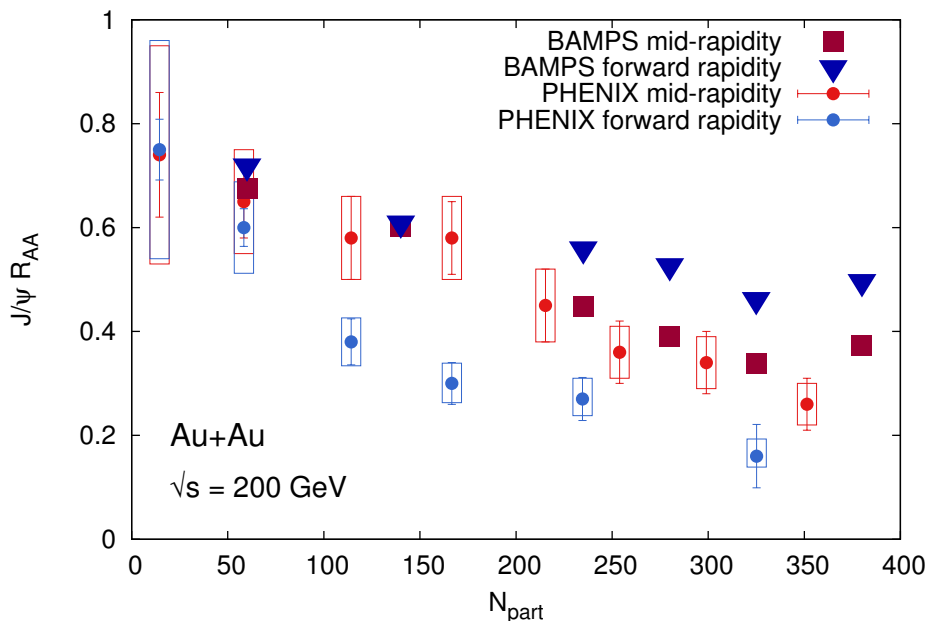


Figure 7.4.: R_{AA} of J/ψ at mid-rapidity $|y| < 0.35$ and forward rapidity $1.2 < y < 2.2$ for Au+Au collisions at RHIC as a function of the number of participants, together with experimental data [PHENIX07c]. Cold nuclear matter effects and a J/ψ formation time of $\tau_0 = 0.6$ fm are included.

charm quarks to J/ψ .

Figure 7.5 shows that in BAMPS even with regeneration the elliptic flow of all J/ψ is compatible with the experimental data. As expected, the v_2 of initial J/ψ is zero apart from small statistical fluctuations. In contrast, the flow of secondary J/ψ depends crucially on its production time. A later time means a larger v_2 since the regenerating charm quarks have already picked up flow from the medium. However, in non-central collisions the number of secondarily produced J/ψ is small and the total J/ψ is dominated by initial production. Therefore, the v_2 of total J/ψ is very small and consistent with the data. To get an idea of the relevant scale of the J/ψ elliptic flow, we also plot the v_2 of charm quarks. The finding of a very small J/ψ elliptic flow is in agreement with the results of other transport models that study J/ψ [ZER13, LXZ10].

In the following, we investigate in a qualitative study the effect of regeneration on flow—in particular, the impact of the production time of secondary J/ψ on the elliptic flow. To keep things simple, we consider only the elliptic flow of secondary J/ψ , which are created in the medium from the recombination of two charm quarks. As shown in Figure 7.5, initial J/ψ has (nearly) vanishing v_2 and must be taken into account if one wants to compare to data.

In Figure 7.6 we show the number of secondary J/ψ as a function of time and their elliptic flow as a function of transverse momentum for two (academic) scenarios. In one scenario the J/ψ melting temperature is large. Hence, secondary J/ψ can be formed already in the early phase of the medium evolution where the temperature is still large. In the other scenario we choose a small melting temperature, which only allows secondary J/ψ production at late times.

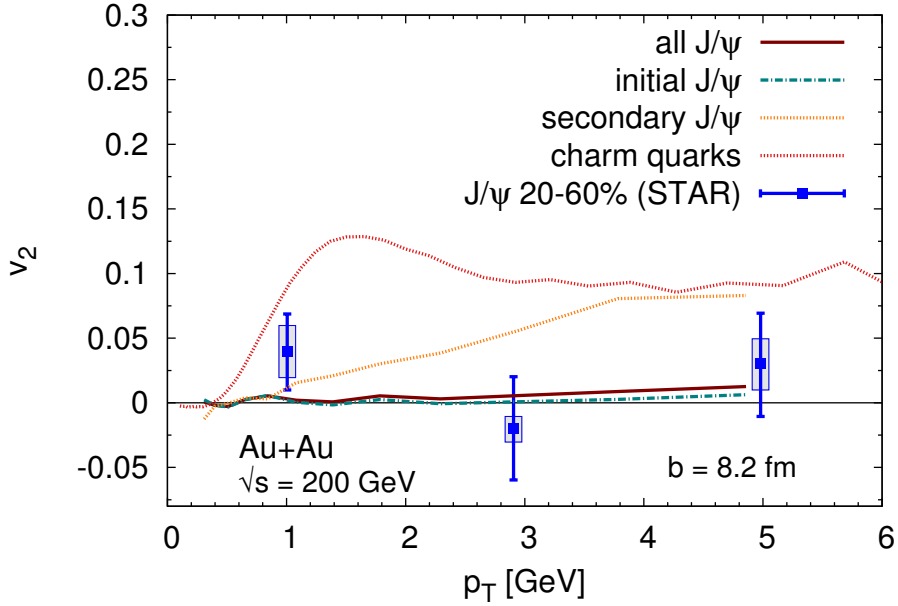


Figure 7.5.: Elliptic flow of J/ψ as a function of the transverse momentum with data [STAR11b]. For comparison the charm quark v_2 with only binary interactions and $K = 3.5$ (see Section 6.1) is also shown.

The total number for both scenarios is normalized to one since the v_2 is an averaged quantity and does not depend on the number and we only want to emphasize the different production times in both scenarios.

J/ψ from the first scenario only have a small v_2 since they are produced early and their constituent charm quarks could not build up a sizeable flow. The second scenario corresponds more to the coalescence picture. Due to the late production, the regenerating charm quarks have already a sizeable v_2 close to the final value, which is also depicted in Figure 7.6. As in the coalescence picture, the J/ψ v_2 is shifted to twice as large values at twice as large p_T compared to the charm flow,

$$v_2^{J/\psi}(p_T) \approx 2v_2^c(p_T/2) . \quad (7.1)$$

Hence, the fraction of initial J/ψ at large p_T must be considerably larger than secondary J/ψ to bring down the v_2 of the total J/ψ in a region that is compatible with the data.

At the LHC, the experimental v_2 data is still small but slightly larger than zero, at least for one p_T bin [ALICE13a]. This might enable models to pin down the contribution from regeneration and learn more about the production time and fraction of secondarily produced J/ψ . It will be also interesting to study this in more detail with BAMPS in the future.

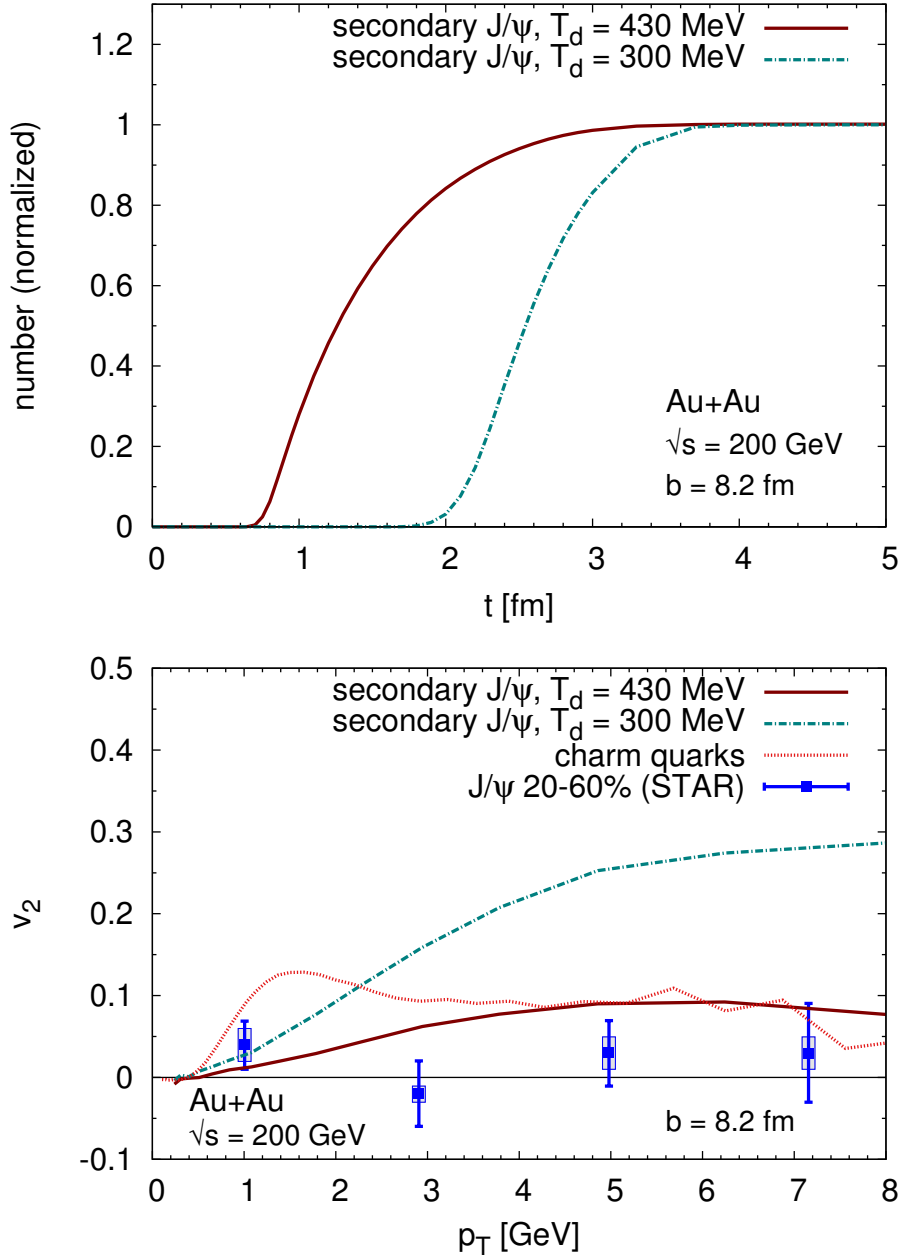


Figure 7.6.: Time evolution (top) of the number of secondary J/ψ (normalized) and their elliptic flow (bottom) as a function of transverse momentum at the end of the QGP phase at RHIC for small and large J/ψ melting temperature T_d . For comparison, the charm v_2 and experimental data on J/ψ [STAR11b] are also shown. Since the curves reflect a mainly academic study, the data points are only to guide one's eye and not for quantitative comparison. As a note, the contribution of initial J/ψ with vanishing v_2 is not depicted.

8. Conclusions

There is something fascinating about science. One gets such wholesale returns of conjecture out of such a trifling investment of fact.

Life on the Mississippi
MARK TWAIN

In the following, the content of this work is briefly summarized and an outlook on future studies and possible improvements is given.

8.1. Summary

In this work hard probes in ultra-relativistic heavy-ion collisions are studied within the partonic transport model *Boltzmann Approach to MultiParton Scatterings* (BAMPS). The focus is put on open heavy flavor, but also light particles are considered, in particular, to highlight differences due to mass effects. Furthermore, we investigate the dissociation and regeneration of J/ψ mesons in the hot and dense medium produced in heavy-ion collisions.

BAMPS is a partonic transport model that solves the BOLTZMANN equation for on-shell particles and perturbative QCD (pQCD) interactions. For light partons, all possible $2 \rightarrow 2$ and $2 \leftrightarrow 3$ processes are included. As part of this work, all relevant elastic and radiative collisions of heavy quarks with other medium constituents have been implemented in BAMPS, while the running of the coupling is explicitly taken into account for elastic as well as radiative light and heavy flavor processes. The divergent t channel of heavy flavor scatterings is regularized with a screening mass μ that is determined by matching elastic energy loss calculations with leading order pQCD cross sections to results from hard thermal loop (HTL) calculations. The comparison of both results shows that the screening mass μ is smaller than the usually employed DEBYE mass m_D , more precisely, $\mu^2 = \kappa_t m_D^2$ with $\kappa_t = 1/(2e) \approx 0.2$.

For radiative processes we recalculate the commonly used approximation to the leading order pQCD matrix element for partonic $2 \rightarrow 3$ processes, which was first derived by GUNION and BERTSCH (GB) for massless quarks, to be also valid for massive partons. In the GB approximation the radiative matrix element factorizes in an elastic part and a factor that describes the radiation. During the course of this work we found that the original GB matrix element deviates from the exact result in characteristic regions of the phase space, which becomes important when employing the matrix element to obtain rates or cross sections from phase space integration. Therefore, based on a detailed analytic investigation of the underlying approximations, we propose an improved version of the GB matrix element for all light and heavy partons. A very good agreement between the improved GB result and the exact calculation is found in all phase space regions by performing extensive numerical comparisons of the total cross sections as well as more differential quantities, while taking

the full kinematics for the phase space integration into account. Furthermore, we calculate the radiative heavy quark matrix element within FEYNMAN gauge (in contrast to light cone gauge in the GB case) as well as for slightly different approximations and show that the results from both gauges are consistent. In accordance to binary interactions, radiative processes are implemented in BAMPS by explicitly taking the running coupling into account.

We specifically verify the presence of the dead cone suppression in our results. Due to this effect gluon radiation off heavy quarks is suppressed at small angles. While our result of the dead cone suppression factor is consistent with the calculation of DOKSHITZER and KHARZEEV, it extends their result by being valid for all heavy quark masses and all angles. Furthermore, the BAMPS implementation of the LANDAU-POMERANCHUK-MIGDAL (LPM) effect that describes coherence effects of multiple in-medium gluon radiation is extended to include also finite heavy quark mass effects.

As a note, during the course of this work we also implemented the running coupling for light parton interactions in addition to the heavy flavor processes. Hence, if one does not employ the improved screening procedure from HTL for heavy quarks—thus, setting $\kappa_t = 1$ —both heavy and light partons are treated on the same footing.

The analytic calculation of PESHIER and PEIGNE for the energy loss of energetic heavy quarks in a static thermal medium within the HTL approach for quantum statistics is outlined and recalculated for BOLTZMANN statistics to enable comparisons to BAMPS. Employing the improved screening procedure we find a good agreement with the numerical BAMPS results. Furthermore, we derive an analytic formula for the elastic heavy quark energy loss in a flowing medium, which also agrees well with the numerical calculations. In an extensive numerical study, the elastic as well as radiative energy loss of heavy quarks is investigated for constant and running coupling as well as standard and improved DEBYE screening. Although the improved screening procedure reproduces the overall energy loss per unit length of the analytic HTL calculation, it is not clear whether more differential quantities, for instance, a small energy loss per collision and a huge rate, are correctly featured or just a result of the effective treatment of the screening.

Due to the LPM implementation and the huge binary rate with $\kappa_t = 0.2$, the radiative heavy quark energy loss with the improved screening is found to be very small. With a standard DEBYE screening, however, the radiative energy loss of light and heavy quarks is about a factor of two larger than the elastic energy loss. Although the rates of elastic and radiative collisions are comparable, the energy loss per collision for radiative processes is increased due to the three-body phase space in the final state. Comparing the radiative energy loss of charm and light quarks with standard DEBYE screening, we find that both are very similar for constant and running coupling because the LPM effect produces a second dead cone at small emission angles that overshadows the dead cone due to the heavy quark mass. In contrast, the mass dead cone for bottom quarks is large enough to be still visible in the presence of the LPM effect. We investigate in detail the sensitivity of the results on the LPM effect by modifying the LPM cut-off and employing the mean free path of the jet or the emitted gluon in the LPM implementation.

To compare with experimental open heavy flavor data, we study heavy quarks in full BAMPS simulations of ultra-relativistic heavy-ion collisions with the running coupling and the improved screening procedure. The initial heavy quark distributions are obtained with MC@NLO, which gives good agreement with heavy flavor data in proton+proton collisions at RHIC and LHC. Quantitative comparisons show that elastic processes are responsible for a large fraction of

the observed suppression of heavy quarks. However, they alone are not able to reproduce the data of the nuclear modification factor R_{AA} or the elliptic flow v_2 of any heavy flavor particle species.

Before radiative heavy quark processes have been implemented in BAMPS, we mimicked their influence by effectively increasing the elastic cross section by a factor $K = 3.5$, which is tuned to the elliptic flow data of heavy flavor electrons at RHIC. Simultaneously, the nuclear modification factor of heavy flavor electrons at RHIC can be described with the same parameter. Having fixed this parameter to the RHIC data, we find a good agreement with the experimentally measured nuclear modification factor of D mesons, non-prompt J/ψ (from B meson decays), and heavy flavor muons at the LHC energy of $\sqrt{s} = 2.76$ TeV. Furthermore, we made predictions for the nuclear modification factor of heavy flavor electrons as well as the non-prompt J/ψ , D meson, electron, and muon elliptic flow at the LHC. Recently released data on the nuclear modification factor of electrons and the elliptic flow of electrons and D mesons show an excellent agreement with our predictions.

It is striking that both the nuclear modification factor and elliptic flow of various heavy flavor particles at RHIC and LHC can be simultaneously described with only elastic heavy quark interactions if their cross sections are scaled with $K = 3.5$. While the agreement indicates the consistency of the experimental data at both colliders as well as of our model, the need of the phenomenological K factor is rather unsatisfying from the theory perspective.

Therefore, the question arises whether radiative processes can account for the missing contribution parameterized by the K factor. To this end, we carried out BAMPS calculations with elastic and radiative processes for both light and heavy particles in a common framework.

Since the improved screening prescription is only derived for heavy quarks, we first employed the standard screening to treat light and heavy partons consistently and to study finite mass effects. Analogous to what we observe in the case of a static medium, the energy loss of charm and light quarks in full heavy-ion collisions is very similar for constant and running coupling. This is again because of a second dead cone due to the LPM effect that overshadows the dead cone due to the charm mass. In contrast, gluons are more suppressed than light quarks (and charm quarks) due to a larger color factor. However, mass effects in the fragmentation of gluons and light quarks to charged hadrons and charm quarks to D mesons lead to a very similar suppression of charged hadrons and D mesons in BAMPS. This is a remarkable explanation of the heavy flavor puzzle at RHIC and LHC, which denotes the experimental observation that charged hadrons and D mesons are equally suppressed.

Although the shape of the nuclear modification factor as a function of the transverse momentum is nicely reproduced by BAMPS, the overall suppression is underestimated. The reason for this discrepancy is probably the effective implementation of the LPM effect in BAMPS, which discards all possible interference effects and only allows independent scatterings. If we introduce a factor $X < 1$ that modifies the LPM cut-off and effectively allows more radiative interactions, a good agreement with the experimental data of charged hadrons and D mesons is found for $X = 0.3$. Although the exact value of X is a free parameter, we expect that a more sophisticated implementation of the LPM effect would effectively correspond to an $X < 1$ and might make the need of the X parameter obsolete. We want to emphasize that light partons and heavy quarks are treated consistently in this calculation and we can, thus, provide a microscopic explanation of the heavy flavor puzzle with the dead cone effect being explicitly present in the employed matrix elements. For bottom quarks the dead cone suppression is stronger. Hence, our calculated nuclear modification factor of non-prompt J/ψ

is larger than that of D mesons, but also slightly larger than the data.

If the improved screening procedure is applied to heavy quarks, radiative processes are strongly suppressed due to the large rate of binary scatterings and its effect on the LPM treatment. Hence, the nuclear modification factor of heavy flavor particles is larger than the data. However, if we set the LPM parameter to $X = 0.2$, we find a good agreement with the nuclear modification factor of D mesons, non-prompt J/ψ , and heavy flavor electrons at LHC. It is noteworthy, that the value of X lies in the same regime as for the case without the improved screening.

Although the heavy flavor data of the nuclear modification factor is nicely reproduced with $X = 0.2$, the same calculations cannot describe the heavy flavor elliptic flow data simultaneously. Compared to the binary interactions scaled with $K = 3.5$, which give a good agreement with the nuclear modification factor and elliptic flow data, elastic and radiative processes with $X = 0.2$ but without a K factor have a very similar energy loss but a considerably smaller transport cross section. Since the latter is the relevant quantity for isotropization and the build-up of elliptic flow, the v_2 of elastic and radiative collisions is smaller than the data, whereas the v_2 of the scaled binary collisions agrees with the data. An explanation for the small elliptic flow could be the lack of event-by-event fluctuations and coalescence effects in BAMPS, which might increase the v_2 .

Our results are in accordance with most of the findings in the literature. All models that include radiative contributions (except the model of the Nantes group) cannot describe the nuclear modification factor and elliptic flow simultaneously. With only binary interactions (either with scaled pQCD cross sections as presented in this work or resonance scattering) some models can explain both. However, as we showed in this work, the inclusion of radiative processes influences the results on the nuclear modification factor and elliptic flow differently. Hence, it is not clear whether these models can still describe both if radiative processes are taken into account.

Lattice QCD calculations suggest that J/ψ mesons survive in the quark gluon plasma to some extent. Therefore, we included in BAMPS in addition to gluons, light quarks, and heavy quarks also J/ψ mesons, which can be dynamically dissociated by interactions with gluons or if the medium temperature becomes larger than the J/ψ dissociation temperature T_d . Furthermore, two independent charm quarks can bind together to form a J/ψ during the evolution of the quark gluon plasma. The initial J/ψ distribution is parameterized from experimental proton+proton data and the inclusion of cold nuclear matter effects such as shadowing, nuclear absorption, and the Cronin effect.

In full heavy-ion collisions at RHIC simulated with BAMPS, we study the time dependence of the dynamic J/ψ dissociation and regeneration. Including cold nuclear matter effects and a J/ψ formation time of $\tau_0 = 0.6$ fm to prevent melting during a stage where the temperature cannot be reliably defined, a good agreement with the experimental data of the J/ψ nuclear modification factor at mid-rapidity is found for different centralities. However, in contrast to experimental data, the J/ψ suppression at forward rapidity in central and semi-central events is smaller than the suppression at mid-rapidity, which is due to a smaller temperature in BAMPS at forward rapidity compared to the mid-rapidity region.

Experimental measurements at RHIC reveal that the elliptic flow of J/ψ is very small. This is in contradiction with the regeneration picture where the flow of the charm quarks should be transferred to the J/ψ mesons. BAMPS is an ideal framework to study this in more detail since it can reproduce the D meson flow and also allows recombination of charm

of a more sophisticated treatment of the LPM effect on the microscopic level seems to be possible. To this end, the emitted gluon in $2 \rightarrow 3$ processes accumulates additional transverse momentum and decreases its formation time until it is eventually formed. Only then, the other partons involved in this process are allowed to rescatter. Possible prescriptions in this regard are outlined, for instance, in Refs. [ZSW09, ZSW11, CSBS11, CSM12].

A theoretically more advanced implementation of the LPM effect would certainly allow more radiative collisions and might be able to explain the factor $X = 0.2 - 0.3$ in the current implementation that is needed to describe the measured suppression of light and heavy high-energy particles in heavy-ion collisions.

For the evolution of heavy quarks in heavy-ion collisions, not only the interactions of heavy quarks with the medium play an important role but also the medium evolution itself. For instance, a recent study [GVvH⁺11] suggests that the medium evolutions of two different models can lead to about a factor of two difference in heavy flavor observables, even if the same heavy quark interactions are employed. Therefore, when comparing different heavy flavor models, one does not know whether differences come from different heavy quark interactions or different medium evolutions. To entangle both and gain more insight about the microscopic interaction properties of heavy quarks, we are convinced that it would be very helpful to compare the heavy flavor energy loss and the transport rate in a controlled environment of a thermalized static medium for all models on the market. First comparisons of these quantities with the Nantes group proofed to be very fruitful.

Several further studies would be interesting to investigate within the BAMPS framework presented in this work with light and heavy partons as well as elastic and radiative collisions. To understand the impact of the dead cone effect in more detail, it would be insightful to compare jet shower shapes of fully reconstructed light particle jets and bottom tagged jets. These quantities might be accessible in LHC experiments [CMS12b, CMS13c, CMS13a, ATLAS13]. A study that is experimentally more challenging is the angular correlation of D mesons [Z⁺07, Mis11, NAGW13]. The transport model BAMPS is well suited for such investigations since it contains from MC@NLO a very accurate initial heavy quark (angle) distribution and it has access to all heavy quark space-time properties throughout the quark gluon plasma evolution.

In this work, we proposed the improved GUNION-BERTSCH matrix element and employed it for heavy quarks as well as for energetic light partons. To this end, it is also planned to study its impact on the bulk medium in more detail. Although we expect a decrease of the elliptic flow and an increase of the shear viscosity compared to the original GB cross section, one must wait for the numerical results to see how large the effect will actually be. While the running coupling is currently only implemented for $2 \rightarrow 2$ and $2 \rightarrow 3$ interactions, we also want to include it in $3 \rightarrow 2$ collisions. Moreover, the influence of the inclusion of a hadronization scheme (such as the coalescence model) on the bulk medium observables will be of great interest. Subsequent hadronic interactions might also affect observables like the elliptic flow. The latter is also sensitive on initial event-by-event fluctuations. Although it is challenging to include such effects in BAMPS on a particle basis due to the test particle method, it might be possible by sampling initial test particles according to a smeared distribution that includes fluctuation effects [PSB⁺08, SJG11].

Coalescence and initial stage fluctuations might also affect heavy quarks at low transverse momenta. Both are expected to increase the elliptic flow of heavy flavor particles. Thus, neglecting these effects in BAMPS could be an explanation why we observe an elliptic flow smaller than the data if we consider elastic and radiative processes.

Finally, it would be interesting to extend the presented J/ψ study from RHIC to LHC energy. An abundance of experimental data [ALICE12d, CMS12f] is already available at low and high transverse momenta, which can help to further constrain theoretical considerations. In addition, a more detailed study of the sensitivity of the experimentally accessible observables on the input values of the cold nuclear matter parameterizations as well as on the J/ψ dissociation temperature and formation time would be worthwhile. The implementation of Υ states in BAMPS is in principle also possible and would allow for further comparisons to data [CMS11a, CMS12d].

With the wealth of new data and detailed experimental analysis from the LHC and also from RHIC, heavy-ion theorists are in a great position to constrain their models and confront their calculations with the measurements to gain deeper insight in the properties of the quark gluon plasma. As we showed in this thesis, the partonic transport model BAMPS is a great tool to study the dynamics of the quark gluon plasma on a microscopic level—not only for hard probes but also for the bulk medium. It will be highly interesting to employ this unique framework also for the suggested future studies outlined in this section.

A. Appendices

To the small part of ignorance that we arrange and classify we give the name of knowledge.

The Devil's Dictionary
AMBROSE BIERCE

A.1. Natural units

The laws of physics are, of course, independent of any unit system. However, if one wants to calculate numbers, it is convenient to choose a proper system suitable to the problem at hand. The standard unit system in physics is the SI¹ system. However, it is designed for the usual scales of the world around us. In contrast, the scales in high-energy physics are very different and quantities expressed in SI units are not very handy. Therefore, natural units are widely used in high-energy physics. To reduce the complexity of equations, the most relevant physical constants, that is, the speed of light c , the PLANCK constant \hbar , and the BOLTZMANN constant k_B , are set to 1,

$$c = \hbar = k_B = 1 . \quad (\text{A.1})$$

This implies that space and time as well as energy and momentum have the same units, respectively. The former are usually expressed in femtometer ($1 \text{ fm} = 10^{-15} \text{ m}$) and the latter in gigaelectronvolt ($1 \text{ GeV} = 10^6 \text{ eV}$). In principle, however, only one of these two units is necessary since both are related via

$$1 = \hbar c = 0.197 \text{ GeV fm} . \quad (\text{A.2})$$

Cross sections are usually given in millibarn (mb), which is the unit of an area. It is related to the units given above via

$$1 \text{ mb} = 0.1 \text{ fm}^2 = 2.568 \text{ GeV}^{-2} . \quad (\text{A.3})$$

A.2. Mandelstam variables

The MANDELSTAM variables [Man58] are useful to express matrix elements or cross sections since they do not depend on the frame of reference. For $2 \rightarrow 2$ processes they are defined by

$$\begin{aligned} s &= (p_1 + p_2)^2 = (p_3 + p_4)^2 \\ t &= (p_1 - p_3)^2 = (p_2 - p_4)^2 \\ u &= (p_1 - p_4)^2 = (p_2 - p_3)^2 , \end{aligned} \quad (\text{A.4})$$

¹*International System of Units*, abbreviated SI from French: *Le Système international d'unités*

where p_1 and p_2 are the incoming and p_3 and p_4 the outgoing momenta (cf. also Figure 3.3 on page 27 for the notation). From the definitions it is obvious that the MANDELSTAM variables are indeed LORENTZ invariant quantities. The variable s also happens to be the squared center-of-mass energy.

The MANDELSTAM variables are related to each other and the masses of the particles via

$$s + t + u = \sum_{i=1}^4 m_i^2, \quad (\text{A.5})$$

which can be easily derived from Equation (A.4).

The previous definitions can also be generalized to a $2 \rightarrow 3$ process,

$$\begin{aligned} s &= (p_1 + p_2)^2, & s' &= (p_3 + p_4)^2, \\ u &= (p_1 - p_4)^2, & u' &= (p_2 - p_3)^2, \\ t &= (p_1 - p_3)^2, & t' &= (p_2 - p_4)^2, \end{aligned} \quad (\text{A.6})$$

where we defined the momenta of the involved particles as $p_1 + p_2 \rightarrow p_3 + p_4 + p_5$. Accordingly to the binary case, the MANDELSTAM variables are related to the masses by

$$s + t + u + s' + t' + u' = 2 \sum_{i=1}^4 m_i^2 + m_5^2. \quad (\text{A.7})$$

Clearly, if the momentum p_5 is much softer than the other momenta and m_5 vanishes, the dashed variables are redundant, $s' \rightarrow s$, $t' \rightarrow t$, and $u' \rightarrow u$, as in the binary case. Also Equation (A.5) can be recovered from Equation (A.7) for this configuration.

A.3. Binary light parton cross sections

According to Equation (3.5) the $2 \rightarrow 2$ differential cross section for light partons ($m = 0$) is given by

$$\frac{d\sigma}{dt} = \frac{1}{16\pi s^2} |\overline{\mathcal{M}}_{2 \rightarrow 2}|^2. \quad (\text{A.8})$$

In the following we write down all the $2 \rightarrow 2$ matrix elements for light parton scatterings, which are taken from Refs. [CKR77, PS95] if not indicated otherwise. Furthermore, the explicit expression for the matrix element with a running coupling and DEBYE screening is stated. As we discussed in Section 3.1.3, the coupling of each channel is evaluated at the scale of the given channel, which is the momentum transfer of the internal propagator, i.e., s , t , and u for the respective channel. Furthermore, the coupling in the DEBYE mass definitions from Equations (3.18) and (3.19), which screen the propagator, is also evaluated at the corresponding virtuality.

A.3.1. Matrix elements

$gg \rightarrow gg$

The matrix element of the process was first calculated in Ref. [CS78], although with a wrong term for the constant. The result was corrected in Ref. [CKR77], which also agrees with

Ref. [PS95].

$$\text{Matrix element} \quad |\overline{\mathcal{M}}_{gg \rightarrow gg}|^2 = 72\pi^2 \alpha_s^2 \left[3 - \frac{tu}{s^2} - \frac{su}{t^2} - \frac{st}{u^2} \right] \quad (\text{A.9a})$$

$$\text{Small angle behavior } t \rightarrow 0 \quad |\overline{\mathcal{M}}_{gg \rightarrow gg}|^2 = 72\pi^2 \alpha_s^2 \frac{s^2}{t^2} \quad (\text{A.9b})$$

$$\text{Large angle behavior } u \rightarrow 0 \quad |\overline{\mathcal{M}}_{gg \rightarrow gg}|^2 = 72\pi^2 \alpha_s^2 \frac{s^2}{u^2} \quad (\text{A.9c})$$

With running coupling and DEBYE screened propagators the matrix element reads

$$|\overline{\mathcal{M}}_{gg \rightarrow gg}|^2 = 72\pi^2 \left[3\alpha_s^2(s) - \alpha_s^2(s) \frac{tu}{[s + m_D^2(\alpha_s(s))]^2} - \alpha_s^2(t) \frac{su}{[t - m_D^2(\alpha_s(t))]^2} - \alpha_s^2(u) \frac{st}{[u - m_D^2(\alpha_s(u))]^2} \right]. \quad (\text{A.9d})$$

Since the first term cannot be attributed to one specific channel, we set the scale for the running coupling to the squared center-of-mass energy. However, we checked that the cross section is not very sensitive on this choice.

qg → qg and q̄g → q̄g

The matrix element from Refs. [CKR77, PS95] is simplified to such an extent that the internal propagators cannot be identified. Therefore, we take the matrix element for heavy quark scattering with a gluon $Qg \rightarrow Qg$ [Com79], see Equation (3.12), which is given for all channels individually, and set the mass to zero. Without screening or running coupling it agrees with the simplified result [CKR77, PS95].

$$\text{Matrix element} \quad |\overline{\mathcal{M}}_{qg \rightarrow qg}|^2 = 16\pi^2 \alpha_s^2 \left[-\frac{4}{9} \left(\frac{su}{s^2} + \frac{su}{u^2} \right) - 2\frac{su}{t^2} - \frac{su}{ts} - \frac{su}{tu} \right] \quad (\text{A.10a})$$

$$\text{Small angle behavior } t \rightarrow 0 \quad |\overline{\mathcal{M}}_{qg \rightarrow qg}|^2 = 32\pi^2 \alpha_s^2 \frac{s^2}{t^2} \quad (\text{A.10b})$$

$$\text{Large angle behavior } u \rightarrow 0 \quad |\overline{\mathcal{M}}_{qg \rightarrow qg}|^2 = \frac{64\pi^2 \alpha_s^2}{9} \frac{s}{-u} \quad (\text{subdominant}) \quad (\text{A.10c})$$

As a note, the ratio of the small angle result to the small angle result for $gg \rightarrow gg$ is just the color factor 4/9.

The MANDELSTAM variables in the different terms, e.g., su/u^2 , have not been canceled in order to screen the full propagator (in this case $1/u^2$). With running coupling and DEBYE screened propagators the matrix element reads

$$|\overline{\mathcal{M}}_{qg \rightarrow qg}|^2 = 16\pi^2 \left[-\frac{4}{9} \left(\alpha_s^2(s) \frac{su}{[s + m_q^2(\alpha_s(s))]^2} + \alpha_s^2(u) \frac{su}{[u - m_q^2(\alpha_s(u))]^2} \right) - 2\alpha_s^2(t) \frac{su}{[t - m_D^2(\alpha_s(t))]^2} - \alpha_s(s)\alpha_s(t) \frac{su}{[s + m_q^2(\alpha_s(s))][t - m_D^2(\alpha_s(t))]} - \alpha_s(t)\alpha_s(u) \frac{su}{[t - m_D^2(\alpha_s(t))][u - m_q^2(\alpha_s(u))]} \right]. \quad (\text{A.10d})$$

qq' → qq'

For this process there is only one t channel diagram. Hence, the matrix element looks rather simple.

$$\text{Matrix element} \quad |\overline{\mathcal{M}}_{qq' \rightarrow qq'}|^2 = \frac{64\pi^2 \alpha_s^2}{9} \left[\frac{u^2 + s^2}{t^2} \right] \quad (\text{A.11a})$$

$$\text{Small angle behavior } t \rightarrow 0 \quad |\overline{\mathcal{M}}_{qq' \rightarrow qq'}|^2 = \frac{128\pi^2 \alpha_s^2 s^2}{9 t^2} \quad (\text{A.11b})$$

$$\text{Large angle behavior } u \rightarrow 0 \quad |\overline{\mathcal{M}}_{qq' \rightarrow qq'}|^2 = \frac{64\pi^2 \alpha_s^2}{9} \quad (\text{subdominant}) \quad (\text{A.11c})$$

The ratio of the small angle result to the small angle result for $gq \rightarrow gq$ is again the color factor 4/9. With running coupling and DEBYE screened propagators the matrix element reads

$$|\overline{\mathcal{M}}_{qq' \rightarrow qq'}|^2 = \frac{64\pi^2}{9} \alpha_s^2(t) \frac{u^2 + s^2}{[t - m_D^2(\alpha_s(t))]^2}. \quad (\text{A.11d})$$

qq → qq and q̄q̄ → q̄q̄

In addition to the t channel diagram, which is the same as for $qq' \rightarrow qq'$, there is also a u channel diagram present.

$$\text{Matrix element} \quad |\overline{\mathcal{M}}_{qq \rightarrow qq}|^2 = \frac{64\pi^2 \alpha_s^2}{9} \left[\frac{u^2 + s^2}{t^2} + \frac{t^2 + s^2}{u^2} - \frac{2}{3} \frac{s^2}{tu} \right] \quad (\text{A.12a})$$

$$\text{Small angle behavior } t \rightarrow 0 \quad |\overline{\mathcal{M}}_{qq \rightarrow qq}|^2 = \frac{128\pi^2 \alpha_s^2 s^2}{9 t^2} \quad (\text{A.12b})$$

$$\text{Large angle behavior } u \rightarrow 0 \quad |\overline{\mathcal{M}}_{qq \rightarrow qq}|^2 = \frac{128\pi^2 \alpha_s^2 s^2}{9 u^2} \quad (\text{A.12c})$$

The small angle result is exactly the same as the small angle result for $qq' \rightarrow qq'$. Due to the symmetry of the process the contribution for small u is the same as for small t . With running coupling and DEBYE screened propagators the matrix element reads

$$|\overline{\mathcal{M}}_{qq \rightarrow qq}|^2 = \frac{64\pi^2}{9} \left[\alpha_s^2(t) \frac{u^2 + s^2}{[t - m_D^2(\alpha_s(t))]^2} + \alpha_s^2(u) \frac{t^2 + s^2}{[u - m_D^2(\alpha_s(u))]^2} - \frac{2}{3} \alpha_s(t) \alpha_s(u) \frac{s^2}{[t - m_D^2(\alpha_s(t))][u - m_D^2(\alpha_s(u))]} \right]. \quad (\text{A.12d})$$

q̄q → q̄q

The matrix element for this process can be easily obtained from the process $qq \rightarrow qq$ by crossing s and u channel.

$$\text{Matrix element} \quad |\overline{\mathcal{M}}_{q\bar{q} \rightarrow q\bar{q}}|^2 = \frac{64\pi^2 \alpha_s^2}{9} \left[\frac{u^2 + s^2}{t^2} + \frac{t^2 + u^2}{s^2} - \frac{2}{3} \frac{u^2}{st} \right] \quad (\text{A.13a})$$

$$\text{Small angle behavior } t \rightarrow 0 \quad |\overline{\mathcal{M}}_{q\bar{q} \rightarrow q\bar{q}}|^2 = \frac{128\pi^2 \alpha_s^2 s^2}{9 t^2} \quad (\text{A.13b})$$

$$\text{Large angle behavior } u \rightarrow 0 \quad |\overline{\mathcal{M}}_{q\bar{q} \rightarrow q\bar{q}}|^2 = \frac{128\pi^2 \alpha_s^2}{9} \quad (\text{subdominant}) \quad (\text{A.13c})$$

The small angle result is exactly the same as the small angle result for $qq' \rightarrow qq'$. With running coupling and DEBYE screened propagators the matrix element reads

$$|\overline{\mathcal{M}}_{q\bar{q} \rightarrow q\bar{q}}|^2 = \frac{64\pi^2}{9} \left[\alpha_s^2(t) \frac{u^2 + s^2}{[t - m_D^2(\alpha_s(t))]^2} + \alpha_s^2(s) \frac{t^2 + u^2}{[s + m_D^2(\alpha_s(s))]^2} - \frac{2}{3} \alpha_s(t) \alpha_s(s) \frac{u^2}{[t - m_D^2(\alpha_s(t))][s + m_D^2(\alpha_s(s))]} \right]. \quad (\text{A.13d})$$

$g\bar{g} \rightarrow q\bar{q}$

The matrix element for this process can be obtained from $qg \rightarrow qg$ by crossing the s and t channel and multiplying with $3/8$ due to the color and spin averaging.

$$\text{Matrix element} \quad |\overline{\mathcal{M}}_{g\bar{g} \rightarrow q\bar{q}}|^2 = 6\pi^2 \alpha_s^2 \left[\frac{4}{9} \left(\frac{tu}{t^2} + \frac{tu}{u^2} \right) + 2 \frac{tu}{s^2} + \frac{tu}{st} + \frac{tu}{su} \right] \quad (\text{A.14a})$$

$$\text{Small angle behavior } t \rightarrow 0 \quad |\overline{\mathcal{M}}_{g\bar{g} \rightarrow q\bar{q}}|^2 = \frac{8\pi^2 \alpha_s^2}{3} \frac{s}{-t} \quad (\text{A.14b})$$

$$\text{Large angle behavior } u \rightarrow 0 \quad |\overline{\mathcal{M}}_{g\bar{g} \rightarrow q\bar{q}}|^2 = \frac{8\pi^2 \alpha_s^2}{3} \frac{s}{-u} \quad (\text{A.14c})$$

Due to the symmetry of the process the behavior for small t and u is the same. With running coupling and DEBYE screened propagators the matrix element reads

$$|\overline{\mathcal{M}}_{g\bar{g} \rightarrow q\bar{q}}|^2 = 6\pi^2 \left[\frac{4}{9} \left(\alpha_s^2(t) \frac{tu}{[t - m_q^2(\alpha_s(t))]^2} + \alpha_s^2(u) \frac{tu}{[u - m_q^2(\alpha_s(u))]^2} \right) + 2\alpha_s^2(s) \frac{tu}{[s + m_D^2(\alpha_s(s))]^2} + \alpha_s(s) \alpha_s(t) \frac{tu}{[s + m_D^2(\alpha_s(s))][t - m_q^2(\alpha_s(t))]} + \alpha_s(s) \alpha_s(u) \frac{tu}{[s + m_D^2(\alpha_s(s))][u - m_q^2(\alpha_s(u))]} \right]. \quad (\text{A.14d})$$

$q\bar{q} \rightarrow g\bar{g}$

This process can be obtained through detailed balance from the previous process $g\bar{g} \rightarrow q\bar{q}$, taking the extra factor $(8/3)^2$ for color and spin averaging into account.

$$\text{Matrix element} \quad |\overline{\mathcal{M}}_{q\bar{q} \rightarrow g\bar{g}}|^2 = \frac{128\pi^2 \alpha_s^2}{3} \left[\frac{4}{9} \left(\frac{tu}{t^2} + \frac{tu}{u^2} \right) + 2 \frac{tu}{s^2} + \frac{tu}{st} + \frac{tu}{su} \right] \quad (\text{A.15a})$$

$$\text{Small angle behavior } t \rightarrow 0 \quad |\overline{\mathcal{M}}_{q\bar{q} \rightarrow g\bar{g}}|^2 = \frac{512\pi^2 \alpha_s^2}{27} \frac{s}{-t} \quad (\text{A.15b})$$

$$\text{Large angle behavior } u \rightarrow 0 \quad |\overline{\mathcal{M}}_{q\bar{q} \rightarrow g\bar{g}}|^2 = \frac{512\pi^2 \alpha_s^2}{27} \frac{s}{-u} \quad (\text{A.15c})$$

With running coupling and DEBYE screened propagators the matrix element reads

$$\begin{aligned}
 |\overline{\mathcal{M}}_{q\bar{q}\rightarrow gg}|^2 = & \frac{128\pi^2}{3} \left[\frac{4}{9} \left(\alpha_s^2(t) \frac{tu}{[t - m_q^2(\alpha_s(t))]^2} + \alpha_s^2(u) \frac{tu}{[u - m_q^2(\alpha_s(u))]^2} \right) \right. \\
 & + 2\alpha_s^2(s) \frac{tu}{[s + m_D^2(\alpha_s(s))]^2} + \alpha_s(s)\alpha_s(t) \frac{tu}{[s + m_D^2(\alpha_s(s))][t - m_q^2(\alpha_s(t))]} \\
 & \left. + \alpha_s(s)\alpha_s(u) \frac{tu}{[s + m_D^2(\alpha_s(s))][u - m_q^2(\alpha_s(u))]} \right]. \quad (\text{A.15d})
 \end{aligned}$$

$q\bar{q} \rightarrow q'\bar{q}'$

For this process only s channel scattering is allowed, which makes the matrix element very small compared to the other processes. The matrix element can be obtained from $qq' \rightarrow qq'$ by crossing s and t .

$$\text{Matrix element} \quad |\overline{\mathcal{M}}_{q\bar{q}\rightarrow q'\bar{q}'}|^2 = \frac{64\pi^2\alpha_s^2}{9} \left[\frac{t^2 + u^2}{s^2} \right] \quad (\text{A.16a})$$

$$\text{Small angle behavior } t \rightarrow 0 \quad |\overline{\mathcal{M}}_{q\bar{q}\rightarrow q'\bar{q}'}|^2 = \frac{64\pi^2\alpha_s^2}{9} \quad (\text{A.16b})$$

$$\text{Large angle behavior } u \rightarrow 0 \quad |\overline{\mathcal{M}}_{q\bar{q}\rightarrow q'\bar{q}'}|^2 = \frac{64\pi^2\alpha_s^2}{9} \quad (\text{A.16c})$$

With running coupling and DEBYE screened propagators the matrix element reads

$$|\overline{\mathcal{M}}_{q\bar{q}\rightarrow q'\bar{q}'}|^2 = \frac{64\pi^2}{9} \alpha_s^2(s) \frac{t^2 + u^2}{[s + m_D^2(\alpha_s(s))]^2}. \quad (\text{A.16d})$$

A.3.2. Overview of the processes

Figure A.1 shows an overview of all t channel dominated cross sections from above for a constant coupling. In addition, the respective heavy quark processes from Section 3.1 are also depicted. In the large s limit all cross sections converge to the same number if the trivial differences due to color factors are scaled out. It is rather instructive to determine this number in a back-of-the-envelope calculation. As mentioned before, the processes are dominated by the t channel. An integration about this part, see, for instance, Equation (A.11b) for $qq' \rightarrow qq'$ (and add the DEBYE mass in the denominator), gives in the large s limit

$$\sigma_{qq'\rightarrow qq'}^{\text{small angle}} = \frac{8\pi\alpha_s^2}{9} \left(\frac{1}{m_D^2} - \frac{1}{s + m_D^2} \right) \xrightarrow{s \rightarrow \infty} \frac{8\pi\alpha_s^2}{9m_D^2}. \quad (\text{A.17})$$

For the parameters of Figure A.1 the value is 0.34 GeV^{-2} , which agrees perfectly with the asymptotic limit in the figure.

Figure A.2 shows an overview of the cross sections with a running coupling. A similar asymptotic behavior with a slightly larger value is visible.

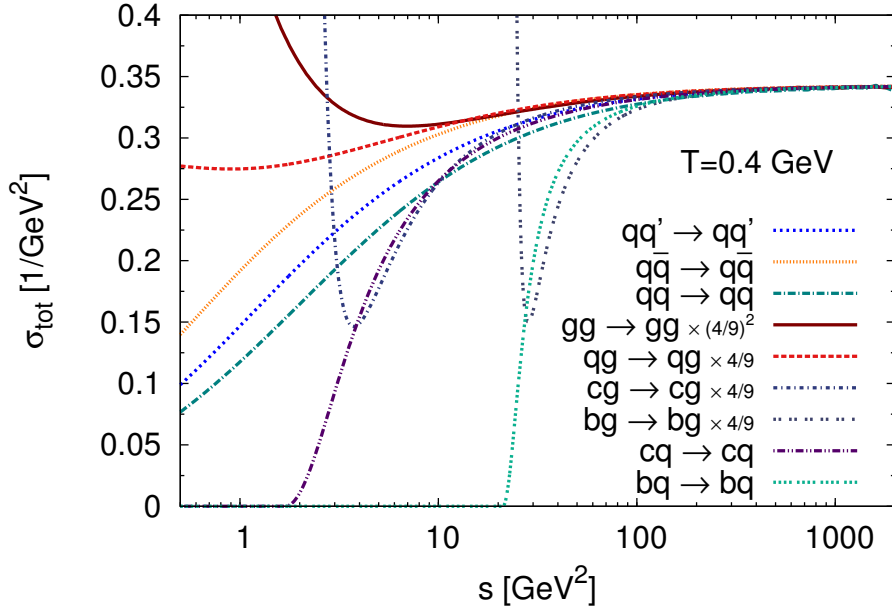


Figure A.1.: Total cross sections with a constant coupling $\alpha_s = 0.3$ of various processes with the same asymptotic behavior as a function of the squared center-of-mass energy s . Processes that involve gluons are scaled with a color factor. In addition, heavy quark processes from Section 3.1 are also included. The DEBYE mass is calculated for an equilibrated medium with a temperature of $T = 400$ MeV.

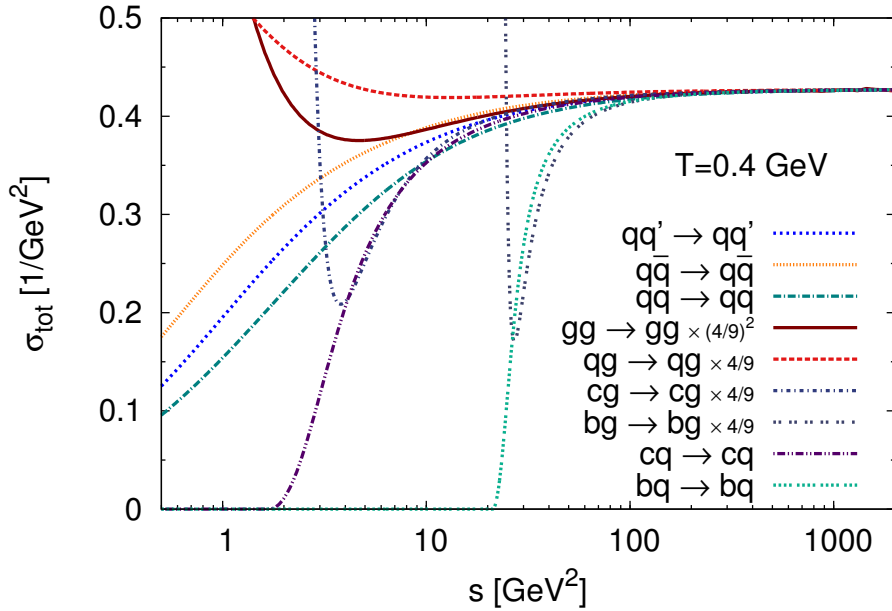


Figure A.2.: Same as Figure A.1 with a running coupling.

A.4. Detailed balance

In contrast to the weak interaction², there is no experimental indication that QCD is not invariant under time reversal transformations. In fact, the time reversal invariance of the QCD Lagrangian from Equation (2.1) can be explicitly shown [PS95]. As a consequence, all processes in QCD obey detailed balance [Sac87]. That is, the cross sections of the reaction $a + b \rightarrow c + d$ and its back reaction $c + d \rightarrow a + b$ are—apart from degeneracy factors—identical. The deeper reason for that lies in the time reversal invariance of the squared matrix elements. Applying the time reversal operator on the matrix element yields that the matrix element of the back reaction is the complex conjugated matrix element of the original reaction, $\mathcal{M}_{c+d \rightarrow a+b} = \mathcal{M}_{a+b \rightarrow c+d}^*$ [Smi06]. Since the cross section of the reaction and its back reaction are proportional to the squared matrix element $|\mathcal{M}|^2$, both cross sections have the same value.

A.5. Glauber model

The GLAUBER model is widely used for describing the initial stage of heavy-ion collisions. It assumes that a heavy-ion collision is given as a superposition of nucleon-nucleon interactions. The latter can be sampled according to geometric considerations.

Within the GLAUBER model the *nuclear thickness function* of a nucleus with mass number A is defined as

$$T_A(\mathbf{b}) = \int dz n_A(\mathbf{r} = (\mathbf{b}, z)) \quad (\text{A.18})$$

with the impact parameter \mathbf{b} and the nuclear density function n_A of the nucleus A . The quantity $\frac{1}{A} T_A(\mathbf{b}) d\mathbf{b}$ resembles the probability for a nucleon-nucleon collision with impact parameter \mathbf{b} [Won94].

A good description of the nuclear density function of heavy nuclei is the WOODS SAXON distribution,

$$n_A(\mathbf{x}_T, z) = \frac{\gamma n_0}{1 + \exp \left[\left(\sqrt{\mathbf{x}_T^2 + (\gamma z)^2} - R_A \right) / d \right]}, \quad (\text{A.19})$$

where $R_A = (1.12A^{1/3} - 0.86A^{-1/3})$ fm is the radius of the nucleus and $d = 0.54$ fm the thickness of its skin. The LORENTZ factor $\gamma = [1 - (v/c)^2]^{-1/2}$ ensures the length contraction of the relativistic nucleus with velocity v . The maximum density can be obtained from the normalization $\int d^3\mathbf{r} n_A = A$.

The overlap region in a collision of two nuclei $A+B$ is described by the *nuclear overlap function*

$$T_{AB}(\mathbf{b}) = \int d^2\mathbf{x}_{T1} dz_1 \int d^2\mathbf{x}_{T2} dz_2 n_A(\mathbf{r}_1) n_B(\mathbf{r}_2) \delta^2(\mathbf{b} - (\mathbf{x}_{T1} - \mathbf{x}_{T2})). \quad (\text{A.20})$$

² In 1964 CHRISTENSON, CRONIN, FITCH, and TURLAY discovered that the weak interaction is not invariant under \mathcal{CP} transformations. \mathcal{C} stands for charge conjugation, i.e., interchanging particles and anti-particles, and \mathcal{P} for parity, i.e., flipping the sign of the spatial coordinates. However, in the 1950s LÜDERS, PAULI, and independently BELL proofed the \mathcal{CPT} theorem, which states that any LORENTZ invariant local quantum field theory with a hermitian Hamiltonian is \mathcal{CPT} invariant. \mathcal{T} describes a time reversal transformation. Since the \mathcal{CPT} invariance, therefore, also applies to the weak interaction, being not invariant under \mathcal{CP} transformations, implies that the weak interaction is also not invariant under \mathcal{T} transformations.

The total number of binary nucleon-nucleon collisions in a heavy-ion collision is then given by [Won94]

$$N_{\text{bin}}(\mathbf{b}) = \sigma_{\text{p+p}} T_{AB}(\mathbf{b}) , \quad (\text{A.21})$$

where $\sigma_{\text{p+p}}$ is the inelastic p+p cross section. The values for RHIC and LHC are $\sigma_{\text{p+p}} \approx 42$ mb and 64 mb, respectively. As a note, the number of binary collisions in a central collision of two identical nuclei ($A = B$) scales with $A^{4/3}$ since $T_{AA} \sim A^2/R_A^2 \sim A^{4/3}$ with $R_A \sim A^{1/3}$.

A.6. Sampling with the rejection method and the Metropolis algorithm

Monte Carlo codes rely strongly on random numbers due to the employed stochastic methods. The random number generator used in BAMPS is based on the MERSENNE twister algorithm [MN98] as implemented in the Boost library³. Like most other generators it produces uniformly distributed numbers between zero and one. However, often the random numbers x should lie in a range $x \in [a, b]$ and should not be sampled uniformly but according to a probability density function $p(x)$. Several methods deal with this problem, two of which—the rejection method and the METROPOLIS algorithm—are employed in BAMPS and described in more detail in this section. The rejection method is very fast if an analytic comparison function is known that is always larger than $p(x)$ and invertible. The Metropolis algorithm on the other hand works also very well if such a function is not available.

The probability density function $p(x)$ shall be normalized to one. If $p(x)$ has a form such that the cumulative distribution function

$$A(x) = \int_a^x p(x') dx' \quad (\text{A.22})$$

is invertible, there is no need to employ sophisticated sampling algorithms. Instead, we can sample a random number for A between zero and one and obtain from the inverse function $x(A)$ an x that is distributed according to $p(x)$.

If $A(x)$ is not invertible, the rejection method can be employed. For that, we need another function $f(x)$ (often called comparison function) that is invertible and always larger than $p(x)$, i.e., $f(x) \geq p(x)$ for all x . To this end, we define

$$\tilde{A}(x) = \int_a^x f(x') dx' . \quad (\text{A.23})$$

The algorithm looks as follows:

1. Sample a random number for \tilde{A} in the interval $[0, \tilde{A}(b)]$ and calculate $x(\tilde{A})$.
2. Sample a second random number y between zero and one.
3. If $y f(x) \leq p(x)$, the number x is accepted. Otherwise it is rejected and the procedure starts again at step 1.

³<http://www.boost.org>. More precisely, the *mt19937* variant of the MERSENNE twister algorithm provided by the Boost libraries is used in BAMPS.

Due to this prescription, x is distributed according to $p(x)$. It is immediately clear that a well chosen comparison function $f(x)$ that is only slightly larger than $p(x)$ reduces the number of rejected x significantly.

If such a comparison function is not available or if its resembling of the original function is poor and, thus, the number of rejections large, the METROPOLIS algorithm is an efficient method to sample random numbers according to the probability density function $p(x)$. Moreover, $p(x)$ does not have to be normalized. Therefore, a time consuming computation of the normalization constant is not needed.

The METROPOLIS algorithm was first proposed by METROPOLIS et al. [MRR⁺53] to sample numbers according to the BOLTZMANN distribution. It was then extended by HASTINGS to general probability density functions [Has70].⁴ The idea of the algorithm is to produce a sequence of random numbers that are distributed according to $p(x)$ by performing a random walk in probability space. New candidates for random numbers are proposed solely depending on the current position—thus, being a Markov process—and, subsequently, accepted or rejected according to a criterion derived from the probability and proposal distributions.

In detail, the algorithm looks as following. The first number x_1 is randomly chosen in the range $[a, b]$. Having the number x_i given, the next number in the sequence x_{i+1} is calculated as follows:

1. Propose a new candidate x' according to a probability density $Q(x' | x_i)$ of your choice.
2. Calculate an acceptance probability $\alpha = \min \{\alpha_p \alpha_Q, 1\}$, where α_p is the likelihood ratio and α_Q the ratio of the proposal densities of x' and x_i ,⁵

$$\alpha_p = \frac{p(x')}{p(x_i)} \quad \alpha_Q = \frac{Q(x_i | x')}{Q(x' | x_i)}. \quad (\text{A.24})$$

3. Sample a random number $y \in [0, 1]$. If $y \leq \alpha$, accept x' and set $x_{i+1} = x'$, otherwise go back to the first step.

After the *burn-in* phase, i.e., after the initial state x_1 is “forgotten”, this procedure generates a sequence of random numbers that are distributed according to $p(x)$. The burn-in is achieved by discarding a sufficiently large number of initial states—a number that varies from problem to problem and has to be determined empirically.

The proposal probability density $Q(x' | x_i)$ is often chosen to be symmetric, $Q(x' | x_i) = Q(x_i | x')$ (for instance, a Gaussian distribution), which results in $\alpha_Q = 1$. However, it is most efficient to use a proposal probability density that is close to $p(x)$, i.e., $Q(x' | x_i) = f(x') \approx p(x')$ since α is then close to one, as can be seen from Equation (A.24). Due to step 1 in the enumeration above, $f(x')$ must be invertible. Since $f(x')$ does not depend on the previous number x_i , it can also be employed for sampling the first number x_1 , which shortens the burn-in process.

Although the METROPOLIS algorithm seems to be rather complex at first, the basic idea is obvious. Numbers that have a larger probability density $p(x)$ than the previous number are always accepted. Numbers that have a smaller probability are accepted or rejected proportional

⁴Therefore, it is often named METROPOLIS-HASTINGS algorithm.

⁵Since $p(x)$ only enters as a ratio in α_p , it does not have to be normalized.

to this probability, which leads to clusters where $p(x)$ is large and only occasional samplings in regions where $p(x)$ is small.

In BAMPS, for sampling the differential cross section $d\sigma/dt$, for instance, the probability density function changes for each collision. Therefore, we do not need a sequence of random numbers but only one sampled number for a given collision. Consequently, the iteration is aborted after the burn-in phase and the last number is taken.

Both the rejection method and METROPOLIS algorithm can be straight forwardly extended to multi-dimensional probability density functions. In general, the rejection probability in the rejection method increases exponentially with the number of dimensions. Thus, the METROPOLIS algorithm might become more efficient for high dimensions. In BAMPS a multi-dimensional rejection method is applied for sampling the outgoing momenta of $2 \rightarrow 3$ processes, whereas the METROPOLIS algorithm is employed for samplings in $2 \rightarrow 2$ and $3 \rightarrow 2$ interactions.

Bibliography

- [ABDP⁺11] W. Alberico, A. Beraudo, A. De Pace, A. Molinari, M. Monteno et al., *Heavy-flavour spectra in high energy nucleus-nucleus collisions*, Eur.Phys.J. C71, 1666 (2011), [1101.6008].
- [ABDP⁺13] W. Alberico, A. Beraudo, A. De Pace, A. Molinari, M. Monteno et al., *Heavy flavours in AA collisions: production, transport and final spectra*, (2013), [1305.7421].
- [ABMRS07] A. Andronic, P. Braun-Munzinger, K. Redlich and J. Stachel, *Statistical hadronization of heavy quarks in ultra-relativistic nucleus-nucleus collisions*, Nucl.Phys. A789, 334–356 (2007), [nucl-th/0611023].
- [ABMRS11] A. Andronic, P. Braun-Munzinger, K. Redlich and J. Stachel, *The thermal model on the verge of the ultimate test: particle production in Pb-Pb collisions at the LHC*, J.Phys. G38, 124081 (2011), [1106.6321].
- [Acc02] A. Accardi, *Cronin effect in proton nucleus collisions: A survey of theoretical models*, (2002), [hep-ph/0212148].
- [ACD⁺06] N. Armesto, M. Cacciari, A. Dainese, C. A. Salgado and U. A. Wiedemann, *How sensitive are high-p(T) electron spectra at RHIC to heavy quark energy loss?*, Phys.Lett. B637, 362–366 (2006), [hep-ph/0511257].
- [ACG⁺12] N. Armesto, B. Cole, C. Gale, W. A. Horowitz, P. Jacobs et al., *Comparison of Jet Quenching Formalisms for a Quark-Gluon Plasma 'Brick'*, Phys.Rev. C86, 064904 (2012), [1106.1106].
- [ADSW05] N. Armesto, A. Dainese, C. A. Salgado and U. A. Wiedemann, *Testing the color charge and mass dependence of parton energy loss with heavy-to-light ratios at RHIC and CERN LHC*, Phys.Rev. D71, 054027 (2005), [hep-ph/0501225].
- [AEF⁺06] Y. Aoki, G. Endrodi, Z. Fodor, S. Katz and K. Szabo, *The Order of the quantum chromodynamics transition predicted by the standard model of particle physics*, Nature 443, 675–678 (2006), [hep-lat/0611014].
- [AGGA02] F. Arleo, P. Gossiaux, T. Gousset and J. Aichelin, *Heavy quarkonium hadron cross-section in QCD at leading twist*, Phys.Rev. D65, 014005 (2002), [hep-ph/0102095].
- [AGM⁺12] R. Abir, C. Greiner, M. Martinez, M. G. Mustafa and J. Uphoff, *Soft gluon emission off a heavy quark revisited*, Phys.Rev. D85, 054012 (2012), [1109.5539].

- [AGMM11] R. Abir, C. Greiner, M. Martinez and M. G. Mustafa, *Generalisation of Gunion-Bertsch Formula for Soft Gluon Emission*, Phys.Rev. D83, 011501 (2011), [1011.4638].
- [AH04] M. Asakawa and T. Hatsuda, *J/psi and eta/c in the deconfined plasma from lattice QCD*, Phys.Rev.Lett. 92, 012001 (2004), [hep-lat/0308034].
- [Ait05] I. J. R. Aitchison, *Supersymmetry and the MSSM: An Elementary introduction*, (2005), [hep-ph/0505105].
- [AJMS12] R. Abir, U. Jamil, M. G. Mustafa and D. K. Srivastava, *Heavy quark energy loss and D-Mesons at RHIC and LHC energies*, Phys.Lett. B715, 183–189 (2012), [1203.5221].
- [AKK08] S. Albino, B. Kniehl and G. Kramer, *AKK Update: Improvements from New Theoretical Input and Experimental Data*, Nucl.Phys. B803, 42–104 (2008), [0803.2768].
- [ALICE11a] K. Aamodt et al. (ALICE), *Centrality dependence of the charged-particle multiplicity density at mid-rapidity in Pb-Pb collisions at $\sqrt{s_{NN}} = 2.76$ TeV*, Phys.Rev.Lett. 106, 032301 (2011), [1012.1657].
- [ALICE11b] K. Aamodt et al. (ALICE), *Suppression of Charged Particle Production at Large Transverse Momentum in Central Pb-Pb Collisions at $\sqrt{s_{NN}} = 2.76$ TeV*, Phys.Lett. B696, 30–39 (2011), [1012.1004].
- [ALICE11c] C. Bianchin (ALICE), *Measurement of D^0 v_2 in Pb-Pb collisions at $\sqrt{s_{NN}} = 2.76$ TeV with ALICE at the LHC*, (2011), [1111.6886].
- [ALICE11d] M. Krzewicki (ALICE), *Elliptic and triangular flow of identified particles at ALICE*, J.Phys. G38, 124047 (2011), [1107.0080].
- [ALICE11e] Y. Pachmayer (ALICE), *Heavy-flavour production measurements in pp collisions at the LHC with ALICE*, PoS EPS-HEP2011, 293 (2011), [1110.6462].
- [ALICE11f] Y. Pachmayer (ALICE), *Measurement of the nuclear modification factor of electrons from heavy-flavour decays at mid-rapidity in Pb-Pb collisions at $\sqrt{s_{NN}} = 2.76$ TeV with ALICE*, J.Phys.G G38, 124186 (2011), [1106.6188].
- [ALICE12a] B. Abelev et al. (ALICE), *Inclusive J/ψ production in pp collisions at $\sqrt{s} = 2.76$ TeV*, Phys.Lett. B718, 295–306 (2012), [1203.3641].
- [ALICE12b] B. Abelev et al. (ALICE), *Measurement of charm production at central rapidity in proton-proton collisions at $\sqrt{s} = 7$ TeV*, JHEP 1201, 128 (2012), [1111.1553].
- [ALICE12c] B. Abelev et al. (ALICE), *Heavy flavour decay muon production at forward rapidity in proton-proton collisions at $\sqrt{s} = 7$ TeV*, Phys.Lett. B708, 265–275 (2012), [1201.3791].
- [ALICE12d] B. Abelev et al. (ALICE), *J/ψ suppression at forward rapidity in Pb-Pb collisions at $\sqrt{s_{NN}} = 2.76$ TeV*, Phys.Rev.Lett. 109, 072301 (2012), [1202.1383].

- [ALICE12e] B. Abelev et al. (ALICE), *Production of muons from heavy flavour decays at forward rapidity in pp and Pb-Pb collisions at $\sqrt{s_{NN}} = 2.76$ TeV*, Phys.Rev.Lett. 109, 112301 (2012), [1205.6443].
- [ALICE12f] B. Abelev et al. (ALICE), *Suppression of high transverse momentum D mesons in central Pb-Pb collisions at $\sqrt{s_{NN}} = 2.76$ TeV*, JHEP 1209, 112 (2012), [1203.2160].
- [ALICE12g] A. Dainese (ALICE), *Suppression of high-pT heavy-flavour particles in Pb-Pb collisions at the LHC, measured with the ALICE detector*, (2012), [1212.0995].
- [ALICE12h] S. LaPointe (ALICE), *Open heavy-flavour measurements in pp and Pb-Pb collisions with ALICE at the LHC*, (2012), [1209.6198].
- [ALICE12i] G. Ortona (ALICE), *Open-Charm Meson Elliptic Flow Measurement in Pb-Pb Collisions at $\sqrt{s_{NN}} = 2.76$ TeV with ALICE at the LHC*, (2012), [1207.7239].
- [ALICE13a] E. Abbas et al. (ALICE), *J/ ψ Elliptic Flow in Pb-Pb Collisions at $\sqrt{s_{NN}} = 2.76$ TeV*, (2013), [1303.5880].
- [ALICE13b] B. Abelev et al. (ALICE), *D meson elliptic flow in non-central Pb-Pb collisions at $\sqrt{s_{NN}} = 2.76$ TeV*, (2013), [1305.2707].
- [ALICE13c] B. Abelev et al. (ALICE), *Centrality Dependence of Charged Particle Production at Large Transverse Momentum in Pb-Pb Collisions at $\sqrt{s_{NN}} = 2.76$ TeV*, Phys.Lett. B720, 52–62 (2013), [1208.2711].
- [ALICE13d] B. Abelev et al. (ALICE), *Measurement of electrons from beauty hadron decays in pp collisions at $\sqrt{s} = 7$ TeV*, Phys.Lett. B721, 13–23 (2013), [1208.1902].
- [ALICE13e] Z. Conesa del Valle (ALICE), *Heavy-flavor suppression and azimuthal anisotropy in Pb-Pb collisions at $\sqrt{s_{NN}} = 2.76$ TeV with the ALICE detector*, Nucl.Phys. A904-905, 178c–185c (2013), [1212.0385].
- [ALICE13f] A. Grelli (ALICE), *D meson nuclear modification factors in Pb-Pb collisions at $\sqrt{s_{NN}} = 2.76$ TeV with the ALICE detector*, Nucl.Phys. A904-905, 635c–638c (2013), [1210.7332].
- [ALICE13g] S. Sakai (ALICE), *Measurement of R_{AA} and ν_2 of electrons from heavy-flavour decays in Pb-Pb collisions at $\sqrt{s_{NN}} = 2.76$ TeV with ALICE*, Nucl.Phys. A904-905, 661c–664c (2013).
- [AMY02] P. B. Arnold, G. D. Moore and L. G. Yaffe, *Photon and gluon emission in relativistic plasmas*, JHEP 0206, 030 (2002), [hep-ph/0204343].
- [Arm06] N. Armesto, *Nuclear shadowing*, J.Phys. G32, R367–R394 (2006), [hep-ph/0604108].
- [Arn94] M. Arneodo, *Nuclear effects in structure functions*, Phys.Rept. 240, 301–393 (1994).

- [ATLAS10] G. Aad et al. (ATLAS), *Observation of a Centrality-Dependent Dijet Asymmetry in Lead-Lead Collisions at $\sqrt{s_{NN}} = 2.77$ TeV with the ATLAS Detector at the LHC*, Phys.Rev.Lett. 105, 252303 (2010), [1011.6182].
- [ATLAS12a] G. Aad et al. (ATLAS), *Measurement of the azimuthal anisotropy for charged particle production in $\sqrt{s_{NN}} = 2.76$ TeV lead-lead collisions with the ATLAS detector*, Phys.Rev. C86, 014907 (2012), [1203.3087].
- [ATLAS12b] G. Aad et al. (ATLAS), *Observation of a new particle in the search for the Standard Model Higgs boson with the ATLAS detector at the LHC*, Phys.Lett. B716, 1–29 (2012), [1207.7214].
- [ATLAS13] G. Aad et al. (ATLAS), *Measurement of the jet radius and transverse momentum dependence of inclusive jet suppression in lead-lead collisions at $\sqrt{s_{NN}} = 2.76$ TeV with the ATLAS detector*, Phys.Lett. B719, 220–241 (2013), [1208.1967].
- [AV07] A. Adil and I. Vitev, *Collisional dissociation of heavy mesons in dense QCD matter*, Phys.Lett. B649, 139–146 (2007), [hep-ph/0611109].
- [B⁺98] S. A. Bass et al., *Microscopic models for ultrarelativistic heavy ion collisions*, Prog.Part.Nucl.Phys. 41, 255–369 (1998), [nucl-th/9803035].
- [B⁺04] N. Brambilla et al., *Heavy quarkonium physics*, (2004), [hep-ph/0412158].
- [B⁺09] I. Bouras et al., *Relativistic shock waves in viscous gluon matter*, Phys.Rev.Lett. 103, 032301 (2009), [0902.1927].
- [B⁺10] S. Borsanyi et al., *Is there still any T_c mystery in lattice QCD? Results with physical masses in the continuum limit III*, JHEP 1009, 073 (2010), [1005.3508].
- [B⁺11] N. Brambilla et al., *Heavy quarkonium: progress, puzzles, and opportunities*, Eur.Phys.J. C71, 1534 (2011), [1010.5827].
- [BAG11] H. Berrehrhah, J. Aichelin and P. Gossiaux, *Quarkonia propagation in QGP: Study of elastic and inelastic scattering processes*, J.Phys.Conf.Ser. 270, 012036 (2011).
- [BDM⁺97a] R. Baier, Y. L. Dokshitzer, A. H. Mueller, S. Peigne and D. Schiff, *Radiative energy loss and $p(T)$ broadening of high-energy partons in nuclei*, Nucl.Phys. B484, 265–282 (1997), [hep-ph/9608322].
- [BDM⁺97b] R. Baier, Y. L. Dokshitzer, A. H. Mueller, S. Peigne and D. Schiff, *Radiative energy loss of high-energy quarks and gluons in a finite volume quark - gluon plasma*, Nucl.Phys. B483, 291–320 (1997), [hep-ph/9607355].
- [BDO01] N. Borghini, P. M. Dinh and J.-Y. Ollitrault, *Flow analysis from multiparticle azimuthal correlations*, Phys.Rev. C64, 054901 (2001), [nucl-th/0105040].
- [BDPS95] R. Baier, Y. L. Dokshitzer, S. Peigne and D. Schiff, *Induced gluon radiation in a QCD medium*, Phys.Lett. B345, 277–286 (1995), [hep-ph/9411409].

- [Bec09] F. Becattini, *An Introduction to the Statistical Hadronization Model*, (2009), [0901.3643].
- [BEF⁺12] I. Bouras, A. El, O. Fochler, H. Niemi, Z. Xu et al., *Transition From Ideal To Viscous Mach Cones In A Kinetic Transport Approach*, Phys.Lett. B710, 641–646 (2012), [1201.5005].
- [BEGV11] N. Brambilla, M. A. Escobedo, J. Ghiglieri and A. Vairo, *Thermal width and gluo-dissociation of quarkonium in pNRQCD*, JHEP 1112, 116 (2011), [1109.5826].
- [Bel00] M. Bellac, *Thermal Field Theory*, Cambridge University Press, 2000.
- [Bet07] S. Bethke, *Experimental Tests of Asymptotic Freedom*, Prog.Part.Nucl.Phys. 58, 351–386 (2007), [hep-ex/0606035].
- [BG12a] A. Buzzatti and M. Gyulassy, *An overview of the CUJET model: Jet Flavor Tomography applied at RHIC and LHC*, (2012), [1207.6020].
- [BG12b] A. Buzzatti and M. Gyulassy, *Jet Flavor Tomography of Quark Gluon Plasmas at RHIC and LHC*, Phys.Rev.Lett. 108, 022301 (2012), [1106.3061].
- [BGGA12] M. Bluhm, P. B. Gossiaux, T. Gousset and J. Aichelin, *On the Formation of Bremsstrahlung in an Absorptive QED/QCD Medium*, (2012), [1204.2469].
- [BGM⁺09] S. A. Bass, C. Gale, A. Majumder, C. Nonaka, G.-Y. Qin et al., *Systematic Comparison of Jet Energy-Loss Schemes in a realistic hydrodynamic medium*, Phys.Rev. C79, 024901 (2009), [0808.0908].
- [BI02] J.-P. Blaizot and E. Iancu, *The quark-gluon plasma: Collective dynamics and hard thermal loops*, Phys.Rept. 359, 355–528 (2002), [hep-ph/0101103].
- [Bjo82] J. Bjorken, *Energy Loss of Energetic Partons in Quark - Gluon Plasma: Possible Extinction of High $p(t)$ Jets in Hadron - Hadron Collisions*, (1982).
- [BKDC⁺81] F. A. Berends, R. Kleiss, P. De Causmaecker, R. Gastmans and T. T. Wu, *Single bremsstrahlung processes in gauge theories*, Phys.Lett. B103, 124 (1981).
- [BM11] C. Blume and C. Markert, *Strange hadron production in heavy ion collisions from SPS to RHIC*, Prog.Part.Nucl.Phys. 66, 834–879 (2011), [1105.2798].
- [BMDA12] T. Bhattacharyya, S. Mazumder, S. K. Das and J.-e. Alam, *Examination of the Gunion-Bertsch formula for soft gluon radiation*, Phys.Rev. D85, 034033 (2012), [1106.0609].
- [BMN⁺10] I. Bouras, E. Molnar, H. Niemi, Z. Xu, A. El et al., *Investigation of shock waves in the relativistic Riemann problem: A Comparison of viscous fluid dynamics to kinetic theory*, Phys.Rev. C82, 024910 (2010), [1006.0387].
- [BMRS03] P. Braun-Munzinger, K. Redlich and J. Stachel, *Particle production in heavy ion collisions*, in Quark Gluon Plasma 3, edited by X.-N. Wang and R. C. Hwa, World Scientific, 491–599 (2003), [nucl-th/0304013].

- [BMS00] P. Braun-Munzinger and J. Stachel, *(Non)thermal aspects of charmonium production and a new look at J/ψ suppression*, Phys.Lett. B490, 196–202 (2000), [nucl-th/0007059].
- [BMS01] P. Braun-Munzinger and J. Stachel, *On charm production near the phase boundary*, Nucl.Phys. A690, 119–126 (2001), [nucl-th/0012064].
- [BMS03] S. Bass, B. Müller and D. Srivastava, *Parton rescattering and screening in Au+Au collisions at RHIC*, Phys.Lett. B551, 277–283 (2003), [nucl-th/0207042].
- [BMW09] P. Braun-Munzinger and J. Wambach, *The Phase Diagram of Strongly-Interacting Matter*, Rev.Mod.Phys. 81, 1031–1050 (2009), [0801.4256].
- [BP79] G. Bhanot and M. E. Peskin, *Short Distance Analysis for Heavy Quark Systems. 2. Applications*, Nucl.Phys. B156, 391 (1979).
- [BP90] E. Braaten and R. D. Pisarski, *Soft Amplitudes in Hot Gauge Theories: A General Analysis*, Nucl.Phys. B337, 569 (1990).
- [BP02] V. Barone and E. Predazzi, *High-energy particle diffraction*, Springer-Verlag, 2002, P. 166ff.
- [BR99] J. Berges and K. Rajagopal, *Color superconductivity and chiral symmetry restoration at non-zero baryon density and temperature*, Nucl.Phys. B538, 215–232 (1999), [hep-ph/9804233].
- [BRAHMS05] I. Arsene et al. (BRAHMS), *Quark gluon plasma and color glass condensate at RHIC? The perspective from the BRAHMS experiment*, Nucl.Phys. A757, 1–27 (2005), [nucl-ex/0410020].
- [BT91a] E. Braaten and M. H. Thoma, *Energy loss of a heavy fermion in a hot plasma*, Phys.Rev. D44, 1298–1310 (1991).
- [BT91b] E. Braaten and M. H. Thoma, *Energy loss of a heavy quark in the quark - gluon plasma*, Phys.Rev. D44, 2625–2630 (1991).
- [Bub05] M. Buballa, *NJL model analysis of quark matter at large density*, Phys.Rept. 407, 205–376 (2005), [hep-ph/0402234].
- [BvDM⁺93] T. S. Biro, E. van Doorn, B. Müller, M. H. Thoma and X. N. Wang, *Parton equilibration in relativistic heavy ion collisions*, Phys.Rev. C48, 1275–1284 (1993), [nucl-th/9303004].
- [BY91] E. Braaten and T. C. Yuan, *Calculation of screening in a hot plasma*, Phys.Rev.Lett. 66, 2183–2186 (1991).
- [BZS⁺99] M. Bleicher, E. Zabrodin, C. Spieles, S. Bass, C. Ernst et al., *Relativistic hadron hadron collisions in the ultrarelativistic quantum molecular dynamics model*, J.Phys. G25, 1859–1896 (1999), [hep-ph/9909407].
- [CB99] W. Cassing and E. Bratkovskaya, *Hadronic and electromagnetic probes of hot and dense nuclear matter*, Phys.Rept. 308, 65–233 (1999).

- [CB11] S. Cao and S. A. Bass, *Thermalization of charm quarks in infinite and finite QGP matter*, Phys.Rev. C84, 064902 (2011), [1108.5101].
- [CDDW11] J.-W. Chen, J. Deng, H. Dong and Q. Wang, *How Perfect a Gluon Plasma Can Be in Perturbative QCD?*, Phys.Rev. D83, 034031 (2011), [1011.4123], Erratum-ibid. D84 (2011) 039902.
- [CDDW13] J.-W. Chen, J. Deng, H. Dong and Q. Wang, *Shear and Bulk Viscosities of a Gluon Plasma in Perturbative QCD: Comparison of Different Treatments for the $gg \rightarrow ggg$ Process*, Phys.Rev. C87, 024910 (2013), [1107.0522].
- [CDOW10] J.-W. Chen, H. Dong, K. Ohnishi and Q. Wang, *Shear Viscosity of a Gluon Plasma in Perturbative QCD*, Phys.Lett. B685, 277–282 (2010), [0907.2486].
- [CF74] F. Cooper and G. Frye, *Comment on the Single Particle Distribution in the Hydrodynamic and Statistical Thermodynamic Models of Multiparticle Production*, Phys.Rev. D10, 186 (1974).
- [CFH⁺12] M. Cacciari, S. Frixione, N. Houdeau, M. L. Mangano, P. Nason et al., *Theoretical predictions for charm and bottom production at the LHC*, JHEP 1210, 137 (2012), [1205.6344].
- [CGR93] J. Cleymans, V. V. Goloviznin and K. Redlich, *Virtual photon bremsstrahlung in quark gluon plasma*, Phys.Rev. D47, 989–997 (1993).
- [CGW⁺10] X.-F. Chen, C. Greiner, E. Wang, X.-N. Wang and Z. Xu, *Bulk matter evolution and extraction of jet transport parameter in heavy-ion collisions at RHIC*, Phys.Rev. C81, 064908 (2010), [1002.1165].
- [CKR77] B. Combridge, J. Kripfganz and J. Ranft, *Hadron Production at Large Transverse Momentum and QCD*, Phys.Lett. B70, 234 (1977).
- [CLR13a] P. Chesler, M. Lekaveckas and K. Rajagopal, *Far-from-equilibrium heavy quark energy loss at strong coupling*, Nucl.Phys. A904-905, 861c–864c (2013), [1211.2186].
- [CLR13b] P. M. Chesler, M. Lekaveckas and K. Rajagopal, *Heavy quark energy loss far from equilibrium in a strongly coupled collision*, (2013), [1306.0564].
- [CMS10] V. Khachatryan et al. (CMS), *Observation of Long-Range Near-Side Angular Correlations in Proton-Proton Collisions at the LHC*, JHEP 1009, 091 (2010), [1009.4122].
- [CMS11a] S. Chatrchyan et al. (CMS), *Indications of suppression of excited Υ states in PbPb collisions at $\sqrt{s_{NN}} = 2.76$ TeV*, Phys.Rev.Lett. 107, 052302 (2011), [1105.4894].
- [CMS11b] S. Chatrchyan et al. (CMS), *Long-range and short-range dihadron angular correlations in central PbPb collisions at a nucleon-nucleon center of mass energy of 2.76 TeV*, JHEP 1107, 076 (2011), [1105.2438].

- [CMS11c] S. Chatrchyan et al. (CMS), *Observation and studies of jet quenching in PbPb collisions at nucleon-nucleon center-of-mass energy = 2.76 TeV*, Phys.Rev. C84, 024906 (2011), [1102.1957].
- [CMS12a] S. Chatrchyan et al. (CMS), *Inclusive b-jet production in pp collisions at $\sqrt{s(s)}=7$ TeV*, JHEP 1204, 084 (2012), [1202.4617].
- [CMS12b] S. Chatrchyan et al. (CMS), *Measurement of jet fragmentation into charged particles in pp and PbPb collisions at $\sqrt{s_{NN}} = 2.76$ TeV*, JHEP 1210, 087 (2012), [1205.5872].
- [CMS12c] S. Chatrchyan et al. (CMS), *Observation of a new boson at a mass of 125 GeV with the CMS experiment at the LHC*, Phys.Lett. B716, 30–61 (2012), [1207.7235].
- [CMS12d] S. Chatrchyan et al. (CMS), *Observation of sequential Upsilon suppression in PbPb collisions*, Phys.Rev.Lett. 109, 222301 (2012), [1208.2826].
- [CMS12e] S. Chatrchyan et al. (CMS), *Study of high- p_T charged particle suppression in PbPb compared to pp collisions at $\sqrt{s_{NN}} = 2.76$ TeV*, Eur.Phys.J. C72, 1945 (2012), [1202.2554].
- [CMS12f] S. Chatrchyan et al. (CMS), *Suppression of non-prompt J/psi, prompt J/psi, and Y(1S) in PbPb collisions at $\sqrt{s_{NN}} = 2.76$ TeV*, JHEP 1205, 063 (2012), [1201.5069].
- [CMS12g] CMS collaboration (CMS), *Measurement of the b-jet to inclusive jet ratio in PbPb and pp collisions at 2.76 TeV with the CMS detector*, <http://cds.cern.ch/record/1472721/files/HIN-12-003-pas.pdf>, 2012, Physics Analysis Summary.
- [CMS12h] CMS collaboration (CMS), *Prompt and non-prompt J/psi RAA with 150 μb^{-1} integrated PbPb luminosity at $\sqrt{s_{NN}} = 2.76$ TeV*, <https://twiki.cern.ch/twiki/bin/view/CMSPublic/PhysicsResultsHIN12014>, 2012, Analysis note.
- [CMS12i] T. Dahms (CMS), *Quarkonium and open-bottom suppression in PbPb collisions at the LHC with CMS*, <http://indico.cern.ch/getFile.py/access?contribId=58&sessionId=1&resId=0&materialId=slides&confId=182856>, 2012, Talk given at 5th International workshop on heavy quark production in heavy-ion collisions in Utrecht.
- [CMS12j] B. de la Cruz (CMS), *W, Z and photon production in CMS*, (2012), [1208.4927], Proceedings for Hard Probes 2012.
- [CMS12k] C. Mironov (CMS), *Overview of results on heavy flavor and quarkonia from the CMS collaboration*, <https://indico.cern.ch/getFile.py/access?contribId=648&sessionId=41&resId=0&materialId=slides&confId=181055>, 2012, Talk at Quark Matter conference 2012.
- [CMS13a] S. Chatrchyan et al. (CMS), *Identification of b-quark jets with the CMS experiment*, JINST 8, P04013 (2013), [1211.4462].

- [CMS13b] S. Chatrchyan et al. (CMS), *Observation of long-range near-side angular correlations in proton-lead collisions at the LHC*, Phys.Lett. B718, 795–814 (2013), [1210.5482].
- [CMS13c] M. Nguyen (CMS), *b-jet Identification in PbPb Collisions with CMS*, Nucl.Phys. A904-905, 705c–708c (2013), [1211.5285].
- [CNV05] M. Cacciari, P. Nason and R. Vogt, *QCD predictions for charm and bottom production at RHIC*, Phys.Rev.Lett. 95, 122001 (2005), [hep-ph/0502203].
- [Com79] B. L. Combridge, *Associated Production of Heavy Flavor States in $p p$ and anti- $p p$ Interactions: Some QCD Estimates*, Nucl.Phys. B151, 429 (1979).
- [CQBM13] S. Cao, G.-Y. Qin, S. A. Bass and B. Müller, *Collisional vs. Radiative Energy Loss of Heavy Quark in a Hot and Dense Nuclear Matter*, Nucl.Phys. A904-905, 653c–656c (2013), [1209.5410].
- [CS78] R. Cutler and D. W. Sivers, *Quantum Chromodynamic Gluon Contributions to Large $p(T)$ Reactions*, Phys.Rev. D17, 196 (1978).
- [CSBS11] C. Coleman-Smith, S. Bass and D. Srivastava, *Implementing the LPM effect in a parton cascade model*, Nucl.Phys. A862-863, 275–278 (2011), [1101.4895].
- [CSM12] C. E. Coleman-Smith and B. Müller, *Results of a systematic study of dijet suppression measured at the BNL Relativistic Heavy Ion Collider*, Phys.Rev. C86, 054901 (2012), [1205.6781].
- [DA10] S. K. Das and J.-e. Alam, *Soft gluon multiplicity distribution revisited*, Phys.Rev. D82, 051502 (2010), [1007.4405].
- [DAM10] S. K. Das, J.-e. Alam and P. Mohanty, *Dragging Heavy Quarks in Quark Gluon Plasma at the Large Hadron Collider*, Phys.Rev. C82, 014908 (2010), [1003.5508].
- [d'E04] D. G. d'Enterria, *Indications of suppressed high $p(T)$ hadron production in nucleus - nucleus collisions at CERN-SPS*, Phys.Lett. B596, 32–43 (2004), [nucl-ex/0403055].
- [DFE⁺08] S. Durr, Z. Fodor, J. Frison, C. Hoelbling, R. Hoffmann et al., *Ab-Initio Determination of Light Hadron Masses*, Science 322, 1224–1227 (2008), [0906.3599].
- [dFP07] P. de Forcrand and O. Philipsen, *The Chiral critical line of $N(f) = 2+1$ QCD at zero and non-zero baryon density*, JHEP 0701, 077 (2007), [hep-lat/0607017].
- [dFP08] P. de Forcrand and O. Philipsen, *The curvature of the critical surface $(m(u,d),m(s))^{**crit}(\mu)$: A Progress report*, PoS LATTICE2008, 208 (2008), [0811.3858].
- [DGH94] J. F. Donoghue, E. Golowich and B. R. Holstein, *Dynamics of the Standard Model*, Cambridge University Press, 1994.

- [DGVW06] M. Djordjevic, M. Gyulassy, R. Vogt and S. Wicks, *Influence of bottom quark jet quenching on single electron tomography of Au+Au*, Phys.Lett. B632, 81–86 (2006), [nucl-th/0507019].
- [Djo13] M. Djordjevic, *Heavy flavor puzzle at LHC: a serendipitous interplay of jet suppression and fragmentation*, (2013), [1307.4702].
- [DK01] Y. L. Dokshitzer and D. E. Kharzeev, *Heavy quark colorimetry of QCD matter*, Phys.Lett. B519, 199–206 (2001), [hep-ph/0106202].
- [DLP05] A. Dainese, C. Loizides and G. Paic, *Leading-particle suppression in high energy nucleus nucleus collisions*, Eur.Phys.J. C38, 461–474 (2005), [hep-ph/0406201].
- [DMW96] Y. L. Dokshitzer, G. Marchesini and B. R. Webber, *Dispersive Approach to Power-Behaved Contributions in QCD Hard Processes*, Nucl.Phys. B469, 93–142 (1996), [hep-ph/9512336].
- [DNB⁺12] G. Denicol, H. Niemi, I. Bouras, E. Molnar, Z. Xu et al., *Solving the heat-flow problem with transient relativistic fluid dynamics*, (2012), [1207.6811].
- [Dok02] Y. Dokshitzer, *QCD at moderately large distances*, Nucl.Phys. A711, 11–18 (2002), [hep-ph/0510199].
- [DXG12] W.-T. Deng, Z. Xu and C. Greiner, *Elliptic and Triangular Flow and their Correlation in Ultrarelativistic High Multiplicity Proton Proton Collisions at 14 TeV*, Phys.Lett. B711, 301–306 (2012), [1112.0470].
- [EBW⁺12] A. El, I. Bouras, C. Wesp, Z. Xu and C. Greiner, *Dissipative hydrodynamics for multi-component systems*, Eur.Phys.J. A48, 166 (2012), [1206.3465].
- [EC96] W. Ehehalt and W. Cassing, *Relativistic transport approach for nucleus nucleus collisions from SIS to SPS energies*, Nucl.Phys. A602, 449–486 (1996).
- [EKL89] K. J. Eskola, K. Kajantie and J. Lindfors, *Quark and Gluon Production in High-Energy Nucleus-Nucleus Collisions*, Nucl.Phys. B323, 37 (1989).
- [ELW⁺12] A. El, F. Lauciello, C. Wesp, Z. Xu and C. Greiner, *Shear viscosity of an ultrarelativistic Boltzmann gas with isotropic inelastic scattering processes*, (2012), [1207.5331].
- [EMXG09] A. El, A. Muronga, Z. Xu and C. Greiner, *Shear viscosity and out of equilibrium dissipative hydrodynamics*, Phys.Rev. C79, 044914 (2009), [0812.2762].
- [EMXG10] A. El, A. Muronga, Z. Xu and C. Greiner, *A Relativistic dissipative hydrodynamic description for systems including particle number changing processes*, Nucl.Phys. A848, 428–442 (2010), [1007.0705].
- [EPS08] K. J. Eskola, H. Paukkunen and C. A. Salgado, *An improved global analysis of nuclear parton distribution functions including RHIC data*, JHEP 07, 102 (2008), [0802.0139].

- [EPS09] K. J. Eskola, H. Paukkunen and C. A. Salgado, *EPS09 - a New Generation of NLO and LO Nuclear Parton Distribution Functions*, JHEP 04, 065 (2009), [0902.4154].
- [ES86] R. K. Ellis and J. C. Sexton, *QCD radiative corrections to parton-parton scattering*, Nucl.Phys. B269, 445 (1986).
- [EXG08] A. El, Z. Xu and C. Greiner, *Thermalization of a color glass condensate and review of the 'Bottom-Up' scenario*, Nucl.Phys. A806, 287–304 (2008), [0712.3734].
- [EXG10] A. El, Z. Xu and C. Greiner, *Third-order relativistic dissipative hydrodynamics*, Phys.Rev. C81, 041901 (2010), [0907.4500].
- [EZR12] A. Emerick, X. Zhao and R. Rapp, *Bottomonia in the Quark-Gluon Plasma and their Production at RHIC and LHC*, Eur.Phys.J. A48, 72 (2012), [1111.6537].
- [Fei09] J. Feinberg, Wordle, <http://www.wordle.net>, 2009.
- [FNW03] S. Frixione, P. Nason and B. R. Webber, *Matching NLO QCD and parton showers in heavy flavour production*, JHEP 08, 007 (2003), [hep-ph/0305252].
- [Foc11] O. Fochler, *Investigation of high- p_T phenomena within a partonic transport model*, PhD thesis, Johann Wolfgang Goethe-Universität Frankfurt am Main, 2011.
- [FUXG11] O. Fochler, J. Uphoff, Z. Xu and C. Greiner, *Jet quenching and elliptic flow at RHIC and LHC within a pQCD-based partonic transport model*, J.Phys. G38, 124152 (2011), [1107.0130].
- [FUXG13] O. Fochler, J. Uphoff, Z. Xu and C. Greiner, *Radiative parton processes in perturbative QCD – an improved version of the Gunion and Bertsch cross section from comparisons to the exact result*, Phys.Rev. D88, 014018 (2013), [1302.5250].
- [FW02] S. Frixione and B. R. Webber, *Matching NLO QCD computations and parton shower simulations*, JHEP 06, 029 (2002), [hep-ph/0204244].
- [FXG09] O. Fochler, Z. Xu and C. Greiner, *Towards a unified understanding of jet-quenching and elliptic flow within perturbative QCD parton transport*, Phys.Rev.Lett. 102, 202301 (2009), [0806.1169].
- [FXG10] O. Fochler, Z. Xu and C. Greiner, *Energy loss in a partonic transport model including bremsstrahlung processes*, Phys.Rev. C82, 024907 (2010), [1003.4380].
- [G⁺95] R. V. Gavai et al., *Heavy quark production in p p collisions*, Int.J.Mod.Phys. A10, 2999–3042 (1995), [hep-ph/9411438].
- [GA08] P. B. Gossiaux and J. Aichelin, *Towards an understanding of the RHIC single electron data*, Phys.Rev. C78, 014904 (2008), [0802.2525].

- [GA13] P. B. Gossiaux and J. Aichelin, private communication, 2013.
- [GAG12] P. Gossiaux, J. Aichelin and T. Gousset, *Theory of heavy quark energy loss*, Prog.Theor.Phys.Suppl. 193, 110–116 (2012), [1201.4038].
- [GAGG10] P. Gossiaux, J. Aichelin, T. Gousset and V. Guiho, *Competition of Heavy Quark Radiative and Collisional Energy Loss in Deconfined Matter*, J.Phys.G G37, 094019 (2010), [1001.4166].
- [GB82] J. Gunion and G. Bertsch, *Hadronization by color bremsstrahlung*, Phys.Rev. D25, 746 (1982).
- [GBA09] P. B. Gossiaux, R. Bierkandt and J. Aichelin, *Tomography of a quark gluon plasma at RHIC and LHC energies*, Phys.Rev. C79, 044906 (2009), [0901.0946].
- [GJS13a] C. Gale, S. Jeon and B. Schenke, *Hydrodynamic Modeling of Heavy-Ion Collisions*, Int.J.Mod.Phys. A28, 1340011 (2013), [1301.5893].
- [GJS⁺13b] C. Gale, S. Jeon, B. Schenke, P. Tribedy and R. Venugopalan, *Event-by-event anisotropic flow in heavy-ion collisions from combined Yang-Mills and viscous fluid dynamics*, Phys.Rev.Lett. 110, 012302 (2013), [1209.6330].
- [GLV01] M. Gyulassy, P. Levai and I. Vitev, *Reaction operator approach to nonAbelian energy loss*, Nucl.Phys. B594, 371–419 (2001), [nucl-th/0006010].
- [GM92] K. Geiger and B. Müller, *Dynamics of parton cascades in highly relativistic nuclear collisions*, Nucl.Phys. B369, 600–654 (1992).
- [GNB⁺13] P. Gossiaux, M. Nahrgang, M. Bluhm, T. Gousset and J. Aichelin, *Heavy quark quenching from RHIC to LHC and the consequences of gluon damping*, Nucl.Phys. A904-905, 992c–995c (2013), [1211.2281].
- [Gos12] P. B. Gossiaux, *Recent results on heavy quark quenching in ultrarelativistic heavy ion collisions: the impact of coherent gluon radiation*, (2012), [1209.0844].
- [GR02] L. Grandchamp and R. Rapp, *Charmonium suppression and regeneration from SPS to RHIC*, Nucl.Phys. A709, 415–439 (2002), [hep-ph/0205305].
- [GRB⁺13] M. Greif, F. Reining, I. Bouras, G. Denicol, Z. Xu et al., *Investigation of Heat Conductivity in Relativistic Systems using a Partonic Cascade*, Phys.Rev. E87, 033019 (2013), [1301.1190].
- [GRV98] M. Glück, E. Reya and A. Vogt, *Dynamical parton distributions revisited*, Eur.Phys.J. C5, 461–470 (1998), [hep-ph/9806404].
- [Gui06] V. Guiho, *Production de charmonia dans les collisions d'ions lourds ultra-relativistes: vers une approche unifiée*, PhD thesis, Université de Nantes, 2006.
- [GVvH⁺11] P. B. Gossiaux, S. Vogel, H. van Hees, J. Aichelin, R. Rapp et al., *The Influence of bulk evolution models on heavy-quark phenomenology*, (2011), [1102.1114].

- [GW73] D. J. Gross and F. Wilczek, *Ultraviolet behavior of non-abelian gauge theories*, Phys.Rev.Lett. 30, 1343–1346 (1973).
- [GW94] M. Gyulassy and X.-N. Wang, *Multiple collisions and induced gluon Bremsstrahlung in QCD*, Nucl.Phys. B420, 583–614 (1994), [nucl-th/9306003].
- [Has70] W. K. Hastings, *Monte Carlo sampling methods using Markov chains and their applications*, Biometrika 57(1), 97–109 (1970).
- [Hau05] H. Haug, *Statistische Physik*, Springer, 2. edition, 2005.
- [HFR12a] M. He, R. J. Fries and R. Rapp, *Heavy-Quark Diffusion and Hadronization in Quark-Gluon Plasma*, Phys.Rev. C86, 014903 (2012), [1106.6006].
- [HFR12b] M. He, R. J. Fries and R. Rapp, *Non-perturbative Heavy-Flavor Transport at RHIC and LHC*, (2012), [1208.0256].
- [HFR13] M. He, R. J. Fries and R. Rapp, *D_s -Meson as Quantitative Probe of Diffusion and Hadronization in Nuclear Collisions*, Phys.Rev.Lett. 110, 112301 (2013), [1204.4442].
- [HG08] W. Horowitz and M. Gyulassy, *Heavy quark jet tomography of Pb+Pb at LHC: AdS/CFT drag or pQCD energy loss?*, Phys.Lett. B666, 320–323 (2008), [0706.2336].
- [HG11] W. Horowitz and M. Gyulassy, *Quenching and Tomography from RHIC to LHC*, J.Phys. G38, 124114 (2011), [1107.2136].
- [HI03] Y. Hatta and T. Ikeda, *Universality, the QCD critical / tricritical point and the quark number susceptibility*, Phys.Rev. D67, 014028 (2003), [hep-ph/0210284].
- [HJS+98] M. A. Halasz, A. D. Jackson, R. E. Shrock, M. A. Stephanov and J. J. M. Verbaarschot, *On the phase diagram of QCD*, Phys.Rev. D58, 096007 (1998), [hep-ph/9804290].
- [HKH+01] P. Huovinen, P. F. Kolb, U. W. Heinz, P. V. Ruuskanen and S. A. Voloshin, *Radial and elliptic flow at RHIC: further predictions*, Phys.Lett. B503, 58–64 (2001), [hep-ph/0101136].
- [Hor13] W. Horowitz, *Heavy Quark Production and Energy Loss*, Nucl.Phys. A904-905, 186c–193c (2013), [1210.8330].
- [HotQCD10] W. Soldner (HotQCD), *Chiral Aspects of Improved Staggered Fermions with 2+1-Flavors from the HotQCD Collaboration*, PoS LATTICE2010, 215 (2010), [1012.4484].
- [HP10] P. Huovinen and P. Petreczky, *QCD Equation of State and Hadron Resonance Gas*, Nucl.Phys. A837, 26–53 (2010), [0912.2541].
- [HT02] T. Hirano and K. Tsuda, *Collective flow and two pion correlations from a relativistic hydrodynamic model with early chemical freezeout*, Phys.Rev. C66, 054905 (2002), [nucl-th/0205043].

- [HVZ12] Y. He, I. Vitev and B.-W. Zhang, $\mathcal{O}(\alpha_s^3)$ Analysis of Inclusive Jet and di-Jet Production in Heavy Ion Reactions at the Large Hadron Collider, Phys.Lett. B713, 224–232 (2012), [1105.2566].
- [IV03] E. Iancu and R. Venugopalan, *The color glass condensate and high energy scattering in QCD*, in Quark Gluon Plasma 3, edited by X.-N. Wang and R. C. Hwa, World Scientific, 249 (2003), [hep-ph/0303204].
- [JM12] B. V. Jacak and B. Müller, *The exploration of hot nuclear matter*, Science 337, 310–314 (2012).
- [Kir97] E. Kiritsis, *Introduction to superstring theory*, (1997), [hep-th/9709062].
- [KLL87] K. Kajantie, P. V. Landshoff and J. Lindfors, *Minijet Production in High-Energy Nucleus-Nucleus Collisions*, Phys.Rev.Lett. 59, 2527 (1987).
- [KLOT04] S. Kretzer, H. L. Lai, F. I. Olness and W. K. Tung, *CTEQ6 parton distributions with heavy quark mass effects*, Phys.Rev. D69, 114005 (2004), [hep-ph/0307022].
- [Koc97] V. Koch, *Aspects of chiral symmetry*, Int.J.Mod.Phys. E6, 203–250 (1997), [nucl-th/9706075].
- [KPR80] Z. Kunszt, E. Pietarinen and E. Reya, *Transverse momenta of hadronically produced heavy quark systems: $2 \rightarrow 3$ processes in QCD*, Phys.Rev. D21, 733 (1980).
- [KPS10] B. Kopeliovich, I. Potashnikova and I. Schmidt, *Why heavy and light quarks radiate energy with similar rates*, Phys.Rev. C82, 037901 (2010), [1004.3920].
- [KSH00] P. F. Kolb, J. Sollfrank and U. W. Heinz, *Anisotropic transverse flow and the quark-hadron phase transition*, Phys.Rev. C62, 054909 (2000), [hep-ph/0006129].
- [KSS05] P. Kovtun, D. T. Son and A. O. Starinets, *Viscosity in strongly interacting quantum field theories from black hole physics*, Phys.Rev.Lett. 94, 111601 (2005), [hep-th/0405231].
- [KV03] S. R. Klein and R. Vogt, *Inhomogeneous shadowing effects on J/ψ production in $d A$ collisions*, Phys.Rev.Lett. 91, 142301 (2003), [nucl-th/0305046].
- [LCXZ11] Y. Liu, B. Chen, N. Xu and P. Zhuang, Υ Production as a Probe for Early State Dynamics in High Energy Nuclear Collisions at RHIC, Phys.Lett. B697, 32–36 (2011), [1009.2585].
- [Lep78] G. P. Lepage, *A new algorithm for adaptive multidimensional integration*, Journal of Computational Physics 27(2) (May 1978).
- [Li12] W. Li, *Observation of a 'Ridge' correlation structure in high multiplicity proton-proton collisions: A brief review*, Mod.Phys.Lett. A27, 1230018 (2012), [1206.0148].

- [LKL⁺05] Z.-W. Lin, C. M. Ko, B.-A. Li, B. Zhang and S. Pal, *A Multi-phase transport model for relativistic heavy ion collisions*, Phys.Rev. C72, 064901 (2005), [nucl-th/0411110].
- [LM06] T. Lappi and L. McLerran, *Some features of the glasma*, Nucl.Phys. A772, 200–212 (2006), [hep-ph/0602189].
- [LP53] L. D. Landau and I. Pomeranchuk, *Limits of applicability of the theory of bremsstrahlung electrons and pair production at high energies*, Dokl.Akad.Nauk Ser.Fiz. 92, 535–536 (1953).
- [LPSW05] M. A. Lisa, S. Pratt, R. Soltz and U. Wiedemann, *Femtoscopy in relativistic heavy ion collisions*, Ann.Rev.Nucl.Part.Sci. 55, 357–402 (2005), [nucl-ex/0505014].
- [LQXZ09] Y.-p. Liu, Z. Qu, N. Xu and P.-f. Zhuang, *J/psi Transverse Momentum Distribution in High Energy Nuclear Collisions at RHIC*, Phys.Lett. B678, 72–76 (2009), [0901.2757].
- [LQXZ10] Y. Liu, Z. Qu, N. Xu and P. Zhuang, *Rapidity Dependence of J/ψ Production at RHIC and LHC*, J.Phys. G37, 075110 (2010), [0907.2723].
- [LR08] M. Luzum and P. Romatschke, *Conformal Relativistic Viscous Hydrodynamics: Applications to RHIC results at $\sqrt{s_{NN}} = 200$ GeV*, Phys.Rev. C78, 034915 (2008), [0804.4015].
- [LvHSB12a] T. Lang, H. van Hees, J. Steinheimer and M. Bleicher, *Charm quark transport in Pb+Pb reactions at $\sqrt{s_{NN}} = 2.76$ TeV from a (3 + 1) dimensional hybrid approach*, (2012), [1208.1643].
- [LvHSB12b] T. Lang, H. van Hees, J. Steinheimer and M. Bleicher, *Heavy quark transport in heavy ion collisions at RHIC and LHC within the UrQMD transport model*, (2012), [1211.6912].
- [LvHSB13] T. Lang, H. van Hees, J. Steinheimer and M. Bleicher, *Elliptic flow and nuclear modification factors of D-mesons at FAIR in a Hybrid-Langevin approach*, (2013), [1305.1797].
- [LXZ10] Y. Liu, N. Xu and P. Zhuang, *J/psi elliptic flow in relativistic heavy ion collisions*, Nucl.Phys. A834, 317C–319C (2010), [0910.0959].
- [MAB⁺11] M. Monteno, W. Alberico, A. Beraudo, A. De Pace, A. Molinari et al., *Heavy-flavor dynamics in nucleus-nucleus collisions: from RHIC to LHC*, J.Phys. G38, 124144 (2011), [1107.0256].
- [Man58] S. Mandelstam, *Determination of the pion - nucleon scattering amplitude from dispersion relations and unitarity. General theory*, Phys.Rev. 112, 1344–1360 (1958).
- [Mar97] S. P. Martin, *A Supersymmetry Primer*, (1997), [hep-ph/9709356].

- [MBA13] S. Mazumder, T. Bhattacharyya and J.-e. Alam, *Gluon bremsstrahlung by heavy quarks - its effects on transport coefficients and equilibrium distribution*, (2013), [1305.6445].
- [MBAD11] S. Mazumder, T. Bhattacharyya, J.-e. Alam and S. K. Das, *Momentum dependence of drag coefficients and heavy flavour suppression in quark gluon plasma*, Phys.Rev. C84, 044901 (2011), [1106.2615].
- [McL03] L. McLerran, *RHIC physics: The quark gluon plasma and the color glass condensate: 4 lectures*, (2003), [hep-ph/0311028].
- [McL08] L. McLerran, *The Color Glass Condensate and Glasma*, (2008), [0804.1736].
- [MG00] D. Molnar and M. Gyulassy, *New solutions to covariant nonequilibrium dynamics*, Phys.Rev. C62, 054907 (2000), [nucl-th/0005051].
- [Mig56] A. B. Migdal, *Bremsstrahlung and pair production in condensed media at high energies*, Phys.Rev. 103, 1811–1820 (1956).
- [Mis11] A. Mischke, *Jet-like correlations of heavy-flavor particles - from RHIC to LHC*, J.Phys.Conf.Ser. 316, 012009 (2011), [1107.5138].
- [MN98] M. Matsumoto and T. Nishimura, *Mersenne twister: A 623-dimensionally equidistributed uniform pseudo-random number generator*, ACM Trans.Model.Comput.Simul. 8, 3–30 (January 1998).
- [MNR92] M. L. Mangano, P. Nason and G. Ridolfi, *Heavy quark correlations in hadron collisions at next-to-leading order*, Nucl.Phys. B373, 295–345 (1992).
- [Mol07] D. Molnar, *Heavy quarks at RHIC from parton transport theory*, Eur.Phys.J. C49, 181–186 (2007), [nucl-th/0608069].
- [MP07] A. Mocsy and P. Petreczky, *Color Screening Melts Quarkonium*, Phys.Rev.Lett. 99, 211602 (2007), [0706.2183].
- [MPST98] M. G. Mustafa, D. Pal, D. K. Srivastava and M. Thoma, *Radiative energy loss of heavy quarks in a quark gluon plasma*, Phys.Lett. B428, 234–240 (1998), [nucl-th/9711059].
- [MPUG13] A. Meistrenko, A. Peshier, J. Uphoff and C. Greiner, *Collisional energy loss of heavy quarks*, Nucl.Phys. A901, 51–64 (2013), [1204.2397].
- [MRR⁺53] N. Metropolis, A. W. Rosenbluth, M. N. Rosenbluth, A. H. Teller and E. Teller, *Equation of state calculations by fast computing machines*, The Journal of Chemical Physics 21(6), 1087 (1953).
- [MRST02] A. D. Martin, R. G. Roberts, W. J. Stirling and R. S. Thorne, *NNLO global parton analysis*, Phys.Lett. B531, 216–224 (2002), [hep-ph/0201127].
- [MRST05] A. D. Martin, R. G. Roberts, W. J. Stirling and R. S. Thorne, *Parton distributions incorporating QED contributions*, Eur.Phys.J. C39, 155–161 (2005), [hep-ph/0411040].

- [MS86] T. Matsui and H. Satz, *J/psi Suppression by Quark-Gluon Plasma Formation*, Phys.Lett. B178, 416 (1986).
- [MSW12] B. Müller, J. Schukraft and B. Wyslouch, *First Results from Pb+Pb collisions at the LHC*, Ann.Rev.Nucl.Part.Sci. 62, 361–386 (2012), [1202.3233].
- [MT05] G. D. Moore and D. Teaney, *How much do heavy quarks thermalize in a heavy ion collision?*, Phys.Rev. C71, 064904 (2005), [hep-ph/0412346].
- [Mus05] M. G. Mustafa, *Energy loss of charm quarks in the quark-gluon plasma: Collisional vs radiative*, Phys.Rev. C72, 014905 (2005), [hep-ph/0412402].
- [MVL11] A. Majumder and M. Van Leeuwen, *The Theory and Phenomenology of Perturbative QCD Based Jet Quenching*, Prog.Part.Nucl.Phys. A66, 41–92 (2011), [1002.2206].
- [NAGW13] M. Nahrgang, J. Aichelin, P. B. Gossiaux and K. Werner, *Azimuthal correlations of heavy quarks in Pb+Pb collisions at LHC ($\sqrt{s} = 2.76$ TeV)*, (2013), [1305.3823].
- [NO00] P. Nason and C. Oleari, *A Phenomenological study of heavy quark fragmentation functions in e^+e^- annihilation*, Nucl.Phys. B565, 245–266 (2000), [hep-ph/9903541].
- [Nov99] S. F. Novaes, *Standard model: An Introduction*, (1999), [hep-ph/0001283].
- [ORG78] J. F. Owens, E. Reya and M. Glück, *Detailed Quantum Chromodynamic Predictions for High $p(T)$ Processes*, Phys.Rev. D18, 1501 (1978).
- [P+02] J. Pumplin et al., *New generation of parton distributions with uncertainties from global QCD analysis*, JHEP 07, 012 (2002), [hep-ph/0201195].
- [PDG12] J. Beringer et al. (PDG), *Review of Particle Physics (RPP)*, Phys.Rev. D86, 010001 (2012).
- [Pes79] M. E. Peskin, *Short Distance Analysis for Heavy Quark Systems. 1. Diagrammatics*, Nucl.Phys. B156, 365 (1979).
- [Pes12] A. Peshier, *Turning on the Charm*, Nucl.Phys. A888, 7–22 (2012), [0801.0595].
- [PHENIX03] S. Adler et al. (PHENIX), *Scaling properties of proton and anti-proton production in $\sqrt{s_{NN}} = 200$ GeV Au+Au collisions*, Phys.Rev.Lett. 91, 172301 (2003), [nucl-ex/0305036].
- [PHENIX05a] K. Adcox et al. (PHENIX), *Formation of dense partonic matter in relativistic nucleus nucleus collisions at RHIC: Experimental evaluation by the PHENIX collaboration*, Nucl.Phys. A757, 184–283 (2005), [nucl-ex/0410003].
- [PHENIX05b] S. Adler et al. (PHENIX), *Centrality dependence of direct photon production in $\sqrt{s_{NN}} = 200$ GeV Au+Au collisions*, Phys.Rev.Lett. 94, 232301 (2005), [nucl-ex/0503003].

- [PHENIX07a] A. Adare et al. (PHENIX), *Energy Loss and Flow of Heavy Quarks in Au+Au Collisions at $\sqrt{s_{NN}} = 200$ GeV*, Phys.Rev.Lett. 98, 172301 (2007), [nucl-ex/0611018].
- [PHENIX07b] A. Adare et al. (PHENIX), *J / psi production versus transverse momentum and rapidity in p+p collisions at $\sqrt{s_{NN}} = 200$ GeV*, Phys.Rev.Lett. 98, 232002 (2007), [hep-ex/0611020].
- [PHENIX07c] A. Adare et al. (PHENIX), *J/psi production vs centrality, transverse momentum, and rapidity in Au+Au collisions at $\sqrt{s_{NN}} = 200$ GeV*, Phys.Rev.Lett. 98, 232301 (2007), [nucl-ex/0611020].
- [PHENIX07d] A. Adare et al. (PHENIX), *Scaling properties of azimuthal anisotropy in Au+Au and Cu+Cu collisions at $\sqrt{s_{NN}} = 200$ GeV*, Phys.Rev.Lett. 98, 162301 (2007), [nucl-ex/0608033].
- [PHENIX08a] A. Adare et al. (PHENIX), *Cold Nuclear Matter Effects on J/Psi as Constrained by Deuteron-Gold Measurements at $\sqrt{s_{NN}} = 200$ GeV*, Phys.Rev. C77, 024912 (2008), [0711.3917].
- [PHENIX08b] A. Adare et al. (PHENIX), *Suppression pattern of neutral pions at high transverse momentum in Au+Au collisions at $\sqrt{s_{NN}} = 200$ GeV and constraints on medium transport coefficients*, Phys.Rev.Lett. 101, 232301 (2008), [0801.4020].
- [PHENIX08c] C. Silvestre (PHENIX), *PHENIX first measurement of the J/psi elliptic flow parameter $v(2)$ in Au+Au collisions at $\sqrt{s_{NN}} = 200$ GeV*, J.Phys. G35, 104136 (2008), [0806.0475].
- [PHENIX10] A. Adare et al. (PHENIX), *Enhanced production of direct photons in Au+Au collisions at $\sqrt{s_{NN}} = 200$ GeV and implications for the initial temperature*, Phys.Rev.Lett. 104, 132301 (2010), [0804.4168].
- [PHENIX11a] A. Adare et al. (PHENIX), *Cold Nuclear Matter Effects on J/psi Yields as a Function of Rapidity and Nuclear Geometry in Deuteron-Gold Collisions at $\sqrt{s_{NN}} = 200$ GeV*, Phys.Rev.Lett. 107, 142301 (2011), [1010.1246].
- [PHENIX11b] A. Adare et al. (PHENIX), *Heavy Quark Production in p + p and Energy Loss and Flow of Heavy Quarks in Au+Au Collisions at $\sqrt{s_{NN}} = 200$ GeV*, Phys.Rev. C84, 044905 (2011), [1005.1627].
- [PHENIX12] A. Adare, S. Afanasiev, C. Aidala, N. Ajitanand, Y. Akiba et al. (PHENIX), *Cold-nuclear-matter effects on heavy-quark production in d+Au collisions at $\sqrt{s_{NN}} = 200$ GeV*, (2012), [1208.1293].
- [Phi10] O. Philipsen, *Lattice QCD at non-zero temperature and baryon density*, pages 273–330 (2010), [1009.4089].
- [PHOBOS05] B. B. Back et al. (PHOBOS), *The PHOBOS perspective on discoveries at RHIC*, Nucl.Phys. A757, 28–101 (2005), [nucl-ex/0410022].

- [Pol73] H. D. Politzer, *Reliable perturbative results for strong interactions?*, Phys.Rev.Lett. 30, 1346–1349 (1973).
- [PP08a] S. Peigne and A. Peshier, *Collisional energy loss of a fast heavy quark in a quark- gluon plasma*, Phys.Rev. D77, 114017 (2008), [0802.4364].
- [PP08b] S. Peigne and A. Peshier, *Collisional Energy Loss of a Fast Muon in a Hot QED Plasma*, Phys.Rev. D77, 014015 (2008), [0710.1266].
- [PS95] M. E. Peskin and D. V. Schroeder, *An introduction to quantum field theory*, Westview Press, 1995.
- [PSB⁺08] H. Petersen, J. Steinheimer, G. Burau, M. Bleicher and H. Stoecker, *A Fully Integrated Transport Approach to Heavy Ion Reactions with an Intermediate Hydrodynamic Stage*, Phys.Rev. C78, 044901 (2008), [0806.1695].
- [PSS01] G. Policastro, D. T. Son and A. O. Starinets, *The shear viscosity of strongly coupled $N = 4$ supersymmetric Yang-Mills plasma*, Phys.Rev.Lett. 87, 081601 (2001), [hep-th/0104066].
- [PSSZ83] C. Peterson, D. Schlatter, I. Schmitt and P. M. Zerwas, *Scaling Violations in Inclusive $e^+ e^-$ Annihilation Spectra*, Phys.Rev. D27, 105 (1983).
- [PTVF07] W. H. Press, S. A. Teukolsky, W. T. Vetterling and B. P. Flannery, *Numerical Recipes 3rd Edition: The art of scientific computing*, Cambridge University Press, 3 edition, September 2007.
- [PV98] A. M. Poskanzer and S. A. Voloshin, *Methods for analyzing anisotropic flow in relativistic nuclear collisions*, Phys.Rev. C58, 1671–1678 (1998), [nucl-ex/9805001].
- [RBC10] R. Rapp, D. Blaschke and P. Crochet, *Charmonium and bottomonium production in heavy-ion collisions*, Prog.Part.Nucl.Phys. 65, 209–266 (2010), [0807.2470].
- [RBE⁺12] F. Reining, I. Bouras, A. El, C. Wesp, Z. Xu et al., *Extraction of shear viscosity in stationary states of relativistic particle systems*, Phys.Rev. E85, 026302 (2012), [1106.4210].
- [Rei76] F. Reif, *Physikalische Statistik und Physik der Wärme*, Walter de Gruyter, 1976.
- [RHPE11] T. Renk, H. Holopainen, R. Paatelainen and K. J. Eskola, *Systematics of the charged-hadron p_T spectrum and the nuclear suppression factor in heavy-ion collisions from $\sqrt{s} = 200$ GeV to $\sqrt{s} = 2.76$ TeV*, Phys.Rev. C84, 014906 (2011), [1103.5308].
- [Ris04] D. H. Rischke, *The quark-gluon plasma in equilibrium*, Prog.Part.Nucl.Phys. 52, 197–296 (2004), [nucl-th/0305030].
- [Ros01] J. L. Rosner, *The Standard model in 2001*, (2001), [hep-ph/0108195].

- [RR07] P. Romatschke and U. Romatschke, *Viscosity Information from Relativistic Nuclear Collisions: How Perfect is the Fluid Observed at RHIC?*, Phys.Rev.Lett. 99, 172301 (2007), [0706.1522].
- [RvH10] R. Rapp and H. van Hees, *Heavy Quarks in the Quark-Gluon Plasma*, in Quark Gluon Plasma 4, edited by R. C. Hwa and X.-N. Wang, World Scientific, 111 (2010), [0903.1096].
- [RW00] K. Rajagopal and F. Wilczek, *The Condensed matter physics of QCD*, (2000), [hep-ph/0011333].
- [RWvH09] R. Rapp, J. Wambach and H. van Hees, *The Chiral Restoration Transition of QCD and Low Mass Dileptons*, (2009), [0901.3289].
- [Sac87] R. G. Sachs, *The Physics of Time Reversal*, University of Chicago Press, 1987, p. 80.
- [SAMA⁺12] C. Salgado, J. Alvarez-Muniz, F. Arleo, N. Armesto, M. Botje et al., *Proton-Nucleus Collisions at the LHC: Scientific Opportunities and Requirements*, J.Phys. G39, 015010 (2012), [1105.3919].
- [SB12] M. Strickland and D. Bazow, *Thermal Bottomonium Suppression at RHIC and LHC*, Nucl.Phys. A879, 25–58 (2012), [1112.2761].
- [Sch06] F. Schwabl, *Statistische Mechanik*, Springer, 3. edition, 2006.
- [Sch08] B. Schenke, *Collective Phenomena in the Non-Equilibrium Quark-Gluon Plasma*, (2008), [0810.4306].
- [Sem09] A. Semenov, *LanHEP: A Package for the automatic generation of Feynman rules in field theory. Version 3.0*, Comput.Phys.Commun. 180, 431–454 (2009), [0805.0555].
- [SFU⁺13] F. Senzel, O. Fochler, J. Uphoff, Z. Xu and C. Greiner, *Influence of multiple in-medium scattering processes on the momentum imbalance of reconstructed di-jets*, submitted to Phys.Rev.C (2013), [1309.1657].
- [SGJ09] B. Schenke, C. Gale and S. Jeon, *MARTINI: An Event generator for relativistic heavy-ion collisions*, Phys.Rev. C80, 054913 (2009), [0909.2037].
- [SJJ11] B. Schenke, S. Jeon and C. Gale, *Elliptic and triangular flow in event-by-event (3+1)D viscous hydrodynamics*, Phys.Rev.Lett. 106, 042301 (2011), [1009.3244].
- [Smi06] B. M. Smirnov, *Principles of Statistical Physics: Distributions, Structures, Phenomena, Kinetics of Atomic Systems*, Wiley-VCH, 2006, p. 200.
- [SMM97] D. K. Srivastava, M. G. Mustafa and B. Müller, *Expanding quark - gluon plasmas: Transverse flow, chemical equilibration and electromagnetic radiation*, Phys.Rev. C56, 1064–1074 (1997), [nucl-th/9611041].

- [SMMR01] O. Scavenius, A. Mocsy, I. N. Mishustin and D. H. Rischke, *Chiral phase transition within effective models with constituent quarks*, Phys.Rev. C64, 045202 (2001), [nucl-th/0007030].
- [SMS06] T. Sjostrand, S. Mrenna and P. Skands, *PYTHIA 6.4 physics and manual*, JHEP 05, 026 (2006), [hep-ph/0603175].
- [SMS08] T. Sjostrand, S. Mrenna and P. Z. Skands, *A Brief Introduction to PYTHIA 8.1*, Comput.Phys.Commun. 178, 852–867 (2008), [0710.3820].
- [STAR03] J. Adams et al. (STAR), *Transverse momentum and collision energy dependence of high $p(T)$ hadron suppression in Au+Au collisions at ultrarelativistic energies*, Phys.Rev.Lett. 91, 172302 (2003), [nucl-ex/0305015].
- [STAR05] J. Adams et al. (STAR), *Experimental and theoretical challenges in the search for the quark gluon plasma: The STAR collaboration's critical assessment of the evidence from RHIC collisions*, Nucl.Phys. A757, 102–183 (2005), [nucl-ex/0501009].
- [STAR06] B. Abelev et al. (STAR), *Identified baryon and meson distributions at large transverse momenta from Au+Au collisions at $\sqrt{s_{NN}} = 200$ GeV*, Phys.Rev.Lett. 97, 152301 (2006), [nucl-ex/0606003].
- [STAR07] B. I. Abelev et al. (STAR), *Transverse momentum and centrality dependence of high- pt non-photonic electron suppression in Au+Au collisions at $\sqrt{s_{NN}} = 200$ GeV*, Phys.Rev.Lett. 98, 192301 (2007), [nucl-ex/0607012].
- [STAR09] B. Abelev et al. (STAR), *Long range rapidity correlations and jet production in high energy nuclear collisions*, Phys.Rev. C80, 064912 (2009), [0909.0191].
- [STAR10] M. Aggarwal et al. (STAR), *Measurement of the Bottom contribution to non-photonic electron production in $p + p$ collisions at $\sqrt{s}=200$ GeV*, Phys.Rev.Lett. 105, 202301 (2010), [1007.1200].
- [STAR11a] H. Agakishiev et al. (STAR), *High p_T non-photonic electron production in $p + p$ collisions at $\sqrt{s} = 200$ GeV*, Phys.Rev. D83, 052006 (2011), [1102.2611].
- [STAR11b] C. B. Powell (STAR), *Quarkonium Production at STAR*, PoS EPS-HEP2011, 485 (2011), [1111.6944].
- [STAR12] L. Adamczyk et al. (STAR), *Measurement of J/ψ Azimuthal Anisotropy in Au+Au Collisions at $\sqrt{s_{NN}} = 200$ GeV*, (2012), [1212.3304].
- [STAR13a] M. Mustafa (STAR), *Measurements of Non-photonic Electron Production and Azimuthal Anisotropy in $\sqrt{s_{NN}} = 39, 62.4$ and 200 GeV Au+Au Collisions from STAR at RHIC*, Nucl.Phys. A904-905, 665c–668c (2013), [1210.5199].
- [STAR13b] D. Tlusty (STAR), *Open charm hadron production via hadronic decays at STAR*, Nucl.Phys. A904-905, 639c–642c (2013), [1211.5995].

- [Ste06] M. A. Stephanov, *QCD phase diagram: An overview*, PoS LAT2006, 024 (2006), [hep-lat/0701002].
- [SVZ09] R. Sharma, I. Vitev and B.-W. Zhang, *Light-cone wave function approach to open heavy flavor dynamics in QCD matter*, Phys.Rev. C80, 054902 (2009), [0904.0032].
- [SW03] C. A. Salgado and U. A. Wiedemann, *Calculating quenching weights*, Phys.Rev. D68, 014008 (2003), [hep-ph/0302184].
- [Tho95] M. H. Thoma, *Applications of high temperature field theory to heavy ion collisions*, in Quark Gluon Plasma 2, edited by R. C. Hwa, World Scientific, 51 (1995), [hep-ph/9503400].
- [TKS05] R. Thomas, B. Kampfer and G. Soff, *Gluon emission of heavy quarks: Dead cone effect*, Acta Phys.Hung. A22, 83–91 (2005), [hep-ph/0405189].
- [TM06] R. L. Thews and M. L. Mangano, *Momentum spectra of charmonium produced in a quark-gluon plasma*, Phys.Rev. C73, 014904 (2006), [nucl-th/0505055].
- [UFXG10a] J. Uphoff, O. Fochler, Z. Xu and C. Greiner, *Heavy quark production at RHIC and LHC within a partonic transport model*, Phys.Rev. C82, 044906 (2010), [1003.4200].
- [UFXG10b] J. Uphoff, O. Fochler, Z. Xu and C. Greiner, *Production and elliptic flow of heavy quarks at RHIC and LHC within a partonic transport model*, J.Phys.Conf.Ser. 230, 012004 (2010), [1004.4091].
- [UFXG10c] J. Uphoff, O. Fochler, Z. Xu and C. Greiner, *Production, elliptic flow and energy loss of heavy quarks in the quark-gluon plasma*, J.Phys.Conf.Ser. 270, 012028 (2010), [1008.1995].
- [UFXG11a] J. Uphoff, O. Fochler, Z. Xu and C. Greiner, *Elliptic flow and energy loss of heavy quarks in ultra-relativistic heavy ion collisions*, Phys.Rev. C84, 024908 (2011), [1104.2295].
- [UFXG11b] J. Uphoff, O. Fochler, Z. Xu and C. Greiner, *Heavy quarks at RHIC and LHC within a partonic transport model*, Nucl.Phys. A855, 444–447 (2011), [1011.6183].
- [UFXG12a] J. Uphoff, O. Fochler, Z. Xu and C. Greiner, *Open heavy flavor at RHIC and LHC in a partonic transport model*, Acta Phys.Polon.Supp. 5, 555 (2012), [1112.1559].
- [UFXG12b] J. Uphoff, O. Fochler, Z. Xu and C. Greiner, *Open Heavy Flavor in Pb+Pb Collisions at $\sqrt{s} = 2.76$ TeV within a Transport Model*, Phys.Lett. B717, 430–435 (2012), [1205.4945].
- [UFXG13a] J. Uphoff, O. Fochler, Z. Xu and C. Greiner, *Open heavy flavor and J/ψ at RHIC and LHC*, Nucl.Phys. A910-911, 401–404 (2013), [1208.1970].

- [UFXG13b] J. Uphoff, O. Fochler, Z. Xu and C. Greiner, *Open heavy flavor and J/ψ at RHIC and LHC within a transport model*, J.Phys.Conf.Ser. 446, 012044 (2013), [1212.0358].
- [Uph09] J. Uphoff, *Produktion von schweren Quarks in ultrarelativistischen Kern-Kern-Kollisionen*, Diplomarbeit, Johann Wolfgang Goethe-Universität Frankfurt am Main, 2009.
- [Uph12] J. Uphoff, *Evolution of the quark gluon plasma in Pb+Pb collisions at the LHC in a BAMPS simulation*, <http://th.physik.uni-frankfurt.de/~uphoff/videos.php>, 2012.
- [UZF⁺11] J. Uphoff, K. Zhou, O. Fochler, Z. Xu and C. Greiner, *Heavy quarks and charmonium at RHIC and LHC within a partonic transport model*, PoS BORMIO2011, 032 (2011), [1104.2437].
- [Ven05] R. Venugopalan, *The color glass condensate: An overview*, Eur.Phys.J. C43, 337–344 (2005), [hep-ph/0502190].
- [VG02] I. Vitev and M. Gyulassy, *High p_T tomography of $d+Au$ and $Au+Au$ at SPS, RHIC, and LHC*, Phys.Rev.Lett. 89, 252301 (2002), [hep-ph/0209161].
- [VGWA11] S. Vogel, P. B. Gossiaux, K. Werner and J. Aichelin, *Heavy Quark Energy Loss in High Multiplicity Proton Proton Collisions at LHC*, Phys.Rev.Lett. 107, 032302 (2011), [1012.0764].
- [vHGR06] H. van Hees, V. Greco and R. Rapp, *Heavy-quark probes of the quark-gluon plasma at RHIC*, Phys.Rev. C73, 034913 (2006), [nucl-th/0508055].
- [vHMGR08] H. van Hees, M. Mannarelli, V. Greco and R. Rapp, *Nonperturbative heavy-quark diffusion in the quark-gluon plasma*, Phys.Rev.Lett. 100, 192301 (2008), [0709.2884].
- [vHR05] H. van Hees and R. Rapp, *Thermalization of Heavy Quarks in the Quark-Gluon Plasma*, Phys.Rev. C71, 034907 (2005), [nucl-th/0412015].
- [Vit04] I. Vitev, *Jet tomography*, J.Phys. G30, S791–S800 (2004), [hep-ph/0403089].
- [Vog10] R. Vogt, private communication, 2010.
- [VZ96] S. Voloshin and Y. Zhang, *Flow study in relativistic nuclear collisions by Fourier expansion of Azimuthal particle distributions*, Z. Phys. C70, 665–672 (1996), [hep-ph/9407282].
- [WA9802] M. Aggarwal et al. (WA98), *Transverse mass distributions of neutral pions from Pb-208 induced reactions at 158 A GeV*, Eur.Phys.J. C23, 225–236 (2002), [nucl-ex/0108006].
- [WBG05] M. R. Whalley, D. Bourilkov and R. C. Group, *The Les Houches Accord PDFs (LHAPDF) and Lhaglu*, (2005), [hep-ph/0508110].

- [WER⁺11] C. Wesp, A. El, F. Reining, Z. Xu, I. Bouras et al., *Calculation of shear viscosity using Green-Kubo relations within a parton cascade*, Phys.Rev. C84, 054911 (2011), [1106.4306].
- [WG91] X.-N. Wang and M. Gyulassy, *HIJING: A Monte Carlo model for multiple jet production in $p p$, $p A$ and $A A$ collisions*, Phys.Rev. D44, 3501–3516 (1991).
- [WHDG07] S. Wicks, W. Horowitz, M. Djordjevic and M. Gyulassy, *Elastic, Inelastic, and Path Length Fluctuations in Jet Tomography*, Nucl.Phys. A784, 426–442 (2007), [nucl-th/0512076].
- [WKP11] K. Werner, I. Karpenko and T. Pierog, *The 'Ridge' in Proton-Proton Scattering at 7 TeV*, Phys.Rev.Lett. 106, 122004 (2011), [1011.0375].
- [Won94] C.-Y. Wong, *Introduction to High-Energy Heavy-Ion Collisions*, World Scientific Publishing Co. Pte. Ltd., 1994.
- [Won96a] S. M. H. Wong, *Thermal and chemical equilibration in relativistic heavy ion collisions*, Phys.Rev. C54, 2588–2599 (1996), [hep-ph/9609287].
- [Won96b] S. Wong, *Thermal and chemical equilibration in a gluon plasma*, Nucl.Phys. A607, 442–456 (1996), [hep-ph/9606305].
- [XDZ05] W.-C. Xiang, H.-T. Ding and D.-C. Zhou, *Radiative energy loss of heavy quark and dead cone effect in ultra-relativistic heavy ion collisions*, Chin.Phys.Lett. 22, 72–75 (2005).
- [XG05] Z. Xu and C. Greiner, *Thermalization of gluons in ultrarelativistic heavy ion collisions by including three-body interactions in a parton cascade*, Phys.Rev. C71, 064901 (2005), [hep-ph/0406278].
- [XG06] Z. Xu and C. Greiner, *Thermalization of gluons at RHIC: Dependence on initial conditions*, Eur.Phys.J. A29, 33–37 (2006), [hep-ph/0511145].
- [XG07] Z. Xu and C. Greiner, *Transport rates and momentum isotropization of gluon matter in ultrarelativistic heavy-ion collisions*, Phys.Rev. C76, 024911 (2007), [hep-ph/0703233].
- [XG08] Z. Xu and C. Greiner, *Shear viscosity in a gluon gas*, Phys.Rev.Lett. 100, 172301 (2008), [0710.5719].
- [XG09] Z. Xu and C. Greiner, *Elliptic flow of gluon matter in ultrarelativistic heavy-ion collisions*, Phys.Rev. C79, 014904 (2009), [0811.2940].
- [XG10] Z. Xu and C. Greiner, *Dependence of elliptic flow on number of parton degrees of freedom*, Phys.Rev. C81, 054901 (2010), [1001.2912].
- [XGS08] Z. Xu, C. Greiner and H. Stöcker, *PQCD calculations of elliptic flow and shear viscosity at RHIC*, Phys.Rev.Lett. 101, 082302 (2008), [0711.0961].
- [XS94] L. Xiong and E. V. Shuryak, *Gluon multiplication in high-energy heavy ion collisions*, Phys.Rev. C49, 2203–2211 (1994), [hep-ph/9309333].

- [YS10] C. Young and E. Shuryak, *Recombinant Charmonium in strongly coupled Quark-Gluon Plasma*, Phys.Rev. C81, 034905 (2010), [0911.3080].
- [YSJG12] C. Young, B. Schenke, S. Jeon and C. Gale, *MARTINI event generator for heavy quarks: Initialization, parton evolution, and hadronization*, Phys.Rev. C86, 034905 (2012), [1111.0647].
- [Z⁺07] X. Zhu et al., *D-Dbar Correlations as a sensitive probe for thermalization in high-energy nuclear collisions*, Phys.Lett. B647, 366–370 (2007), [hep-ph/0604178].
- [Zak96] B. Zakharov, *Fully quantum treatment of the Landau-Pomeranchuk-Migdal effect in QED and QCD*, JETP Lett. 63, 952–957 (1996), [hep-ph/9607440].
- [ZCK05] B. Zhang, L.-W. Chen and C.-M. Ko, *Charm elliptic flow at RHIC*, Phys.Rev. C72, 024906 (2005), [nucl-th/0502056].
- [ZER13] X. Zhao, A. Emerick and R. Rapp, *In-Medium Quarkonia at SPS, RHIC and LHC*, Nucl.Phys. A904-905, 611c–614c (2013), [1210.6583].
- [ZEUS03] L. Gladilin (ZEUS), *Charm hadronization in gamma p collisions with ZEUS at HERA*, pages 721–726 (2003), [hep-ex/0309044].
- [Zha98] B. Zhang, *ZPC 1.0.1: A parton cascade for ultrarelativistic heavy ion collisions*, Comput.Phys.Commun. 109, 193–206 (1998), [nucl-th/9709009].
- [Zha13] B. Zhang, *Toward parton equilibration with improved parton interaction matrix elements*, J.Phys.Conf.Ser. 420, 012035 (2013), [1208.1224].
- [ZR08] X. Zhao and R. Rapp, *Transverse Momentum Spectra of J/ψ in Heavy-Ion Collisions*, Phys.Lett. B664, 253–257 (2008), [0712.2407].
- [ZR11] X. Zhao and R. Rapp, *Medium Modifications and Production of Charmonia at LHC*, Nucl.Phys. A859, 114–125 (2011), [1102.2194].
- [ZSW09] K. Zapp, J. Stachel and U. A. Wiedemann, *A Local Monte Carlo implementation of the non-abelian Landau-Pomeranchuk-Migdal effect*, Phys.Rev.Lett. 103, 152302 (2009), [0812.3888].
- [ZSW11] K. C. Zapp, J. Stachel and U. A. Wiedemann, *A local Monte Carlo framework for coherent QCD parton energy loss*, JHEP 1107, 118 (2011), [1103.6252].
- [Zwi04] B. Zwiebach, *A first course in string theory*, Cambridge, UK: Univ. Pr., 2004.
- [ZWW04] B.-W. Zhang, E. Wang and X.-N. Wang, *Heavy quark energy loss in nuclear medium*, Phys.Rev.Lett. 93, 072301 (2004), [nucl-th/0309040].
- [ZXZ10] K. Zhou, N. Xu and P. Zhuang, *Transverse Momentum Distribution as a Probe of J/ψ Production Mechanism in Heavy Ion Collisions*, Nucl.Phys. A834, 249c–252c (2010), [0911.5008].
- [ZZX07] X. Zhang, D. Zhou and W. Xiang, *Dead cone effect of heavy quark in medium*, Int.J.Mod.Phys. E16, 2123–2129 (2007).

Index

- AdS/CFT correspondence, 13, 18
Asymptotic freedom, 7, 16
- BOLTZMANN distribution, 96, 100–101, 104, 176
BOLTZMANN equation, 77, 93
BOSE-EINSTEIN distribution, 96, 98
- Chiral symmetry, 6
Coalescence, 14, 82, 124, 156
Cold nuclear matter effect, 12, 14, 87–91, 151
Color glass condensate, 10, 12, 92
Color superconductivity, 8
Confinement, 6, 8, 17
COOPER-FRYE freeze-out, 11
Coupling, 6
 constant, 97, 107
 running, 7, 30–32, 34–36, 49, 103–104, 107, 138, 168
CRONIN effect, 14, 88
- Dead cone effect, 18, 51–56, 64, 74, 110, 138
DEBYE mass, 29, 168
DEBYE screening, 22, 29–30, 67, 71, 168
 improved, 20, 101, 107–109, 111, 122
- Eikonal approximation, 40, 41
Elliptic flow, 12, 16, 18
- Factorization scale, 14, 84, 87
FERMI-DIRAC distribution, 96, 98
FEYNMAN gauge, 50
FONLL heavy quark production, 87
Fragmentation, 14
 light quark, 139
 PETERSON, 81, 124
- Gauge invariance, 50, 51
- Glasma, 10
GORDON identity, 40
- Hard-thermal-loop approximation, 96, 99, 101–103
Heavy flavor decay, 17, 82, 122
HIGGS boson, 6, 7
Hydrodynamics, 10, 13, 93
- JÜTTNER distribution, 104
- Langrangian of QCD, 6
Lattice QCD, 8
LANDAU-POMERANCHUK-MIGDAL effect, 60–65, 110, 111, 115, 138, 140
- MANDELSTAM variables, 27–29, 50, 66, 98, 167–168
- Matrix element, 25
 $gQ \rightarrow gQ$, 28, 32
 $qQ \rightarrow qQ$, 32
 $gg \rightarrow ggg$ (exact), 66
 $qq' \rightarrow qq'g$ (exact), 66
 $qQ \rightarrow qQg$ (exact), 66
 GUNION and BERTSCH (improved), 45
 GUNION and BERTSCH (original), 44
 light quark $2 \rightarrow 2$, 168–172
- MATSUBARA frequency, 36
MC@NLO, 81
Medium modified fragmentation function, 14, 139
METROPOLIS algorithm, 176–177
Mini-jet model, 10, 92
- Natural units, 25, 167
Nuclear absorption, 88
Nuclear modification factor, 15–16, 18, 85
- p+A collision, 12, 22

Parton distribution function, 14
Parton hadron duality, 82
Perturbative QCD, 7, 77
PETERSON fragmentation, *see* Fragmentation
PYTHIA, 10, 81, 82, 91

QCD phase diagram, 8–9

Rejection sampling, 175–176
Relative velocity, 25
Renormalization scale, 14, 30, 84
Ridge in two particle correlations, 12

Shadowing, 14, 87
Spontaneous symmetry breaking, 5, 6

Test particle method, 78
Thermalization, 92
Transport cross section, 136
Transport model, 10, 13, 77, 122

Acknowledgements

First of all I would like to thank Prof. Carsten Greiner for giving me such an interesting topic for my PhD thesis and for his helpful and continuous supervision throughout the last years. He always offers good advice, valuable insights as well as constructive suggestions and supports me in all my endeavors.

I am also very grateful to Prof. Xu Zhe who supervised me as well during his time in Frankfurt. We have had many interesting discussions about BAMPS and my work in particular and physics in general—even after he moved to Beijing.

Special thanks go to Dr. Oliver Fochler and Florian Senzel for proof-reading this thesis and many fruitful discussions about physics-related—and also non-physical—topics. I particularly enjoyed the nice and cooperative working atmosphere within our group. The persons responsible for that include Philipp Bahavar, Max Beitel, Ioannis Bouras, Dr. Gerhard Bura, Dr. Andrej El, Dr. Oliver Fochler, Dr. Kai Gallmeister, Moritz Greif, Prof. Carsten Greiner, Dr. Hendrik van Hees, Benjamin Linnik, Alex Meistrenko, Dr. Frank Michler, Felix Reining, Julian Schmidt, Florian Senzel, Christian Wesp, and Prof. Xu Zhe. I am also thankful to Denise Meixler for helping with all administrative issues.

Sincere thanks go to Prof. André Peshier for many insightful discussions on the improved screening procedure derived from HTL calculations and the kind hospitality at the University of Cape Town. A fruitful exchange on this topic as well as on the GUNION-BERTSCH matrix element has also been established with the Nantes group around Prof. Pol Gossiaux, Prof. Jörg Aichelin, and Prof. Thierry Gousset. I appreciate the many helpful discussions and the kind hospitality in Nantes, where we performed important comparisons between our models.

I am very grateful to Prof. Xu Zhe and Prof. Zhuang Pengfei for inviting me to Tsinghua University in Beijing. A big “xièxie” goes to their group for introducing me to the Chinese culture and making my stay very pleasant. In particular with Dr. Liu Yunpeng and Zhou Kai, I performed several model comparisons and gained insightful knowledge on the J/ψ sector.

I would like to thank Prof. Marcus Bleicher, Prof. Dirk Rischke, Prof. Owe Philipsen, and Prof. Elena Bratkovskaya for helpful discussions as well as interesting questions concerning this work. Sincere thanks go to Prof. Marcus Bleicher for reviewing this thesis. It was always a pleasure to have insightful discussions with Thomas Lang, Dr. Hendrik van Hees, and Prof. Marcus Bleicher, who study heavy flavor in UrQMD.

Furthermore, I want to thank Dr. Raktim Abir, Dr. Mauricio Martinez Guerrero, and Prof. Munshi Mustafa for our fruitful collaboration on the calculation of the GUNION-BERTSCH matrix element for massive quarks in FEYNMAN gauge, which proofed to be an efficient collaboration between India, Spain, and Germany—based entirely on Skype and e-mails.

Furthermore, I would like to thank (omitting the titles in the following) Anton Andronic, Steffen Bass, Andrea Beraudo, Christopher Coleman-Smith, Thorsten Dahms, Andrea Dainese, Gabriel Denicol, Magdalena Djordjevic, Adrian Dumitru, Min He, Will Horowitz, Andre Mischke, Berndt Müller, Mustafa Mustafa, Ralf Rapp, Carlos Salgado, Björn Schenke, Konrad Tywoniuk, Sascha Vogel, Ramona Vogt, Xunlei Wu, and Nu Xu for many fruitful and interesting

discussions about theoretical and experimental issues.

I am very grateful to Prof. Harald Appelshäuser for his continuous interest in my work and his constructive questions at our half-yearly PhD committee, where he helped to ensure that my work is still on track. Many thanks go to Prof. Henner Büsching for several stimulating discussions and his organization of the H-QM lecture weeks. To this end, I would like to thank all other participants and the lecturers for providing an insightful and enjoyable time during these events.

I am also very thankful for financial support from the Helmholtz Research School for Quark Matter studies (H-QM), the Helmholtz Graduate School for Hadron and Ion Research (HGS-HIRe), the German Academic Exchange Service (DAAD), the Helmholtz International Center for FAIR (HIC4FAIR) within the framework of the LOEWE program launched by the State of Hesse, and the Bundesministerium für Bildung und Forschung (BMBF). The numerical computations have been performed at the Center for Scientific Computing (CSC) at the Goethe University Frankfurt.

Last but not least I would like to thank my family for their continuous support.